CRANFIELD UNIVERSITY

Charilaos Zervos

The Application of Electrolytic In –Process Dressing to
Precision Grinding Processes

School of Applied Sciences

PhD Thesis

ProQuest Number: 10832186

ProQuest 10832186

Published by ProQuest LLC (2018). Copyright of the Dissertation is held by Cranfield University.

ProQuest LLC.
789 East Eisenhower Parkway
P.O. Box 1346
Ann Arbor, MI 48106 – 1346

CRANFIELD UNIVERSITY

School of Applied Sciences

PhD THESIS

Academic Year 2006-2007

Charilaos Zervos

The Application of Electrolytic In –Process Dressing to
Precision Grinding Processes

Supervisors: D. Stephenson – M. Robinson

June 2007

ABSTRACT

Electrolytic In-Process Dressing (ELID) has attracted a lot of attention in recent years as it is a promising method of grinding a wide range of materials, including ones that are difficult to machine, to high quality finishes. The EC funded project Nanogrind undertook the construction of a high precision grinding machine which will incorporate an ELID system, applying the technique on a spherical wheel for the production of components with intricate geometries (e.g. freeforms, aspherics).

In this project, the main objective was to understand the basic features of ELID, such as the electrochemical properties of the oxide layer and its effect on the final finish of the produced components (glass, a hard and brittle material was the main focus).

Acoustic emission studies, a promising in-process monitoring tool, verified the effectiveness of ELID grinding when the contact area between the wheel and workpiece is increased. Compared to conventional resin bond wheel grinding, ELID ground components were of higher quality with less damage introduced in them.

ELID current monitoring also gave excellent results when it was correlated to surface finish achieved across the surface of the testpieces ground.

Electrochemical Impedance Spectroscopy was an innovative technique that was applied in order to acquire basic information about the metal bond wheel, such as the charge transfer resistance. Its correlation to the oxide layer thickness gave an indication of the way corrosion rates change with the presence or not of an oxide film on the wheel surface.

Finally, sub-surface damage introduced into glass components was evaluated and was compared to the depths of damage predicted by theoretical models, giving further insight into the way the overall processing time of a component should be optimised in order to acquire high quality, damage-free finished components in a time efficient, cost effective way.

IF YOU CAN TALK WITH CROWDS AND KEEP YOUR VIRTUE,
OR WALK WITH KINGS--NOR LOSE THE COMMON TOUCH,
IF NEITHER FOES NOR LOVING FRIENDS CAN HURT YOU;
IF ALL MEN COUNT WITH YOU, BUT NONE TOO MUCH,
IF YOU CAN FILL THE UNFORGIVING MINUTE
WITH SIXTY SECONDS' WORTH OF DISTANCE RUN,
YOURS IS THE EARTH AND EVERYTHING THAT'S IN IT,
AND--WHICH IS MORE--YOU'LL BE A MAN, MY SON !

Rudyard Kipling

SUMMARY

This thesis is divided into 6 chapters

Chapter 1 is the literature review, focusing on four main topics:

a. Initially, basic concepts of grinding, critical depth of cut and chip thickness models are presented, along with the Zhang-Howes sub-surface damage prediction model.

b. The principles of Electrochemical In-process Dressing (ELID) are presented, as well as advances and applications of the technique in recent years

c. Electrochemical Impedance Spectroscopy (EIS) is also presented as a technique that is used to understand and evaluate parameters such as charge transfer resistance and oxide film resistance. With EIS being a new technique applied to the study of ELID, an insight into its principles is given.

d. Acoustic emission for in-process monitoring of precision grinding has been used in this project and some of its basic characteristics are presented.

In chapter 2 the experimental methods utilised are presented. A conceptual flowchart explains the logic and concepts that lead to specific choices of methods in this project and is presented along with a detailed description of the experimental equipment and methods used, as well as the experiments performed. Grinding Experiments were performed on two grinding machines (the Tetraform C and the Edgetek Sam) and acoustic emission monitoring of these experiments was implemented. EIS, FIB and SEM studies were undertaken, focusing on the grinding wheels used, both metal bond wheels with ELID and resin bond wheels. An innovative no-grit metal bond grinding wheel is used in order to study the way the build up and thinning of the ELID oxide fim affects the final surface finish achieved on testpieces. The sub-surface damage evaluation techniques are also presented along with a short reference to initial grinding fluid conductivity experiments.

In chapter 3, the results of these experiments are presented. The successful application of ELID grinding when the contact area between the wheel and the

workpiece increases is presented, together with acoustic emission results that prove the advantage of the technique over conventional resin bond wheel grinding. Monitoring of current flow during ELID grinding with a no-grit metal bond wheel shows the excellent correlation between current fluctuations and the achieved surface finish on glass testpieces. The condition of the wheel is also evaluated through the study of the results of EIS FIB and SEM experiments. EIS also allowed the calculation of parameters such as the charge transfer resistance and solution resistance that give insight to the way corrosion rates change with different oxide film thicknesses in different environments.

In chapter 4 the results are discussed, focusing on:

A. The correlation between oxide film thickness (theoretically predicted and experimentally observed) and charge transfer resistance and the way it affects the final surface finish achieved on glass test pieces.

B. Sub-surface damage characterisation and correlation to existing sub-surface damage and critical chip thickness models. In the work undertaken in this thesis, excellent correlation between predicted depths of damage and experimentally measured ones was observed.

C. Acoustic emission results and characterisation of the topography of both resin bond and metal bond wheels when grinding with ELID. Results indicate that loading seems to be an important issue when grinding with resin bond wheels over large contact areas but does not affect the ground components' quality during the application of ELID grinding

Chapter 5 presents the final conclusions that were extracted from this work and in chapter 6 some directions for future work are suggested.

CHAPTER 1: LITERATURE REVIEW

1.A THE GRINDING PROCESS

1.B ELECTROCHEMICAL IN-PROCESS DRESSING (ELID)

1.C ELECTROCHEMICAL IMPEDANCE SPECTROSCOPY

1.D ACOUSTIC EMISSION FOR MONITORING PRECISION CUTTING PROCESSES

CHAPTER 2: EXPERIMENTAL METHODS

2.A INTRODUCTION – NANO GRIND

2.B CONCEPTUAL FLOWCHART

2.C GRINDING EXPERIMENTS

2.D FIB, SEM AND IES STUDIES OF GRINDING WHEELS

2.E SUB-SURFACE DAMAGE (SSD) EVALUATION

3.D ELID GRINDING AND RESIN BOND WHEEL GRINDING STABILITY – ACOUSTIC EMISSION SIGNAL ACQUISITION

3.E GRINDING FLUID PROPERTIES

CHAPTER 4: DISCUSSION

4.A ANALYSIS OF EXPERIMENTAL RESULTS

4.B GENERAL COMMENTS

CHAPTER 5: CONCLUSIONS

5.A CONCLUSIONS

CHAPTER 6: FUTURE WORK

6.A FUTURE WORK

REFERENCES

APPENDIX

List of Figures

CHAPTER 3: EXPERIMENTAL STUDIES AND RESULTS

Figure 3.38: Time and Spectrum display when grinding with a (a) ELID wheel, and (b) resin bonded wheel at 180mm^2 wheel/workpiece contacting area

Figure 3.39: AE signals from a CIB bond wheel at different amounts of material removal (a) 71-75 mm^3, (b) 106-110 mm^3 (c) 110-114 mm^3 and (d) 114-118 mm^3

CHAPTER 4: DISCUSSION

Figure 4.1: Current and Voltage Pre-dressing curves

Figure 4.2: FIB picture for the estimation of the depth into which the fully grown oxide layer extends.

Figure 4.2: Resistance values distribution with oxide layer thickness

Figure 4.3: Linear distribution of experimental points in the values of charge transfer resistance and oxide layer thickness

Figure 4.4: Evolution of the ELID current and its imprint on the glass testpiece B

Figure 4.5: Depth of damage for BK7 testpieces under varying processing conditions

Figure 4.6: Depth of damage for BK7 testpieces when grinding with 2 µm ELID grinding wheel. Comparison between an as-received testpiece and a polished testpiece

Figure 4.7: Subsurface damage depth vs. feed rate (a.) and maximum chip thickness (b.) Comparison between experimental results and theoretical prediction

Figure 4.8: Subsurface damage depth maximum chip thickness. Position of Critical Chip thickness

List of Tables

CHAPTER 4: DISCUSSION

CHAPTER 1: LITERATURE REVIEW

1.A THE GRINDING PROCESS

1.A.1 INTRODUCTION

The grinding process is used to produce a high surface finish with a close tolerance and for machining hard materials. The process is a variation of polishing using abrasive materials held together by an adhesive generally in the form of a solid wheel. The wheel is rotated at high speeds and the circumferential surface of the rotating wheel is brought into contact with the material being machined. [1]

The most common types of grinding processes are:

-Cylindrical grinding: OD(Outside Diameter), ID (Internal Diameter), centerless and surface grinding.
-Cup wheel grinding (vertical spindle)

Figure 1.1 gives an overview of different grinding operations.
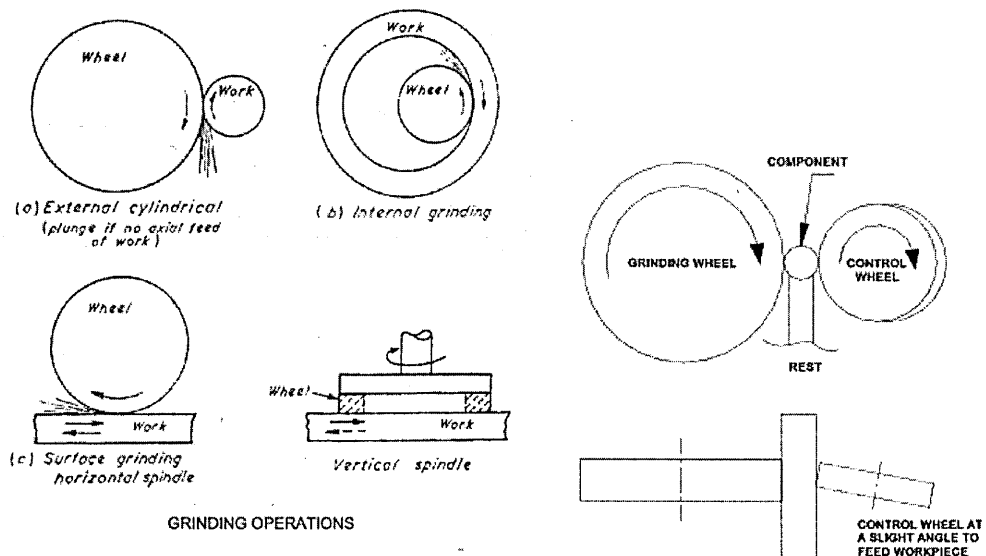
Figure 1.1: Overview of different grinding operations [1]

Hard and brittle materials such as ferrite, optical glass and ceramics have been used in many fields and still gain increasing attention. They are difficult to machine and it is hard to obtain good surface quality [2]. Removing material in a ductile way, rather than through fracture, it is possible to grind surfaces with high quality surface finish, with minimal or no damage introduced.

1.A.2 CRITICAL DEPTH OF CUT-CRITICAL CHIP THICKNESS MODELS

Bifano's critical chip thickness model [3] uses a fracture mechanics approach and is developed from indentation studies together with data generated from diamond grinding trials. The critical depth of penetration for initiating fracture is given by [3]

$$d_c = \psi \left[\frac{E}{H} \right] \left[\frac{K_c}{H} \right]^2 \qquad (1)$$

where

d_c is the critical penetration depth for fracture initiation

ψ is a dimensionless constant depending on indenter geometry

E is the Young's Modulus

H is the hardness, and K_c is the fracture toughness

Results from the ductile mode grinding of glass have been used to calculate a value for ψ by correlating measured values to the calculated critical depth predicted by equation 1. The point of transition to brittle fracture can be arbitrarily defined as a surface exhibiting 10% of surface fracture and 90% of apparent ductile removal during grinding [3]. The critical depth is then given by [3],[5]:

$$d_c = 0.15 \left[\frac{E}{H} \right] \left[\frac{K_c}{H} \right]^2 \qquad (2)$$

Blake and Scattergood have also studied the transition from ductile to brittle fracture using an "interrupted cut method" [4]. A fast tool servo was used to retract the tool rapidly from the surface of the workpiece to reveal the uncut shoulder region. This region was observed using an optical microscope to assess the point along the shoulder where transition from ductile to brittle fracture occurred. Knowing the machining parameters and tool geometry involved in each test, the critical chip thickness (d_c) for the onset of brittle fracture could be calculated. This demonstrated that a 'damage free' surface was not necessarily produced solely by a ductile mode of material removal. In fact ductile mode turned surfaces in silicon and germanium were found to be produced by a combination of brittle fracture and ductile mode removal mechanisms. This is shown in Figure 1.2. True ductile mode machining probably only occurs near the apex of the tool and the critical chip thickness (d_c) can be defined as that which does not propagate fracture damage beyond the finished surface plane of the workpiece.
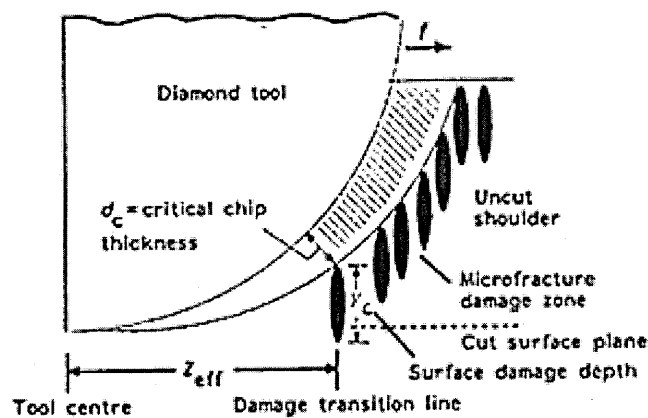
Figure 1.2. Diamond machining cutting geometry [4].

From this basis equation (3) can be used to predict the maximum feedrate (f_{max}) for a given tool such that microfracture damage does not propagate below the cut surface plane [5]:

$$f_{max} = d_c \sqrt{\frac{R}{2(d_c + y_c)}}$$

(3)

Where:

d_c is the critical chip thickness,

y_c is the depth of surface damage and

R is the tool radius.

The critical chip thickness determined from equation (2) for BK7 is 40-70 nm (the range being a function of the variation in measured hardness and fracture toughness). For BK7, according to Booij et al [6], E=581 GPa, Kc=50.86 MPa, and H= 55.2 GPa were chosen, which resulted in a critical depth of 64 nm.

The maximum chip thickness, which depends on the cutting tool geometry, the depth of cut, cutting velocity, and work speed, can be calculated by the expression [7]

$$h_{max} = \left(\frac{4V_w}{V_c Cr} \sqrt{\frac{a_e}{d_c}} \right)^{\frac{1}{2}}$$

(4)

where

V_c is the speed of the wheel;

V_w is the work speed;

r is ratio of mean chip width to chip thickness;

d_c is the wheel diameter;

a_e is the depth of cut;

C is the active grit concentration

Equation (4) predicts a maximum chip thickness of 50 nm at the ductile/brittle boundary, a value similar to that predicted from equation (2). Thus, ductile regime grinding conditions can be identified based on the critical chip thickness concept (i.e. the force per grit is below a critical value) and damage free surfaces can be produced that exhibit surface finish in the range 1-3 nm Ra.

A different expression for maximum chip thickness is proposed by Fathima et al. [34]:

$$h_{max} = 2L_s \left(\frac{V_w}{V_c} \right) \sqrt{\frac{a_e}{d_c}} \quad (5)$$

where Ls is the distance between adjacent grits.

1.A.3 KINEMATICS OF CUP WHEEL GRINDING

Figure 1.3 illustrates the kinematics of the cup wheel grinding process as proposed by Weinert [8]. The primary material removal process occurs at the periphery of the grinding wheel, in a manner similar to external cylindrical grinding. However, since the complete grinding system has only a finite stiffness (for example due to the elasticity of the wheel, work holding and other components, the underside of the grinding wheel remains in contact with the workpiece surface, giving rise to a secondary material removal zone), figure 1.3 illustrates how this finite stiffness of the complete grinding system can be reduced to the response of individual abrasive grits. Thus, grits within the secondary material removal zone are also responsible for creating the final ground surface.
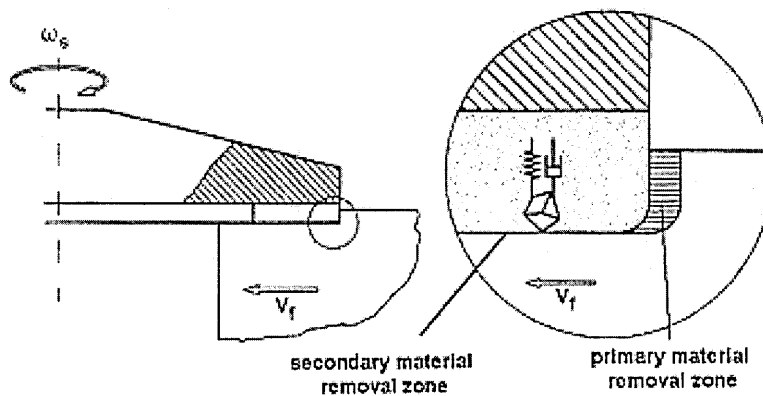
Figure 1.3: Kinematics of the cup wheel grinding process as proposed by Weinert [8]

The primary material removal zone can be considered to be a roughing process, while the secondary zone equates to a final finishing process. According to Weinert

{Weinert in [8]}, it is these different kinematics, characteristic of the cup wheel grinding process, that enable surface finishes to be generated typically three or four times better than for external cylindrical grinding. To ensure the best possible surface finish and minimal sub-surface damage it is essential to control the CBN grit/workpiece surface interaction within the secondary finishing zone.

1.A.4 SUBSURFACE DAMAGE EVALUATION

Grinding damage is induced by grinding forces, predominantly the normal force [9]. The normal force on a single grit that is proportional to the maximum chip thickness can be expressed as:

$$F_n = \alpha K_o h_{max}^{2(1-\varepsilon)} \qquad (6)$$

Where α is the ratio of the normal to the tangential grinding forces, and is a constant for a given grinding condition; K_o and ε are constants determined by the material properties of a given workpiece and h_{max} is the critical chip thickness. [9]

On the other hand, a correlation between the subsurface damage and externally applied load can be obtained [10]:

$$F_n \propto \delta^m \qquad (7)$$

The exponent m is in the range of $1/2 \leq m \leq 3/2$ for different loading conditions. By substituting equation (7) into equation (6) we then obtain:

$$\delta = \left(\Psi a_g\right)^\psi \qquad (8)$$

It is assumed that ψ is predominantly a function of material properties and Ψ a function of grinding parameters. Based on experimental results [9]:

$$\Psi = 200 \text{ and } \psi = 1/\log(\lambda H / K_c).$$

In the expression for ψ, the concept of using H/K_c as an index of brittleness, proposed by Lawn and Marshall [12], is used. The proposed model then becomes:

$$\delta = \left(200a_g\right)^{1/\log(\lambda H/K_c)} \qquad (9)$$

Shaw calculated that the mean force per grit would be dependent on the ratio of F_t (thrust component of the force) and F_c (cutting force component), undeformed chip thickness (h) and grit size (g) [11]:

$$F_t^{''} \propto \left(\frac{F_t}{F_c}\right)(gh)^{1/2} \qquad (10)$$

From the standpoint of a critical mean force per grit to avoid subsurface median cracks, the following should pertain:

• Small undeformed chip thickness h

• Small grit size g

• Small F_t/F_c

The third item, which is most important, explains why subsurface damage is particularly troublesome for very hard work materials and for very small undeformed chip size where the force ratio F_t/F_c is unusually large [11].

As previously indicated by Blake and Scatergood [4], as long as fracture damage does not propagate beyond the finished surface plane of the workpiece, damage free surfaces (and hence sub-surface) can be obtained. Thus, by grinding in a ductile regime, which can also be interpreted as producing chips with thicknesses under the critical one; it is possible to not introduce any subsurface damage in the finished component. Figure 1.4 [12] describes the simplified case of a Vickers indenter, P being the applied normal force, with (A) describing the initiation and (B) the propagation of median cracks which should be avoided in order to achieve the production of damage free components.
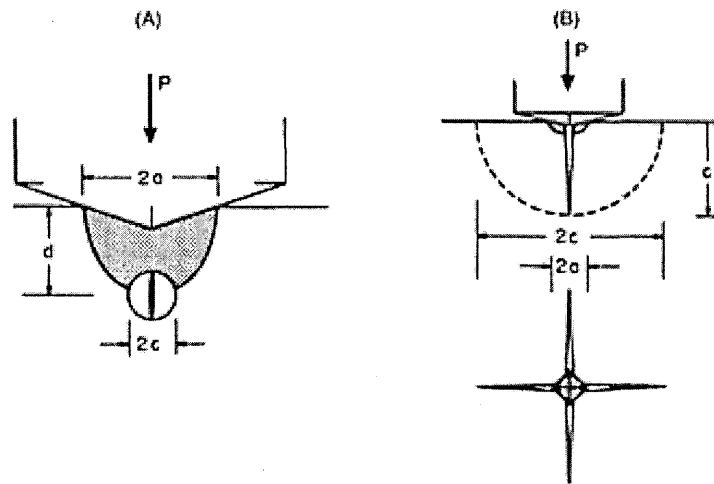
Figure 1.4: Idealised deformation/fracture patterns for Vickers indentation, showing (A) initiation and (B) propagation of median crack development [12]

Ohmori and Nakagawa correlated the amount of subsurface damage present with obtained surface finish on components [13] but as will be discussed in detail later on, this is not always the case.

1.B ELECTROCHEMICAL IN-PROCESS DRESSING (ELID)

1.B.1 INTRODUCTION TO ELID

Büttner and Lindenbeck first proposed electrolytic dressing of diamond-grit wheels in 1969 [14] in order to improve the grinding of steels. More recent work has been done by Nakagawa and Ohmori, who used this technique for the grinding of silicon [15] and since then, it has been applied for processing ceramics and steels [16], [17], [18], [19], [20]. ELID has been used for the grinding of silicon wafers [21], Cermet disposal tips [22], ferroelectric ceramics [23], TiAlN films [24], hard steels and aluminium alloys [25], quartz [26], Cerium-doped GdSi2O5 (used in applications of nuclear medical diagnosis and underground inspections) [27]

This technique is used to ensure an adequate grain exposure is maintained during grinding. In order to grind hard and brittle materials, the grinding wheel is initially prepared (dressed) in order to ensure diamond grit protrusion. During grinding, the grits wear away, and thus lose their cutting efficiency. This leads to worse grinding conditions and the ground components have poor surface quality. That is why the grinding procedure has to be stopped, in order for the wheel to be redressed so as sharp cutting grits to surface and continue with an effective grinding procedure.
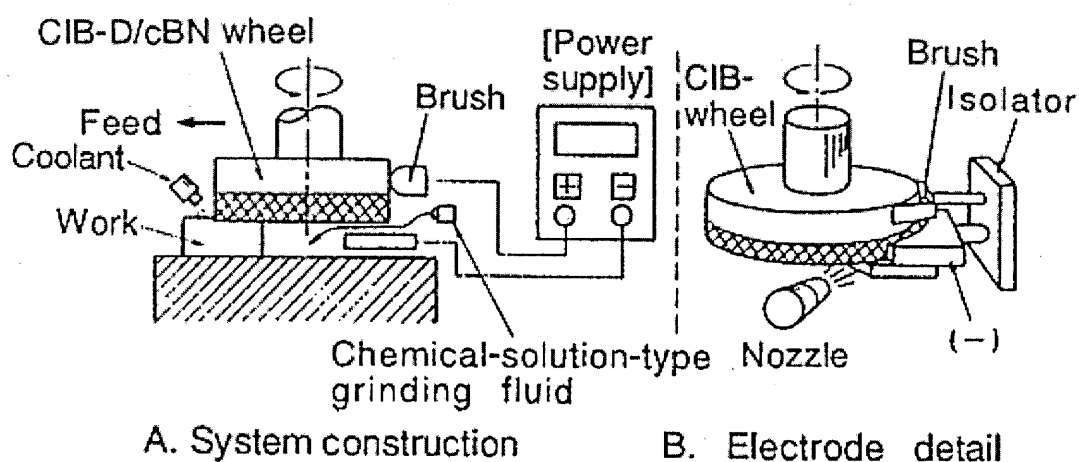
Figure 1.5: The essential features of the ELID system (cup wheel) [15]
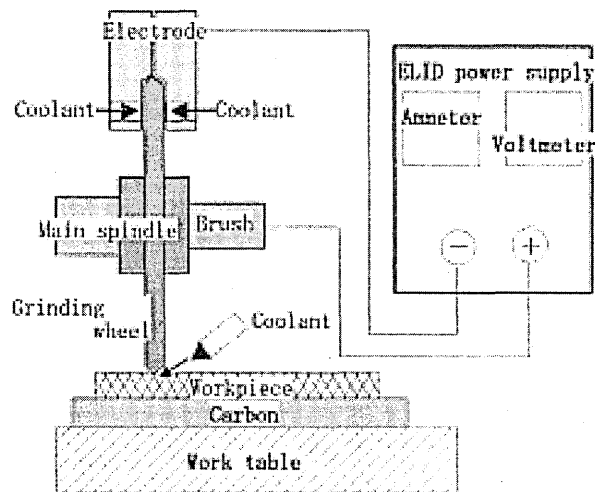
Figure 1.6: The essential features of the ELID system (peripheral wheel) [28]

The essential features of the ELID system are a metal-bonded grinding wheel, a power supply, a grinding fluid and an electrode. Configurations may vary as can be seen in the cases presented in figures 1.5 and 1.6 for the cases of a cup wheel and a peripheral wheel respectively [15], [28].

Its principle is that an insulated electrode is positioned close (at a distance of approximately 100 μm) to the grinding wheel surface whereas a brush-type electrode contacts the wheel. A water-based electrolyte is passed through the gap between the grinding wheel and the electrode and ensures electrical conduct between them.

Application of an electrical potential makes the wheel the positive pole and the stationary electrode the negative pole. Through ionisation of the metal bonded wheel, a ferrous-oxide layer is created (electrolysis occurs by the supply of electrical current), which is scraped off through friction between the wheel and the workpiece surface.

The nature of the process is electrochemical. The bond material of the grinding wheel is a metal. Through the applied voltage, a current passes through the wheel which leads to erosion of the bond material. The friable oxide that is produced is brittle and easily removed from the wheel during grinding and diamonds that are embedded deeper inside the grinding wheel reach the surface. In this way, sharp diamonds are continuously being exposed and so the grinding wheel remains effective for longer

periods of time. This ensures a continuous grain exposure of the wheel throughout the grinding process, which can be maintained even in ultra fine grinding.

1.B.2 WHEEL TRUING, ELECTROLYTIC PRE-DRESSING, IN-PROCESS ELECTROLYTIC WHEEL DRESSING

The main stages during the ELID procedure are:

I. WHEEL TRUING:

The surface of the grinding wheel that will be in contact with the workpiece is ground perfectly flat so that any vertical wheel-deflection is smaller in magnitude than the average grain size. This ensures full surface contact between the wheel and the workpiece and constant grinding forces.

II. ELECTROLYTIC PRE-DRESSING:

The water-based electrolyte that is used as the grinding fluid passes through the gap between the wheel and the electrode (which are connected to the positive and the negative pole of the power supply respectively). A brush electrode is in continuous conduct with the rotating wheel and thus the electrical circuit is completed. A square wave current is applied across the electrodes. It is characterised by a time on (t_{on}) and a time off (t_{off}) as shown in the following figure. (figure 1.7)
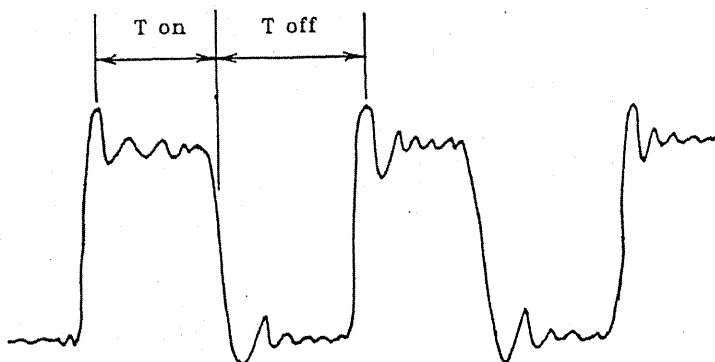
Figure 1.7: Pulse waveform provided by the power supply [29]

Simultaneous electrolysis of the bond material and the water in the grinding liquid occurs resulting in the formation of the ferrous oxide layer and subsequently the

electrolytic erosion of the surface of the metal bonded wheel. This part of the process provides the required even protrusion of the diamond grits from the surface of the wheel.

ELECTRIC CHARACTERISTICS OF THE PRE-DRESSING STAGE

The formation of the surface oxide layer affects the electrical circuit characteristics. Initially the wheel is conducting and the current and voltage across the electrode are at a maximum and a minimum value respectively. As the oxide layer begins to form and increases in thickness, the conductivity decreases resulting in a drop in the value of current and a corresponding increase in the value of the voltage (see figure 1.8 below).
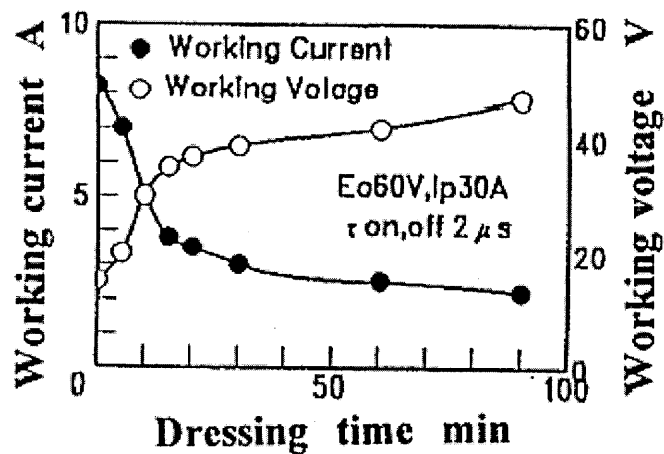
Figure 1.8: Voltage and current during the pre-dressing phase [17]

This process continues until the voltage reaches a maximum value, which is governed by the power supply settings. This saturation of the characteristic is an indication of the completion of the wheel pre-dressing stage.

III. IN-PROCESS ELECTROLYTIC DRESSING

The grinding procedure begins right after the pre-dressing. Machining of the work piece causes the surface of the wheel to wear away. The brittle oxide layer wears away easily compared with a non-electrolytically dressed cast iron bonded wheel [15], [30], [31]. This aids the removal of debris and prevents the "glazing" of the wheel. The removal of the oxide layer causes a subsequent decrease of resistivity and thus, a

rise in current and a drop in voltage is observed. This induces a further formation of the oxide layer and so a dynamic equilibrium is achieved where a constant-thickness oxide layer is maintained. The result of this controlled erosion of the wheel surface is the constant protrusion of the diamond grits on the wheel. Figure 1.9 shows schematically the phenomena during the pre-dressing and in-process dressing stages.
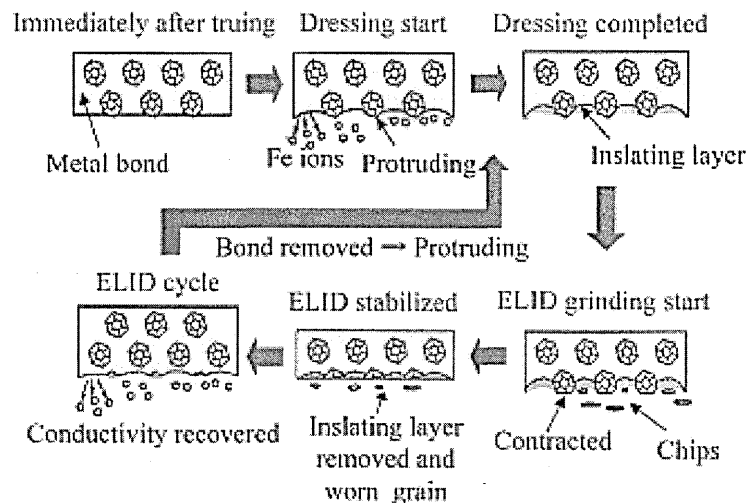
Figure 1.9: Schematic representation of the electrolytic dressing cycle [26]

Figure 1.10 shows the change in the values of voltage and current during the pre-dressing period and their stabilisation once the grinding procedure has started. The formation of insulation on the wheel surface during the electrolytic pre-dressing as a result of the hydration or oxidation of the bond material leads to a reduction and finally the stabilisation of the electrolytic effect [32].After grinding is initiated, the oxide layer becomes thinner but the electrical conductivity of the wheel increases as well and by this electrolytic process, the thickness of the oxide layer is maintained [31].

Electrolytically assisted grinding with cast iron bonded wheels has the advantage of reduced wheel wear over the conventional resin-bonded wheels [33]. Wear on the softer resin bond relies on self-dressing by the grinding debris. These wheels do not achieve dynamic equilibrium by this process alone and so they glaze. Furthermore, there is no suitable in process dressing technique for this kind of wheel.
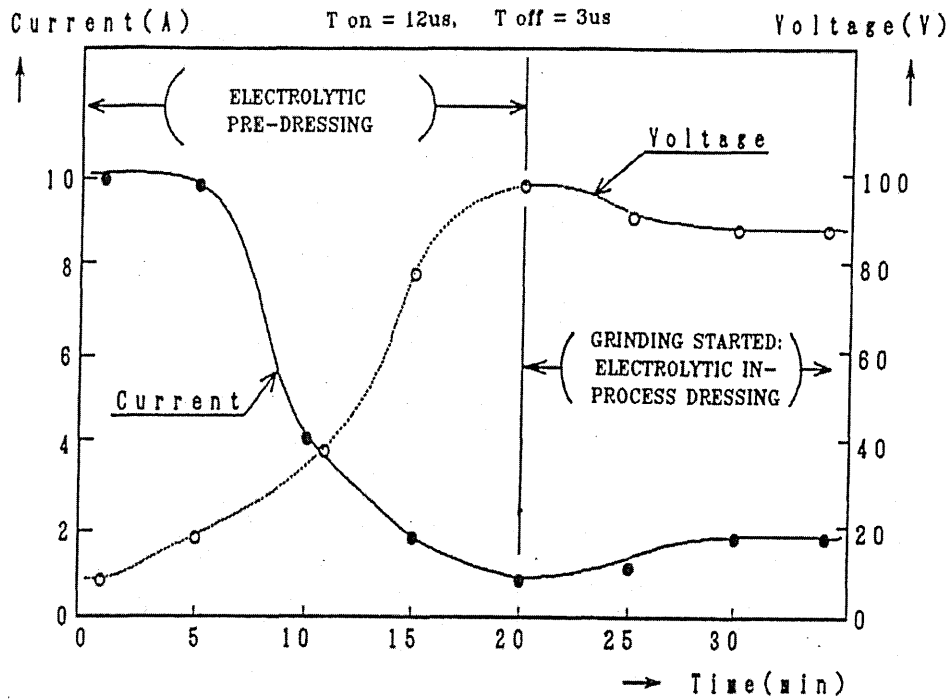
Figure 1.10: Voltage and current characteristic for the ELID system [15]

Fathima et al. correlated wheel wear with the maximum grit holding force exerted by the bond strength (f_h) and the grinding force per grit (f_g) [34]. When the holding force f_h is lower than f_g (dislodged grit), the grit cannot penetrate into the workpiece and is removed from the matrix due to the hardness of the workpiece material. For a sharp grit f_h is greater than f_g and the grit penetrates and cuts the workpiece material. The depth of penetration depends on the sharpness and size of the grit. Due to grit wear, the grit grinding force gradually increases and when fg exceeds fh, cracks are propagated throughout the wheel-working surface. When the insulating layer is separated from the wheel surface due to macrofracture, the electrical conductivity of the grinding wheel is increased and that stimulates ELID. [34]

1.B.3 ELECTROCHEMICAL REACTIONS

At the beginning of the electrolysis, the current passes through the electrolyte and converts the metallic irons into oxides and hydroxides [11].

These reactions continue until a non-conductive oxide layer (Fe_2O_3) is formed on the surface of the grinding wheel. The non-conductive oxide layer deposition on the wheel surface prevents the bonding material from further oxidising, which is supported by the constant dressing current and voltage [34].

In the process of electrolysis, an anodic reaction is generated on the wheel surface, the main chemical reaction being as follows. [35]

Positive electrode:

$$Fe \rightarrow Fe^{2+} + 2e \qquad\qquad (A)$$
$$Fe \rightarrow Fe^{3+} + 3e^-$$

Negative electrode:

$$O_2 + 2H_2O + 4e \rightarrow 4OH^- \qquad\qquad (B)$$

The F_e ion and the hydroxyl ion from the above two reactions integrate with the following reactions:

$$Fe^{2+} + 2OH^- \rightarrow Fe(OH)_2 \qquad\qquad (C)$$
$$Fe^{3+} + 3OH^- \rightarrow Fe(OH)_3$$
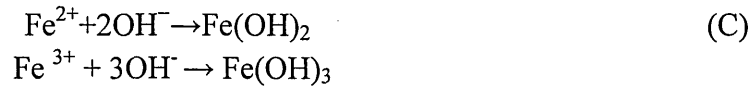
It can be seen from chemical reaction (C) that the main ingredients of the passivating film on the cast iron bond wheel surface are $Fe(OH)_2$ and $Fe(OH)_3$. In the process of electrolysis, the graphite or copper electrode as negative electrode cannot be electrolyzed, so there is no electrode loss [35]

1.B.4 ELID CHIP THICKNESS

Critical chip thickness has been shown to be also affected by the bond strength of the grinding wheel [34]. Hence, the general expression for h_{max} can be re-written as:

$$h_{max} = 2kL_s \left(\frac{V_w}{V_c} \right) \sqrt{\frac{a_e}{d_s}} \qquad (11)$$

Where k is the ELID dressing constant and is dependent on

I_p: Peak current

V: Voltage and

R_c: current duty ratio [34].

Changing the duty ratio with a constant current intensity led to decreasing bond strength and a corresponding increase in the oxide layer thickness. These experimental results show that maximum chip thickness varies with bond strength and explains the presence of the ELID dressing constant in the expression for maximum chip thickness [34].

1.B.5 OXIDE LAYER THICKNESS / WHEEL PROFILE

Pan et al present details on the oxide layer grown when using an ELID grinding system with a minimum quantity of fluid. According to their studies, for varying mist supplies the thickness varies somewhere between 25 and 45 microns [36]. Oxide thickness measurements are also presented by Ohmori and Nakagawa [37] for different metal bonded wheels (cast iron, cobalt and bronze bond wheels). Different oxide layer thicknesses are also observed after pre-dressing when the power source and the grinding fluid are changed. The thicknesses observed here vary between 40 and 60 microns. *Fathima et al* observe an increase in wheel diameter of a peripheral cast iron bond wheel after pre-dressing by approximately 200 microns. A wheel was partially dressed (without rotating) and its profile was consequently examined. When comparing the pre-dressed and undressed wheel profile, the pre-dressed portion of the wheel shows a significant increase in diameter [34].

Oxide layer thickness has also been measured after grinding samples. Kim and Lee [11] propose an optimum in process electrolytic dressing technique, during which, the oxide layer is kept constant throughout 5, 10, 15 and 20 minutes of grinding of sintered carbide at a thickness of approximately 2 microns. When dressing control is not utilised, oxide layer thickness fluctuates randomly.

A method is also proposed to measure the insulating layer in real time (during grinding) using two gap sensors, a capacitance type and an eddy current type [38], [39].

For three different grinding conditions, varying the supplied voltage and peak current during the grinding process, the thickness experimentally measured with the two gap sensors varies between 4 and 6 microns, with the more aggressive current and voltage conditions resulting in the thicker insulating layer.

1.B.6 EFFECT OF ELID

As it has already been mentioned, when the pre-dressing stage is completed, the grinding procedure begins and the friable, brittle oxide layer wears away easily and prevents glazing of the wheel and the embedment of swarf. The following picture comparison in figure 1.11 shows the difference observed on two metal-bonded grinding wheels (these examples are cup-wheels used on the Tetraform-C at Cranfield University) after the grinding operation is finished. One of them was used without ELID and the other one was used with the application of ELID.

The difference in the grit protrusion is readily obvious, as the grits on the wheel, which was used without ELID, have been worn out. On the other hand, the grits on the wheel that was used with ELID applied still protrude evenly throughout the grinding surface. The characteristic red colour of the wheel on the second picture is due to the colour of the oxide produced during the electrolytic reactions that take place.

Other effects of ELID include lower grinding forces (normal and tangential) when compared to conventional grinding processes ([30], [34], [55]) which ensure the production of higher quality components in terms of surface finish and sub-surface damage introduced. Even lower grinding forces and improved surface finish are achieved by the application of optimum In-Process Electrolytic Dressing, as proposed and reported by Kim and Lee [40], [53].
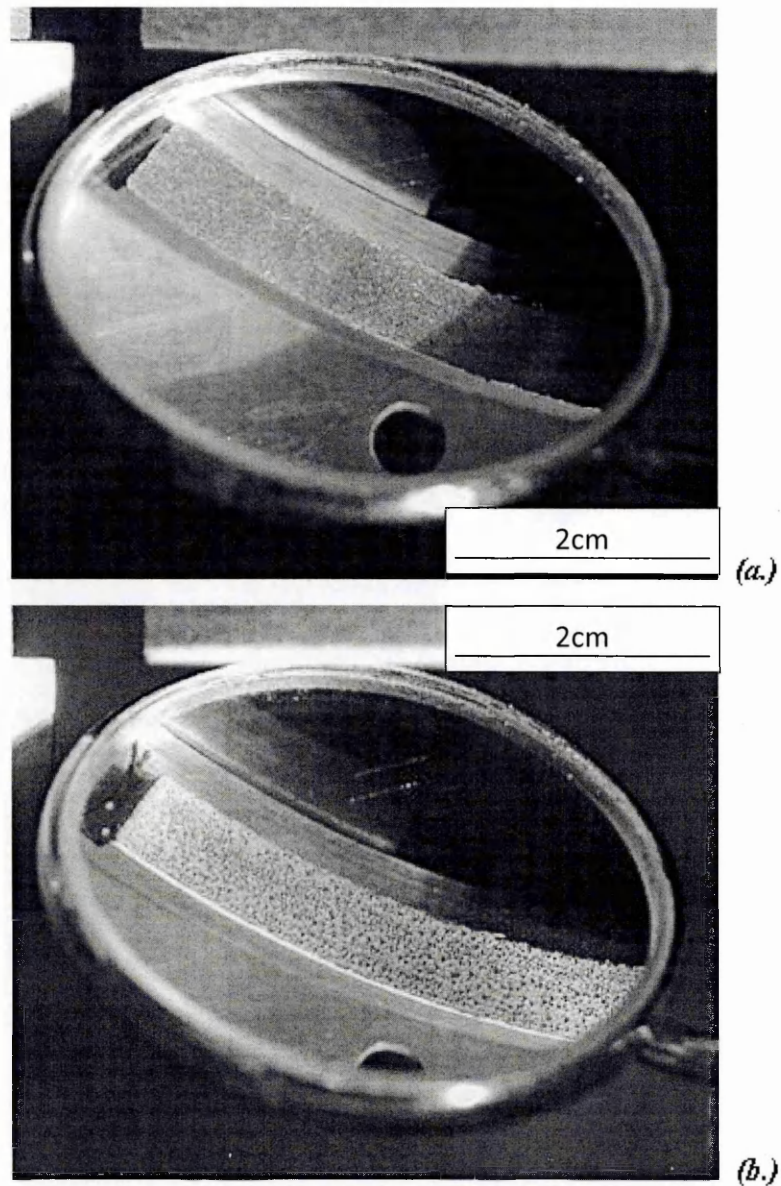
Figure 1.11: The grinding wheel after being used without (a.) and with ELID (b.)

1.B.7 ELID AND FARADAY'S LAW

ELID involves an electrochemical process, in which the electrolysis plays a role in the formation of the insulating oxide layer on the surface of the grinding wheel. Faraday's Law for electrolysis has been used to develop an expression for the theoretical volumetric material removal [40], as follows:

$$v_{vol} = \frac{MIt}{zF\rho_{bond}} \quad (12)$$

Hence:

$$\frac{dv_{vol}}{dt} = \frac{MI}{zF\rho_{bond}} \quad (13)$$

where M is the atomic weight of the reacting ions; I is the current; t is the reacting time; z is the valence of the reacting ions; F is Faraday's constant; ρ_{bond} is the density of the metal bond. From these equations, the rate of metal removal is proportional to the current. High current density means high reaction rates. The current and its distribution over the metal surface are one of the determining parameters in the electrolytic process.
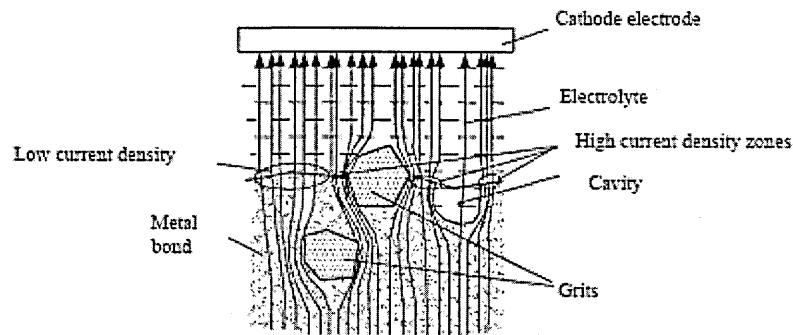
Figure 1.12: Current distribution in the metal bond and electrolyte [41]

In the electrolytic system, if the anode grinding wheel is considered to be a homogeneous metal without the abrasive grains, the current density on the wheel surface should be approximately uniform without considering the boundary conditions [41]. Actually, the grinding wheel is a porous metallic electrode with a rough surface and many non-conductive abrasive particles embedded inside. The abrasive grains, such as diamond, can be considered to be an insulator and inert to electrolysis. A non-uniform current distribution between the bulk of the electrolyte and the metal surface can therefore be expected. The field shown in Figure 1.12 can be used to represent current flow in the metal bond and electrolyte, in which the

20

streamlines represent the current density. It can be seen that the abrasive grains and cavities disturb current flow. They cause a local increase in flux concentration around their periphery. The geometry and the distribution of the inner grits can also influence the current distribution at the top layer of the metal matrix. [43] The state of field concentration will increase with the increment of the grain size and density of the grain distribution in the metal matrix. These indicate that the uneven electrochemical reaction across the metal matrix surface of the grinding wheel will be caused by the non-uniform current distribution, which causes different electrolytic reaction rates on the metal bond surface. [41]

1.B.8 ELID: NEW CONCEPTS AND APPLICATIONS

The minimal requirements of components in order to implement ELID grinding in any grinding machine, makes it easy to install at a low cost. The FANUC ROBOnanoUi [26] (figure 1.13) is an example of a 5-axis grinding machine , is an example of that with minimal requirements and cost for ELID implementation.
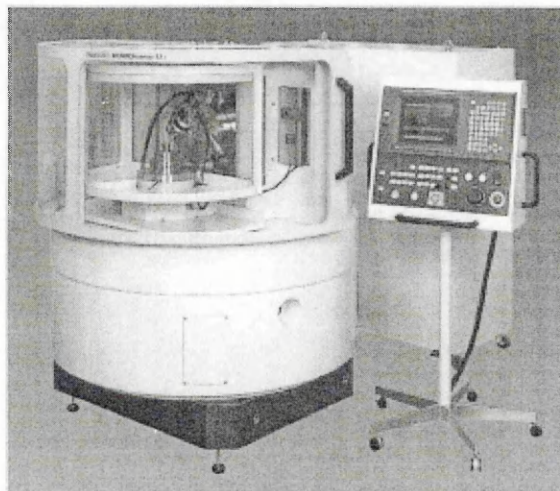
Figure 1.13: The FANUC ROBOnanoUi grinding machine [26]

The ELID method has proved to be a successful dressing method for metal bonded wheels in high efficiency precision surface grinding of various hard-to-machine materials and external cylindrical grinding. Nevertheless, in the case of internal cylindrical grinding, especially when the diameter of the workpiece is slightly bigger

than that of the grinding wheel, it becomes very difficult to fix a dressing electrode mounted parallel to the wheel as in the common ELID system. Moreover, there could be electrolytic corrosion on the ground surface if the workpiece is conductive, in which case electrolysis occurs between the dressing electrode and the workpiece.

To cope with these problems, an electrolytic interval dressing technique with a pipe shape dressing electrode (referred to as "ELID II") has been developed initially on an ordinary grinding machine [42], [26]. However, in ELID II, additional dressing time is unavoidable and sometimes it is still very difficult to ensure sufficient dressing when grinding a long internal surface and the wheel mandrel in this case must be longer because of the additional space necessary for the dressing electrode (figure 1.14), resulting in the weakening of the rigidity of the wheel mandrel.
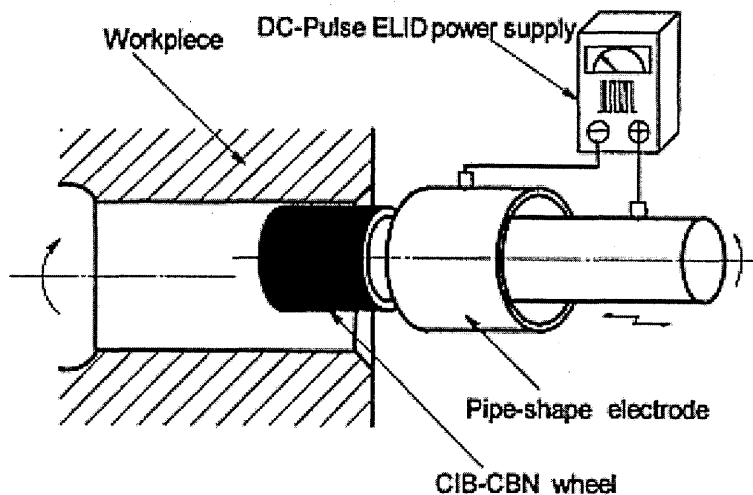
Figure 1.14: The ELID II system [42]

The existing ELID grinding process is not suitable for micro-hole machining because of the difficulty in mounting of electrodes. Using the combination of sintered metal-bonded grinding wheels of small diameter, Electric Discharge Truing (EDT) and Electrolytic Interval Dressing (ELID-II) could solve the problems in micro-hole machining. Figure 1.15 shows the novel method of micro-hole machining using ELID –II [44].
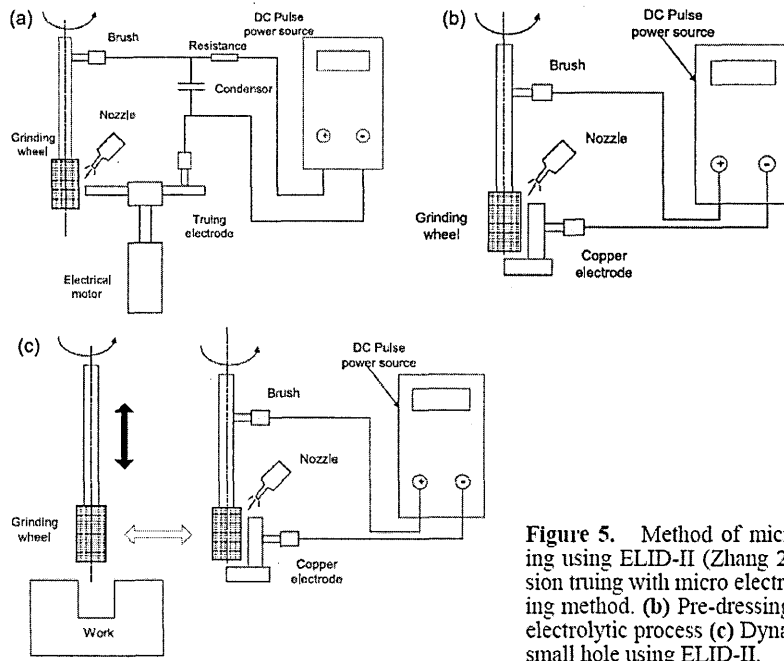
Figure 5. Method of micro-hole machining using ELID-II (Zhang 2000). (a) Precision truing with micro electric discharge truing method. (b) Pre-dressing with nonlinear electrolytic process (c) Dynamic grinding of small hole using ELID-II.

Figure 1.15: Method of micro-hole machining using ELID-II (after Zhang in [44])

A new kind of grinding wheel, a metal-resin-bond CBN (MRB-CBN) wheel, has been developed and used for internal cylindrical grinding (referred to as ELID III). In ELID III, the dressing electrode is removed and the workpiece itself acts as the dressing electrode (figure 1.16) [42], [45].
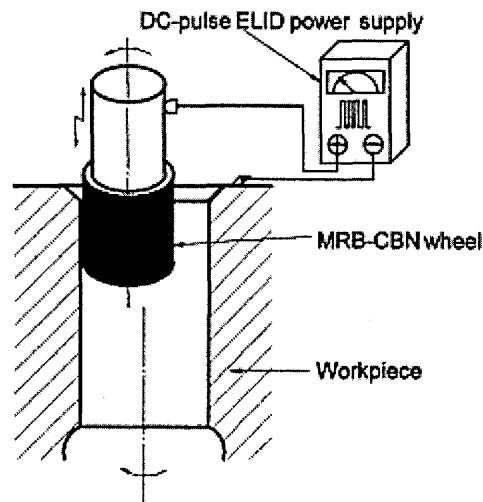
Figure 1.16: The ELID III system [42])

Theoretically the metal-bond is removed by electrolysis, but the experimental results showed that the grinding wheel surface contains cavities, which are caused by electric

discharge. When high electric parameters are chosen, the amount of electric discharge increases and causes damage on both the wheel and ground surfaces. For better surface finish, low voltage, low current, low duty ratio and low in-feed rate should be selected [44].

The difficulties of using electrode-less in-process dressing could be eliminated with the application of ELID-IIIA. Figure 1.17 shows the ELID-IIIA principle, and the difference between ELID-III and ELID-IIIA. The alternative current produces a thick oxide layer film on the surface of the workpiece, which prevents direct contact between the grinding wheel and the workpiece. Thus the electric discharge between the wheel and workpiece is completely eliminated and the ground surface finish is improved [44].
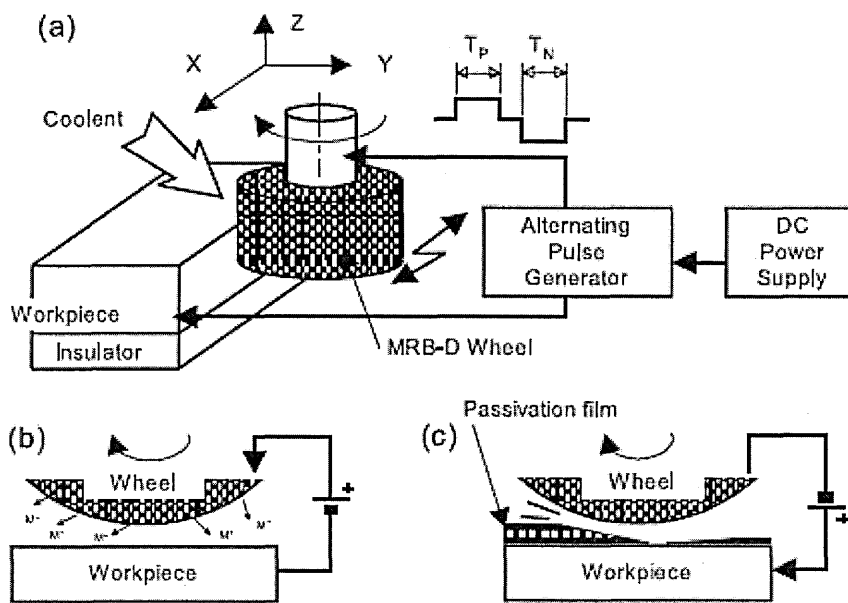
Figure 1.17: Schematic diagram of ELID-IIIA (a) ELID-3 machining system with alternating cuttent. (b) ELID without electrode. (c) Electrolysis of workpiece. (Lim in [44])

Further work based on the ELID principles led to mirror surface finishes on components ground on a double-sided lapping machine. Constant pressure grinding is known to produce good results in terms of surface roughness and flatness and both

single-sided and double-sided grinding, with the use of fine grain wheels yield good results. The main feature of double-sided grinding is that same size wheels are mounted in the top and bottom spindles and the work pieces which were fixed by a holder are sandwiched between the two wheels. [46]

A new electrical grinding technique was proposed for application on biomaterials (such as stainless steels and titanium alloys) in order to achieve enhanced chemical stability and wear resistance [47]. The formation of a stable oxidized layer can lead to significant improvement of the surface properties of the processed component. During the proposed process, the applied potential decomposes the conductive alkaline grinding fluid, thereby generating hydroxide ions. When appropriate positive potential is applied to the work piece, free hydroxide ions are attracted to the surface being processed resulting in the formation of a stable oxide layer. Samples prepared with both alumina polishing and electrical grinding where analysed using energy dispersed X-ray diffraction. Elemental oxygen was detected on the electrically ground samples which supports the hypothesis that the electrochemical reaction described above promotes oxide-layer growth. Corrosion resistance was also evaluated using the AC impedance method, scanning from low to high frequencies (10 mHz to 20 KHz), and lower corrosion rates were observed on the electrically ground workpieces than on the alumina polished ones.
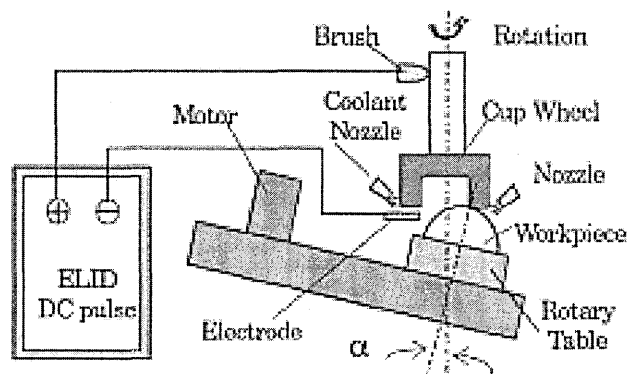
Figure 1.18: Schematic of ELID CG grinding [48]

ELID is also used in grinding of spherical and microspherical lenses using cup wheels to generate the spherical surface (CG-grinding), mounting the workpiece on a tilted rotary table [48] as shown in figure 1.18.

Theoretical calculation of the radius of curvature of the produced lenses comes from equations:

$$R= D_{si}/(2\sin\alpha) \quad (14)$$

For convex lenses and

$$R= D_{so}/(2\sin\alpha) \quad (15)$$

For concave lenses.

R is the curvature radius of the produced lenses, D_{si} is the internal diameter of the grinding wheel, D_{so} the external diameter of the grinding wheel and α is the inclination angle of the rotation axis of the workpiece from that of the wheel. [48]

The results indicate ELID CG-grinding to be a promising method in order to fabricate such components and the following figures (figures 1.19 and 1.20) show the shape accuracy achieved for spherical and microspherical lenses respectively.
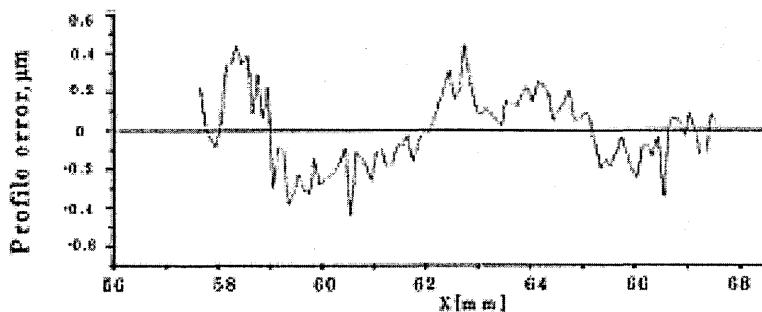
Figure 1.19: Shape accuracy of produced spherical lens [48]
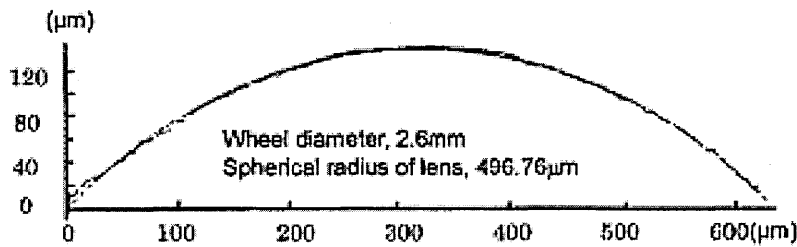
***Figure 1.20: Shape accuracy of produced microspherical lens* [48]**

Figure 1.21 illustrates a solution to issues relating to grinding and ELID grinding, in order to overcome problems such as fluid delivery. The new type of wheel that was proposed, with its innovative design, helps the efficient delivery of grinding fluid at the area of contact between the wheel and the workpiece [49].
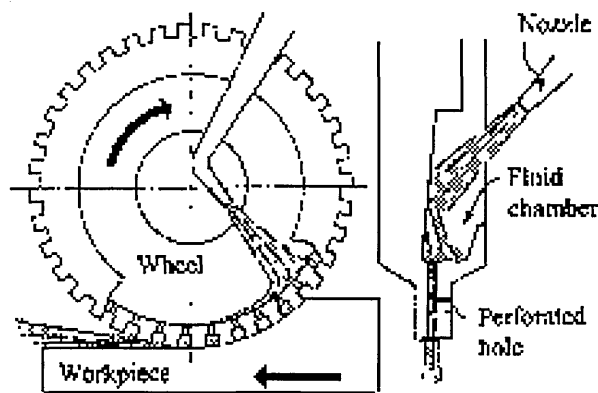
Figure 1.21: Innovative wheel design for fluid delivery for ceramic grinding [49]

Recent research has also been targeted towards the development of metal-free conductive diamond wheels for environmentally-friendly ELID [50], [51]. In the case of a metal-free conductive bonded wheel, although oxides cannot be generated on the matrix metal as in metal bonded wheels, the components in the grinding fluid precipitate as oxides on the surface of the grinding wheel due to anodic oxidation to form a corrected layer, and this corrected layer is thought to contribute to stable grinding [50]. In order to clear metal contamination of the ground surface a metal-free electro conductive carbon-resin bond wheel has been developed and its tribological properties have been tested [51].

27

Japanese tool manufacturer FUJI Die Co., which specialises in the production of ELID power supply units provide updates on their website on new ELID-related technology [52]. Some of the examples mentioned there are:

o   Multi-layer cast-iron bonded wheel: A multi-layer wheel with two types of abrasive sizes in the diamond layer of the wheel, allowing roughing and finishing to be performed at the same time. Contact Fuji Die for details.

o   Cemented carbide alloy thin cutting wheel: ELID cutting wheel with resin-metal hybrid bonded diamond layer in the cemented carbide alloy thin blade. Non-ELID cutting wheels with resin bonded abrasive layer can also be made.

o   The forming cast-iron bonded diamond wheel with grooves is used for the chamfering of the inner and outer edges of glass hard discs. The purposes of such forming processes are expected to increase in the future. "Electric discharge forming in the mist" is the most convenient process.

o   A new type of diamond/CBN wheel is being developed in FUJI Die with multiple chip pockets in the bond layer of the resin or metal bonded wheel for the machining of soft material.

o   Xesel has recently announced their research on electrode-less inner surface grinding using cast-iron bonded wheel. They have also introduced applications of ELID honing using a bronze wheel.

o   In Taiwan, KINIK Co. recently disclosed research on creep-feed grinding based on ELID grinding using a cast-iron bonded wheel.

o   Applications of cast-iron bonded wheels which provide outstanding surface roughness and dimensional accuracy are increasing in the center-less ELID grinding field. [52]

Lee and Kim ([40][53]) proposed an optimised ELID technique in which the worn grains are lost rapidly and new grains protrude, in order to remove any adverse influence on the workpiece surface. In order to achieve optimum in-process electrolytic dressing the dressing current, which is directly affected by the thickness of the insulating layer, is controlled [53].

Kramer and Rehsteiner [54] suggested a different method of controlled electrochemical in-process dressing according to the sharpness of the grinding wheel and the material which is to be ground. By measuring the normal and tangential force,

the value of Fn/Ft (termed k-value) is constantly kept at a specific window and as a result the grinding wheel is maintained in the optimum state of sharpness. This controlled process leads to increased processing reliability and significant improvements in the quality of the manufactured parts in terms of dimensional stability, conformity of shape and superior cutting edges [54].

1.c ELECTROCHEMICAL IMPEDANCE SPECTROSCOPY

1.c.1 INTRODUCTION TO ELECTROCHEMICAL IMPEDANCE SPECTROSCOPY (EIS)

In the study of metals immersed in a solution, analysis of impedance data is sometimes carried out in order to determine the individual components of an equivalent circuit electrical model that represents the metal/solution interface. Extending this concept to the issues that are relevant to nano-grinding, the grinding wheel and the oxide layer that is grown on it during the ELID process is a novel application using the same concept. The response of the grinding wheel to alternating voltages of different frequencies gives a spectrum of impedance values which can be analysed to provide valuable information, such as the resistance of the oxide layer or the resistance of the grinding wheel's base material. With the use of Faraday's law, corrosion rates can be calculated for different ELID voltages applied. Such information is important, especially in cases when the shape of precision components to be manufactured depends critically upon the shape and size of the grinding wheel.

Experimental data is collected and usually graphically represented in two ways:

a. Real versus Imaginary Impedance, known as the Nyquist plot and

b. Logarithm of Impedance versus Logarithm of Frequency, known as the Bode plot

A corroding system in solution has a total resistance that is a combination of resistances such as the charge transfer resistance (resistance of ions going into solution), the solution resistance, the paint film or oxide film resistance (if a film is present). The overall resistance determines the current flowing through the system and hence the corrosion rate. The overall response of the system can be represented with combinations of resistors and capacitors that give characteristic Bode and Nyquist plot shapes. Appropriate analysis of these plots can be used to predict the values of the individual components that comprise the equivalent circuit model [56].

1.c.2 MODELLING METALS IN SOLUTION

A metal immersed in an aqueous electrolyte undergoes corrosion which involves the transfer of electrons between the metal surface and an aqueous electrolyte solution. The metal surface usually possesses sites for an oxidation (or anodic chemical

reaction) that produces electrons in the metal, and a reduction (or cathodic reaction) that consumes the electrons produced by the anodic reaction (figure 1.22). These "sites" together make up a "corrosion cell" through which flows corrosion current. The anodic reaction is the dissolution of the metal to form either soluble ionic products or an insoluble compound of the metal, usually an oxide. Several cathodic reactions are possible depending on what reducible species are present in the solution. Typical reactions are the reduction of dissolved oxygen gas, or the reduction of the solvent (water) to produce hydrogen gas. [79]
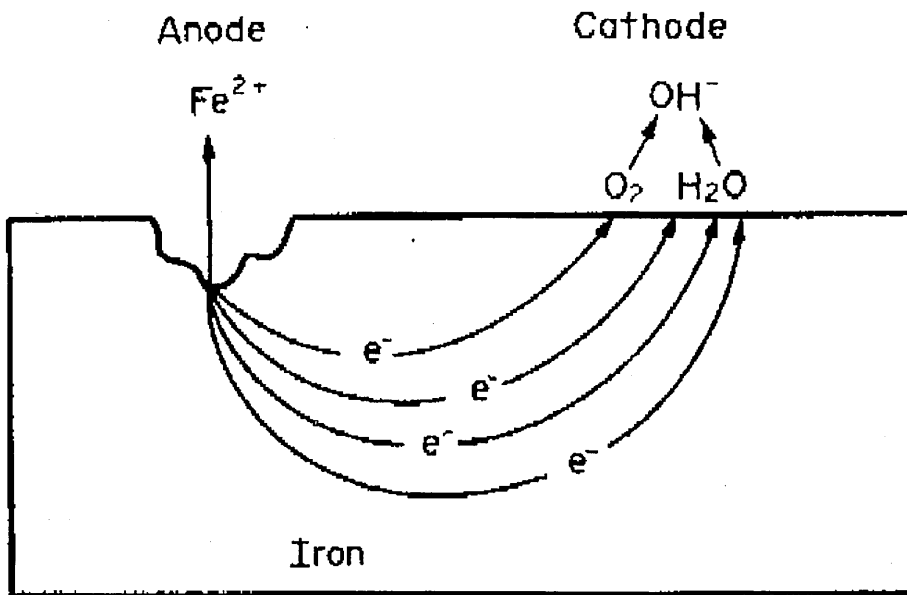
Figure 1.22: The electrochemical cell set up between anodic and cathodic sites on an iron surface undergoing corrosion [79]

A typical anodic oxidation that produces dissolved ionic product for iron metal is:

$$Fe \Longrightarrow Fe^{2+} + 2e^-$$
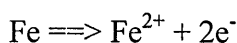
With the cathodic reduction being:

$$O_2 + 2H_2O + 4e^- \Longrightarrow 4OH^-$$
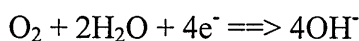
The total resistance of the cell R_{total} is influenced by factors such as:

a. The resistance to the oxidation step which is termed as the charge transfer resistance R_t (the difficulty with which ions go into solution)

31

    b.   Transport of ions in the electrolyte (solution resistance R_s)

    c.   Electron transfer inside the metal (insignificant)

A combination of resistors and capacitors leads to the representation of the corrosion cell with a simple equivalent circuit which will be described in more detail in section 1.c.2.1.

    d. The formation of an oxide film or the presence of a paint film on the metal's surface makes the equivalent circuit more complex

The equivalent circuit that results from this added feature of the cell is presented in detail in section 1.c.2.2.

    e.   Another source of resistance that should be mentioned is mass transport of species towards or away from the metal surface (e.g. dissolved oxygen to cathodic sites).

Walter [56] presents an overview of the impedance behaviour of metals in solution, starting with a simple model of a bare metal in solution and the equivalent circuit that describes it. Mansfeld, et al [57] present a more complex general model that can be used to describe the experimental results in more complicated cases, such as painted metals in solution. The equivalent circuit in that case consists of the solution resistance R_Ω of the test electrolyte, the capacitance C_C of the intact coating layer, the pore resistance R_p, due to penetration of electrolyte and Z_I, a general impedance which characterises the reactions at the metal interface. For many systems, Z_I can be described by a transfer resistance R_t in parallel with a double layer capacitance C_{dl} or by R_t in series with a Warburg impedance W. R_t corresponds to the corrosion reaction at the metal/coating interface. The generalised Warburg impedance can be expressed as [56]:

$$W = k \, (j\omega)^{\alpha} \, [57] \quad (16)$$

or

$$W = \sigma\omega^{-1/2} \, (1\text{-}j) \quad (17)$$

σ: Warburg impedance co-efficient (ohm. $s^{\frac{1}{2}}$)

ω: $2\pi f$ (rad.s^{-1})

In this expression, rate control by diffusion of charged species within pores in the film is taken into account [58] [56]. In the following sections, more details on each model (bare metal in solution, film-covered metal in solution) and the increasing complexity of equivalent circuits are presented.

1.C.2.1 BARE METAL SURFACE IN SOLUTION

The simple case of a bare piece of metal in solution (a corroding electrode) can be represented by the equivalent circuit in figure 1.22 (Warburg resistance is not taken into account in this simple model). The circuit consists of the resistance, R_Ω, which includes the resistance of the electrolyte, surface films, circuit leads, etc. The polarisation resistance, R_p, is in parallel with the capacitance, C, which represents in simple cases the double layer capacitance, C_{dl}.

For the circuit elements in figure 1.22 the impedance is given by:

$$\overline{Z} = Z' + jZ' = R_\Omega + \frac{R_p}{1 + j\omega R_p C} = R_\Omega + \frac{R_p}{1 + \omega^2 C^2 R_p^2} - \frac{j\omega C R_p^2}{1 + \omega^2 C^2 R_p^2} \quad (18)$$

For impedance analysis, an equivalent series circuit is considered in figure 1 where $Z' = R_s$ and $Z'' = 1/\omega C_s$.

Considering admittance Y:

$$\overline{Y} = Y' + jY'' \quad (19)$$

The real (Z') and imaginary part (Z") of the impedance Z can be calculated as functions of frequency for known values of R_Ω, R_p and C by use of equations:

$$Z' = \frac{Y'}{Y'^2 + Y''^2} \quad (20A) \quad \text{and} \quad Z'' = \frac{Y''}{Y'^2 + Y''^2} \quad (20B)$$

Elimination of ω leads to:

$$\left[Z' - \left(R_\Omega + \frac{1}{2} R_p \right) \right]^2 + \left(Z'' \right)^2 = \left(\frac{R_p}{2} \right)^2 \quad (21)$$

which is the equation of a circle with a radius of $\frac{1}{2} R_p$, the centre of which lies on the Z' axis at $Z_0' = R_\Omega + \frac{1}{2} R_p$. At the apex of the semicircle:

$$\omega_{max} = \frac{1}{C R_p} \quad (22)$$

It is possible, therefore, to obtain all three parameters from a complex impedance plot as shown in figure 1.22 provided a sufficient frequency range is investigated. [58] Another method of evaluating impedance data is the analysis of the frequency dependence of the absolute value of $|Z| = \sqrt{Z'^2 + Z''^2}$ and the phase angle δ which is defined as:

$$\delta = \frac{Z''}{Z'} = (\omega C_s R_s)^{-1} \quad (23)$$

From plots of $\log|Z|$ and δ as a function of $\log\omega$ –so called Bode plots as displayed in figure 1.22- the parameters of the circuit can be determined.

At very high and very low frequencies, $|Z|$ becomes independent of frequency and so from these horizontal lines the values of R_Ω and R_p can be determined. For an intermediate frequency range, $|Z|$ is inversely proportional to ω and a straight line with a slope of -1 is observed on a $\log|Z|$ - $\log\omega$ plot. From an extrapolation of this line to $\omega=1$, the capacitance can be determined as $|Z|=1/C$. The break points for this plot have been determined by Haruyama as [58]:

$$\omega_h = \frac{1}{R_\Omega C} \quad (24A) \quad \text{and} \quad \omega_l = \frac{1}{(R_\Omega + R_p)C} \quad (24B)$$

Figure 1.23 is a presentation of examples of Nyquist and Bode plots for a metal in solution along with the corresponding equivalent circuit. Unlike the Nyquist plot, the Bode plot explicitly shows frequency information. [65].

In the equivalent circuit, R_s represents the electrolyte's resistance and is determined by the offset of the semicircle on the real impedance axis, the diameter of the semicircle determines the charge transfer resistance in the absence of diffusion/adsorption effects (R_t) and C_d is the electrical double layer capacitance at the metal/solution interface.

-ImZ

Frequency decreasing

ω

Nyquist plot

$|Z|$

$\omega=\infty$

$\omega=0$

ϕ

0

RealZ

Bode plot

log |Z|

log ω

ϕ

0°

-90°

log ω

Equivalent circuit

Cd

Rs

Rt
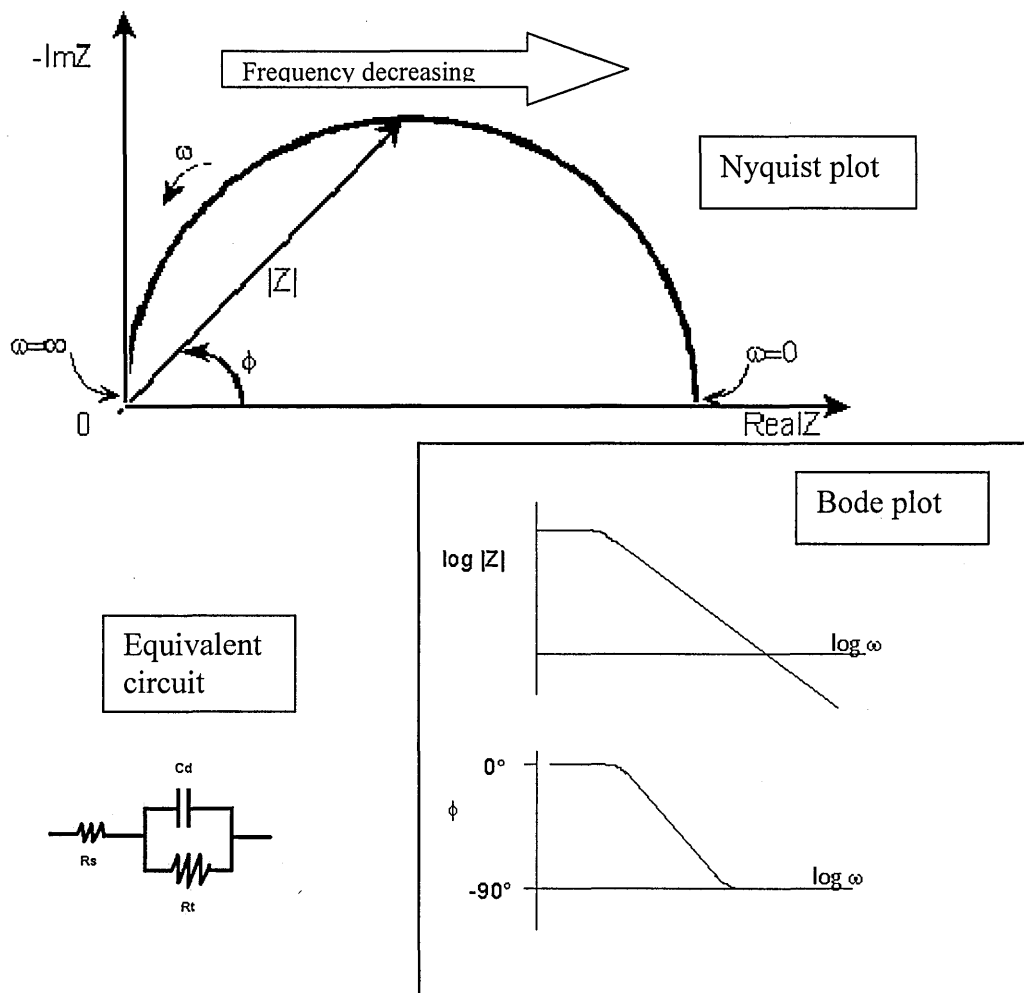
Figure 1.23: Nyquist and Bode plots and equivalent circuit used to represent metal/solution interface [65]

1.C.2.2 METAL WITH OXIDE LAYER IN SOLUTION

An equivalent circuit model for a painted metal/solution interface requires inclusion of the film parameters to the circuit. Several models have been proposed to represent the impedance response of such systems (referenced in the comprehensive study by Walter [56]). The one presented here is shown in the following figure (figure 1.24), accompanied by the corresponding Nyquist and Bode plots. R_{pf} has been interpreted as the film resistance affected by the pore resistance due to electrolyte penetration and at damaged areas of the film, or areas were more rapid solution uptake occurs (e.g. pre-existing holes). The capacitor C_{pf} has been interpreted as the capacitance between

the metal and the electrolyte, with the film as dielectric R_t, C_d and R_s have been previously defined and their meaning is the same.
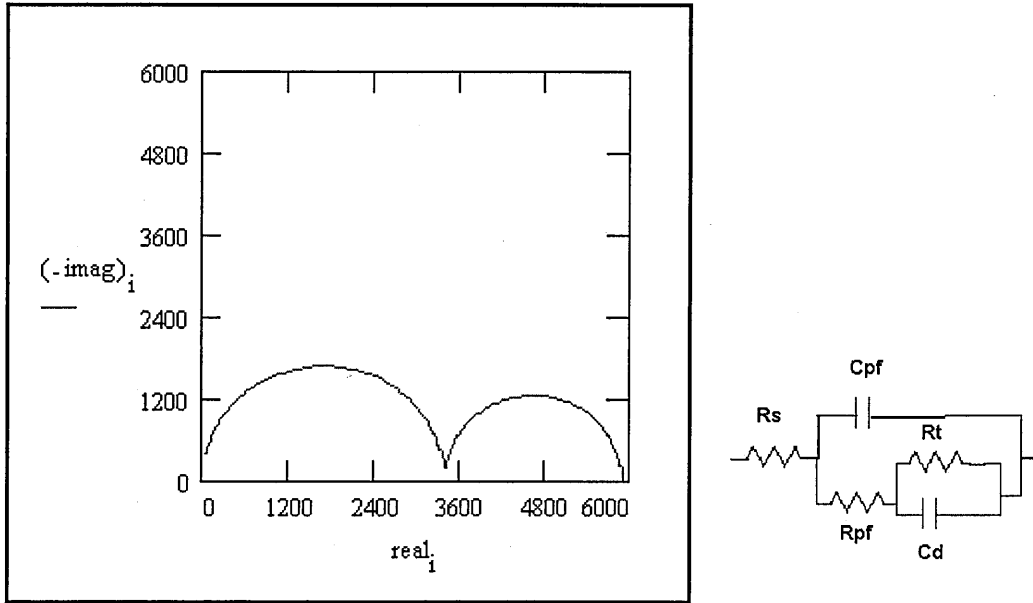
Figure 1.24: Nyquist plot and equivalent circuit used to represent the painted metal/solution interface [65]

As can be seen in figure 1.24, the Nyquist complex plane plot in this case is made up of two semicircles with time constants for the paint film and metal respectively [56]:

$$\tau_{pf} = R_{pf}C_{pf} \quad (25)$$

$$\tau_m = R_t C_d \quad (26)$$

The semicircle occurring at higher frequencies will be caused by the paint film if:

$$\tau_{pf} > \tau_m,$$

which is usually the case. The shape of the plot will appear as two distinct semicircles as in figure 1.24 if both of the following criteria are met[56]:

$$0.2 \leq (Rt/Rpf) \leq 5 \quad \text{and} \quad \tau_m / \tau_{pf} \geq 20 \quad (27)$$

If these criteria are not met the two semicircles will interact with each other. Causing difficulties in separating the components of the equivalent circuit (figure 1.25)
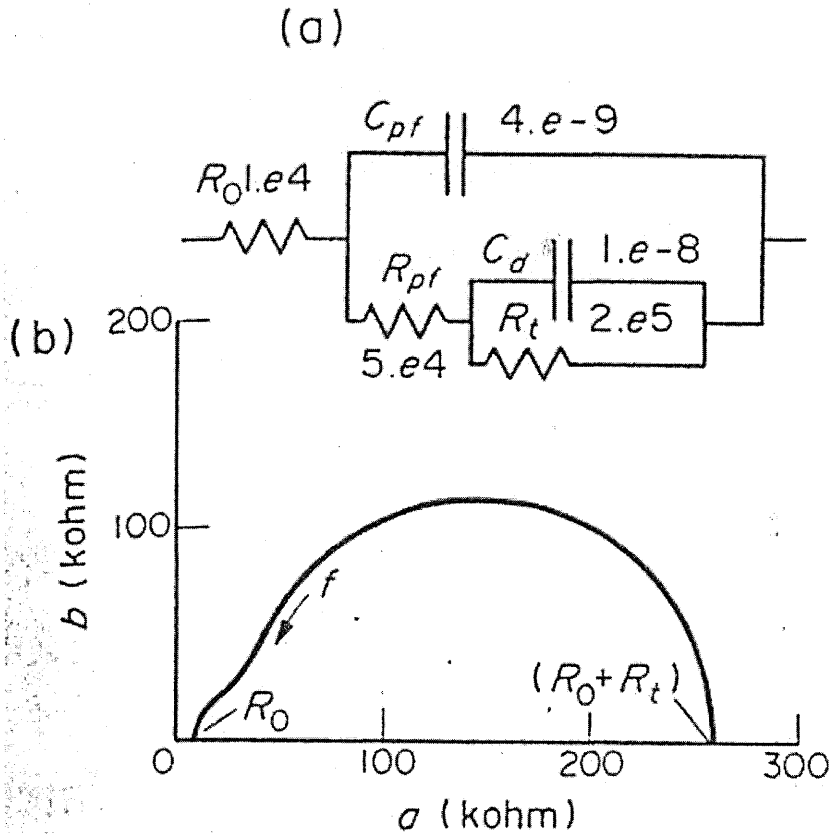
Figure 1.25: Equivalent circuit (a) and Nyquist plot (b) used to represent the painted metal/solution interface: Interacting semicircles [56]

More complex models take into account diffusion processes by including Warburg impedance Z_ω in series with R_t. This inclusion results in Bode and Nyquist plots of the form that is shown in figure 1.26. The Warburg impedance co-efficient σ varies and larger coefficient values result in the linear part of the graph being more pronounced, corresponding to increasing diffusion effects on the surface of the film.

37
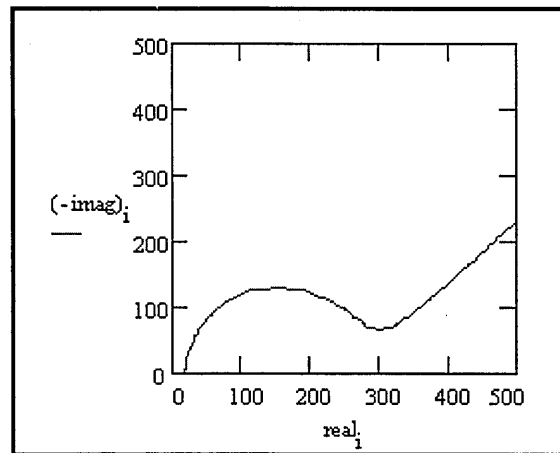
Figure 1.26: Nyquist plot used to represent the painted metal/solution interface: Inclusion of diffusion impedance by use of the Warburg co-efficient σ [65]

1.C.3 BEHAVIOUR OF REAL CORRODING SYSTEMS

For real corroding systems, it has been observed that deviations from the results expected for simple equivalent circuits occur. Polarisation resistance, which is mentioned before is defined as [59], [60]:

$$R_p = \lim_{\omega \to 0} \mathrm{Re}\{Z_f\} E_{corr} \quad (28)$$

When measured by the A.C. impedance technique in the vicinity of the corrosion potential E_{corr}.

Re $\{Z_f\}$ denotes the real part of the complex Faradaic impedance.

For simple corrosion systems, the polarisation resistance can be determined from the DC limit of the impedance modulus $|Z|$ [61]:

$$R_p = \lim_{\omega \to 0} |Z| \quad (29)$$

38

Based on experimental results for iron in sulphuric acid containing propargyl alcohol and a non uniform corrosion model, it was found necessary to define the charge transfer resistance:

$$R_t = \lim_{\omega \to \infty} \text{Re}\{Z_f\} E_{corr} \quad (30)$$

A better agreement of weight loss data with R_t than with R_p has been observed and reported by Epelboin, *et al* (as mentioned in [58], [59].

1.C.4 IMPEDANCE MEASUREMENTS IN LOW CONDUCTIVITY MEDIA

Mansfeld, *et al*, [62] also observe that, contrary to statements by other authors, impedance measurements in low conductivity media are possible, as demonstrated by experiments with iron and Al 2024 in tap water. Due to the advantage that the ohmic resistance and the Faradaic Impedance can be determined in the same experiment, there have been efforts of extending the use of A.C. impedance measurements in low conductivity media such as tap water. Experiments conducted for iron in tap water lead to the conclusion that only one time constant determines the corrosion reaction at E_{corr} [63].

Other experimental difficulties and restraints include time restraints when measuring at very low frequencies, the frequencies at which polarisation resistance and double layer capacitance are accessible [64].

1.D ACOUSTIC EMISSION FOR MONITORING PRECISION CUTTING PROCESSES

1.D.1 ACOUSTIC EMISSION- BASIC PRINCIPLES

Monitoring precision cutting processes is difficult by means of some of the sensors
that commonly employed in conventional machining operations. However, the
acoustic emissions (A.E.) signal has proven to be sensitive enough for precision
grinding monitoring, and is better suited for monitoring very fast events than, e.g.,
force measurements [67][68][69]. Because A.E. waves propagate with frequencies
from 100 kHz to 1 MHz, well above most structural natural frequencies, machine
vibrations will not influence the AE signal [68]. Acoustic emissions are therefore
regarded as an ideal method for characterizing material removal activity, providing
tool condition and part quality information.

An example of results obtained by Valente and Dornfeld [74} is shown in figure 1.27
where the polar A.E. map is compared to an actual OFHC Cu workpiece.

(a)   (b)
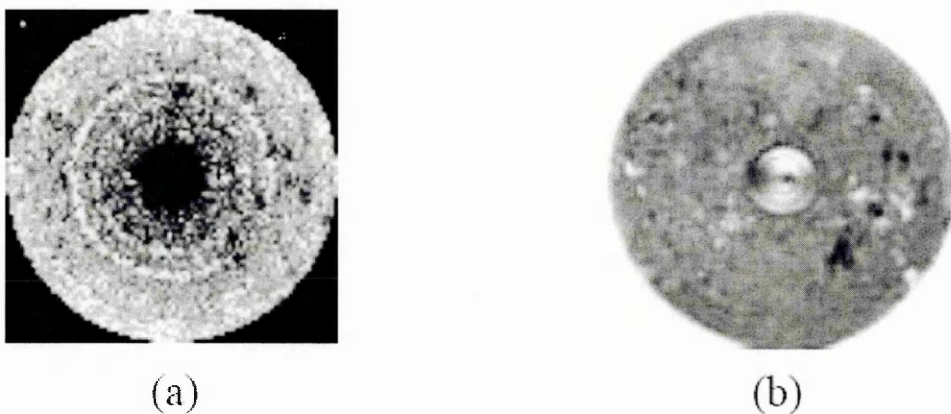
*Figure 1.27: Comparison between the microstructure presented in the polar AE
map (a) and the actual workpiece (b) [74]*

A good correlation can be made between the large individual grains on the workpiece
and the large dark regions on the AE polar map [74].

AE waves can be detected by an AE sensor (piezoelectric transducer) which is mounted at a position near the ground surface. The sources of acoustic emissions are the combination of elastic impact, friction, indentation cracks, bond fracture, chip fracture, grain fracture, and grit removal at the wheel/workpiece interface [66][67]. Previous research has indicated that worn grits, wheel loading, heavy friction, and hard bonded material can result in large AE energy [69][70][71].

From the aspect of wheel loading, ploughing, and sliding contribute to the main source of acoustic emission energy. Ploughing, characterized as plastic deformation of the workpiece without material removal, consumes energy due to this deformation. Sliding energy is expended due to sliding friction between wear surfaces on the abrasive grains and the workpiece. The effect of wheel loading during extended grinding operations reduces the efficiency of the abrasive cutting action resulting in large ploughing and sliding (rubbing) components of grit-work interaction. This is expected to increase the energy of the acoustic emission from the process.

Much effort has been directed towards developing on-line condition monitoring systems that make use of features extracted from the AE signal. A relatively reliable method for industrial implementation is the detection of root mean square (RMS) value of the AE signal [69][72][73]. The root mean square (RMS) value of the AE signal, AE_{RMS}, is defined by:

$$AE_{RMS} = \sqrt{\frac{1}{T} \int_0^T V^2(t)dt} \quad (31)$$

where V(t) is the AE raw signal and T is the integration period. The AE_{RMS} value carries information of the AE raw signal power during each interval of time. AE energy has been commonly used as one of the most significant methods to analyse AE signals [69], [72], [73]. As the energy rate, dE/dt, of the acoustic emission signal, can be expressed as $dE/dt \propto (AE_{RMS})^2$ [73], AE_{RMS} has been used to assess AE energy by previous studies [69], [72], [73].

CHAPTER 2: EXPERIMENTAL METHODS

2.A INTRODUCTION – NANO GRIND

2.A.1 INTRODUCTION

Process optimization for the handling and production of components for the optics, electronics and in general precision industries is a continuous challenge that has to be faced. Miniaturisation of devices, the demand for increase in sensitivity and accuracy (e.g. in shape and form) for technologically advanced products, drive the demand for component production processes with enhanced capabilities that can satisfy the needs of the modern world.
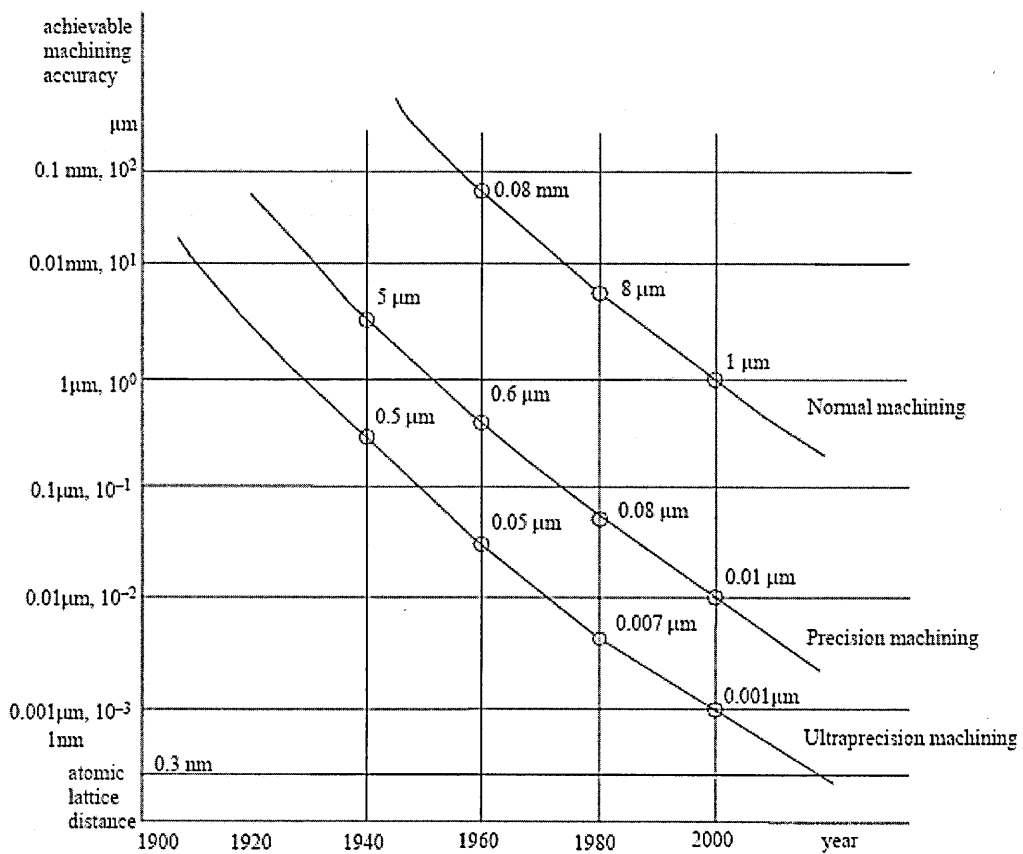
Figure 2.1: Achievable Machining Accuracy according to Taniguchi [75]

In 1983, Taniguchi demonstrated that the smallest achievable accuracy (and, as a consequence, smallest reproducible feature) decreases as a function of time [75]. Figure 2.1 is the plot of achievable machining accuracy for machining, precision and ultraprecision machining and its evolution with time. It indicates that the ability exists to produce highly accurate components – with achievable accuracies comparable to the atomic lattice distance- with today's ultra-precision machines under the right processing conditions. With large scale production of these components being the next step, optimizing machine tools and processing parameters will eventually lead to acquiring the desired products at a low cost and a short production time.

The main objective of the research conducted in the framework of this project was to establish practical, cost-effective and time-efficient ways of processing components made of hard and brittle materials. In order to achieve that objective, grinding and more specifically ELID grinding was used as the main processing method, coupled with polishing when it was deemed necessary to add a short polishing step in order to achieve higher component quality. The work undertaken was in support of the Nano Grind project, funded by the European Community under the 'Competitive and Sustainable Growth' Programme (1998 - 2002). A more detailed description of the aims and objectives of Nano Grind follow in paragraph 2.A.2.

In this chapter, an overview of the experimental methods is given, from the initial conception of ideas and definition of project objectives, down to the choice of specific routes followed (e.g. experimental techniques, instrumentation and equipment,), in order to study, evaluate and optimize component processing. Finally, a detailed description of each experimental technique is presented along with the specific experiments performed.

2.A.2 NANO GRIND

The main objective of Nano Grind was the realisation of curved surfaces with optical quality by means of nano-precision grinding based on ELID technology. Traditionally, most optical surfaces are produced by grinding, followed by lapping and polishing. More recently lenses were produced by moulding (typically plastic spectacle lenses and lenses for low-cost cameras) but this also required the moulds to be produced using traditional, time-consuming methods. [76]

Nano Grind aimed at producing cheap, smooth and curved optical surfaces (in glass, ceramics or hard metal) using an innovative grinding machine tool with electrolytic in-process dressing (ELID). The objective was a significant machining cost reduction with equal specifications on dimensional accuracy and surface quality. This would be realized by a faster overall production process for direct manufacturing and by offering longer standing moulds for replication that would result in an important cost reduction for the end-user. Nano Grind would enable the production of curved surfaces with high quality average roughness as well as a very high dimensional accuracy. [76]

The basic result of this project was that products with surfaces of optical quality could be produced using a highly accurate and efficient grinding phase without (or with a much shorter) time-consuming polishing phase. Process improvement was not only dominated by the effect of the production time reduction but also the avoidance of the shape distorting effects of polishing which could be abandoned or radically minimised.

The envisaged machine and technology would have multiple applications. Examples include semiconductor components processing, aspherics, freeform optics, sophisticated optics for remote monitoring applications and reflectors for the automotive industry [76].

2.B CONCEPTUAL FLOWCHART

2.B.1 CONCEPTUAL FLOWCHART AND ITS DESCRIPTION

Figure 2.2 is a flowchart that summarizes the concepts, reasons and logic behind the choice of the specific experimental techniques that were used during this project. Starting from the basic definition and application of processing conditions, the work undertaken was based on the following objective:

"Defining and applying **optimal processing conditions** will lead to the **production of defect-free components**, with high quality surface finish and minimal or no subsurface damage."

The main processing method during this project was precision grinding and was applied on the production of components made of hard and brittle materials (glass being the specific material studied).

The interaction between the machine tool (the grinding wheel) and the workpiece (glass sample) in the grinding fluid environment lead to the production of the final component which was in effect, the measure to judge the choice of processing conditions: Optimal grinding parameters would lead to the production of high quality, low subsurface damage (SSD) workpieces by a grinding wheel with a good cutting efficiency. On the contrary, choice of non-optimal parameters would lead to producing low quality workpieces containing defects, with extended SSD, potentially related to the poor state of the grinding wheel (e.g. cutting grits worn out, cracks appearing on the wheel surface). Re-definition of grinding conditions was thus necessary, in order to be able to improve the quality of the ground workpieces.

Post-grinding inspection of both the grinding wheel and the workpiece could give the necessary indications that would lead to the choice of optimum processing parameters. The effect of the grinding process on the workpiece and on the grinding wheel itself would enable the fine tuning of the required parameters and hence the choice of grinding conditions that would lead to the production of high quality components.
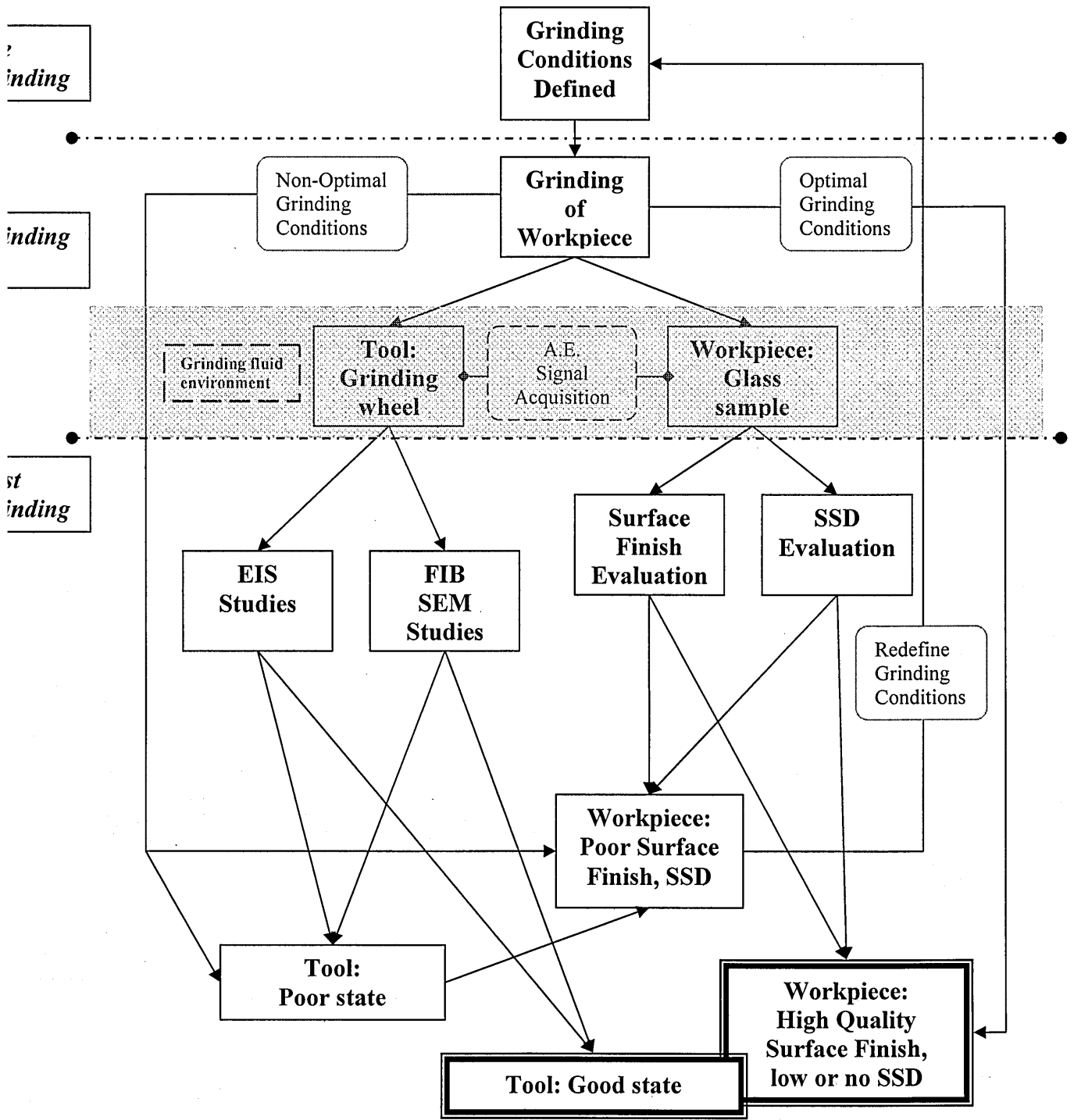
Figure 2.2: Flowchart outlining the main conceptual framework of this project

- Grinding Wheel: Grinding wheels were inspected by using Scanning Electron Microscope (SEM), so that their structure and the way grinding affects their surface, grits and general morphology could be closely observed. In the case of ELID grinding, the presence of the oxide layer lead to requirements of more specific studies of its thickness and properties in order to understand its nature, structure, properties and its effects. Electrochemical methods were required to study its characteristics, Electrochemical Impedance Spectroscopy (EIS) being the one that was chosen for the purposes of this project. The use of the Focused Ion Beam (FIB) and Scanning Electron Microscopy (SEM) facilities also gave the opportunity to study the matrix material and the transition zone on the wheel between the matrix material and the grown oxide layer.

- Glass Workpiece: Inspection of the ground workpieces was undertaken in order to evaluate their quality after grinding. White light interferometry and diamond-tip stylus tracing gave us details about the surface finish achieved through specific grinding conditions. After the necessary information was recorded from the surface of each workpiece, the evaluation of the sub-surface damage (SSD) followed. Lacking non-destructive techniques for the evaluation of the workpieces, they were polished until all defects were removed. Measuring the depth into which damage extended in each workpiece yielded the necessary SSD information that related to specific grinding conditions.

- Grinding Fluid: Initial tests of grinding fluid conductivity were performed in order to study its changes during the grinding process and the potential effects it might have on the final surface finish of the components produced.

- The operations described above (which will be presented in more detail in the next paragraphs) were applied once the grinding process was complete. The possibility of establishing a means of monitoring the process while it was taking place rather than post-operation was of great interest as it would allow for processing flexibility and the ability to optimise grinding conditions without the necessity of time-consuming, post-grinding inspection methods. This route was followed by the acquisition and evaluation of Acoustic Emission (A.E.) signals during grinding in order to establish the possibility of using it as a reliable process monitoring tool.

2.c GRINDING EXPERIMENTS

2.c.1 MACHINE TOOLS/ ELID EQUIPMENT

Grinding experiments were performed on two different grinding machines: The Tetraform C for cupwheel grinding and the Edgetek SAM (Super Abrasive Machining) machine tool for peripheral grinding, both situated at Cranfield University.

The Tetraform C design is based on a triangular, pin-jointed 'tetrahedral' space frame structure, with all the loads carried in closed loops (figure 2.3). The resulting design gives very high static stiffness coupled with exceptional dynamic stiffness. It is equipped with a 6000 rpm spindle and is primarily aimed at the highly accurate machining of silicon, glass, ceramics, tool steel and similar materials.

The Edgetek SAM is a 5-axis machine tool that is mainly used to investigate the thermal effects of grinding over a wide range of removal regimes from creep feed to High Efficiency Deep Grinding (figure 2.4), is equipped with a 14,000 rpm spindle and can reach wheel speeds greater than 200 m/s.
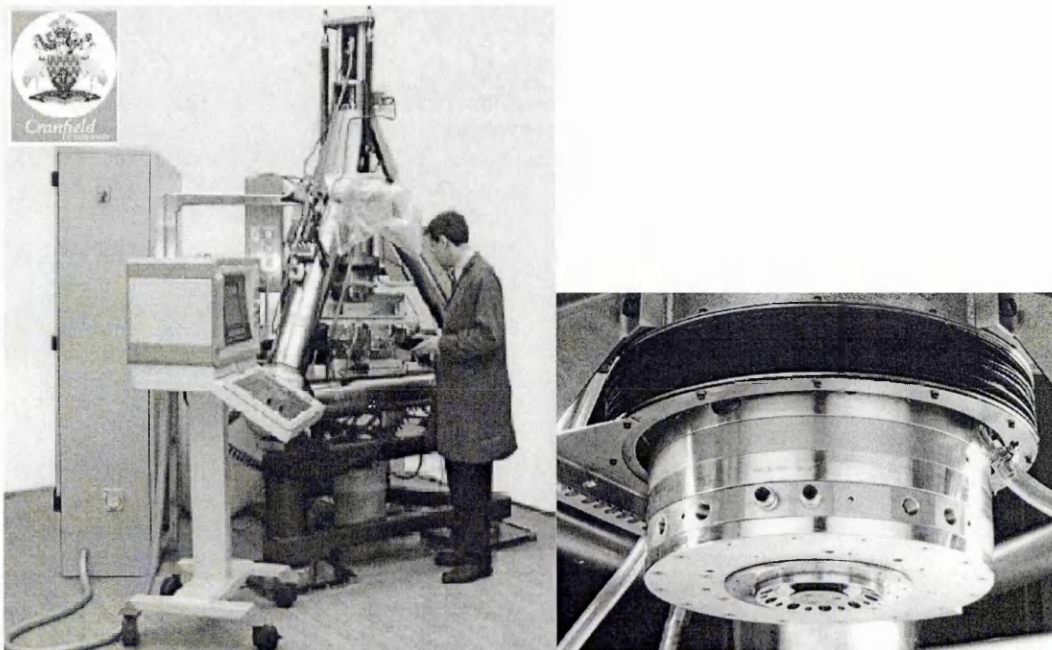
Figure 2.3: The Tetraform C and a detail of its spindle.
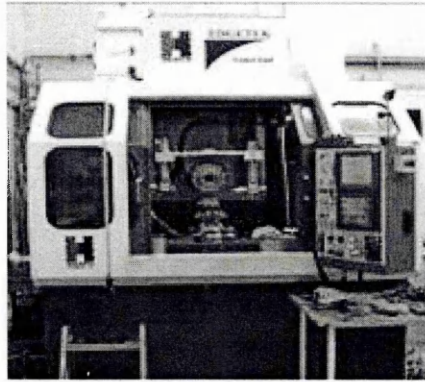
Figure 2.4: Edgetek SAM

The cupwheels and peripheral wheels used for the grinding trials were both resin bond and metal bond wheels (when applying ELID technology,). The ELID power supply used was the ED921 from Fuji Die Co, Japan (figure 2.5). It is capable of supplying different output voltages (90V and 60V), current settings (40A and 20A), and duty ratios (from 10% to 70%). Duty ratio and the applied voltage/current amplitude determined the dressing process directly. High duty ratios and high amplitude level resulted in a quicker dressing process, and vice versa. A proper combination of ELID parameters could meet various grinding conditions. The versatility of the ELID process made it easy to apply on different types of machine tools, without the necessity for expensive parts. Figure 2.6 shows how the ELID components were fitted on the Tetraform C.
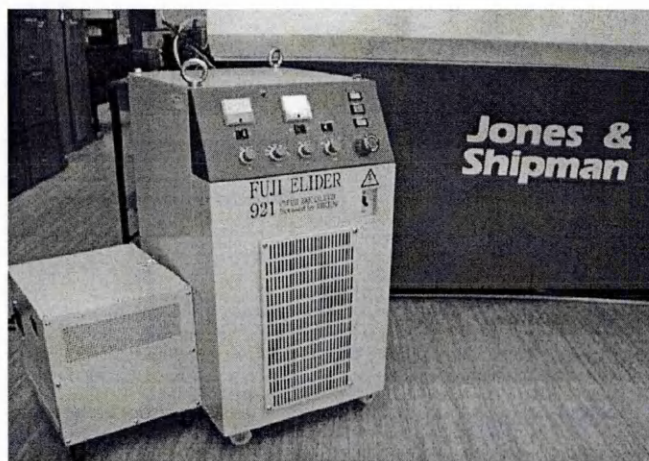
Figure 2.5: The ELID ED921 power supply at Cranfield University
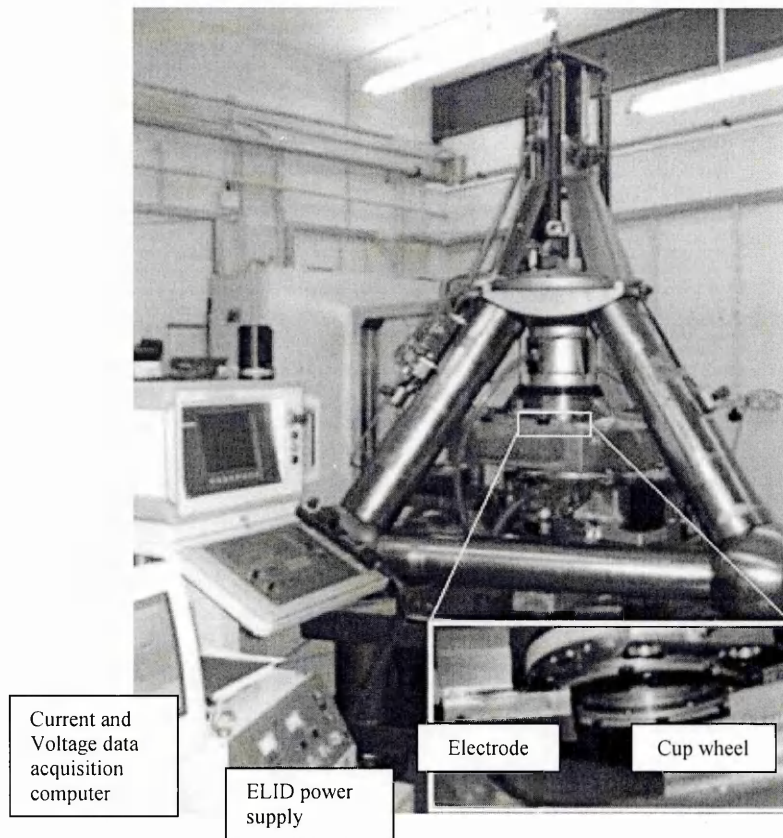
Figure 2.6: The TETRAFORM-C, fitted with the ELID power supply and data acquisition computer

Currently, numerous solution fluids are available in the market. Following suggestions from the ELID power supply manufacturers that an ideal grinding fluid should have the appropriate alkalinity (around pH 11), and demonstrate high electrical conductivity at the dilution rate used, a chemical solution type grinding fluid, CEM (Fuji Die Japan), diluted 50 times with tap water was applied as coolant and electrolyte at Cranfield University.

2.C.2 GRINDING WHEELS/ ELID ELECTRODES DESIGN

2.C.2.1 TETRAFORM C GRINDING WHEELS

Due to the size and shape of the grinding cupwheel, difficulties arose when it was attempted to place it in the FIB and SEM apparatus for observation. The sample stages were too small for the whole wheel to be placed in them. In order to overcome

that problem, modifications had to be performed on the grinding wheel in order to make it more manageable when studied post-grinding.

The grinding wheel was segmented in four pieces, two larger ones and two smaller ones that could be easily placed in the FIB and SEM facilities but still representative of the whole surface of the wheel. A mounting ring was designed, on which the segments were fixed using screws in order for the grinding process to take place. They were then bolted down with a second ring with a diameter that is slightly larger than that of the grinding wheel and thus secured the segments from moving (fig. 2.8). The ring dimensions were carefully selected in order to fit perfectly on the Tetraform C so as not to obstruct the machine or the segmented cupwheel in any way. Hence, the integrity and stability of the wheel was not compromised and all the segments are kept together and in place in order to achieve efficient grinding.

Another innovative point in the approach adopted in some of the experiments performed was the effort to focus on the effect that the oxide layer had on the final product. In all work reported in the literature, the grinding wheels used for ELID grinding contained different kinds and sizes of cutting agents (diamond grits, CBN grits, etc.). In order to investigate the effect of the presence of the oxide layer, a custom wheel was manufactured by Wendtboard, Germany that contained no grits at all. In that way, the oxide layer effects are isolated from the cutting action of the diamonds and thus, immediately observed due to their impact on the final surface of the ground samples.
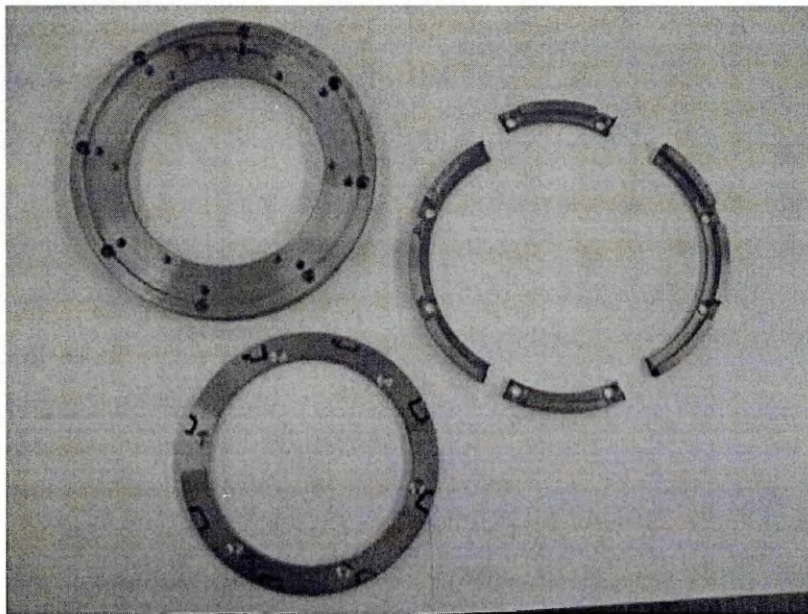
Figure 2.7: Segmented wheel, mounting ring and bolting ring

At the end of the grinding procedure, the glass samples and the segments of the wheel were removed from the Tetraform C for observation or further experiments. Since the experiments and observation techniques were non-destructive ones, the segments were subsequently replaced back on the mounting ring for further grinding without compromising the wheel and the quality of the grinding.

2.C.2.2 EDGETEK SAM GRINDING WHEELS

Along with the peripheral grinding wheels which are commonly used on the EDGETEK machine, a new kind of wheel was designed, which would eventually be fitted onto the Nanogrind Machine.

The grinding wheel used was a spherical wheel of a diameter of 175mm and a width of 30mm. The ability to effectively grind freeform shapes as efficiently as possible, which was one of the objectives of the Nanogrind project, led to the concept and design of the spherical wheel. The use of this kind of wheel increased the versatility of the tool and the variety of shapes that could be processed. It also required the design of a more specific electrode that would conform to the shape of the wheel. The wheel itself was manufactured by Wendt Board, Belgium whereas the ELID electrode was manufactured at Cranfield University.

The electrodes for 175mm and 200mm diameter, 20mm wheel width spherical and cylindrical wheels were produced at Cranfield University. The electrodes are shown in Figure 2.8.. The spherical electrode has a spherical inner curvature, which is the same as the grinding wheel. 21 small holes are distributed in the body of the electrode to enable the electrolyte to flow into the dressing gap. The electrode has an arc covering around 1/5 the circumference of the wheel, which is within the range of 1/6 −1/4 typically reported in the literature. The width of the electrode is 2 mm more than the wheel rim thickness. This electrode was mounted to a stiff and accurate positioning stage for distance/gap adjustments between the wheel surface and the electrode. This feature:

(1) Helped to maintain a fixed dressing gap. The dressing gap eventually becomes larger with the wear/truing of the wheel. A gap adjustable electrode would be able to achieve a consistent dressing gap in various situations. As the dressing gap could influence the dressing current in the gap, and affect the flowing speed and pressure of the electrolyte, its control is of high importance.

(2) Assisted the mounting and surface cleaning of the electrode. The electrode had to be replaced by another one when a wheel of different size is used, or an electrode with a different covering area was needed. On the other hand, the surface of the electrode needed to be cleaned up regularly. In these cases, a gap adjustable electrode showed advantage.
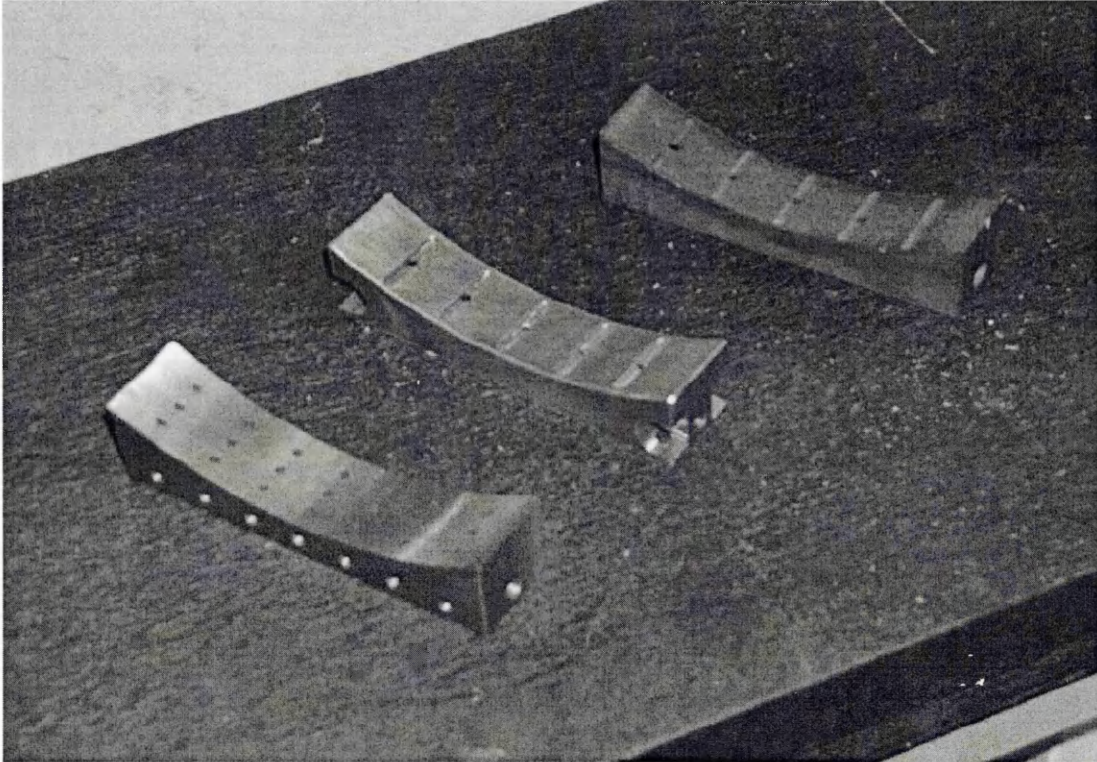
Figure 2.8: Stainless steel, copper and graphite electrodes

An ELID system with a three-direction (X, Y, Z) adjustable feature is shown in Figure 2.9. It is easy to maintain a proper position relative to the grinding wheel. As the structure is quite simple, the cost for its development was low.

The drawings of the ELID electrodes and components of the electrode holder are given in Appendix 1.
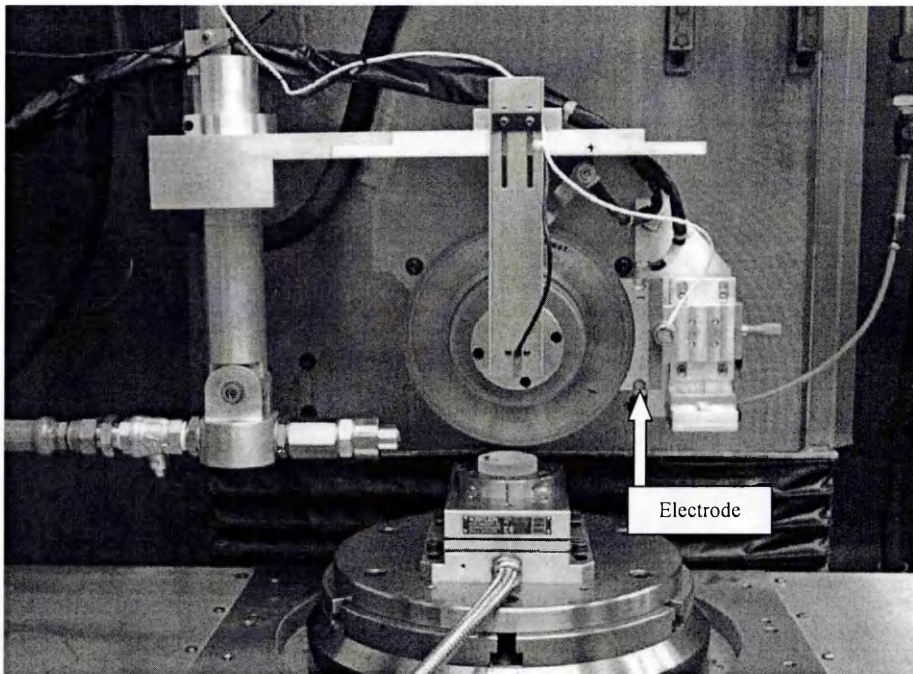
Figure 2.9: Detail of the Edgetek SAM, fitted with the ELID dressing electrode

2.C.2.3 ANODE BRUSH

Dressing current is supplied from the ELID power supply to the anode brush, electrolyte in the dressing gap and electrode. A reliable contact between the anode brush and the metal wheel is critical for proper dressing on the surface of the wheel. As the clearance between the grinding wheel and the cathode electrode is small, approximately 0.1 to 0.3 mm, current will mainly flow through the dressing gap. However, if the anode brush and the grinding wheel lose contact in the dressing process, electrolytic activity could transfer from the surface of the wheel to the surface of some other components of the machine due to current leakage. Therefore, a reliable contact between the anode brush and the wheel can provide not only a proper dressing of the wheel, but also a protection to the machine.

A reliable contact can be obtained by pushing the anode brush toward the side surface of the metal wheel firmly using a spring. To minimize the wear of the brush, the touching position on the side surface of the wheel should be near the centre of the wheel. Fuji Die Co has selected a graphite brush as the contact material. However, Cranfield found that a copper brush can provide a better and more reliable contact compared to a graphite brush. A copper brush has also been adopted by Matsuzawa

for ELID grinding [77]. Copper is suggested to be used as the material of the anode brush for the Nano Grind machine.

2.C.2.4 INSULATION BETWEEN THE SPINDLE AND THE WHEEL

Although the electrolytic activity mainly happens between the electrode and the grinding wheel, some important components of the Nano Grind machine had to be designed to be insulated from the electrolytic zone. The insulation was implemented by placing some insulating rings between the spindle and the grinding wheel. The drawings of such rings are shown in Appendix 2. They were installed on the Edgetek machine at Cranfield for ELID grinding. Such measures effectively stopped current leakage flow from the wheel to the spindle, which minimized the hazard of the spindle and bearings being affected by electrolysis.

Similarly, if a conductive material is to be machined, the fixture should be able to insulate the workpiece from the worktable.

Finally, the detailed design of the 175mm diameter, 20mm width spherical wheel, manufactured by Wendt Board, Belgium, is shown in figure 2.10.
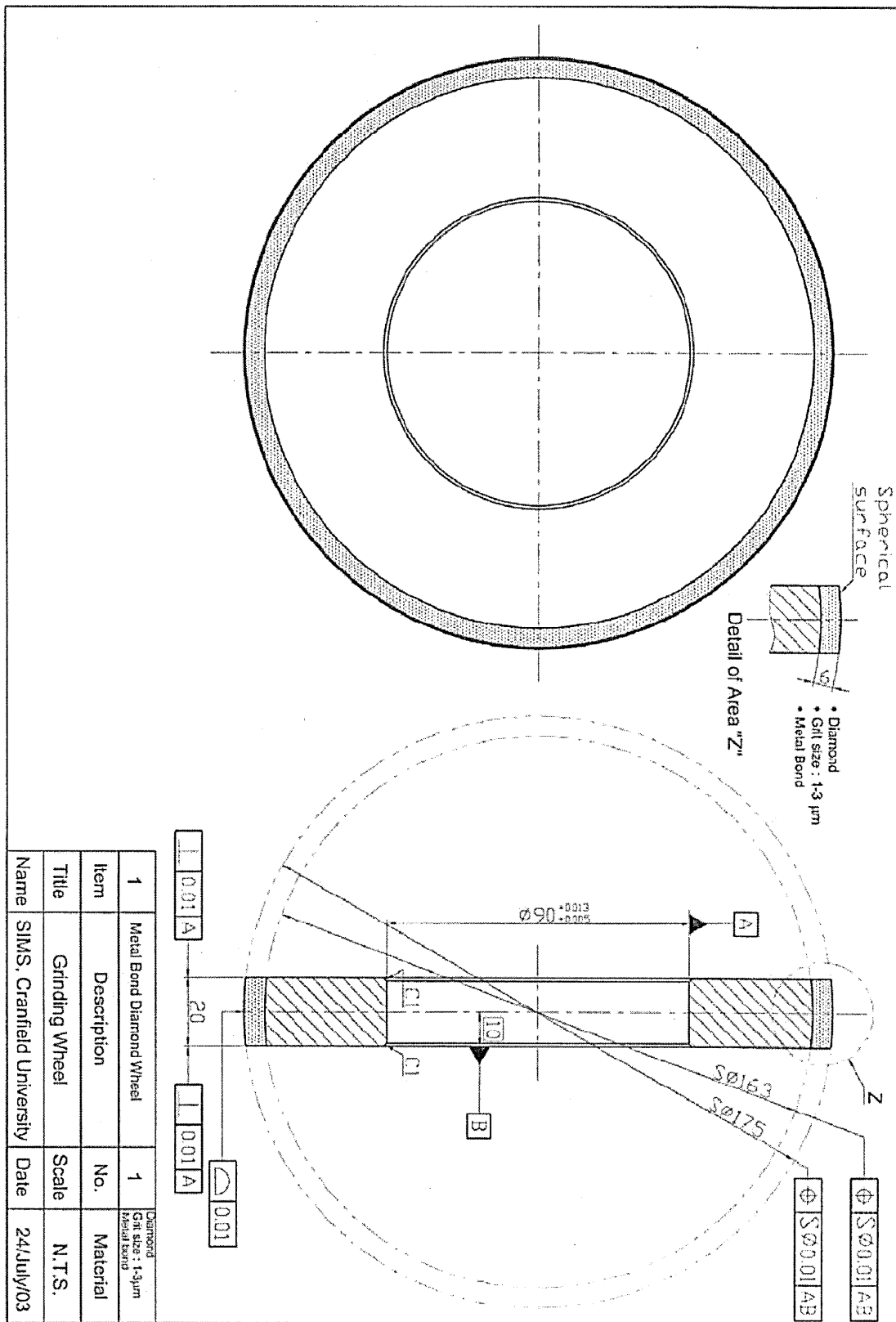
Figure 2.10: Detailed design of the 175mm diameter, 20mm width spherical wheel

2.C.3 GRINDING EXPERIMENTS PERFORMED

The following tables list the experiments performed on each of the two grinding machines that where used for the experimental work of this project, the TETRAFORM C and the EDGETEK SAM.

Tetraform C

The tests listed on Table 1 were performed on square testpieces of BK7 glass (testpiece dimensions: 20mmx20mm). Comparisons were made for different feed rates between ELID grinding and resin bond wheel grinding with grinding wheels that had the same size and concentration of diamond grits. Comparisons are also presented between tests using the rotary table and for different grinding wheel speeds.

Table 1-Tetraform C experiments

Testpiece #	Wheel	Feed rate (mm/min)	d.o.c. (microns)	Rotary table speed	Wheel speed (rpm)
SqA	No grit CIB	3	2	20 rpm	1000
SqB	3-6 micron CIB	3	2	20 rpm	1000
SqC	3-6 micron CIB	3	2	20 rpm	6000
SqD	3-6 micron CIB	30	2	20 rpm	6000
SqE	3-6 micron CIB	6	4	No rotary	6000
SqF	3-6 micron CIB	20	4	No rotary	6000
SqG	3-6 micron CIB	100	4	No rotary	6000

SqH	3-6 micron RB	6	4	No rotary	6000
SqI	3-6 micron RB	20	4	No rotary	6000
SqJ	3-6 micron RB	100	4	No rotary	6000
SqK	3-6 micron RB	30	2	20 rpm	6000
SqL	3-6 micron RB	3	2	20 rpm	6000

Further testing was performed with the no-grit CIB wheel in order to better understand the way the oxide layer affected the overall surface finish of the BK7 testpieces. The conditions for the two tests performed are described in table 2

Table 2-Tetraform C Experiments, No Grit Wheel

No Grit CIB	Testpiece A	Testpiece B
Wheel speed	1000 rpm	1000 rpm
Depth of cut	2μm (nominally)	2μm (nominally)
Feed rate	3mm/min	3mm/min
Rotary table speed	20 rpm	-

2.D. FIB, SEM AND EIS STUDIES OF GRINDING WHEELS

2.D.1 FIB AND SEM STUDIES OF THE WHEEL SEGMENTS

The wheel segments were studied and observed, in order to identify the characteristics of the oxide layer and estimate its thickness over the bond material (cast iron in the case of these cupwheels) using the SEM and FIB facilities at Cranfield.

The procedure during these experiments was as follows:

- The wheel was used on the Tetraform C and was treated in different ways (e.g. pre-dressed, used for grinding samples) in order to achieve different qualities and thicknesses of oxide layer on its surface. Current and voltage data were collected from the ELID power supply during pre-dressing and grinding in order to be able to recognize their fluctuations and appoint to them the corresponding effects of growth and thinning of oxide during these processes.

- The segment was then removed and placed in the FIB facility, where a gallium beam etched a trough on the surface of the wheel, an example of which is shown in the following picture (figure 2.11).

- The wheel segment was subsequently placed in the SEM where further detailed imaging of areas of interest on the segment was performed. Spot analysis was also performed in order to estimate the depth into which the oxide layer extended in the matrix material. The estimation was based on measuring the depth to which oxygen was present on the walls of the trough. That way, different states of the wheel that correspond to different oxide layer depths and final sample surface finish can be correlated.

The wheel segments were also studied using Electrochemical Impedance Spectroscopy (EIS) Techniques, which are described in the following paragraph.

*Figure 2.11: Cupwheel segment surface, trough etched with a gallium ion beam
on the FIB facility*

2.D.2 EIS STUDIES OF THE WHEEL SEGMENTS

2.D.2.1 INITIAL EXPERIMENTS

In order to perform EIS experiments with the cupwheel used on the Tetraform-C, a
special corrosion cell was constructed. The wheel itself was too large to be placed
totally inside a beaker and so, in order to avoid cutting it into pieces (so as to be able
to carry out grinding and electrochemical tests repeatedly on the same wheel), the cell
constructed had a hole at the bottom where a segment of the wheel was inserted
(figure 2.12).

The cell was made of PTFE, and because a perfect fit could not be obtained, silicone
sealant was used around the segment to be tested in order to avoid leaks,. The sealant
was allowed to cure for about 10 hours because the uncured sealant, if immersed in
water, would produce acids that would change the electrical characteristics of the cell.

PTFE cell (Top View)

Hole for
wheel segment
insertion

Grinding wheel
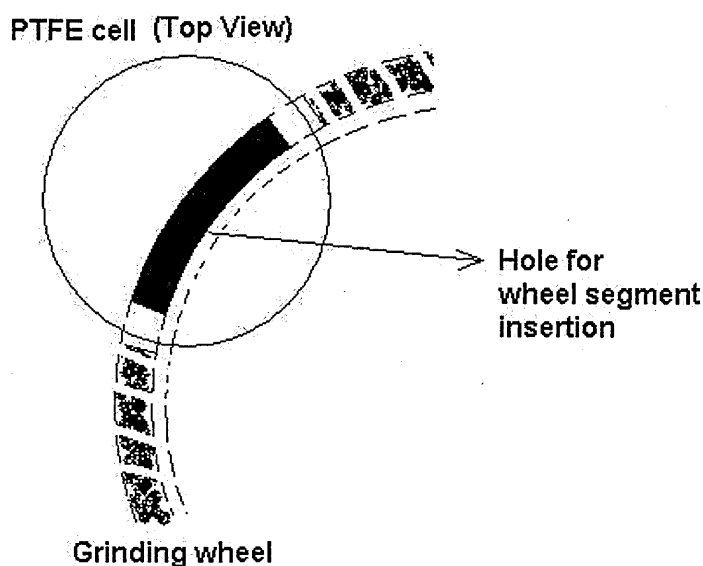
Figure 2.12: Top view of the custom cell constructed for EIS tests. Hole at the bottom made in the shape of a wheel segment

The solution was purged with nitrogen in order to remove the effects of oxygen diffusion or displace them to lower frequencies and allow the development of the semicircles with a minimised oxygen effect. The wheel segments were subsequently subjected to a frequency scan between a high frequency limit of 2×10^4 Hz and a low frequency limit of 10^{-3} Hz.

This experimental set-up had to be modified when performing further tests, due to the following factors:

a. The limited space in the vessel: All electrodes had to be positioned in a very small area containing a small amount of electrolyte which didn't allow for small, accurate corrections in order to get a clearer response from the system.

b. Another problem related to the small size of the vessel used was the fact that when nitrogen (or air) was introduced, the electrolyte was dispersed out of it and the already small quantity of it became even smaller.

c. The electrolyte used was tap water. Its conductivity is limited and sometimes it was too small for the capabilities of the equipment used. This can be observed in the large values of charge transfer resistance observed during these experiments -of the order of 10^4 - 10^5 Ω (i.e. to conditions where the corrosion rate was very low) and also the solution resistance value which was significantly larger than in the cases when the electrolyte used is a NaCl solution.

d. The working electrode (the part of the wheel that was positioned in the vessel) had to be fastened in place with silicone sealant which took about 10 hours to cure. This had an effect on the time scale required to actually perform the measurements, in which case the oxide layer on the grinding wheel could be influenced or altered.

An additional problem with the initial set up was the fact that the grinding wheel itself was bulky and difficult to use in some of the observation equipment (Focused Ion Beam, Scanning Electron Microscope) so the amount of data that could be collected was also limited due to size restrictions.

2.D.2.2 NEW SET-UP DESCRIPTION

Figure 2.13 is a schematic of the set-up when performing EIS measurements on one of the removable pieces of the grinding wheel. The new and improved features of the new set-up are summarized below:

a. The vessel in which the measurements were contained was much larger. It contained about 1 lt of electrolyte which did not spill out when air or nitrogen was supplied.

b. It was also much easier to move the electrodes into position, especially the working electrode and the counter electrode which have to be positioned very close, always making sure they do not touch. The small segment of the grinding wheel was also easier to use in comparison to having to use the whole wheel which limits positioning ability.
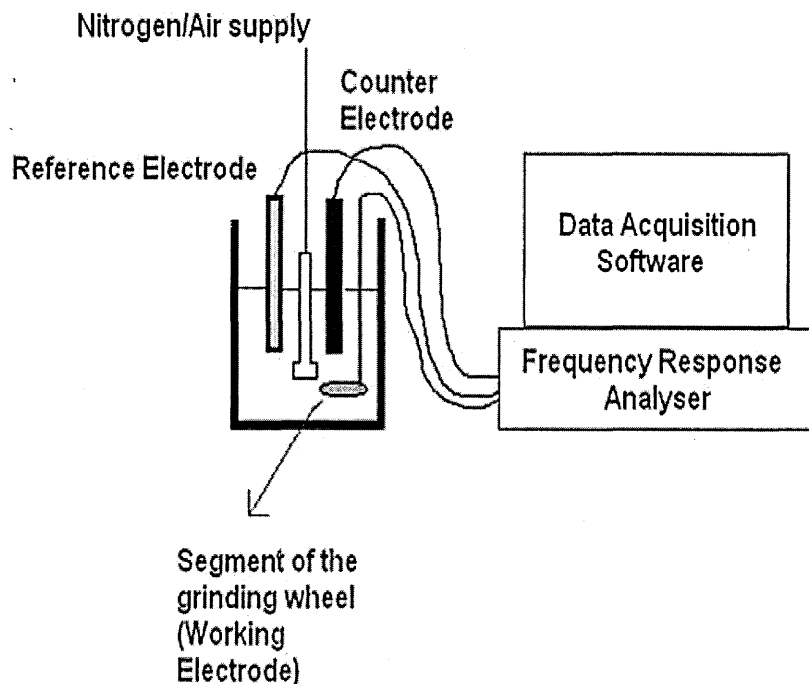
Figure 2.13: EIS measurements new set-up

c. The data acquisition software used (both the software and the frequency response analyzer were supplied by Solartron, UK) is new and more versatile when measuring. It is "user-friendly" and allowed an immediate on-screen observation of the evolution of the test performed in order to make sure that all systems were running properly.

d. The two smaller removable pieces of the segmented wheel made testing much easier. FIB and SEM observation and tests (as described previously) could be performed on one piece while the other, which was assumed to be characterized by the same traits since the wheel undergoes uniform corrosion during grinding, was used for EIS tests without long waiting times.

Note: The studding used to keep the working electrode in place was originally coated with zinc. Zinc was stripped off it though because it was interfering with the measurements performed. When a voltmeter was connected to the studding holding the wheel segment in place, the free potential of zinc was measured rather than that of iron. In order to avoid that problem, the studding was dipped in a HCl solution (100 ml of distilled water, 30 ml of HCl) for a few minutes until the zinc coating dissolved.

The part of the wheel segment that was left uncovered was the surface that actually took part in the grinding process. The rest of the segment, as well as the studding that supported it, was covered in Lacomit laquer which renders that part of the structure non-conductive. In that way, all voltages are applied only at the area of interest.

Finally, in order to achieve optimum conductivity and make sure that the electrolyte would not be limiting the measurement due to its limited conductivity, different electrolyte solutions were tried and the tests where studied in order to choose the best conditions for the measurements. After careful consideration, it was decided to use a 3.5% NaCl solution in which 10ml of CEM grinding fluid (the grinding fluid suggested by Fuji Die for ELID grinding) was added.

With this new set up, experiments were performed both for the case of conventional diamond grit wheels that are segmented as well as for the innovative no-grit wheel. Different oxide layer states were achieved and the segments' impedance response was studied in each of those cases.

2.D.3 APPLICATION OF EIS TO THE STUDY OF ELID GRINDING

Figure 2.14 gives an idea of what the expected results were in the case of a wheel with and without the oxide layer grown on its surface and the corresponding equivalent circuit models.
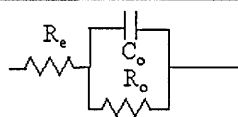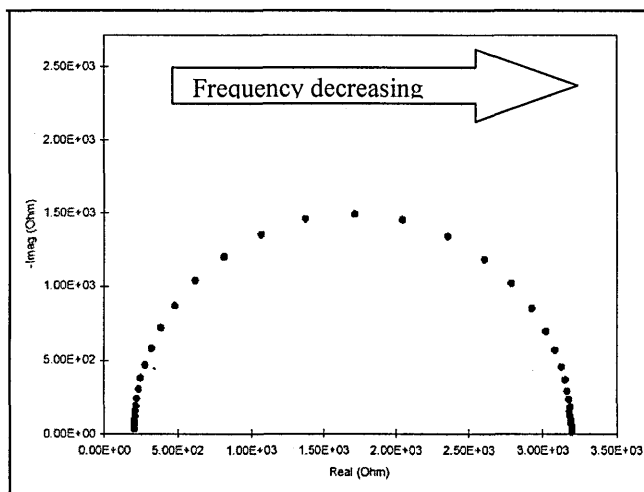
Equivalent circuit for the grinding wheel
without the oxide layer growth

a.

Coating
Region,
C_c and R_c

Steel Corrosion Region,
C_p and R_p

Diffusion
Region,
Z_d

-Z", Imaginary
Impedance,
Ohms

Frequency,
Hz

Frequency decreasing

R_e

$R_e + R_p$

Z', Real Impedance, Ohms
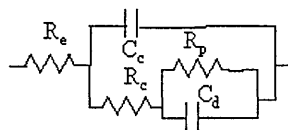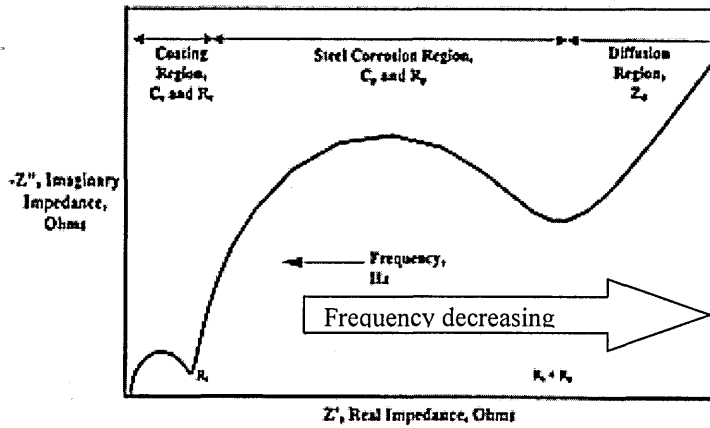
Equivalent circuit for the grinding wheel
with the oxide layer grown on it

b.

Figure 2.14: Expected Nyquist plots and equivalent circuits
a. wheel without oxide layer growth, b. wheel with oxide layer growth

In the case of a metal component covered by an oxide layer and in the absence of oxygen (in order to avoid oxygen diffusion effects on the interface) the Nyquist plot comprises of two semicircles; one corresponds to the metal surface and the other to the oxide layer on it. There is the possibility of an interaction between the two semicircles, depending on the time constants that characterise the capacitive and resistive behaviour of the metal and the oxide layer. In figure 2.14b, the two semicircles and the oxygen diffusion effect are shown

The equivalent circuits that represent the response of the wheel segment to the application of an external excitation such as an alternating current also differ, depending on the presence or not of an oxide layer. In the simple case of a bare metal surface in solution, the equivalent circuit comprises the resistance of the electrolyte R_e, the charge transfer resistance of iron R_0 and the double layer capacitance (between the metal surface and the solution) C_0. The presence of the oxide layer introduces more components to the equivalent circuit such as the layer resistance (R_c in figure 2.14b) as well as the capacitance between the metal and the electrolyte with the film as dielectric, (C_c in figure 2.14b). R_p is again the charge transfer resistance only its

66

value is now different as it is affected by the presence of the oxide layer and C_d is the double layer capacitance at the surface of the segment.

The application of ELID grinding involves the electrochemical removal of the metal bond of metal bonded wheels through the formation of a brittle oxide layer. In this way new diamonds are exposed and blunted ones are removed together with the oxide layer, improving the efficiency of the cutting process. The rate of the oxide formation process is very important for the understanding of the mechanism of ELID and is controlled by the corrosion product, which forms an insulating barrier on the surface, which has a varying thickness that leads to varying electrical properties. Thus, it was important to be able to determine parameters such as the resistance of the oxide layer and the rate of corrosion of the underlying metal bond.

2.D.4 MODELLING THE ELID PROCESS

In order to be able to get optimum results from ELID grinding, it is important to be able to lose grains that have been worn out during the grinding process and replace them with new, more efficient grains. The information gathered through impedance measurements gave an indication of how the insulating layer's resistance changes.

A mass w removed from a metal bond by a current I for in-process electrolytic time t is as follows [53]:

$$It = \frac{wnF}{M}$$

(where n is the valency, F is Faraday's constant and M is the atomic weight).

The theoretical removal volume of the metal bond U_o is:

$$U_o = \frac{MIt}{nFp} = U_s It$$

where U_s is the specific machining volume and p is the density of the metal bond. Considering the current efficiency, η, the actual removal volume U_r is:

$$U_r = \eta U_0$$

So, the volumetric removal rate per unit time, u, is :

$$u = \frac{dU_r}{dt} = \eta U_s I$$

The correlation of resistance values and corrosion rates, along with the control of ELID current values and obtained surface finishes on testpieces can lead to optimisation of the parameters of the ELID procedure.

2.D.4 FIB, SEM AND EIS EXPERIMENTS PERFORMED

FIB-SEM STUDIES

-No oxide layer /Fully Grown Oxide Layer

A segment from a wheel containing diamond grits of 6-12µm was studied in the FIB and SEM facilities in two different conditions: After wheel truing, with no oxide layer grown on its surface, and after electrolytic pre-dressing, with a fully grown oxide layer on its surface.

- State 1 - Equilibrium condition:

The no-grit cupwheel was studied here after conventional pre-dressing and equilibrium oxide layer growth and after having ground 4 glass testpieces. The first testpiece was ground at the maximum rotation speed of the wheel of 6000 rpm only to confirm that the absence of diamond grits led to a very poor surface obtained, characterised by deep scratches and feed marks. The rest of the testpieces were ground at the lower wheel speed of 1000 rpm and much better finishes were produced with higher surface qualities. The two small wheel segments where subsequently removed and observed on the FIB and SEM facilities.

- State 2 - Non-equilibrium condition:

In order to observe the effect of a non-equilibrium oxide layer on the final surface finish obtained, the no-grit wheel was used to grind a sample as for the previous

example, with the main difference of having used an alumina stick on the wheel before the grinding process so as to remove the oxide layer on the segments. After grinding the samples, the wheel segments were removed for further studying on the FIB and SEM.

EIS STUDIES

- Initial Experiments

Initial experiments were performed with the PTFE cell on a grinding wheel that had undergone truing only and on a grinding wheel that was trued and electrolytically pre-dressed with a fully grown oxide layer on its surface. The wheel was immersed in tap water and subjected to a scan over a range of frequencies between 10^{-3} Hz and 2×10^4 Hz. The solution had been previously nitrogen purged in order to move the effects of oxygen diffusion to lower frequencies and allow the development of the semicircles with a minimised oxygen effect.

- Modified Experimental set-up

Once the new experimental set up was complete and the new cell constructed as previously described in section 2.D.2.2, tests were performed on segments of a 2μm diamond wheel after truing and after a fully grown oxide layer was grown on its surface. The electrolyte used in these experiments was an aerated NaCl solution in distilled water (35gr of NaCl in 1lt of distilled water) with the addition of 10ml of the CEM grinding fluid provided by Fuji Die.

Tests were also performed under the following conditions:

-Exposure of the segment in this aggressive NaCl solution for prolonged periods of time

-A segment was tested after an oxide film has naturally grown on it a few days after truing it

- A comparison was made in the EIS properties of segments with a thin and a thick post-grinding oxide layer.

- Finally the no–grit wheel was tested in order to observe the potential effect of the absence of diamonds to the impedance response of the segments.

2.E SUB-SURFACE DAMAGE (SSD) EVALUATION

2.E.1 INTRODUCTION

Precision optics manufacturing is characterised by high demands in several aspects that define the quality of the components produced. Reflective optics require a damage-free surface with exceptional surface finish and high shape accuracy but most other optical applications, in which light is transmitted through optical components, also require damage-free sub-surface in order to avoid scattering phenomena.

The evaluation of the damage introduced immediately under the surface of the manufactured components is a complicated process. Shape accuracy and surface finish can be immediately measured on the finished sample but sub-surface damage is usually evaluated by polishing and identifying damage and defects in increasing depths from the sample surface, a time consuming process that is directly influenced by the depth to which damage is extended.

Another issue relating to sub-surface damage is the identification of the stage of the production of the component in which the damage is introduced. The consecutive processes that are utilised (cutting raw material, shaping, rough grinding and smoothing the final component) can potentially cause defects in the sample. Hence, it is important to make sure that each process induces a controlled amount of damage (or ideally no damage at all) that is removed completely in order to achieve a defect-free end-product.

In the results chapter, sub-surface damage characterisation tests are presented for samples in different stages of the process chain, from the as-received condition to the final finishing passes. The amount of defects is evaluated for each process and optimised conditions are identified for minimal defect introduction with low production times and process efficiency.

2.E.2 SUB-SURFACE DAMAGE CHARACTERISATION: TESTING METHODS DESCRIPTION

Two testing methods were evaluated during these trials and finally, one of the two was chosen to proceed with the bulk of the sub-surface damage characterisation of samples. A small description of each procedure follows.

- **Sample sectioning:**

During this process, each sample that was studied for sub-surface damage was sectioned either perpendicularly to the ground surface, or at an angle of 45°. The sample was then embedded in resin and the cut surfaces were polished so that the damage that was induced during cutting would be removed. The sample was then etched so that cracks and defects were revealed and then observed on the optical microscope. The depth into which damage extends could then be estimated by direct observation of the optical micrographs taken. In the case where the sample was sectioned at an angle of 45°, a magnifying factor of $\sqrt{2}$ was taken into account.

The following optical micrographs in figure 2.15 give an indication of the kind of information on sub-surface damage that can be gathered by studying different samples at different stages of their processing.
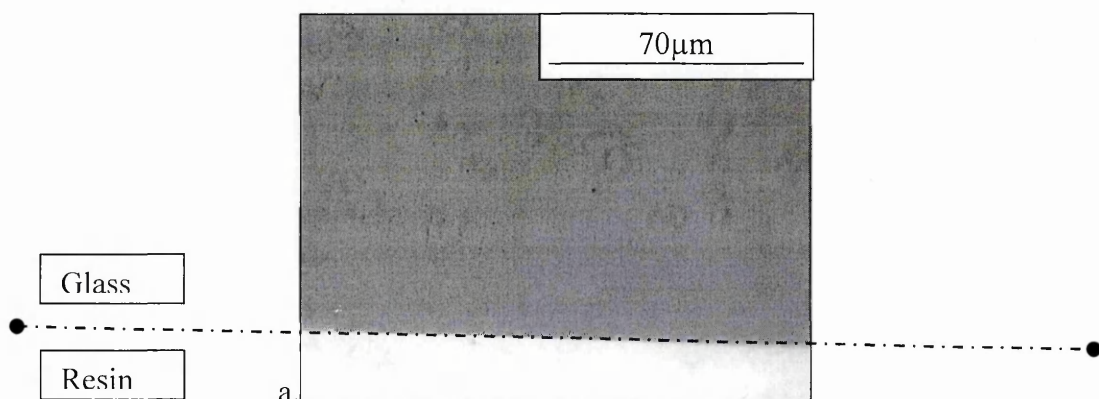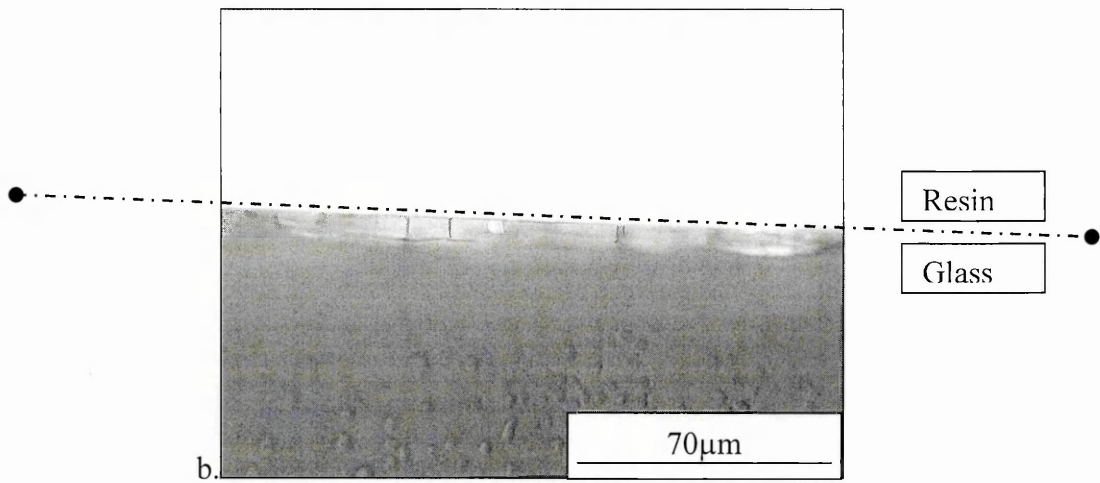
Figure 2.15: Defects (cracks, bubbles) observed in glass samples during SSD evaluation
a. Sectioned ELID ground sample
b. Sectioned resin bond wheel ground sample

- **Sample polishing back:**

This process is more time-consuming but more reliable in terms of revealing possible defects. Indents of a known geometry were introduced in the surface of the sample (Vickers hardness indents in this case) and their dimensions measured. The sample was then polished back and etched. The change in the dimensions of the indents on the surface would give an estimation of the amount of material that was removed while polishing and hence, the depth into which the damage extends once no more damage is visible after polishing. Figure 2.16 shows the difference in the size of the indent as well as the reduction of damage as we proceed further inside the testpiece.
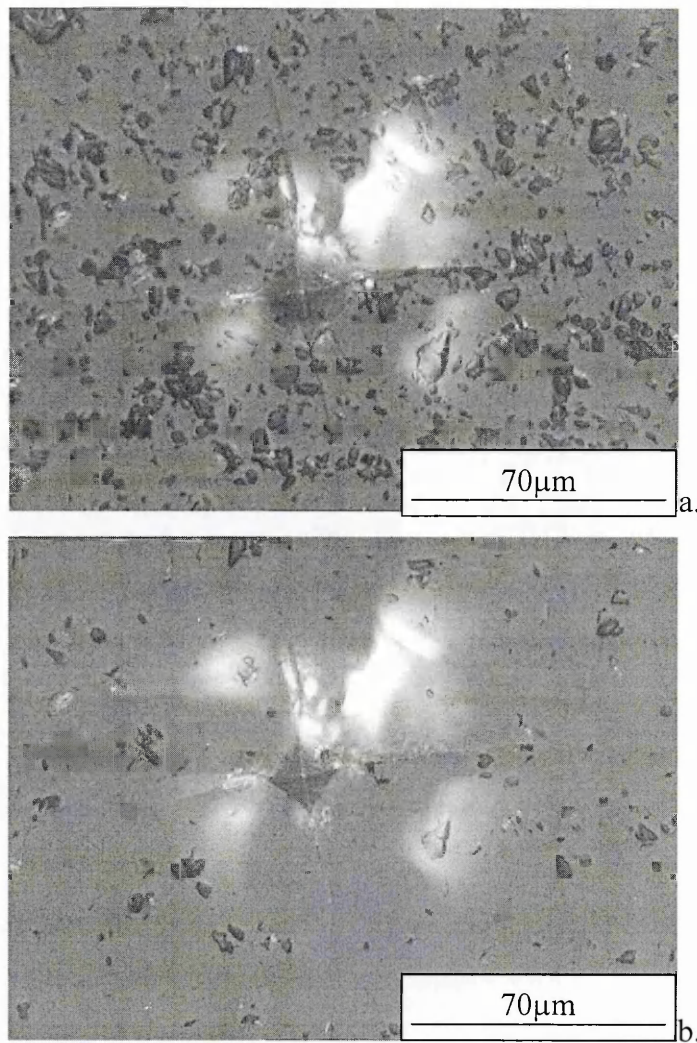
Figure 2.16: Vickers' indent before (a.) and after polishing back (b.). Change in the indent dimensions is apparent and helps estimate the depth or material removed.

The calculation of the amount of material removed was based on the geometry of the indent. The angle of the indenter ($\theta = 136°$ as shown in figure 2.17a) was imprinted on the material studied (in this case BK7 glass) and basic trigonometric functions allowed us to calculate how much material had been removed during polishing, based on the reduction in the size of the diagonals of the indent. The diagonals were measured directly on the optical micrographs of the samples using the optical microscope software tools.

The depth of material removed after each polishing step was calculated by equation:

$$h = \frac{l_1 - l_2}{2 \tan \dfrac{\theta}{2}} \qquad \text{where}$$

h: depth of material removed

l_1: diagonal of indent before polishing

l_2: diagonal of indent after polishing

θ: $136°$

according to the diagram shown in figure 2.17.b.
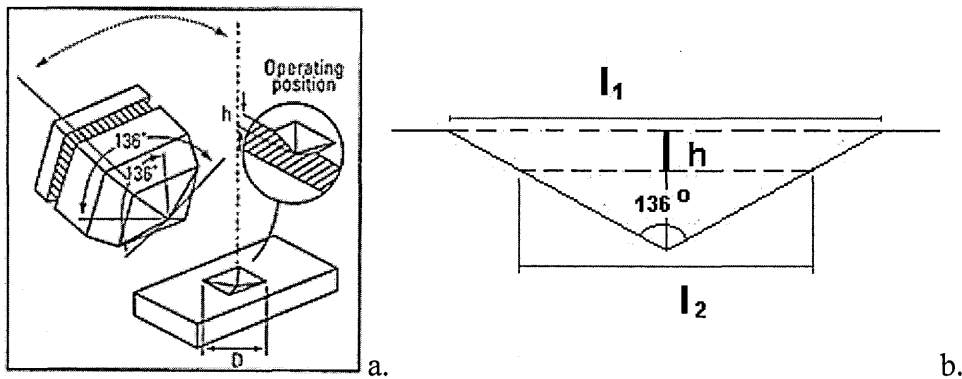
Figure 2.17: a. Vickers indenter b. Schematic for the calculation of depth of material removed after polishing

In cases where damage was deeper than the depth into which the indent extended, new indents were introduced on the sample, which was then again polished back and etched until no more damage was visible on the surface. Adding up the successive polishing steps eventually gave the total depth of damage.

2.E.3 SUB-SURFACE DAMAGE CHARACTERISATION EXPERIMENTS

Round BK7 testpieces of 50mm diameter were ground with different grinding wheels and at different feed rates, in order to study the sub surface damage that was introduced in them through different grinding processes. Table3 summarises the experiments performed on testpieces that were subsequently evaluated in terms of depth of damage post-grinding. The two sub-surface damage evaluation methods used were "sectioning" and "polishing back".

Table 3: Sectioning and Polishing Back experiments performed

Testpieces Used for Sectioning			
Testpiece	Wheel	Depth of cut (µm)	Feed rate (mm/min)
BK7 Square 20mmx20mm	"as received" from manufacturer	-	-
BK7 Square 20mmx20mm	ELID cast iron bond wheel 3-6 µm diamond grit size	5	20
BK7 Square 20mmx20mm	Resin bond wheel 3-6 µm diamond grit size	5	80
Testpieces Used for Polishing Back			
Testpiece	Wheel	Depth of cut (µm)	Feed rate (mm/min)
BK7 50mm diameter	"as received" from manufacturer	-	-
BK7 50mm diameter (from as received)	151 µm grit resin bond wheel	5	50
BK7 50mm diameter (from as received)	151 µm grit resin bond wheel	10	50
BK7 50mm diameter (from as received)	151 µm grit resin bond wheel	15	50

75

BK7 50mm diameter (from as received)	151 μm grit resin bond wheel	20	50
BK7 50mm diameter (from as received)	46 μm grit resin bond wheel	5	50
BK7 50mm diameter (from as received)	2 μm grit cast iron bond spherical ELID wheel	1	50
BK7 50mm diameter (from as received)	2 μm grit cast iron bond spherical ELID wheel	1	210
BK7 50mm diameter (from as received)	2 μm grit cast iron bond spherical ELID wheel	1	470
BK7 50mm diameter (from as received)	2 μm grit cast iron bond spherical ELID wheel	1	830
BK7 50mm diameter *(from polished)	2 μm grit cast iron bond spherical ELID wheel	1	50
BK7 50mm diameter *(from polished)	2 μm grit cast iron bond spherical ELID wheel	1	210
BK7 50mm diameter *(from polished)	2 μm grit cast iron bond spherical ELID wheel	1	470
BK7 50mm diameter *(from polished)	2 μm grit cast iron bond spherical ELID wheel	1	830
BK7 50mm diameter *(from polished)	2 μm grit cast iron bond spherical ELID wheel	1	1200

As can be seen from table 3, the same wheel and grinding parameters were used on an "as received" testpiece and one that was previously polished. In the case of the polished testpiece, there was certainty that all the sub-surface damage present after the grinding process was due to the process itself rather than pre-existing damage in the testpiece (e.g. damage present in the as-received testpiece described previously).

Sub-surface damage data were also gathered from a testpiece ground on a rotary table, with a 7 μm grit resin bond wheel. The experimental details of this set of experiments are listed below:

• Wheel

7 μm diamond grit, resin bond wheel.

• Workpiece

Specification: BK7 glass.
Ground surface: 50 mm diameter.

• Grinding conditions

Speed of rotary worktable: 5.5 rpm.
Radial feed: 0.025 mm/s.
Depth of cut: 5 μm

2.F COMPARISON OF GRINDING STABILITY BETWEEN ELID AND RESIN BOND WHEEL GRINDING-ACOUSTIC EMISSION (A.E.) SIGNAL ACQUISITION/EVALUATION

2.F.1 INTRODUCTION

One of the most important benefits that ELID grinding potentially has to offer is the ability to dress the wheel while grinding of components is taking place. The basic idea is that blunt diamond grits are removed and new sharp grits are exposed while grinding is taking place. This keeps the wheel in a state of high cutting efficiency over prolonged periods of use and the combined use of the friable oxide as a lubrication medium in the secondary grinding zone leads to high quality surface finishes even when the wheel has been used in long grinding cycles. This is a limitation that is difficult to overcome when using conventional resin bond wheels with fine diamond grit sizes as no in-process dressing method has been devised for them. Thus, the grinding process has to be stopped at specific intervals, so that the wheel is re-dressed, in order to avoid wheel loading and to expose sharp cutting grits.

In order to demonstrate the above, a set of comparative tests was performed on testpieces that were ground with a resin bond wheel and samples ground with ELID over different periods of time. The surface finish achieved on two different types of testpieces is presented for different cycle times for both kinds of wheels.

During grinding of the round testpieces, acoustic emission signals were acquired in order to study the possibility of monitoring the grinding process by using this method.

2.F.2 TESTPIECES AND EXPERIMENTS DESCRIPTION

The samples used on these tests were flat round BK7 testpieces, 50 mm in diameter. Due to the large size of the round specimens and the different wheel-testpiece contact area characterizing different parts of them, the potential of changes in the final surface finish on different areas of the surface were identified. Hence, on each sample, five

Talysurf measurements were performed along the centre-line, the stylus trace parallel to the grinding direction, indicating five different regions on each sample (regions I-V as shown in figure 2.18).

Grinding Direction
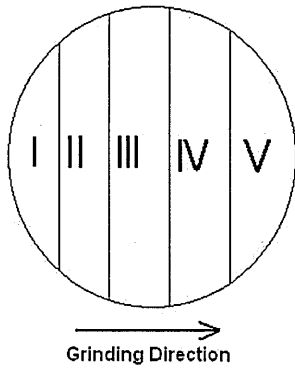
Figure 2.18: Sample regions

The samples were ground over different periods of time, by repeating multiple passes on their surface, both with ELID grinding and with resin bond wheels. Except for sample surface integrity and finish the appearance and characteristics of the grinding wheels were also studied. In the case of ELID grinding current and voltage values were recorded. The removable segments were used in EIS measurements in order to evaluate resistance values and on the FIB and SEM facilities, which were described previously. In the case of the resin bond wheel, its integrity was studied on the SEM.

The samples were ground at a constant feed rate of 3mm/min and a depth of cut of 2µm. This meant that each pass made on each round testpiece lasted for about 17 minutes.

Three sets of experiments were performed:

a. Single-pass ground testpieces (grinding time: 17 minutes): The first sample was initially cleaned up until its surface was completely flat and parallel to the grinding wheel. In the case of ELID the wheel was then pre-dressed once more, so that the oxide layer was again fully grown on the surface of the grinding wheel and then, it was ground once more. In the case of resin bond wheel grinding, the resin bond

wheel was re-trued after the clear up stage. This would ensure that the state of the wheel would be that of a wheel that was used on a sample for the first time.

b. Ten-pass ground testpieces (grinding time: 167 minutes): The second set of samples was prepared in the same way as the previous ones only this time each sample was ground ten times, with the same depth of cut and feed rate as before. The total grinding time for the resin bond wheel was approximately 167 minutes whereas for the ELID wheel it was a bit higher as it was used without re-dressing it after the clean up stage of the sample.

c. Twenty-pass ground testpieces (grinding time: 334 minutes)

2.F.3 ACOUSTIC EMISSION SIGNAL ACQUISITION

The flowchart of the AE signal acquisition system is shown in Figure 2.19. Acoustic emission signals were acquired using piezoelectric transducer sensors. Sensor1, shown in Figure 2.20, is a model WDI with a broad-band of 100-1000 kHz from Physical Acoustics Corp. The sensor was attached to the surface of the workpiece holder using petroleum jelly. The acoustic emission signals were converted into electrical signals by the sensor, amplified to usable voltage levels by the preamplifiers and transferred to the AEDSP-32/16 card, which had a 16-bit resolution for data recording. The preamplifier (1220A) provided a gain of 100 (40 dB) and used a bandwidth filter with 100 kHz-1200 kHz bandwidth to eliminate the mechanical and acoustical background noise that prevails at low frequencies. A frequency of 2 Mega sample rate per second was selected for signal acquisition. The AE facility was used to acquire AE raw signals with short operating duration for AE_{RMS} and Fast Fourier Transformation (FFT) analysis.
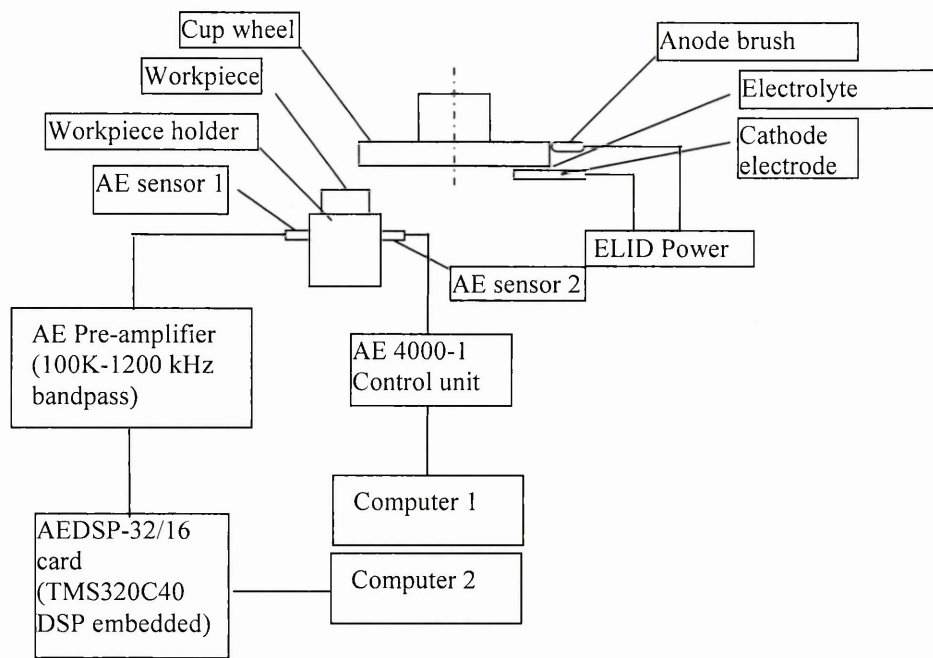
Figure 2.19: Acoustic emission signal acquisition system.

Figure 2.20: WDI acoustic emission sensor from the Physical Acoustics Group.

Another AE system, sensor 2 in Figure 2.19, was an AE4000-1 from Walter Dittel GmbH, with an "S" type sensor. It was used to collect rectified AE signals for monitoring the changes of AE in the whole grinding process. The S type sensor is shown in figure 2.21.
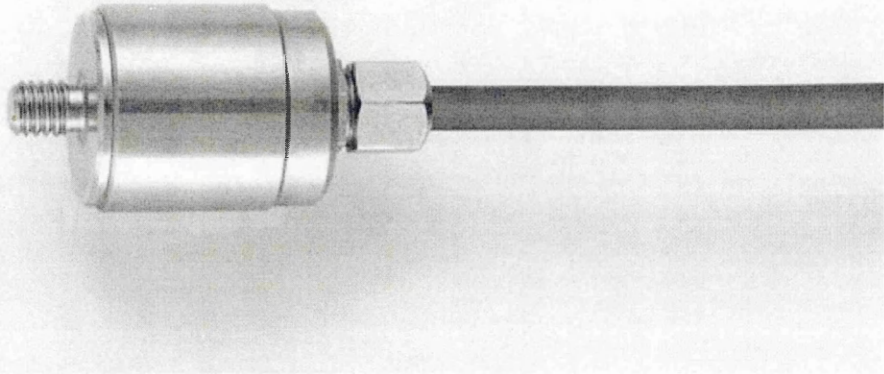
Figure 2.21: AE4000-1 from Walter Dittel, S type sensor

AE signals were acquired during the experiments described in paragraph 2.F.2, which were performed in order to compare the stability over time of ELID grinding and resin bond wheel grinding.

2.G GRINDING FLUIDS CONDUCTIVITY PROPERTIES

2.G.1. INITIAL GRINDING FLUID CONDUCTIVITY EXPERIMENTS

The conductivity properties of grinding fluids were also studied in order to give insight into their role in grinding procedures and ELID grinding in particular.

Two grinding fluids were studied: CEM, the grinding fluid recommended from Fuji Die Co., Japan, for ELID grinding, which is yellow in colour, and DOWEL, a grinding fluid commonly used in the laboratory work taking place in Cranfield University which is dark red in colour.

The fluids were diluted in tap water, with different concentrations (namely 1% and 2%) and the changes in conductivity were evaluated. The concentrations chosen for these solutions were based on the usual fluid concentrations used in the laboratory.

Conductivity was also measured after the CEM grinding fluid had been used for grinding samples. The solution was enriched in ions during the experimental work performed and the changes in its conductivity and appearance were observed and recorded.

CHAPTER 3: EXPERIMENTAL STUDIES AND RESULTS

3.A. OXIDE LAYER THICKNESS STUDIES

3.A.1 INTRODUCTION

The following section deals with the experimental study of the ELID oxide layer. Initial comparative tests were performed for resin bond wheels and cast iron bond wheels using ELID.

The surface finish results on the initial experiments performed are shown in table 4 below, where the R_a values were measured twice for each sample with a Talysurf diamond-tip Stylus. Each of the Talysurf traces was 5mm long.

Table 4- Surface Finish (Ra) achieved for testpieces SqA - SqL

Sample #	Wheel	Feed rate (mm/min)	Depth of cut (µm)	Rotary table speed (rpm)	Wheel speed (rpm)	Surface Finish R_a (nm)
SqA	No grit CIB	3	2	20	1000	3,4
SqB	3-6 micron CIB	3	2	20	1000	28,30
SqC	3-6 micron CIB	3	2	20	6000	18,19
SqD	3-6 micron CIB	30	2	20	6000	17,17
SqE	3-6 micron CIB	6	4	No rotary	6000	11,11
SqF	3-6 micron CIB	20	4	No rotary	6000	13,14
SqG	3-6 micron CIB	100	4	No rotary	6000	17,20
SqH	3-6 micron RB	6	4	No rotary	6000	18,10
SqI	3-6 micron RB	20	4	No rotary	6000	27,40
SqJ	3-6 micron RB	100	4	No rotary	6000	30,42
SqK	3-6 micron RB	30	2	20	6000	23,23
SqL	3-6 micron RB	3	2	20	6000	13,14

The comparison of surface finish values obtained for samples SqE- SqJ, as displayed in figure 3.1, give an indication on how surface finish varies across the testpieces with the increase in feed rate. Surface finish was measured on each sample in two different areas. The values measured on the ELID ground samples show that surface finish is uniform across the testpiece area. The values measured on the resin bond wheel ground samples show more scatter and there is a noticeable difference in surface finish across the area of

the sample. Values of R_a are higher but also differ more across the testpiece (ELID ground testpieces: R_a varies between 11 and 20nm. Resin bond wheel ground samples: R_a varies between 10 and 42nm).
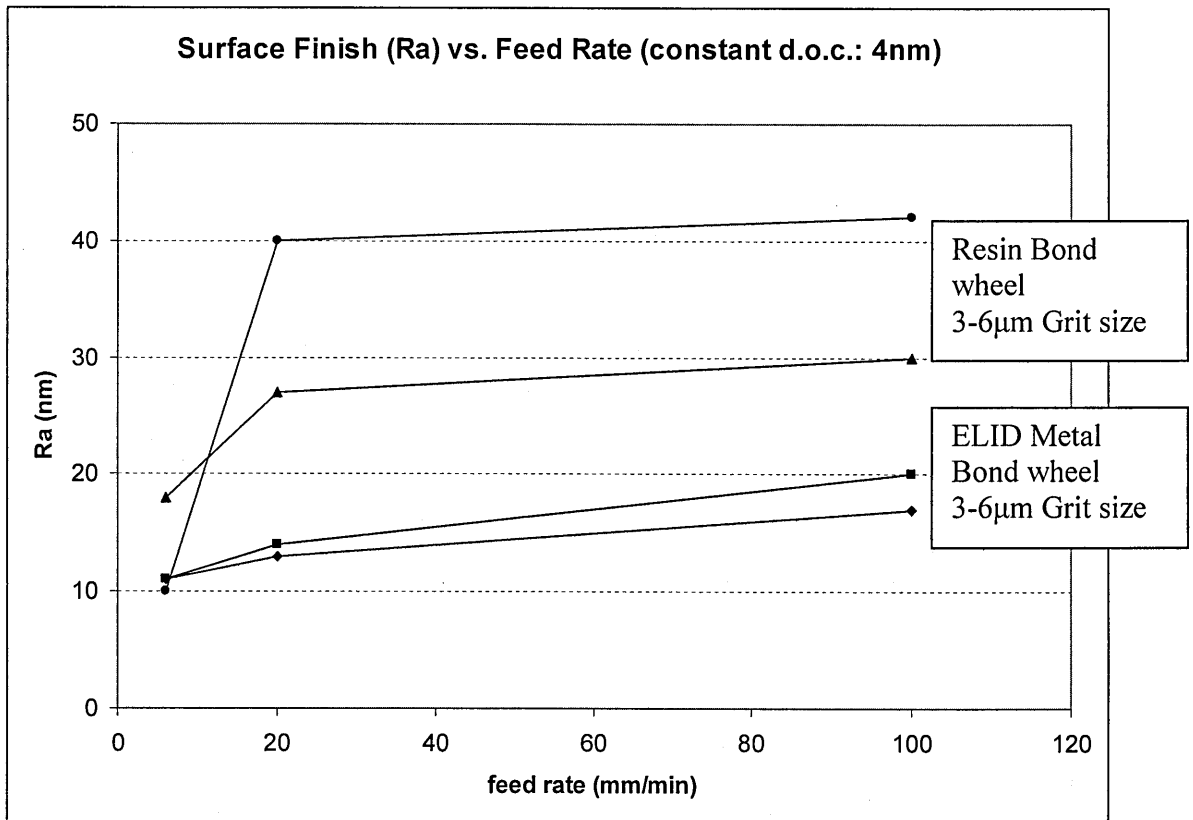
Figure 3.1: Surface finish vs. Feed rate at a constant depth of cut of 4nm: Comparison for resin bond wheel and ELID metal bond wheel. (Comparing samples SqE- SqJ)

Similar indications can be seen when using the rotary table while grinding testpieces with ELID or with a resin bond wheel. A wider variation in achieved surface finish is observed when using the resin bond wheel than when using ELID.

When using the no-grit diamond wheel, as can be seen from table 4, choosing a lower wheel speed leads to higher quality surface finish, which does not apply when using the grinding wheels that contain diamond grits (lower wheel speed leads to worse surface

finish achieved). More details on the no-diamond grit tests are given later on in this chapter when studying testpiece A and testpiece B.

By use of focused ion beam (FIB) and scanning electron microscope (SEM) techniques the thickness and quality of the oxide layer grown on the cupwheel when using ELID were studied. Its different states (fully grown, post-grinding condition) were observed and, where applicable, correlated with the final surface finish achieved on the ground BK7 glass samples. Current and voltage data were again gathered while grinding and are used as a means to monitor the evolution and changes of the thickness of the film that is produced and identify the different thinning and re-growth mechanisms that take place during the grinding process.

In the following sections, different states of the wheel are presented in order to evaluate the effect of the presence of the oxide layer under given conditions.

3.A.2 NO OXIDE LAYER - FULLY GROWN OXIDE LAYER

The pieces of a segmented wheel are presented here in two different states: Immediately after balancing and truing, where no oxide layer was present (figure 3.2a) and also after pre-dressing, when the oxide layer was fully grown (figure 3.2b). The wheel also contained diamond grits of 6-12 μm size.

As the pictures show, the wheel surface before and after ELID pre-dressing was very different. The shiny surface before pre-dressing was replaced by the one covered with a friable layer of corrosion product once the pre-dressing stage was completed.

In the pictures of figure 3.2, diamonds were not detected anywhere on the surface or in the trough that had been etched on the wheel. Placing the segment in the SEM revealed the presence of diamond grits embedded in the matrix material (figure 3.3) which would eventually reach the surface once sufficient layers of it were electrolysed.
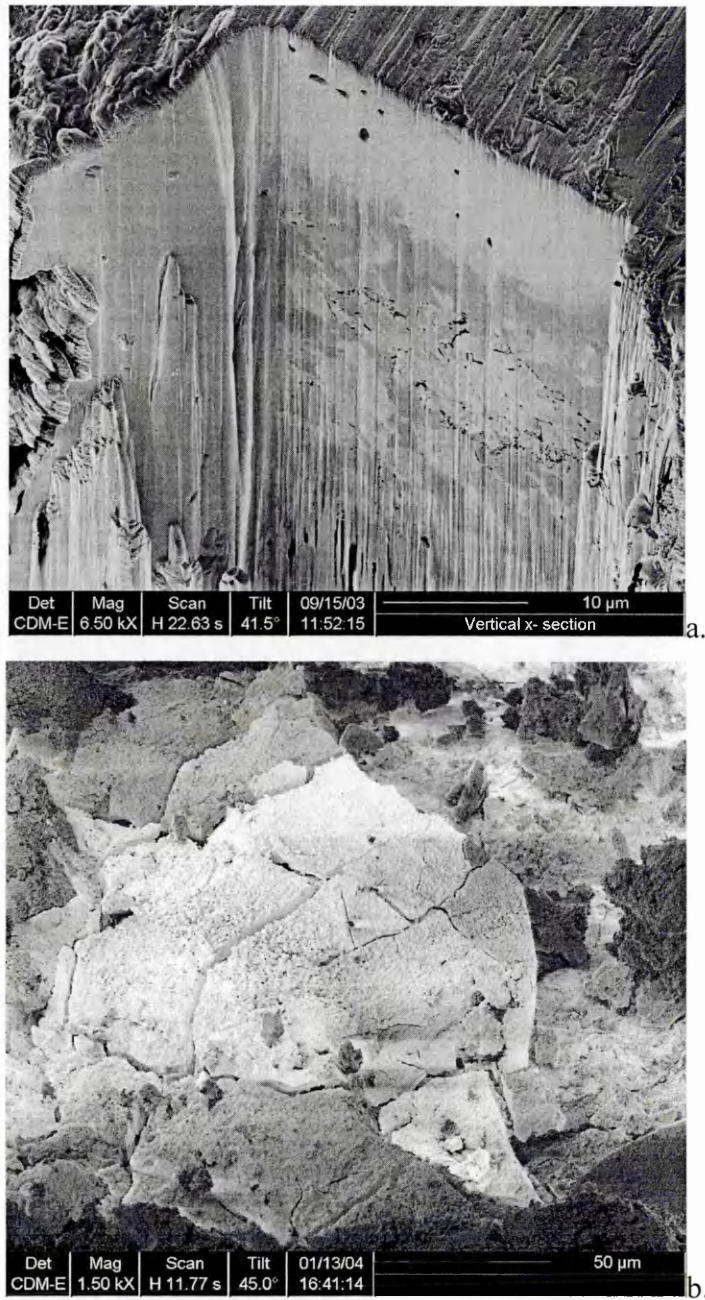
Figure 3.2: a. Trough etched on a trued wheel segment b. Surface of an ELID pre-dressed wheel segment
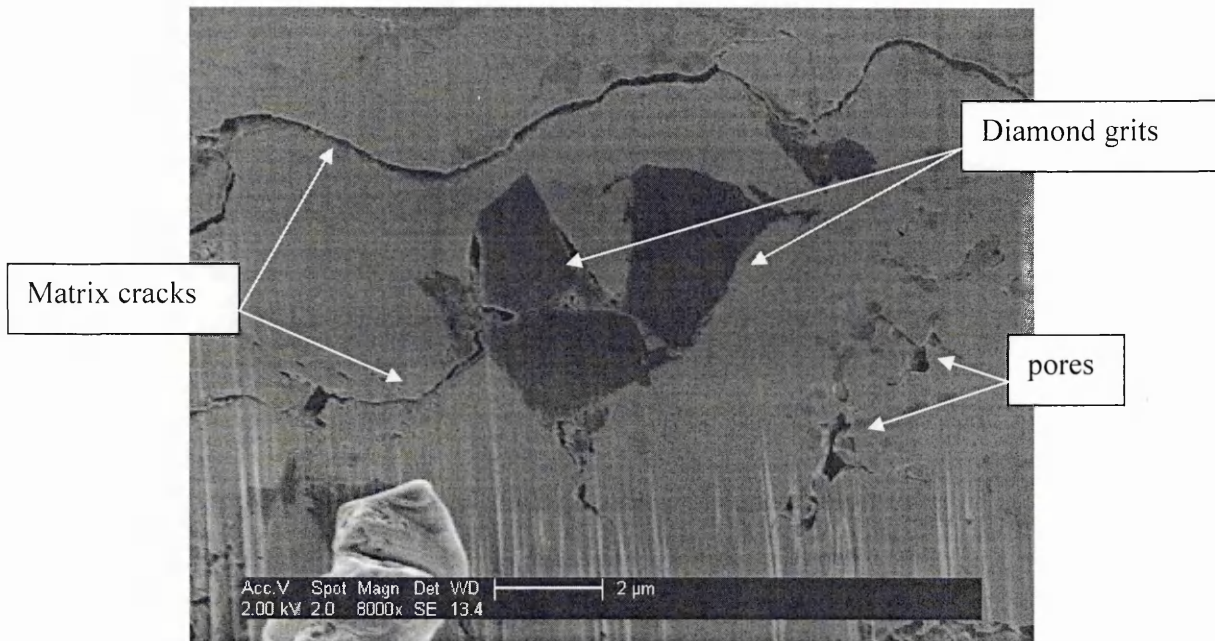
Figure 3.3: Secondary electron SEM image showing the presence of diamonds in the grinding wheel

The diamonds appeared to be clustered together while extended cracks and porosity were also observed in the matrix. These characteristics could be related to the process followed when manufacturing the grinding wheel. Although details are not given by the manufacturing company (Wendt Board) the observed traits indicate some form of powder metallurgy where diamonds and bond material are blended together and sintered.

The depth into which the fully grown oxide layer extends was also studied. Etching a trough on the front of the wheel, allowed the study of the structure of the wheel, moving from the surface to approximately 100 μm deep into the wheel. Figure 3.4 shows the structure that was observed. After a depth of approximately 50 μm into the grinding wheel, the structure changed and became more "compact"; this was considered an indication that the depth of about 50 μm was the depth into which the fully grown oxide layer extended.
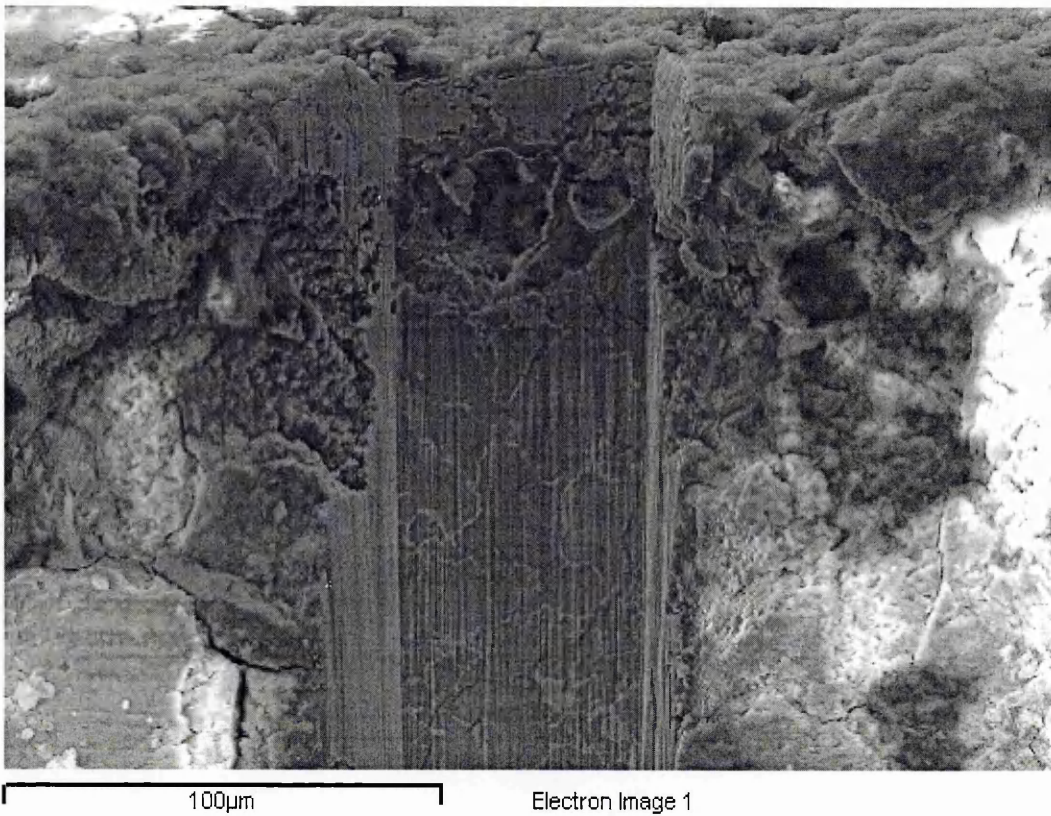
Figure 3.4: SEM image showing the trough etched into the grinding wheel and the structure that was observed.

3.A.2 OXIDE LAYER AFTER GRINDING – EQUILIBRIUM STATE

The friable fully grown oxide layer started being removed once the grinding process began and was essentially used as a lubrication medium in the secondary grinding zone. The conductivity of the wheel was increased and the resulting increase in current lead to a re-growth mechanism. Finally, an equilibrium state was achieved where oxide was removed from the wheel and new oxide was formed due to the current that flowed through the circuit.

This equilibrium condition was studied after having ground 4 glass samples with the no-grit cupwheel. The first sample was ground at the maximum rotation speed of the wheel

of 6000 rpm only to confirm that the absence of diamond grits led to a very poor surface obtained, characterised by deep scratches and feed marks.

The rest of the samples were ground at the lower wheel speed of 1000 rpm and much better finishes were produced with higher surface qualities as can be seen by the Ra values obtained for testpiece SqA in table 4.

After grinding the samples, the wheel segments were removed for further studying. A trough was etched as described previously and can be seen in figure 3.5.
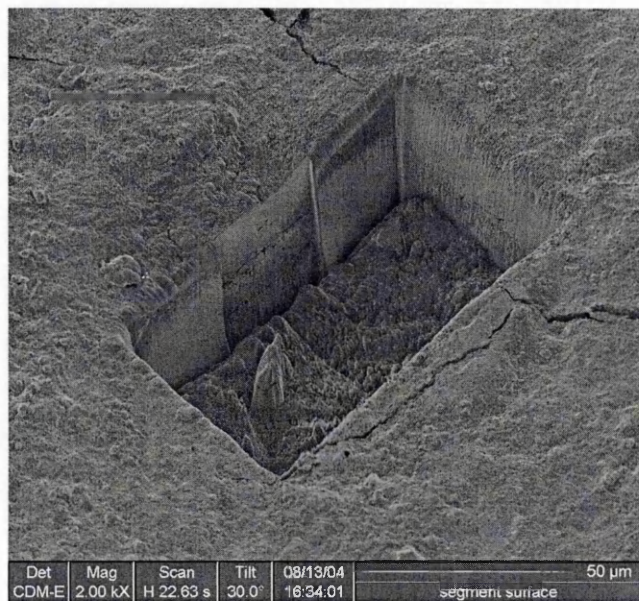
Figure 3.5: Trough etched on the no-grit cupwheel segment after grinding

Cracks were visible on the segment surface that indicate the friability of the layer. At the same time the cracks on that layer were not as pronounced as in the case of the fully grown layer, as expected after having removed a large part of it during grinding.

Focusing on the wall on the left side of the trough (figure 3.6), spot analysis was performed in order to identify the presence of oxygen and observe its variation with depth.

Figure 3.6: Detail of the wall at the left side of the etched area

The spots analysed are shown in figure 3.7 with each spectrum progressively moving lower down the trough wall. The analysis revealed a high concentration of oxygen for 5-6 microns down the wall (spectra 1 and 2 on figure 3.8). Oxygen was concentrated on the leafy/columnar structures that were observed on the SEM. At lower depths the oxygen concentration drops dramatically (spectrum 3 on figure 3.8). A high concentration of Ga was also observed, which was attributed to the Ga ions that bombarded the segment in order to create the pit.
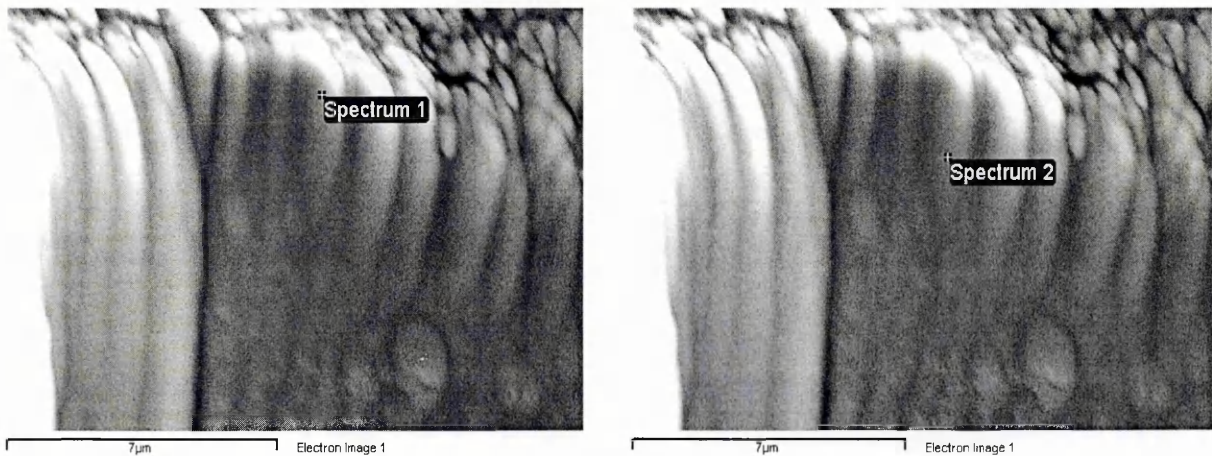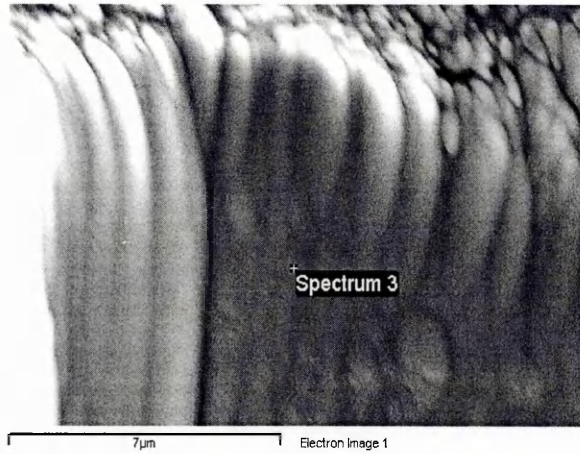
Figure 3.7: SEM pictures of the trough and the points where spot analysis is performed. Spectra 1, 2 and 3 progressively move deeper down the wall of the trough

The interface between the oxide layer and the matrix material was not expected to be characterised by an abrupt depletion of oxygen once the matrix material was reached. The depth where spectrum 3 was taken was assumed to be the depth into which the oxide layer extended. The areas of the wheel deeper inside the trough consisted predominantly of matrix material with minimal oxygen concentration.
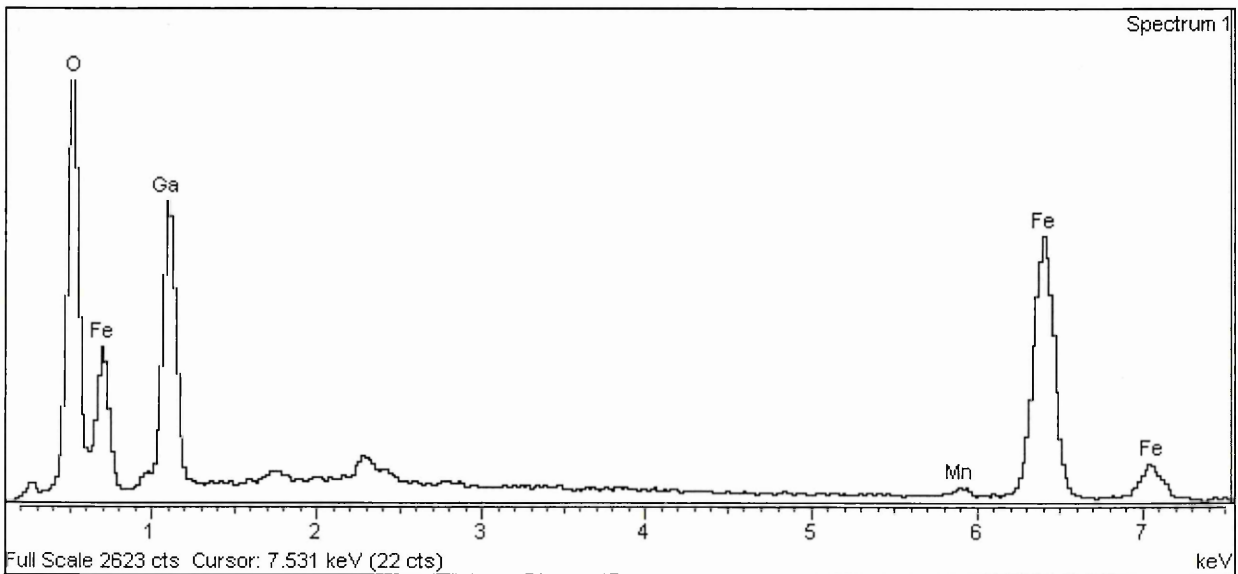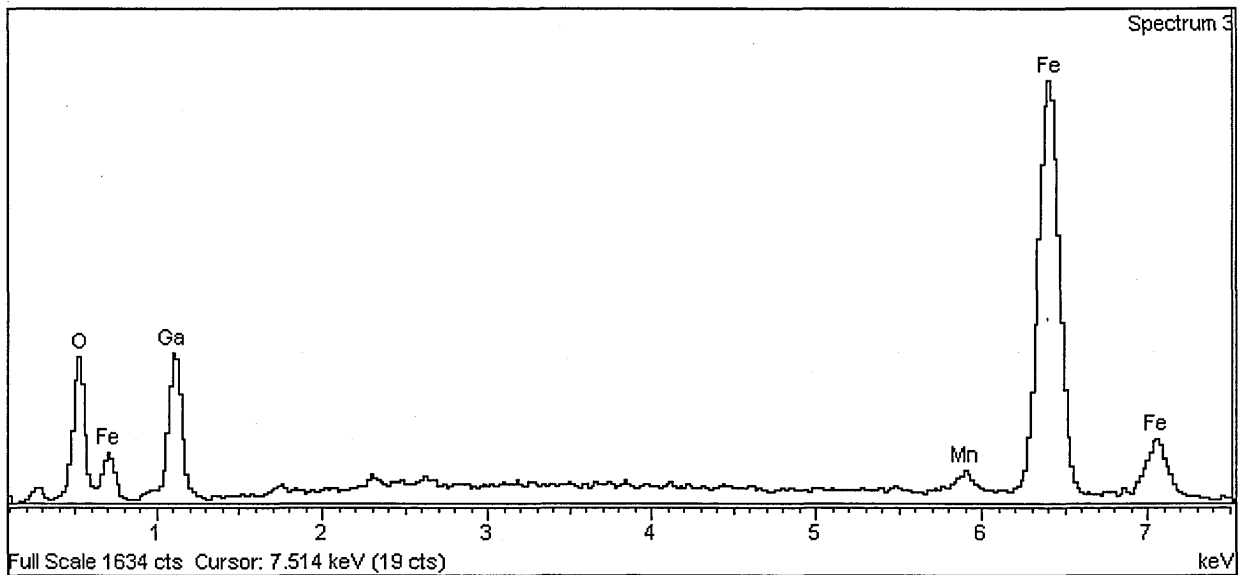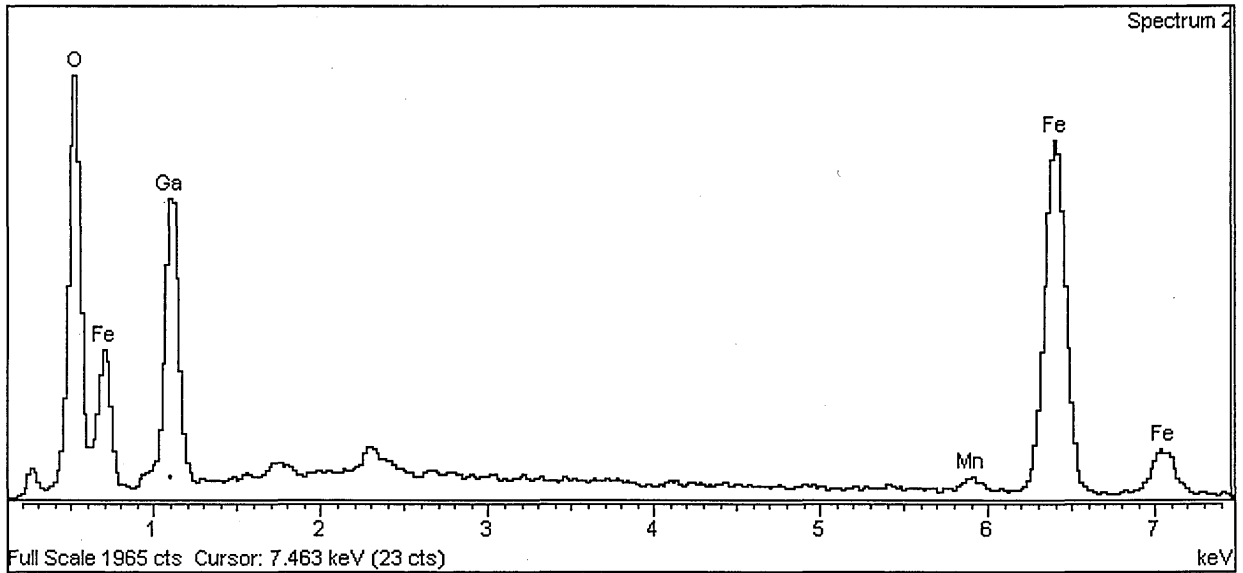
Figure 3.8: Spot analysis results indicating oxygen and gallium concentration. Oxygen concentration drops by moving deeper (from spectrum 1 to spectrum 3) into the trough

Considering this to be the equilibrium condition for the oxide layer, a comparison to a non- balanced state where the thickness of the layer was very small is presented below.

3.A.4 OXIDE LAYER AFTER GRINDING - NON-EQUILIBRIUM STATE

In order to observe the effect of a non-equilibrium oxide layer on the final surface finish obtained, the no-grit wheel was used to grind a sample as for the previous example, with the main difference beong the use of an alumina stick on the wheel before the grinding process so as to remove the oxide layer on the segments. More details on the surface finishes achieved on the samples studied will be presented later since the focus here is on the state of the wheel.

Immediately after removing the oxide layer, data were gathered from the current and voltage supply and, as expected, the conductivity of the wheel increased and so the initial voltage was low and the current was high. As the grinding process begun (figure 3.9), oxide build-up occurred again as the current flowed through the wheel which was verified by the increase in voltage and drop in current values.
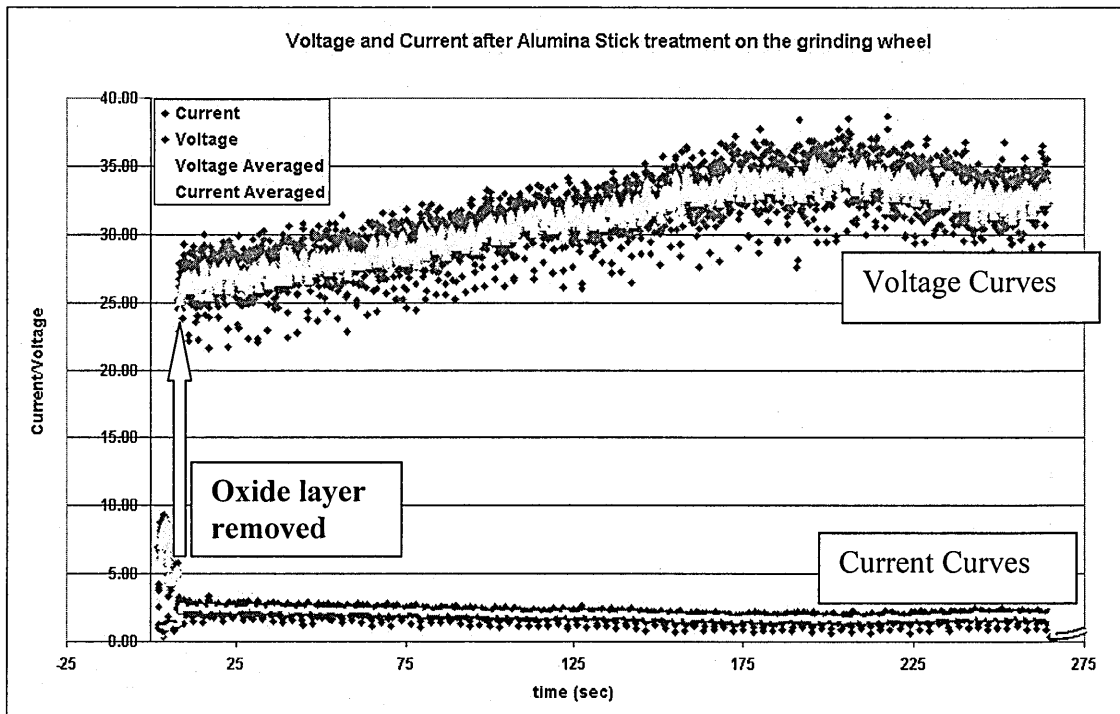
Figure 3.9: Current and Voltage values when grinding after having removed oxide from the wheel segments using an alumina dressing stick. Lighter coloured points represent averaged values of current and voltage.

The lighter coloured points on the graph shown in figure 3.9 are averaged data of the raw current and voltage values received from the ELID power supply. Due to the scatter that the raw data demonstrates, the averaged plots will be presented from now on, in order to be able to observe more clearly the patterns that current and voltage followed during grinding.

As previously described, the wheel segment was removed and placed in the FIB and SEM for spot analysis and the resulting pictures and analysis are presented in figure 3.10 below.

a.

b.

c.
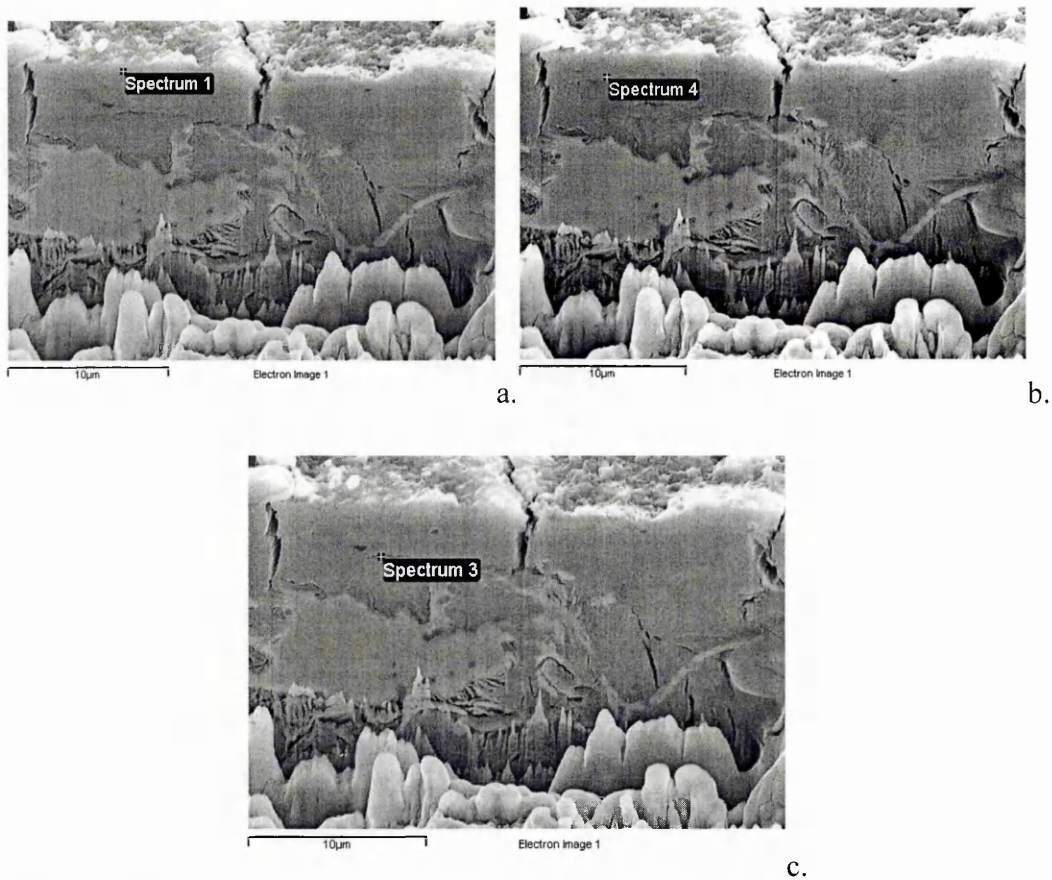
Figure 3.10: SEM pictures of the trough and the points where spot analysis is performed. Pictures a, b and c progressively move deeper down the wall of the trough

Spectra were taken at the three points depicted in pictures a, b and c of figure 3.10 above and the oxygen content is shown in figure 3.11.
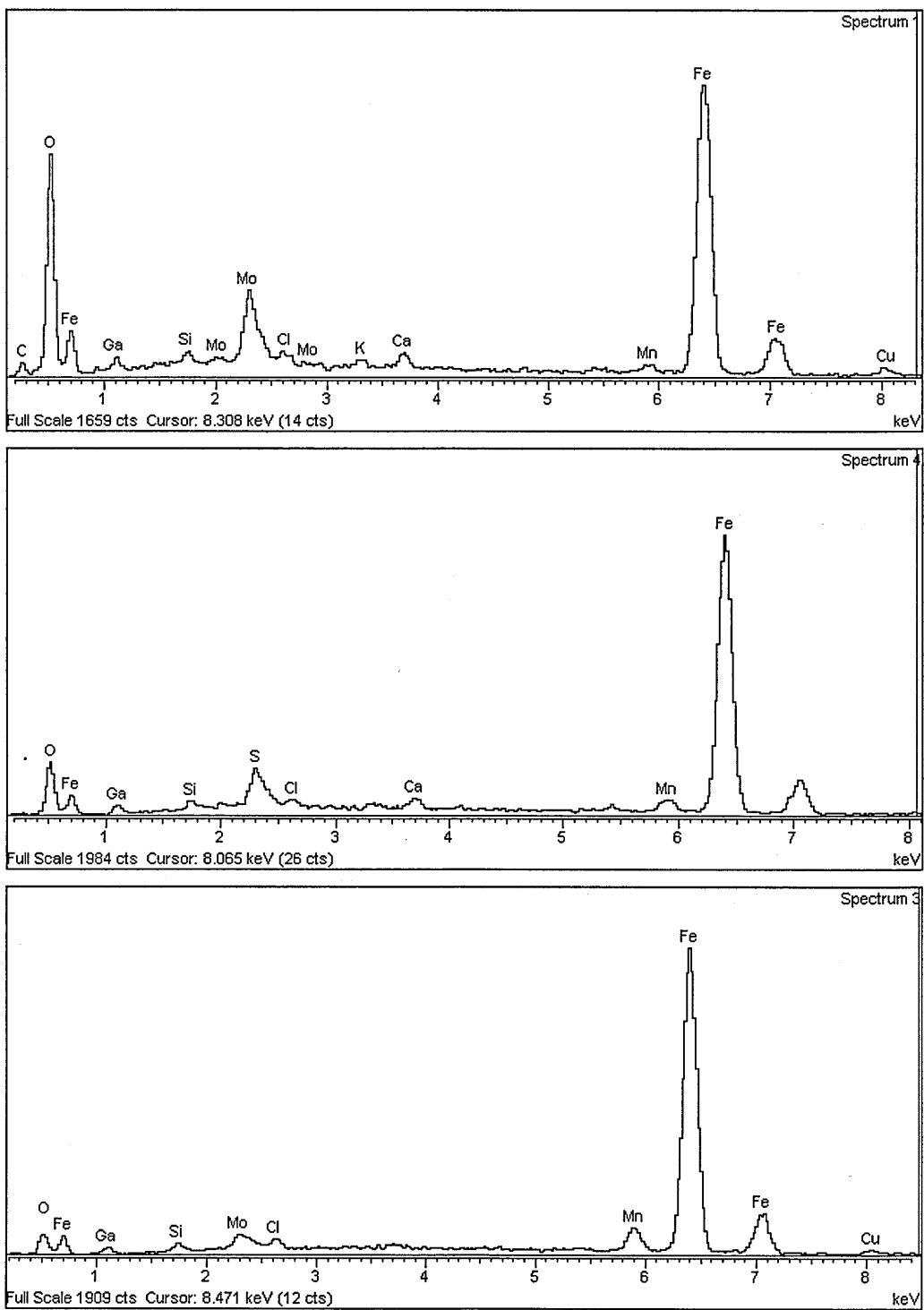
Figure 3.11: Spot analysis results. Oxygen content drops rapidly when moving deeper (from spectrum 1 to spectrum 3) from the surface

As expected, the content of oxygen dropped much quicker in this case as there was less oxide layer present. After a depth of approximately 1-2μm, the oxygen content was already very small and this indicated the depletion of the ferrous oxide. The effects of the oxide layer depletion on surface finish are presented next.

3.A.5 OXIDE LAYER THICKNESS EFFECTS ON SURFACE FINISH

Results from two testpieces ground using a wheel exhibiting slightly different oxide film characteristics are presented. As mentioned before, the lack of cutting agents on the wheel used for these studies makes it easier to focus on the contribution of the ferrous oxide towards the improvement of the workpiece surface without the interference of the cutting action of the diamond grits.

I. TESTPIECE A

Four consecutive passes were performed on a BK7 testpiece in order to observe and record the current and voltage trends and the way they might influence the final appearance of the sample surface. Table 5 shows the grinding parameters adopted for those four passes.

Table 5- Grinding Parameters for testpiece A

Wheel speed	Depth of cut	Feed rate	Rotary table speed
1000 rpm	2μm	3mm/min	20 rpm

Fluctuations in voltage indicate changes in the oxide layer during the process. Increase in voltage, corresponding to a decrease in current, indicate an increase in resistivity, hence oxide layer build-up. Similarly, a decrease in voltage corresponds to oxide layer

thinning and more current is allowed to pass through the wheel leading to consequent oxide layer build-up again.

Figure 3.12 shows the voltage (3.12a) and current (3.12b) changes over the last four passes. The emerging pattern was repetitive and suggested that as the wheel fed into the rotating sample (the wheel first begins to touch onto the corners of the rotating sample intermittently) and the contact area between the wheel and the sample was constantly increasing, the quantity of oxide and the rate of formation were not adequate and so the oxide thinned away as the arrows indicate. It is also possible that during the intermittent touch of the wheel on the testpiece, oxide layer was knocked off and removed from the secondary grinding zone hence, leading to a depletion of oxide. Once continuous contact was established, the oxide layer built up towards a stable state again until the end of the pass.

a
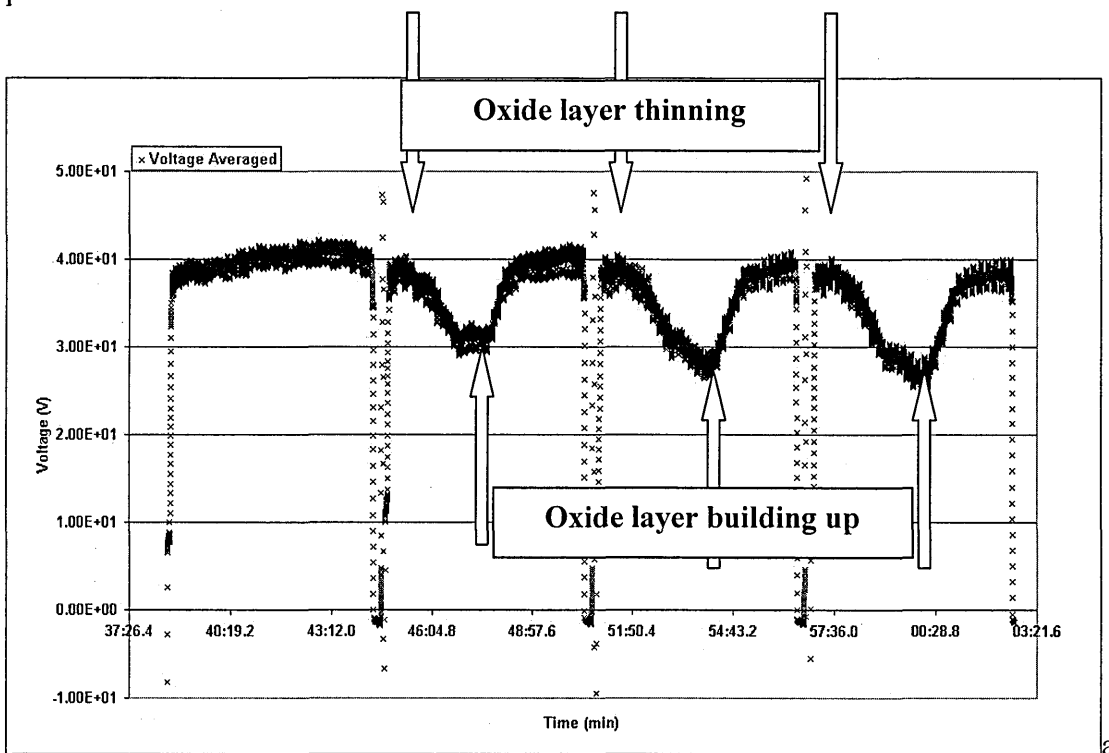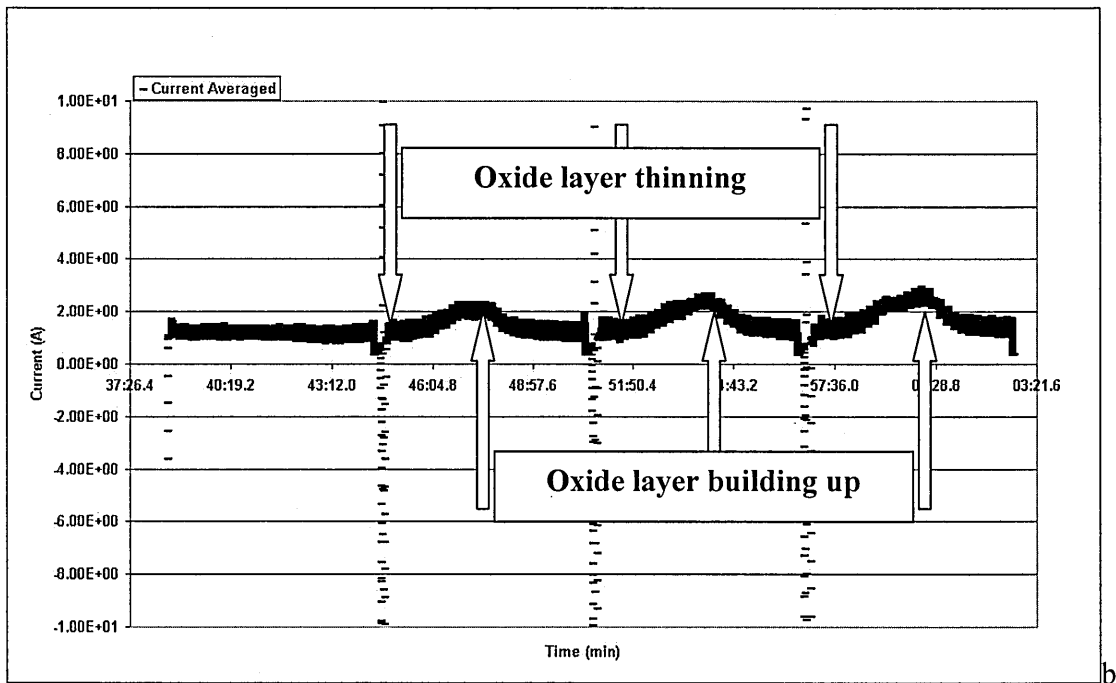
Figure 3.12: Final passes on testpiece A

a. voltage data

b. current data

The effect of the film thickness fluctuations was immediately imprinted onto the testpiece surface. The pattern of the damage is displayed in figure 3.13 as well as pictures of the different areas on the sample which were obtained by optical microscopy. Finally the surface finish was measured using a diamond tip Talysurf stylus.

The appearance of the sample shows the way the damage on the sample was clustered around the corners, the parts of the sample which were in contact with the grinding wheel during the depletion of the oxide layer. Scratches and marks are visible even with a naked eye around those areas although the surface finish achieved was still quite good and around 20 nm Ra. Moving on to the inside of the circular area that is defined by the clustered damage, the surface was damage free and the surface finish value was improved to 5nm Ra. That part of the sample was characterised by:

- Constant contact between the rotating workpiece and the grinding wheel and

- Oxide build up that is observed by the data gathered from the ELID power supply.
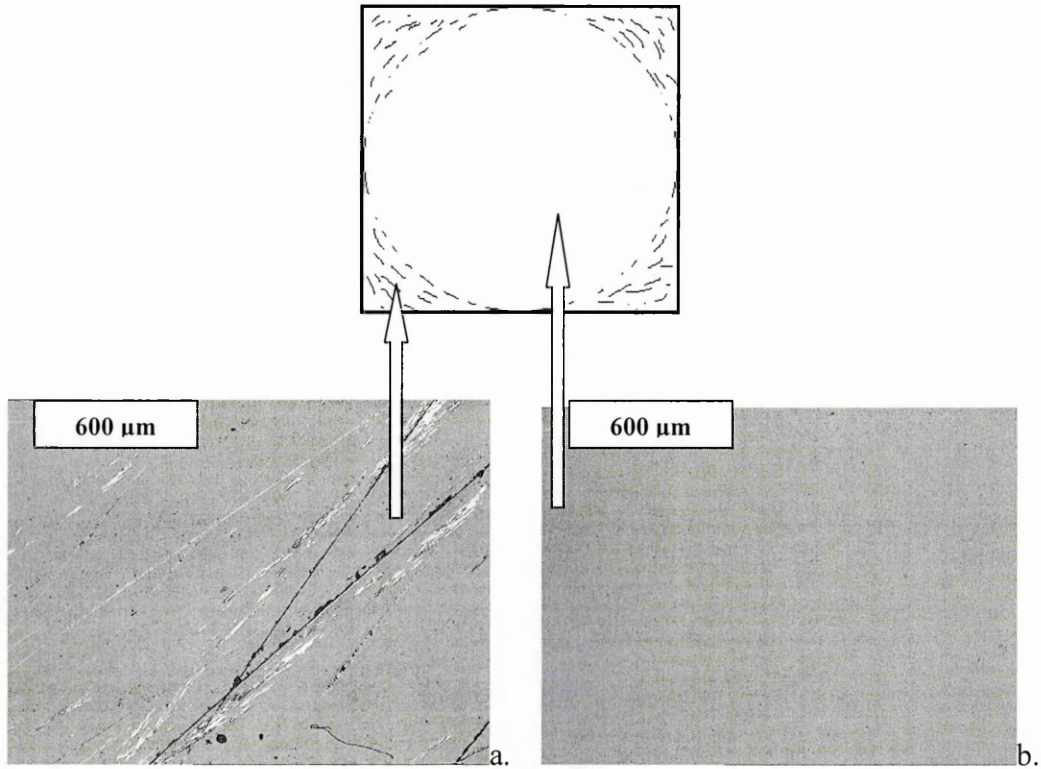
Figure 3.13: Damage patterns on testpiece A
a. Peripheral area b. Central area

II. TESTPIECE B

The same process was followed with testpiece B without the rotary table. This time, before the final passes on the sample the oxide layer covering the wheel was manually removed before grinding using an alumina dressing stick. Current and voltage were recorded before the four final passes and are presented in figure 3.14. As can be seen, an

equilibrium condition of oxide layer thickness is achieved at this point judging by the steady values of current and voltage obtained from the ELID power supply.
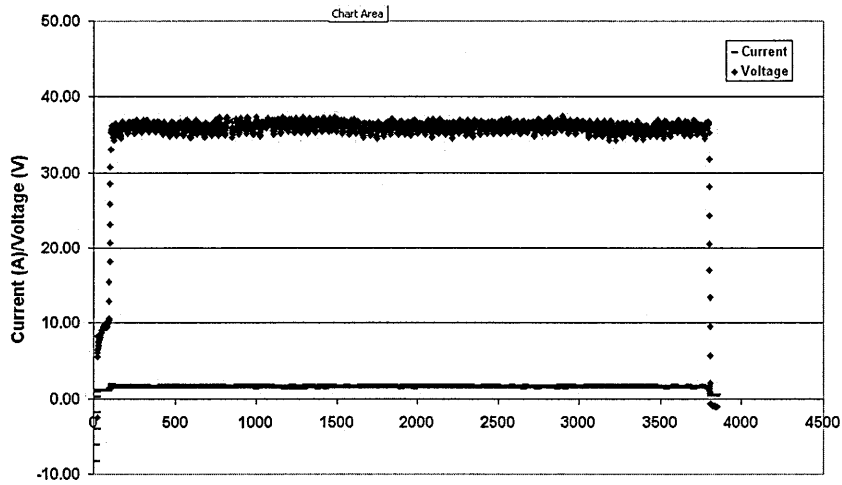
Figure 3.14: Current and voltage vs. time on testpiece B before manual removal of the oxide film

The dressing current and voltage readings over the final four passes are presented in figure 3.15.
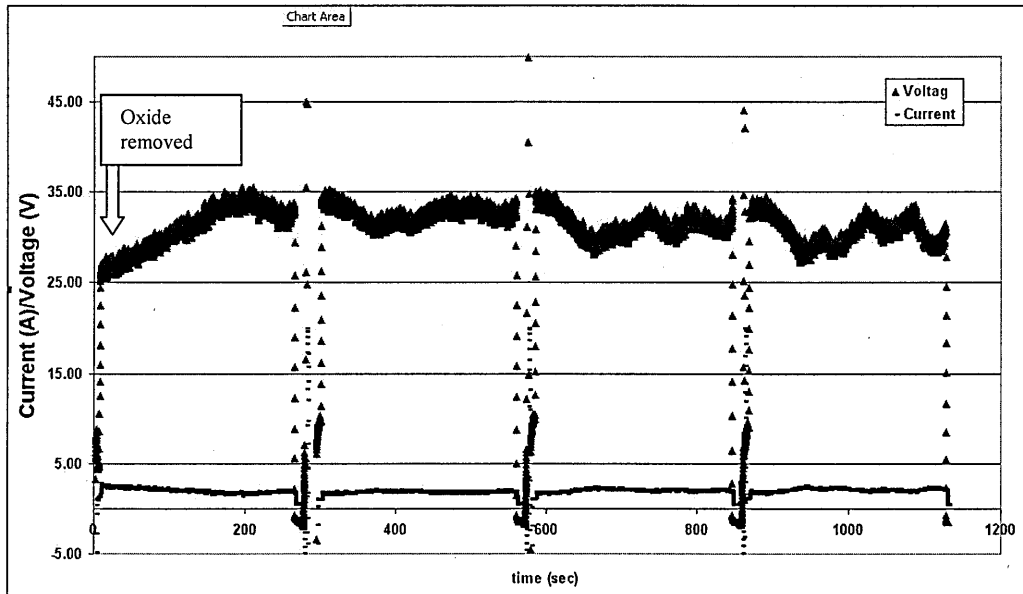
Figure 3.15: Final passes on testpiece B

As expected, with no diamond grits and the oxide layer removed, the surface finish of the sample was very poor with grinding marks in the direction of the wheel feed visible across the surface of the testpiece due to increased metal-to-sample surface contact. Figure 3.16 demonstrates that areas where thinning of the oxide layer is observed have the worst finish.
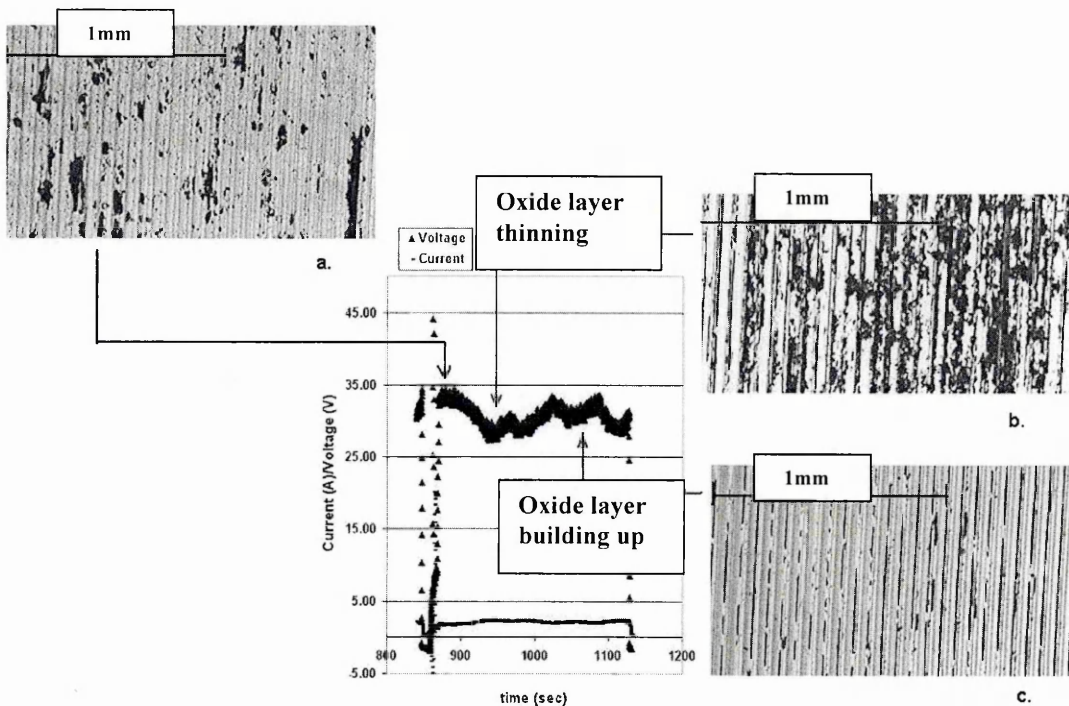
Figure 3.16: Optical micrographs illustrating ground surface finish of BK7 and its correlation to the current and voltage signals recorded

The thinning of the oxide layer during the 4th pass (corresponding to the part where the voltage was dropping right after the initiation of the fourth pass) corresponds to micrograph a. and b. in figure 3.16. As the oxide layer was thinning, the surface became poorer in terms of appearance. This is the part of the sample where the oxide quantity was not adequate to perform the necessary lubricating action, in order to achieve good surface finish. As the pass continued and the oxide built up again (increasing voltage

towards the end of the pass), the surface quality improved although it was still relatively poor (micrograph c.) due to the poor quality of the oxide layer during the last pass and the damage introduced during the previous passes. There appeared to be an excellent correlation between the growth/removal of the oxide and the surface quality achievable. Unfortunately, the equilibrium state displayed in figure 3.14 was not achieved again (continuously fluctuating current and voltage values in figure 3.15 that are also lower than the values observed in figure 3.14) and so, in order to return the wheel back to an optimum condition of oxide film thickness, it had to be re-dressed.

3.B ELECTROCHEMICAL IMPEDANCE SPECTROSCOPY (EIS) EXPERIMENTS

3.B.1 INTRODUCTION – INITIAL EXPERIMENTS

Initial tests were performed on the grinding wheel placed in the electrochemical cell but
the signals obtained were not clear. This was attributed to the effects of oxygen diffusion
taking place, which interacted with the impedance signals of the oxide layer (whenever it
was present) and the metal substrate early in the development of the graph, resulting in
complex Nyquist plots that were difficult to interpret.

Figure 3.17 corresponds to the Nyquist plot obtained for the grinding wheel immersed in
tap water and subjected to a scan over a large range of frequencies (between a high
frequency limit of 2×10^4 Hz and a low frequency limit of 10^{-3} Hz).
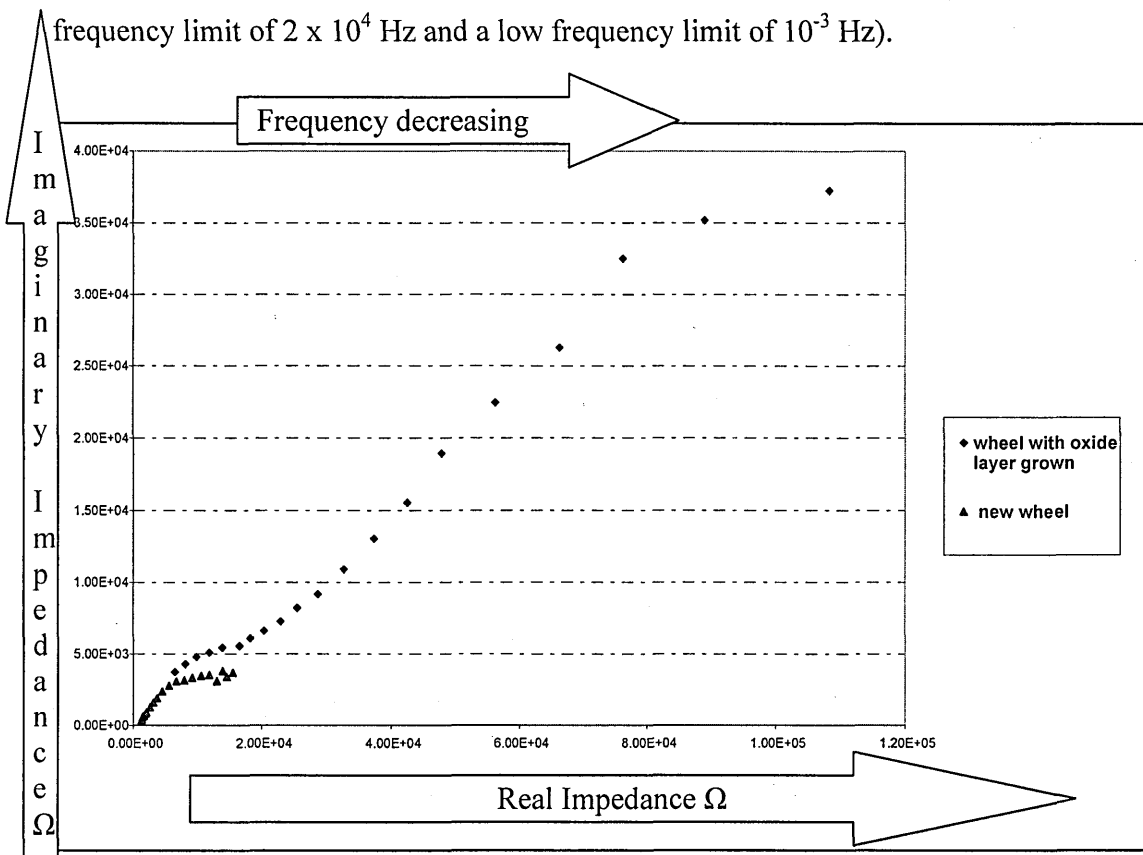
*Figure 3.17: Comparison of the Nyquist plots obtained for a non-predressed wheel and
a wheel with an oxide layer grown on its surface*

Nitrogen was introduced in the solution in order to move the effects of oxygen diffusion to lower frequencies and allow the development of the semicircles with a minimised oxygen effect. The plots compared are the plots obtained for a film-free grinding wheel (not pre-dressed) and a grinding wheel on which the oxide layer was allowed to grow before measurement (pre-dressed). Both wheels were subjected to the same frequency scan.

One of the plots is comprised of a combination of two semicircles whereas the plot of the film-free wheel comprises only one semicircle. In the first case, where the oxide layer film is present, one of the semicircles is attributed to the oxide layer, and the other one is attributed to the impedance response of the metal substrate. In the case where there is no oxide film present, only one semicircle develops, which corresponds to the impedance response of the metal bond (charge transfer resistance).

Using the curve fitting software on the graphs obtained, semicircles were fit to the two graphs (their diameters are the values of resistance), as well as the offset of the curves, which corresponds to the resistance of the solution used during the test (in this case, tap water). Table 6 summarizes the values obtained.

Table 6- Charge transfer resistance and solution resistance values for the Nyquist plots of the wheel segment in tap water

Wheel segment in tap water	Resistance (Ω)
No oxide layer present	$(2.25\pm0.5) \times 10^4$
Fully-grown oxide layer: semicircle 1	$(2.5\pm0.5) \times 10^4$
Fully-grown oxide layer: semicircle 2	$(2.4\pm0.5) \times 10^5$
Solution resistance	$(3.3\pm0.1) \times 10^3$

Comparing the obtained data with what has been reported in the literature, it is found that the observed behaviour has been studied by Walter [56] and Mansfeld et al [57]. The presence of the two semicircles -one corresponding to the metal bond's response and the

other to that of the film on the surface of the metal bond- is representative of the
impedance spectroscopy behaviour of a film-covered metal.

The two semicircles overlap in order to give the overall response of the system, resulting
in a complex equivalent circuit model of a combination of resistances and capacitances.
The interaction between the two semicircles and the amount of overlap depends on the
time constant of each one of them ($\tau_{pf} = R_{pf}C_{pf}$, $\tau_m=R_tC_d$; the criteria that will define
whether the semicircles overlap or are distinct have been studied and presented by Walter
[56]).

The errors included in the values of table 6 are quite large for the resistance calculated
and that is attributed to the fact that the curve fits were not very accurate. The solution
resistance error is lower though as it was much clearer to find the intercept of the curves
with the real impedance.

3.B.2 EXPERIMENTS WITH THE NEW SET-UP

3.B.2.1 WHEEL SEGMENT WITHOUT PRE-DRESSING

The electrolyte used in these experiments was a NaCl solution in distilled water (35g of
NaCl in 1lt of distilled water) with the addition of 10ml of the CEM grinding fluid used
when grinding on the Tetraform. Air was also supplied into the vessel and so, after the
segment was placed in the solution, it took about 30-40 minutes to reach steady state
conditions (solution fully aerated) and when that was achieved, the tests begun. An
oscillating voltage was applied (oscillation of 10mV) at different frequencies. The
frequencies of the scans performed ranged between 10^6 Hz and 10^{-3} Hz and for each
frequency the values of imaginary and real impedance was recorded. From this data,
Nyquist (imaginary impedance vs. real impedance plots) and Bode plots (impedance vs.
frequency plots) were obtained and through the use of the software provided (ZPlot and
ZView) a curve was fitted on the Nyquist plot. The fitted curve allowed the calculation of

the value of charge transfer resistance of the bond material as well as the solution resistance from the low intercept of the circle fit with the real impedance axis. Figure 3.18 presents the fitted curve onto the experimental data (3.18a) and the corresponding simple equivalent circuit that was used to represent the impedance response of the segment tested (a combination of 3 components: the double layer capacitance C_d, the solution resistance R_s and the charge transfer resistance R_t).
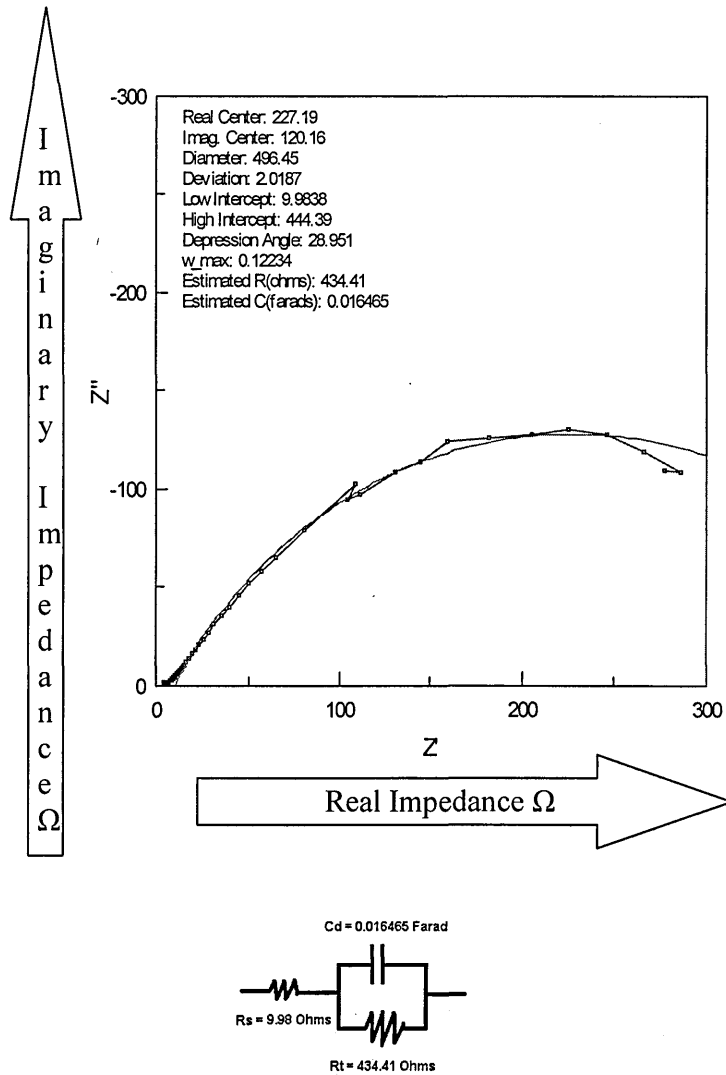
Figure 3.18: Curve fitting with ZPlot and corresponding equivalent circuit for the wheel segment when no oxide layer is present.

The obtained values for charge transfer and solution resistance are summarized in table 7.

Table 7- Charge transfer resistance and solution resistance values for the Nyquist plot of the wheel segment in NaCl solution: No oxide layer grown

Wheel segment in NaCl Solution	Resistance (Ω)
Charge transfer resistance: No oxide layer present	434.41
Solution resistance	9.98

3.B.2.2 WHEEL SEGMENT AFTER PRE-DRESSING

The same procedure was followed for a segment of the wheel that was pre-dressed on the Tetraform and then tested on the EIS cell.

Real Center: 5803
Imag. Center: 2790.4
Diameter: 12860
Deviation: 15.117
Low Intercept: 10.233
High Intercept: 11596
Depression Angle: 25.72
Estimated R(ohms): 11586
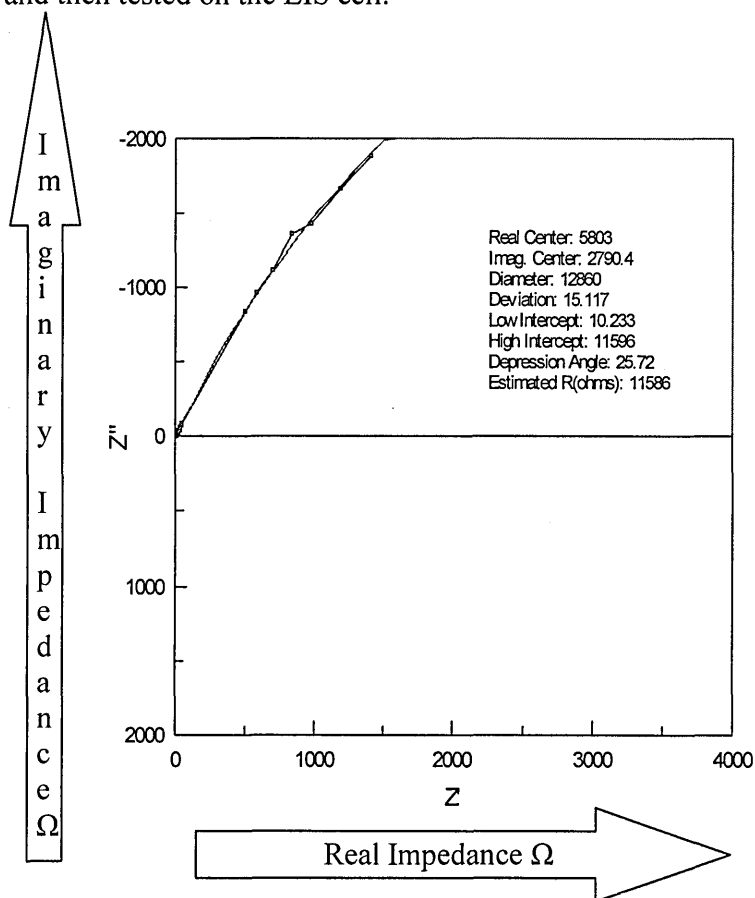
Figure 3.19: Curve fitting for the wheel segment after oxide layer growth.

109

The resulting impedance data spectrum and the curve fit is shown in figure 3.19. As
expected, the charge transfer resistance estimated in this case was much higher (11586
Ohms) as a non-conductive layer of oxide is present and deters iron ions from going into
solution.

The aggressive environment used during these experiments (sodium chloride solution)
was a factor that had to be taken into consideration when testing these samples. Exposure
of the segments in this solution for prolonged periods of time eventually lead to a
breakdown of the protective oxide layer and so, a drop in the charge transfer resistance
value measured was observed.
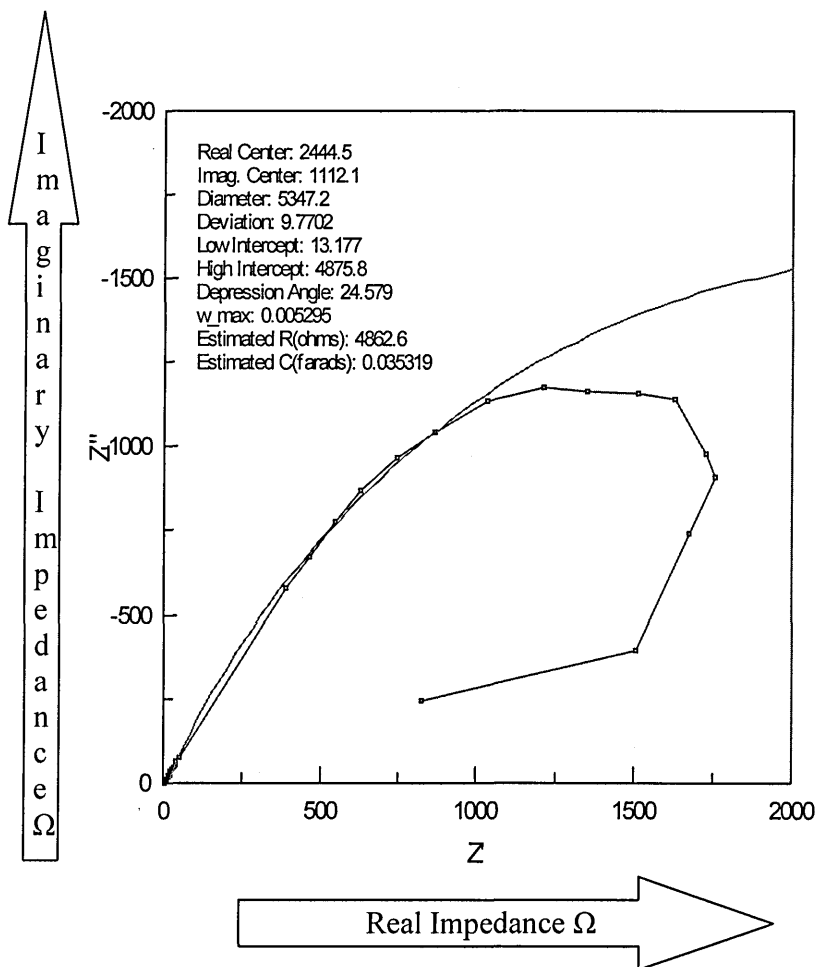
Figure 3.20: Reduction in charge transfer resistance observed on wheel segment on
which a frequency scan is repeated.

The time required for each frequency scan is approximately four hours. Even in that period of time, the protective layer is affected. A repeat measurement was performed immediately after the first one and the impedance spectrum acquired is shown in figure 3.20.

The initial part of the plot displays a large value of resistance (which is still lower than the initial one measured when the segment is placed in the NaCl solution for the first time). Through the loop, at the end of the measurement, impedance values drop down close to values observed for a bare surface with no protective film on it. If the frequency scan was repeated once more, its shape and charge transfer resistance calculated would be very similar to those displayed in figure 3.18. The obtained values are summarized in table 8.

Table 8- Charge transfer resistance and solution resistance values for the Nyquist plots of the wheel segment in NaCl solution: Fully grown oxide layer

Wheel segment in NaCl Solution	Resistance (Ω)
Charge transfer resistance: Fully grown oxide layer	11,586
Solution resistance: Fully grown oxide layer	10.23
Charge transfer resistance-2nd test: Protective film breaking down	4,862.6
Solution resistance: Protective film breaking down	13.18

As can be seen, the solution resistance in the case of the NaCl solution ranged between 10 and 13 Ohms. This highlights the difference when the solution used in the experiments was tap water. The solution resistance in that case was 3,300 Ohms as expected for a medium with lower conductivity and also characterised a less aggressive corrosive environment which explains the much higher values of charge transfer resistance observed in those measurements (table 6).

3.B.2.3 INTERMEDIATE CONDITIONS

Intermediate conditions of the segment refer to states of the wheel that do not correspond to a fully grown oxide film or a bare surface with no oxide grown on the bond material. In such cases, the charge transfer resistance is expected to have a value somewhere in between the value of the fully grown oxide and the bare surface.

As an example of that, figure 3.21 presents the spectrum acquired from a segment that was tested after an oxide film had naturally grown on it a few days after truing it. An oxide layer could be seen on the surface of the segment with a naked eye but it was not as thick as the one produced with ELID pre-dressing. The charge transfer resistance of 1264.2 Ohms that was obtained through curve fitting verified that observation.
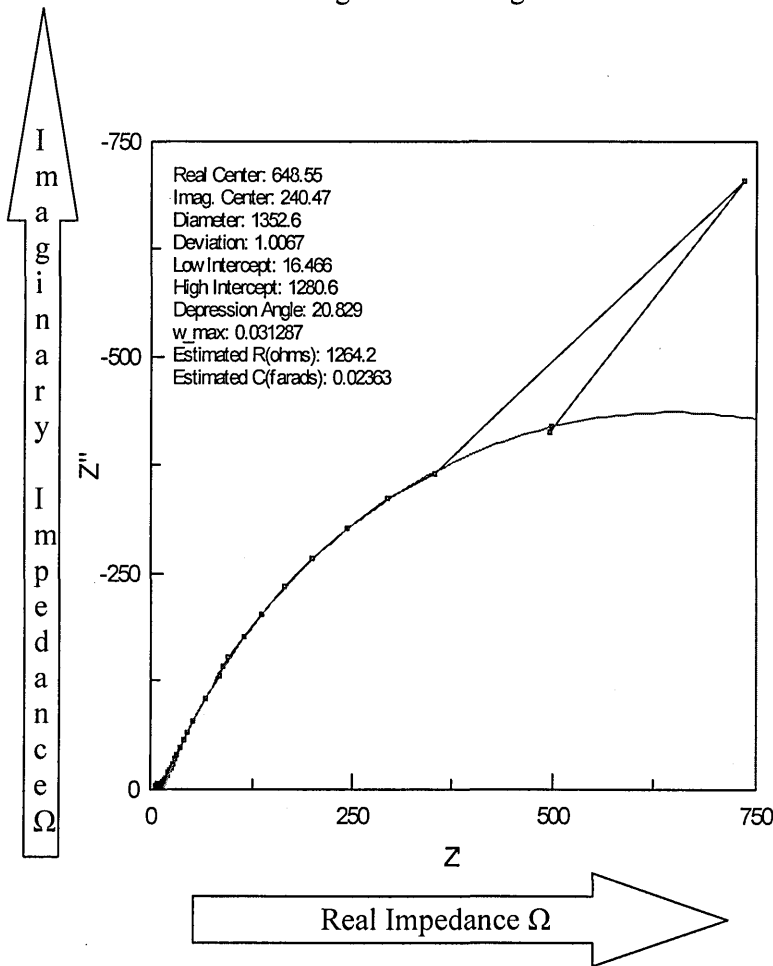
Figure 3.21: Curve fitting on the impedance spectrum obtained for a segment left in atmospheric conditions.

112

The isolated low frequency point is attributed to noise and is not regarded as having physical significance.

3.B.2.4 POST-GRINDING SEGMENT TESTING

The following set of EIS experiments was performed on the segments of the custom made segmented wheel after it was used for grinding and thus, the expected electrochemical characteristics of the oxide layer were changed.

One of the most important benefits that ELID has to offer when compared to conventional grinding methods is the ability of continuously dressing the wheel, while the grinding process is taking place. In this way, cutting efficiency is maintained even when the wheel has been in use for a long time. The wheel was used in a series of tests which was aimed at the evaluation of the stability of ELID grinding over prolonged periods of time.

Samples were ground over different periods of time, by repeating multiple passes on their surface (more details on this set of experiments along with acoustic emission results are presented in section 3.E). The removable segments were subsequently studied with EIS measurements in order to evaluate resistance values and corrosion rates. The samples used were 50mm in diameter and were ground at a constant feed rate of 3mm/min and a depth of cut of 2μm. This meant that each pass made on each sample lasted for about 17 minutes.

EIS measurements were performed on the segments after having performed ten passes (167 minutes total grinding time) and twenty passes (334 minutes total grinding time) with the wheel and the curve fitting results shown in the table 9.

Table 9- Charge transfer resistance values for post-grinding segments of the wheel

	Segment after 167 minutes of grinding	Segment after 334 minutes of grinding
Resistance (Ohms)	776 1027	2,860

In the case of the 10-pass segment the oxide layer is not being properly regenerated during grinding, and that is reflected on the lower charge transfer resistance values obtained. Loss of conductivity was observed once the grinding wheel reached the speed of 6000 rpm. This meant that ELID was only partially functioning and beneficial during grinding, as there was no current passing through the wheel to further stimulate the re-growth of the oxide layer on its surface. The test was repeated and the value obtained was again lower than that achieved for a properly generated oxide film.

In the case of the twenty pass segment, current was flowing freely through the grinding wheel and so a stable condition was achieved that led to the formation of a thicker oxide which translated into a higher charge transfer resistance observed.

Similar experiments to the ones described above were performed on the no-grit diamond wheel that was used in several grinding trials. The segment used in this test was a segment removed from the grinding wheel after it was used for grinding with most of the oxide layer grown on it manually removed with an alumina stick (detailed description of these tests was presented in paragraph 3.A.4).

These experiments gave an idea of the effect of the presence or absence of diamonds when measuring charge transfer resistance on the grinding wheel segments. The value of resistance that was calculated with the curve fit in this case was similar to that previously measured on the diamond grit wheel, in the case where a thin oxide was observed on the grinding wheel (table 9). The curve fit is presented in figure 3.22 and the comparison of charge transfer resistance values for a diamond and a non-diamond wheel is presented in table 10.

The presence or not of diamonds does not seem to be important in the resistance characteristics of the wheel, mainly due to their low concentration and the relatively low electrical conductivity of diamond compared to that of iron.

Table 10- Comparison of charge transfer resistance values for diamond grit and non-diamond grit wheel segments

Wheel segment	Charge transfer resistance
Diamond grit, thin oxide layer	776 Ω / 1027 Ω
No diamond grit, thin oxide layer	719 Ω
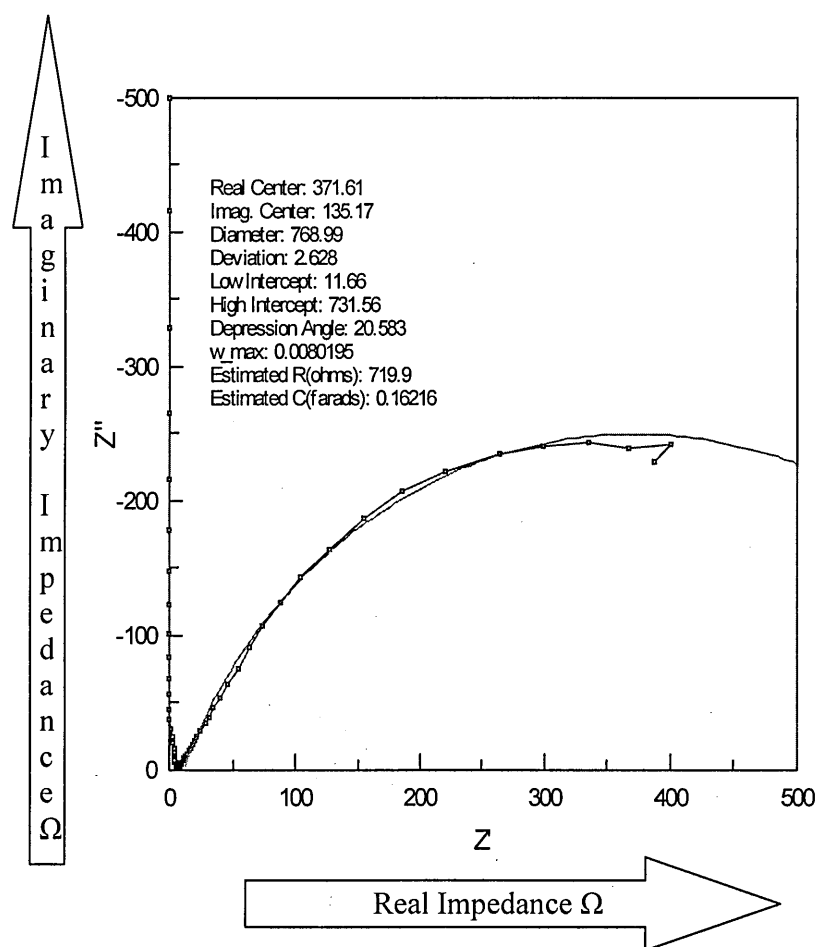
Figure 3.22: Curve fit and estimated charge transfer resistance on the no-grit wheel

3.C SUB-SURFACE DAMAGE CHARACTERISATION

Most of the experiments were performed on the Edgetek SAM machine, with peripheral grinding wheels and the spherical wheel on flat samples. Although flat samples are efficiently ground with cup wheels and the time consumed is smaller than when ground on a peripheral wheel, peripheral wheels were utilised as they are more versatile when grinding more complex geometries (parabolic, spherical and aspheric surfaces). This set of tests gave an indication of the time limitations when non-flat samples are processed. The limits of efficient damage-free grinding were also studied by maximising material removal rates.

3.C.1 SUB-SURFACE DAMAGE CHARACTERISATION:SECTIONING

The "as received" sample (figure 3.23 a), displays around 20 microns of damage before any kind of grinding takes place. This shows that if a damage-free sample is to be produced, that amount of material should be removed so that any pre-existing damage in the testpiece is removed.

70μm   70μm

a.   b.
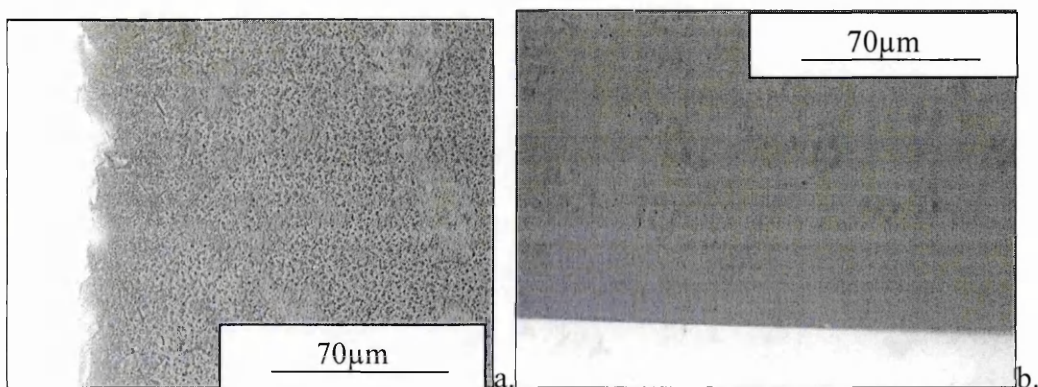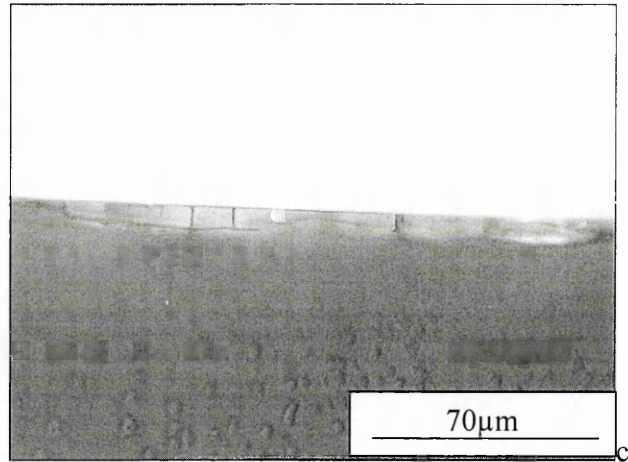
Figure 3.23: a. Sectioned as received sample
b. Sectioned ELID ground sample (5µm d.o.c., 20mm/min feed rate)
c. Sectioned resin bond wheel ground sample (5µm d.o.c., 80mm/min feed rate)

Figures 3.23 b and 3.23 c show different amounts of damage were present after varying processing methods and parameters. The sample in figure 3.23 b displays very little damage after ELID grinding (5µm d.o.c., 20mm/min feed rate) whereas extended networks of cracks and defects are present under the surface in the case of the testpiece shown in figure 3.23 c (resin bond wheel grinding 5µm d.o.c., 80mm/min feed rate).

3.C.2 SUB-SURFACE DAMAGE CHARACTERISATION: "POLISHING BACK" METHOD

BK7 glass testpieces were studied in order to evaluate the amount of sub-surface damage in each one of them after being machined using different grinding parameters. The results are presented in the following section.

117

I. As-received condition

This testpiece was polished back and evaluated for sub-surface damage directly as
received from the manufacturer (Berliner Glas).
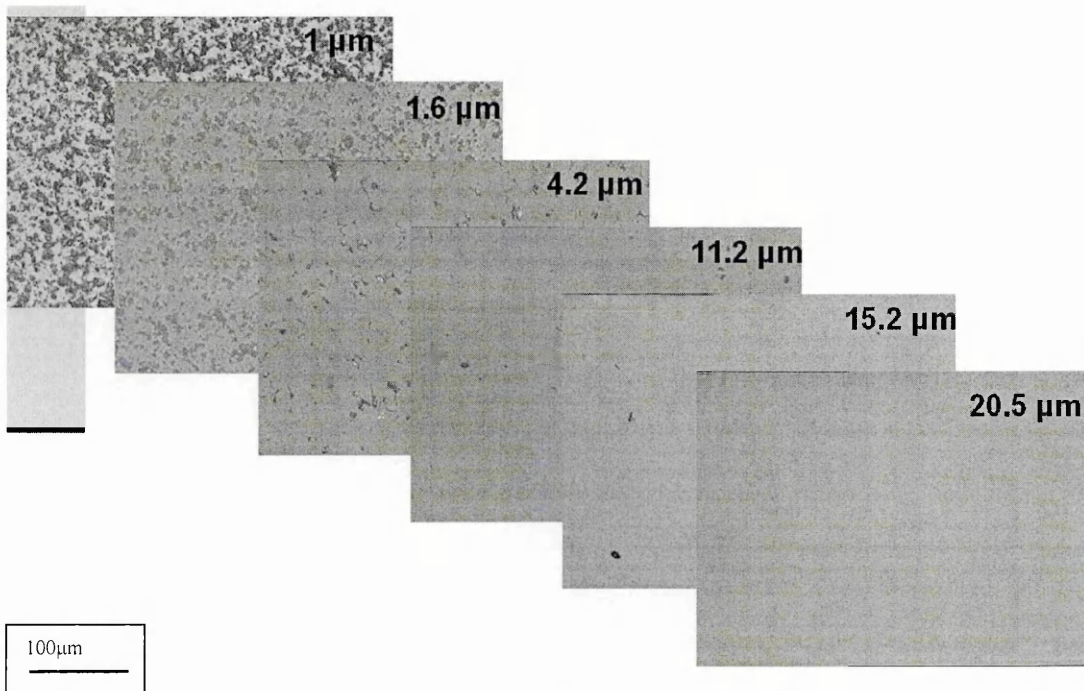
Figure 3.24: Depth of damage for as-received testpiece

The micrographs in figure 3.24 show the surface of the sample as more and more material
was progressively removed.

Moving further down from the surface, the amount of damage present diminished until no
more damage was present at a depth of approximately h=20 μm. This means that if
defect-free components were to be achieved from the as received state, at least 20 μm of
material would have to be removed from the surface so as to make sure that all pre-
existing damage on the component was removed.

II. Ground condition: 151 μm grit wheel

A coarse-grit grinding wheel was used on this testpiece, in order to achieve high removal rates, in preparation for further, more precise grinding with grinding wheels with smaller grit sizes. In this specific case, the diamond grits were of an average size of 151 μm. The surface of the workpiece was divided into 4 areas, and 4 steps were introduced (5 μm, 10 μm, 15 μm and 20 μm). The steps were finally removed by one final flattening pass using a 46 μm wheel. Once flat, the polishing back process was used in order to observe differences in the depth into which damage extends under the surface.

The following pictures (figures 3.25 to 3.28) display the gradual decrease of damage as we move further inside the workpiece and table 11 gives a summary of the depth that was reached in order to observe no damage at all.

Table 11- Depths of damage for different depths of cut with the 151 μm wheel

151 μm wheel. Feed rate: 50mm/min				
Depth of cut	5 μm	10 μm	15 μm	20 μm
Depth of damage (μm)	**31.3**	**24.7**	**25.7**	**25.5**
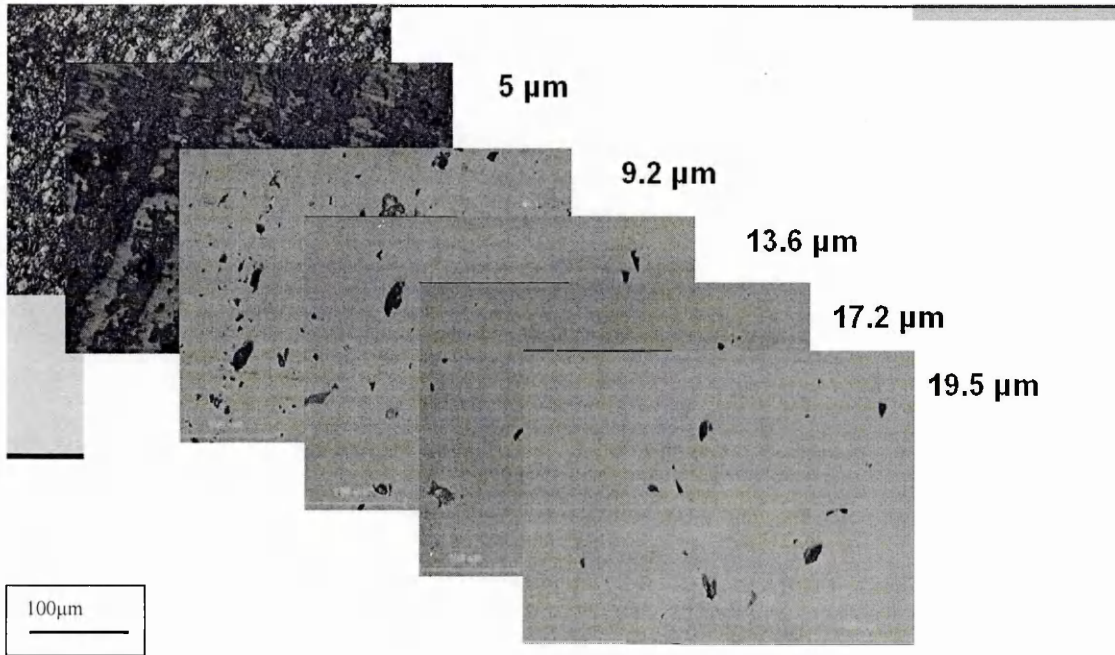
*Figure 3.25: Depth of damage for testpiece ground with the 151 μm wheel,
depth of cut: 5 μm*
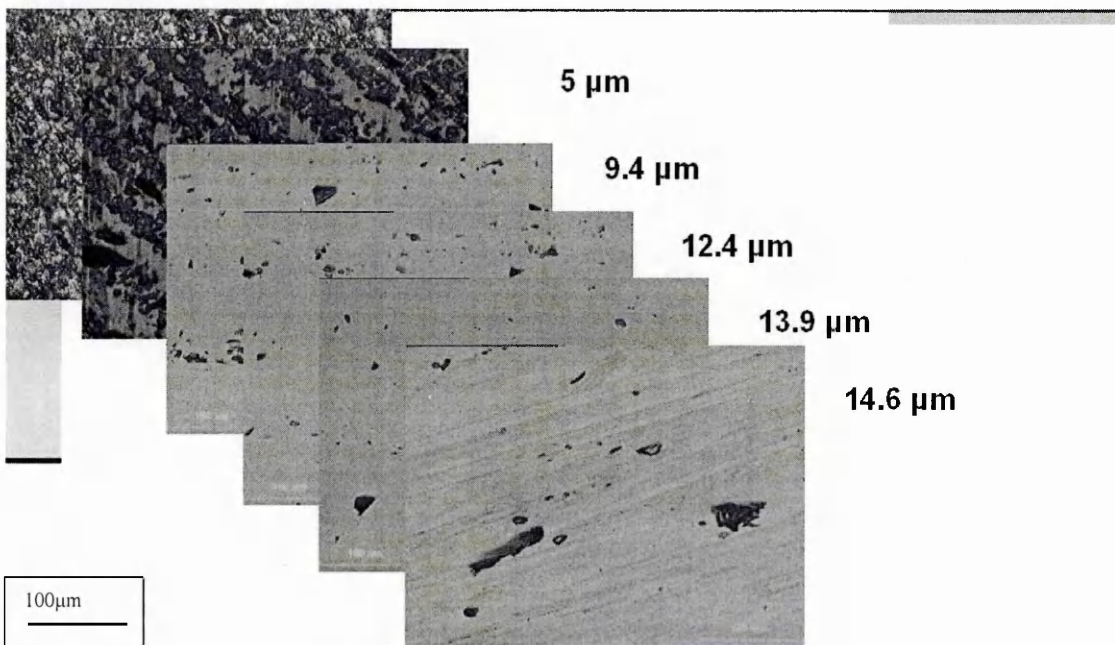
*Figure 3.26: Depth of damage for testpiece ground with the 151 μm wheel,
depth of cut: 10 μm*
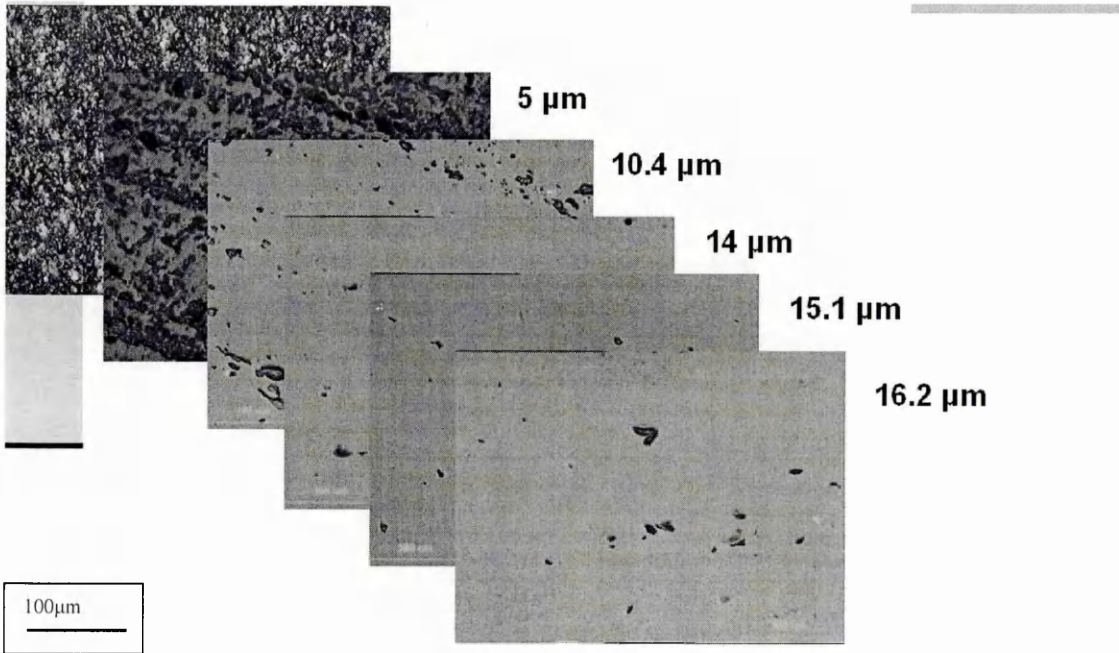
Figure 3.27: Depth of damage for testpiece ground with the 151 μm wheel,
depth of cut: 15 μm
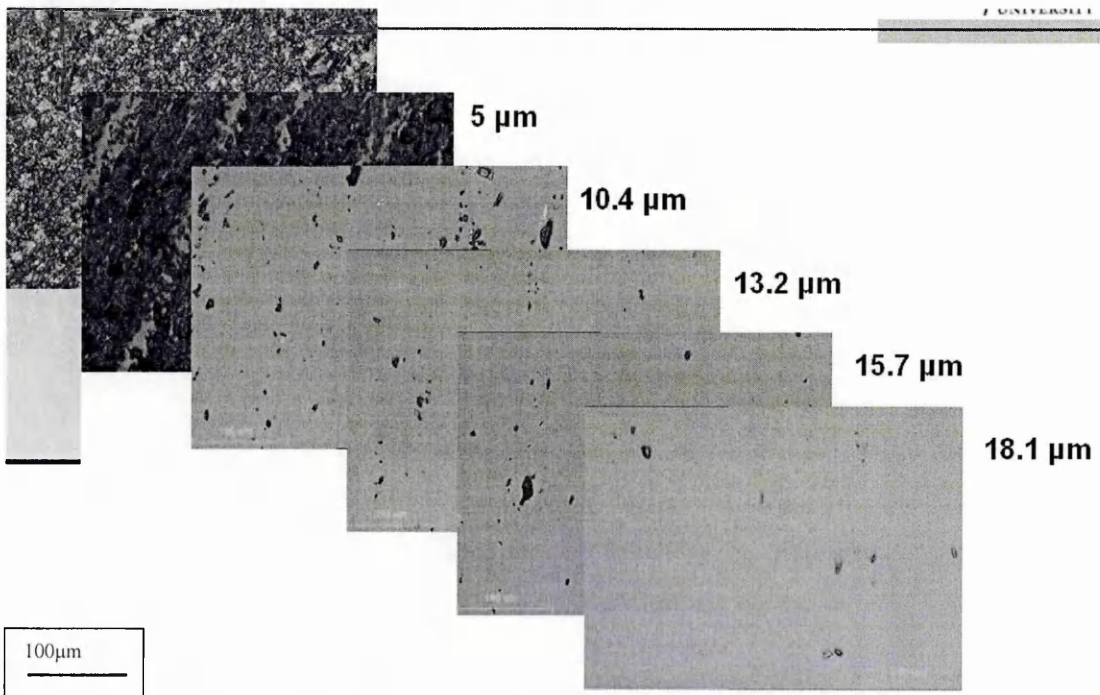
Figure 3.28: Depth of damage for testpiece ground with the 151 μm wheel,
depth of cut: 20 μm

121

III. Ground condition: 46 μm grit wheel

A different coarse-grit wheel was used on this sample, with a diamond-grit size of 46 μm. Using the same procedure, polishing back steps on the sample revealed the depth into which damage extended. Table 12 gives a summary of those steps and the final depth that was reached in order to obtain a damage-free surface which was 33 μm.

Table 12- Depth of damage for the 46 μm wheel

46 μm grit wheel. Feed rate: 50mm/min
Total Depth (μm)
33

IV. Ground condition: 2 μm grit wheel from as-received

The same procedure was followed after using a 2 μm grit metal bond spherical wheel (wheel diameter: 175 mm), using ELID. The testpiece was divided into 4 areas, in which 4 different feed rates were used: 50 mm/min, 210 mm/min, 470 mm/min and 830 mm/min. The depth of cut in all four areas was the same, set at 1μm. The testpiece was initially cleaned up and flattened with respect to the grinding wheel (from the as-received by the manufacturer state) by taking 2 cuts of one μm each across its surface. Table 13 summarizes the depths into which damage extended in each area of the testpiece.

Table 13- Depths of damage for the 2 μm wheel from as received

Depths of damage, 2 μm grit wheel	
Feed rate: 50 mm/min	22.5 μm
Feed rate: 210 mm/min	20.6 μm
Feed rate: 470 mm/min	21 μm
Feed rate: 830 mm/min	17 μm

V. Ground condition: 2 µm grit wheel from polished

The same wheel and grinding parameters (ELID grinding, depth of cut: 1µm, feed rates: 50 mm/min, 210 mm/min, 470 mm/min and 830 mm/min) were used on a testpiece that was previously polished, in which case there was certainty that all the sub-surface damage present after the grinding process was due to the process itself rather than pre-existing damage in the testpiece (e.g. damage present in the as-received testpiece described previously). A further feed rate of 1200mm/min was also studied. Table 14 summarizes the resulting depths of damage

Table 14- Depths of damage for the 2 µm wheel from polished

Depths of damage, 2 µm grit wheel	
Feed rate: 50 mm/min	5.9 µm
Feed rate: 210 mm/min	11.2 µm
Feed rate: 470 mm/min	15.7 µm
Feed rate: 830 mm/min	16.8 µm
Feed rate:1200mm/min	15 µm

VI. Resin Bond wheel Grinding: Rotating testpiece

Sub-surface damage data was also gathered from testpieces ground on a rotary table, with a 7 µm grit resin bond wheel. As with the previous testpieces, polishing steps were performed in order to assess the amount of damage introduced. Figure 3.29 shows the damage introduced, at different distances from the centre of the rotating testpiece. Moving towards the centre of the testpiece (and consequently towards lower maximum chip thicknesses) the amount of material that needs to be removed in order to achieve a damage free surface decreases until a point is reached approximately 9mm from the centre of the testpiece, where there is no sub-surface damage present. That point defines the point of transition from brittle to ductile material removal regime. The R_a values of surface finish in the two areas also varied as a value of 2.9 nm was measured near the centre of the testpiece whereas further away from the transition point the R_a value was measured to be 30.8nm.
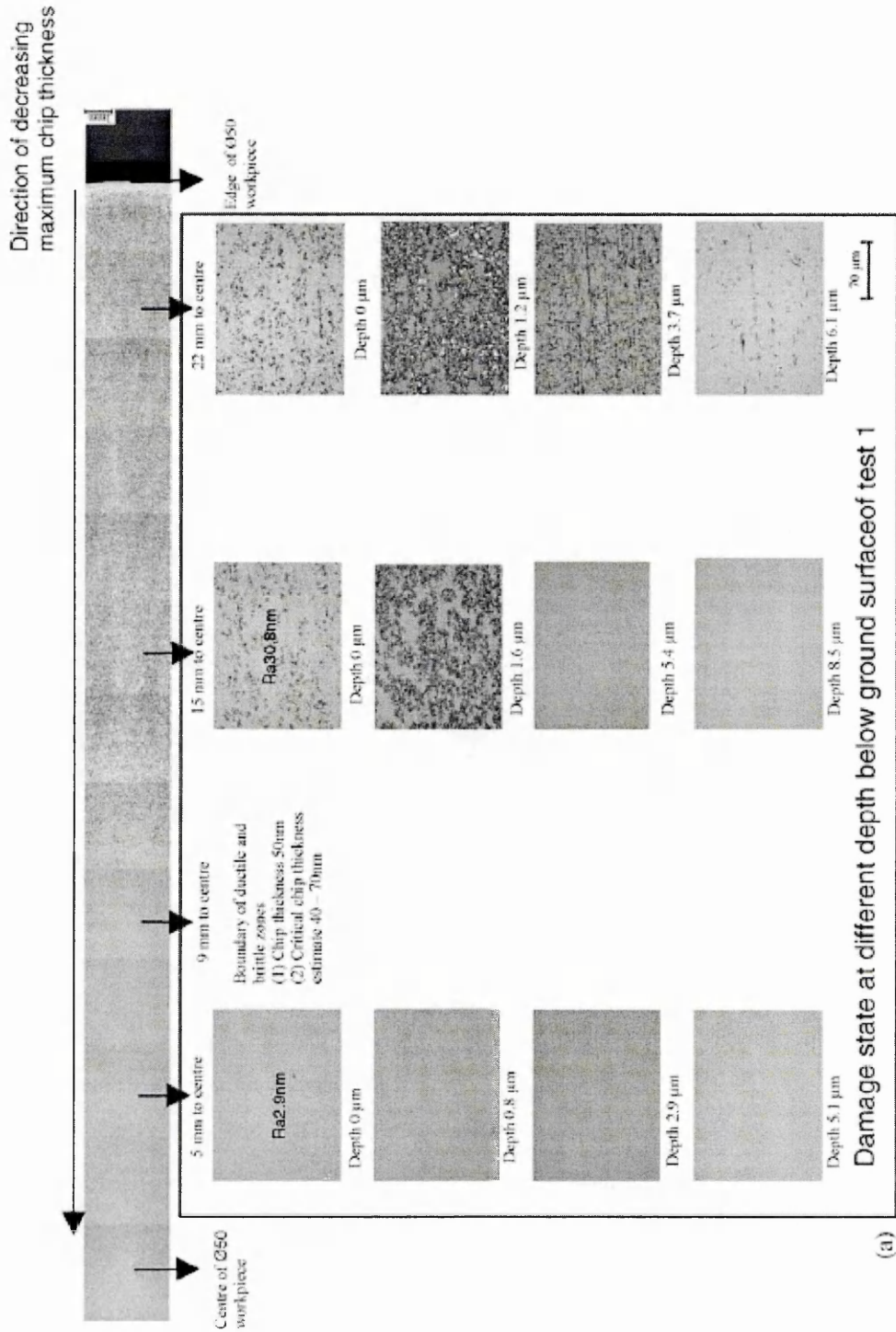
Figure 3.29: Depth of damage at different distances from the centre of the rotating testpiece, ground with a resin bond wheel

3.E ELID GRINDING AND RESIN BOND WHEEL GRINDING STABILITY – ACOUSTIC EMISSION SIGNAL ACQUISITION

3.E.1 ELID GRINDING AND RESIN BOND WHEEL GRINDING STABILITY

I. Single-pass ground testpieces

The first sample was initially cleaned up until its surface was completely flat and parallel to the grinding wheel. In the case of ELID the wheel was then pre-dressed once more, so that the oxide layer was again fully grown on the surface of the grinding wheel and then, it was ground once more. In the case of resin bond wheel grinding, the resin bond wheel was re-trued after the clean up stage. This ensured that the state of the wheel would be that of a wheel that is used on a sample for the first time.

The testpieces were then removed from the fixture and Talysurf traces were taken on the five different regions of their surfaces, as defined in section 2.F.2. The following table shows the values obtained for each sample.

Table 15- Surface finish values of single-pass ground samples for ELID and resin bond wheel grinding

Grinding Time: 17 minutes	R_a value (nm)	
	ELID	Resin Bond
Region I	62	119
Region II	11	14
Region III	12	11 (58, 81)
Region IV	12	15
Region V	15	10

Region III was the most damage-prone area of the specimens as that was the area where there was maximum contact between the wheel and the sample. It was at that part of the grinding cycle that cracks and defects were likely to be induced on the surface of the sample as a large part of the workpiece was in contact with the wheel and thus, it faced the toughest and most demanding conditions in terms of damage–free grinding capacity. Increased wheel/sample contact area gave rise to difficulties in getting fluid into the grinding zone which could potentially lead to higher grinding forces

In the case of the resin bond wheel, at the centre of region III the surface finish achieved was comparable to that achieved with the ELID wheel but at the edges of that region severe grinding marks were observed that brought down the quality of the surface finish to the R_a values displayed in parenthesis in table 15.

Region I is also affected as that was the part where initial contact between the wheel and the sample took place and until stable conditions and contact were established, damage was introduced there. This is obvious in the case of the single pass specimens

Single-pass ground samples
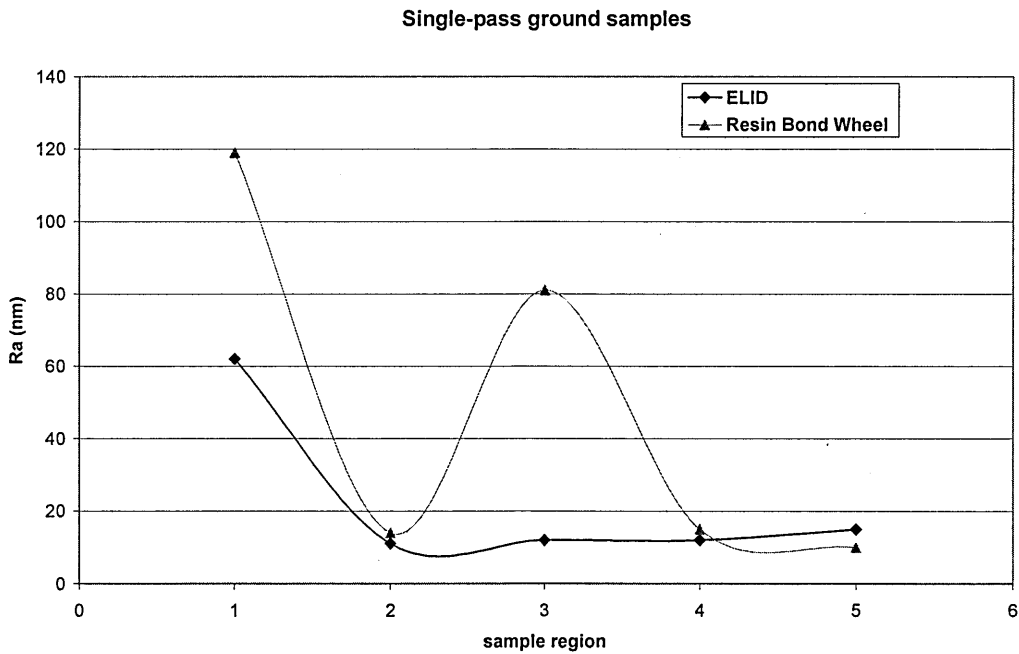
Figure 3.30: Surface finish values on the different specimen regions after one pass

Figure 3.30 shows a graphic representation of the way surface finish varied across the different areas of the samples. After the first region the ELID ground sample seemed to reach a stable state where surface finish did not vary much along its length. The resin bond wheel though displayed an intense fluctuation in region III due to the grinding marks present there. Although parts of the area are characterised by high quality surface finish (around 11 µm in parts of area III), the final quality of the surface is judged based on the overall appearance of the testpiece which is marked by the presence of big scratches.

II. Ten-pass ground samples

The second set of samples was prepared in the same way as the previous ones only this time each sample was ground ten times, with the same depth of cut and feed rate as before. The total grinding time for the resin bond wheel was approximately 167 minutes whereas for the ELID wheel it was slightly higher as it was used without re-dressing it after the clean up stage of the sample. Table 16 gives the Talysurf values obtained along the centre line of the specimens.

Table 16- Surface finish values of ten-pass ground samples for ELID and resin bond wheel grinding

Grinding Time: 167 minutes	R_a value (nm)	
	ELID	Resin Bond Wheel
Region I	65	6
Region II	9	27
Region III	8	12
Region IV	9	17
Region V	19	20

In the first region the surface finish quality was low due to an accident during the clean-up stage of the sample but the rest of the ELID ground testpiece seemed to have a better overall surface finish than the resin bond ground one (see figure 3.31).

10 pass ground samples
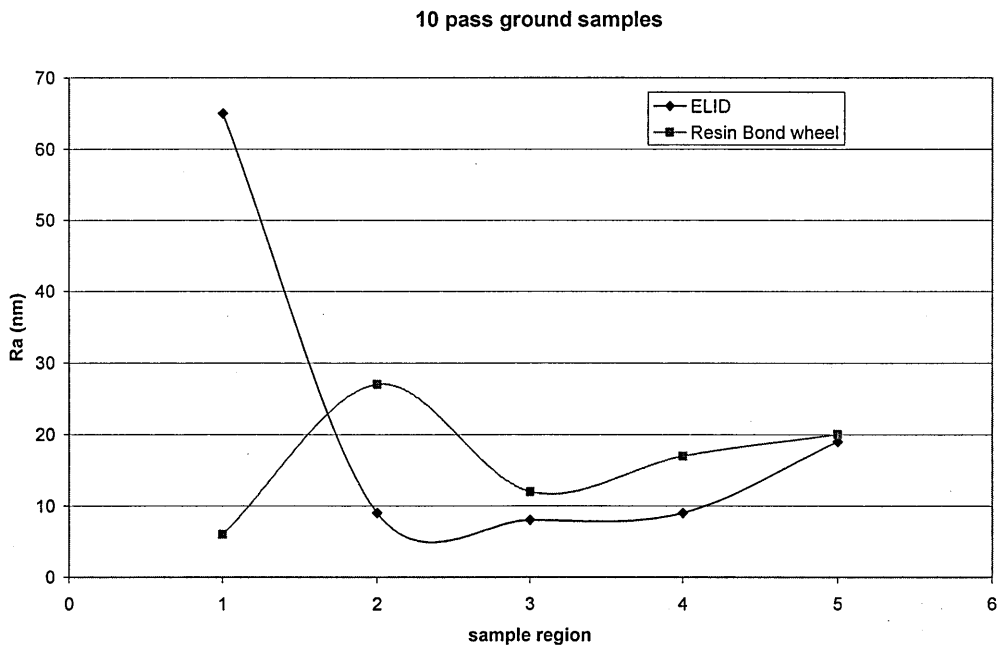
Figure 3.31: Surface finish values on the different specimen regions after ten passes

No rubbing marks were found on the surface ground by the ELID metal bond wheel. On the contrary, severe rubbing damage was observed on the surface generated by the resin-bond wheel,. The comparison of the two surfaces generated by the two different grinding methods is presented in figure 3.32.
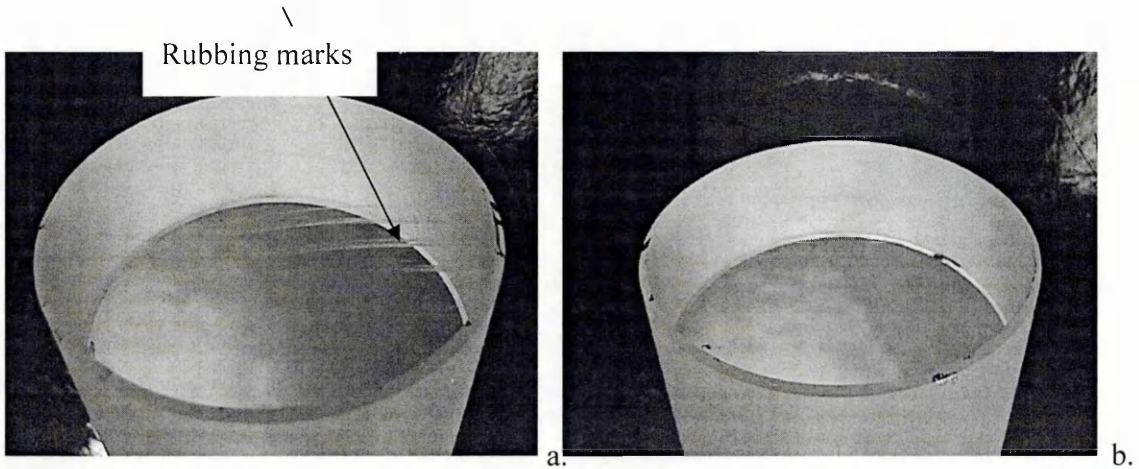
*Figure 3.32: Ground surfaces generated by (a) resin bond wheel (no-ELID) and (b)
CIB wheel (ELID)*

III. Twenty-pass ground samples

The third set of samples was ground for twenty passes and a total grinding time of 334
minutes. The results are shown in table 17 below.

*Table 17- Surface finish values of twenty-pass ground samples for ELID and resin
bond wheel grinding*

Grinding Time: 334 minutes	R_a value (nm)	
	ELID	Resin Bond Wheel
Region I	13	34

Region II	6	20
Region III	6	130
Region IV	12 (84)	9
Region V	6	17

The ELID ground sample showed a stable and good quality surface finish except for region IV where a scratch brought the value up to about 84 nm. This was due to a control problem of the Tetraform towards the end of the trials and caused the surface to lose its overall good appearance. Measuring the surface finish on the same region but away from the scratch giave a much better value and was more representative.

The resin bond wheel ground sample was characterised by an unstable surface finish that alternated between low values and high values of R_a along the different regions. As expected, such long times of grinding without having the grinding wheel redressed lead to loss of cutting efficiency, wheel loading and wheel wear that gravely affected the appearance of the ground specimen.

20 pass sample
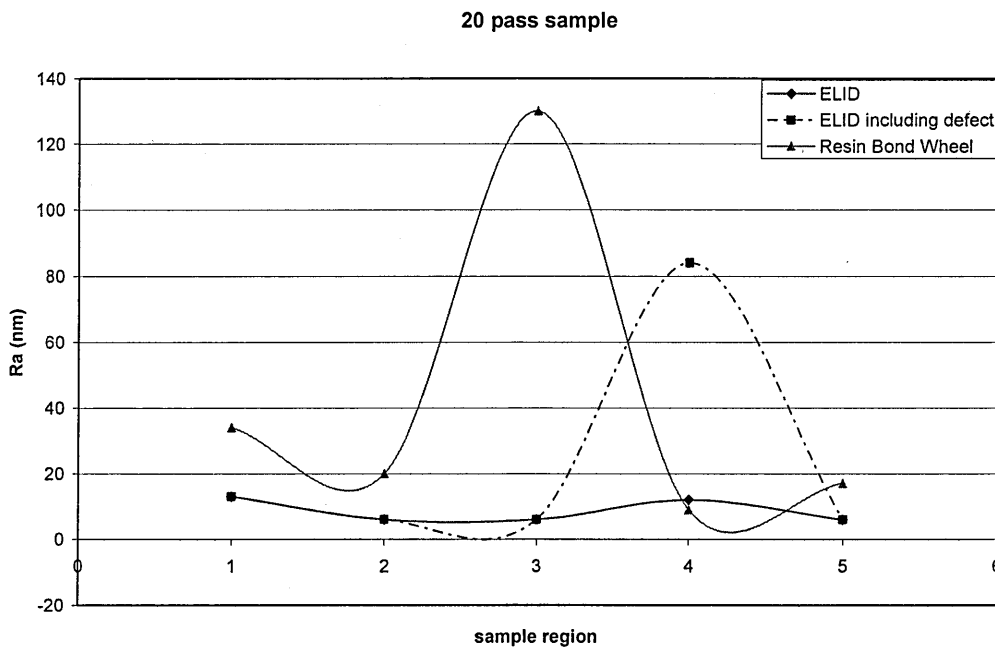
Figure 3.33: Surface finish values on the different specimen regions after twenty passes

Figure 3.33 gives a graph of the way surface finish varied along the samples and, in the case of ELID, two graphs were included: one that included the defect on the surface finish measurement (dotted line) and one that did not (more representative). This proves once more the importance of an overall high quality finish on the workpiece produced as a single defect compromises the whole component and leads to the necessity of further grinding and polishing cycles in order to remove damage.

IV. Comparison of wheel conditions

The appearance of the grinding wheels was compared post-grinding, in order to evaluate their differences which are apparent on the surfaces of the ground samples.

In the case of the samples that were ground for ten passes, dark colour strips can be observed on the resin bond wheel surface with a naked eye, especially in the areas of increased contact between the wheel and the workpiece. This is an indication that the resin bond wheel has lost its cutting efficiency, in direct contrast to the ELID wheel is constantly dressed while grinding. Together with the lubricating action of the oxide layer, the cutting action of the diamond grits remains efficient and results in a surface with high quality surface finish, without any marks, even in the areas of increased wheel/workpiece contact. Figure 3.34 shows SEM micrographs of the resin bond wheel, after having been used for the grinding of the sample. The micrographs were taken in two different areas, one away from and one near the leading edge of the wheel, which faced the most aggressive conditions while grinding. From the comparison of the two pictures, it is readily apparent that the wheel has been damaged during the process with extended cracking in the matrix material and possible signs of loading, especially in the area near the leading edge which primarily takes part in the cutting process. The loaded wheel loses its cutting efficiency and as a result the surface quality of the ground testpieces is compromised due to the appearance of rubbing marks due to extended rubbing/ploughing action, especially in areas of the testpiece with increased wheel/testpiece contact (scratches and marks shown in figure 3.32)
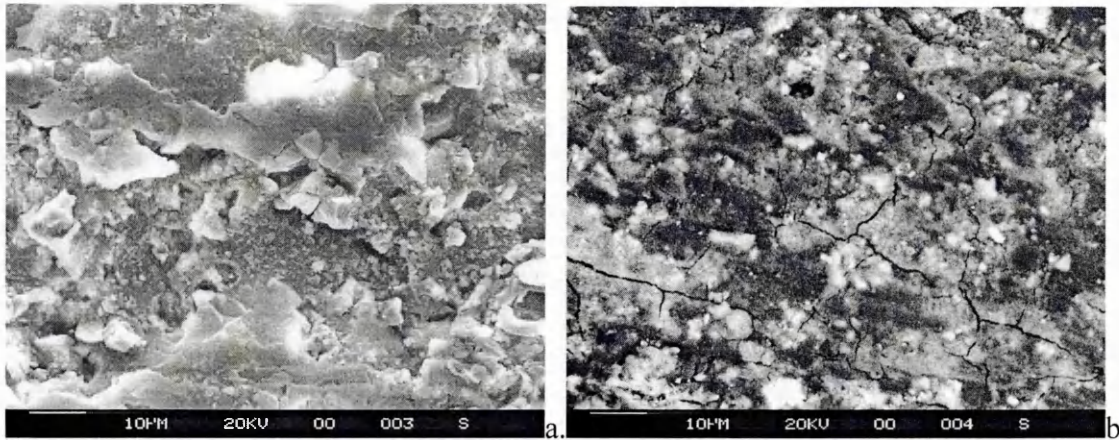
*Figure 3.34: SEM micrographs of resin bond wheel after grinding for ten passes: a.
away from the leading edge. b. near the leading edge*

A segment of the ELID wheel was also observed after the end of the experiment and its
appearance is displayed in figure 3.35. The surface was characterised by the presence of
the layer of ferrous oxide on which cracks have also appeared. The trough that was
etched on the surface revealed the presence of cracks inside the matrix material as well
which were probably present as defects introduced during the manufacturing process of
the wheel.
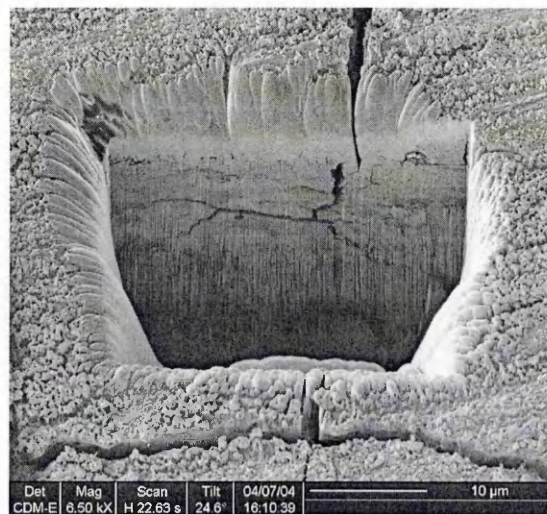
Figure 3.35: Wheel segment as observed on the FIB after ten passes on a BK7 sample.

During these trials, the quality of the ferrous oxide produced was not always the same as, during some of the experiments, some conductivity issues were faced. Current was not properly flowing through the circuit and so the growth of the oxide layer was not totally efficient. As a result, a poor quality oxide layer of very small thickness was present, especially in the part of the tests were the single-pass specimen was ground. The difference in appearance is apparent when comparing figure 3.35 and figure 3.36. Figure 3.36 shows the surface of one of the wheel segments after the single-pass specimen was ground.

The appearance of the segment is different in the case were the oxide was poorly grown as it is smoother than in the case were current flow through the wheel was stable (figure 3.36a). Parts of the wheel are characterised by the oxide flaking off completely and thus appear even smoother (figure 3.36b.). Cracks are still present both on the surface and in the metal-bond matrix. The surface cracks seem to appear as a result of the use of the wheel, combined with the presence of defects inside the matrix and the drying off of the grinding fluid on the segment in order to be observed in the FIB and SEM facilities.
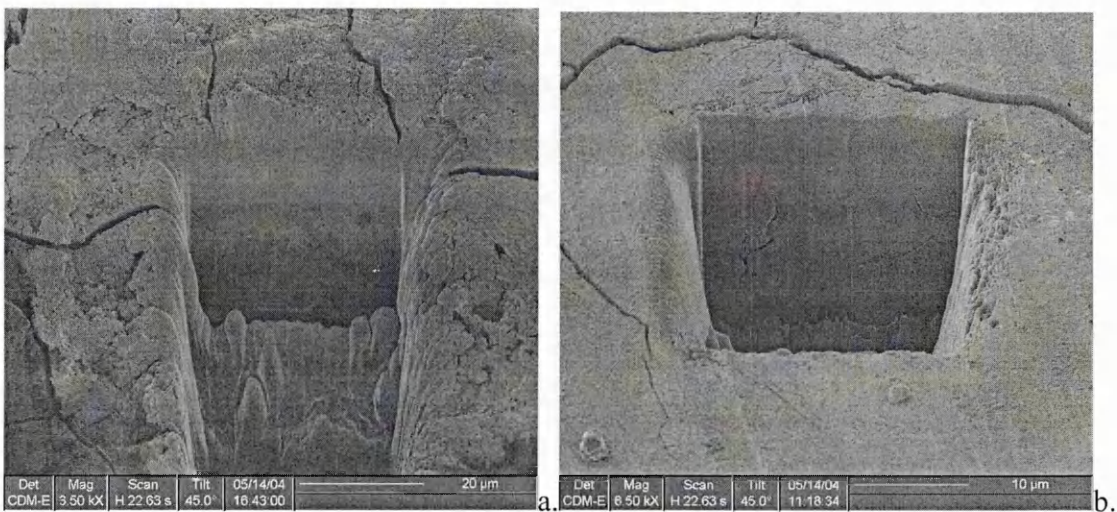
Figure 3.36: Wheel segment as observed on the FIB: a. oxide layer on, after one pass. b. part of the segment where the oxide layer has flaked off

3.E.2 ACOUSTIC EMISSION SIGNALS

Figure 3.37 shows the AE signals corresponding to the variation of the wheel/workpiece
contacting area for the resin bond and metal bond wheels. The total amount of material
removal was below 75mm^3 for each wheel. Figure 3.37 shows that the amplitude of AE
signals reached the peak values at point B before reaching the highest wheel/workpiece
contacting area – 200mm^2.
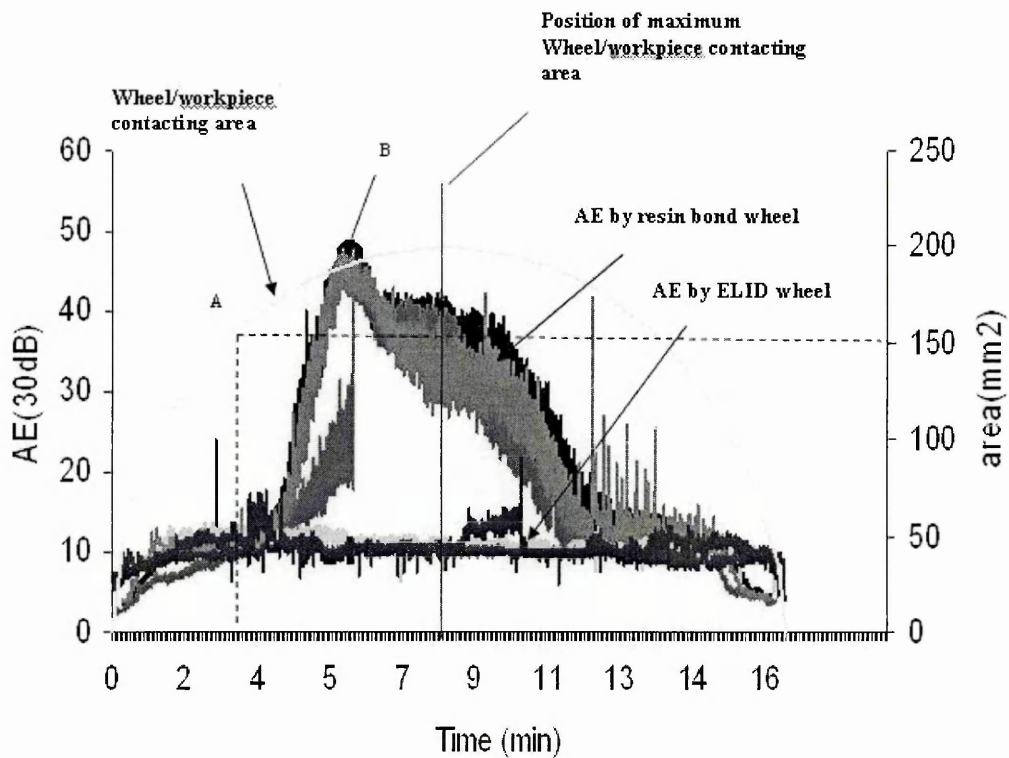
***Figure 3.37: AE signals generated by resin bonded wheel (no-ELID) and CIB wheel
(ELID) with variable wheel/workpiece contacting area***

134
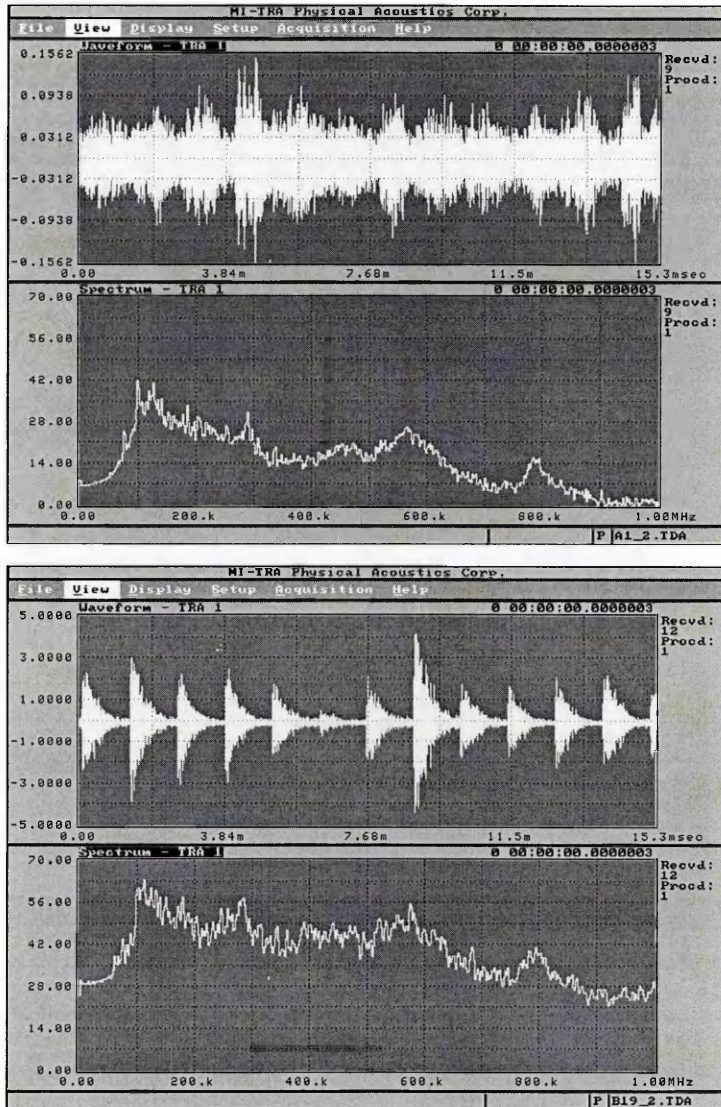
Figure 3.38: Time and Spectrum display when grinding with a (a) ELID wheel, and (b) resin bonded wheel at 180mm^2 wheel/workpiece contacting area

Figure 3.38 captures the display on the screen of the AE signal acquisition software in time and frequency domains when grinding with the resin-bond wheel and metal-bond wheel at a wheel/workpiece contacting area of 180mm^2. The AE signals generated by the resin bond wheel had much larger amplitudes than the signals generated by the metal bond wheel.
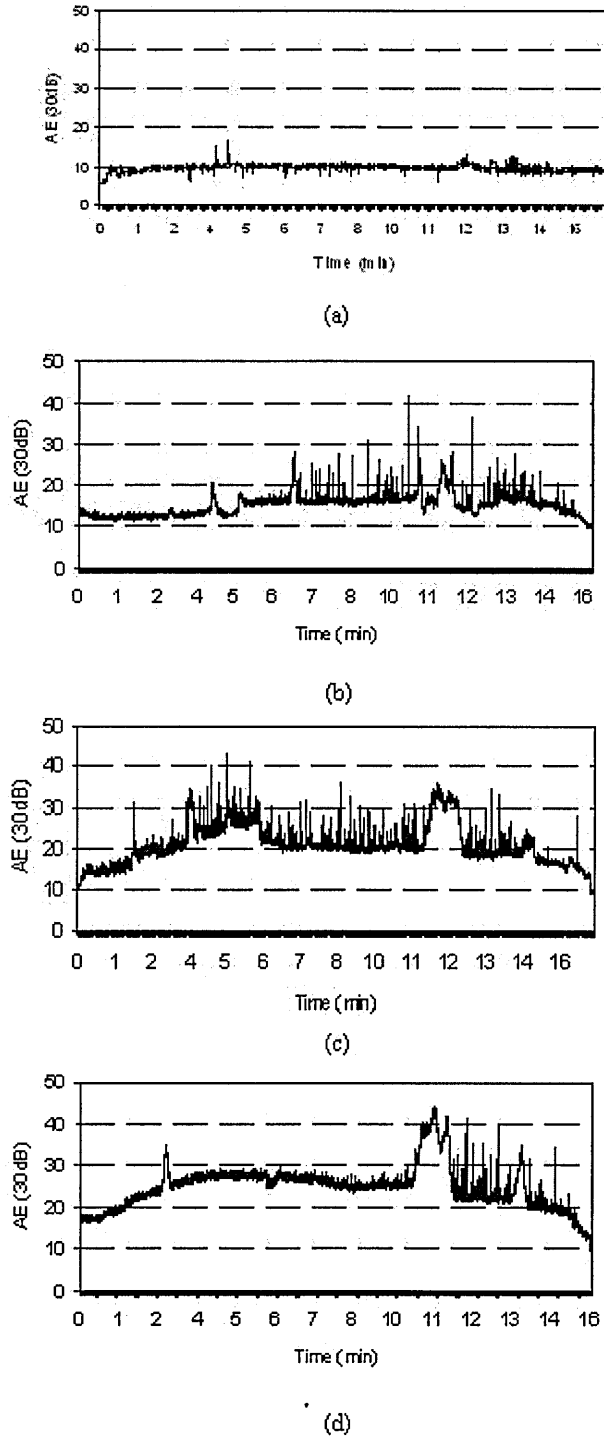
Figure 3.39: AE signals from a CIB bond wheel at different amounts of material removal (a) 71-75 mm^3, (b) 106-110 mm^3 (c) 110-114 mm^3 and (d) 114-118 mm^3

Figure 3.39 shows the variation of AE signals in a series of grinding cycles on BK7 glass. The AE signals were stable, exhibiting relatively small values when the total amount of material removal of the wheel was below 75 mm^3, as shown in Figure 3.39a. Figure 3.39b, c and d shows the AE signals in three subsequent machining cycles with the total material removed increasing from 106 to 118 mm^3. The signal became gradually more unstable with the increase in the amount of material removed.

3.E. GRINDING FLUID PROPERTIES

3.E.1 GRINDING FLUID CONDUCTIVITY CHARACTERISTICS

The following two tables give an indication of the values of conductivity and the differences between the two fluids studied which are displayed in table 18 and the effect of different grinding times on conductivity values on the CEM fluid (table 19).

Table 18 - Comparison of conductivity values for CEM and DOWEL grinding fluids

	CEM 1% in tap water	CEM 2% in tap water	Dowel 1% in tap water	Dowel 2% in tap water
Conductivity (μS)	850	1247	635	925

Table 19 - Conductivity values for CEM at different grinding times

	CEM 1% in tap water	CEM used for grinding the 10-pass sample	CEM used for about 3 months of grinding
Conductivity (μS)	850 (yellow)	1110 (light blue)	2390 (dark blue)

Table 18 indicates that there are no essential differences in the conductivity properties of the two fluids. CEM seems to be more conductive than DOWEL but the difference is relatively small.

Table 19 depicts an interesting effect of fast ion-enrichment of the fluid when grinding. After 10 passes performed on a sample (167 minutes of grinding time) the conductivity value has already increased substantially and as can be seen has almost tripled after about three months of general grinding. The change in conductivity is also followed by intense changes in colour from yellow to light blue to dark blue. This change to blue colour could be due to copper sulphates present in the solution since the brush electrode used is made of copper and there is also a copper coil in the coolant chiller of the Tetraform.

CHAPTER 4: DISCUSSION

4.A ANALYSIS OF EXPERIMENTAL RESULTS

4.A.1 THEORETICAL CALCULATION OF ELID OXIDE LAYER THICKNESS

A theoretical calculation of the oxide layer thickness after the pre-dressing stage, based on the data acquired by the ELID power supply and the use of Faraday's law, is presented below. The simple geometry of the segments of the cupwheel and a few approximations were utilised in order to gain insight on the expected growth of oxide after pre-dressing was complete.

Kim and Lee [40] proposed the following equation when calculating the volumetric bond material oxidation, which is Faraday's law with the addition of a current efficiency factor:

$$V_o = \eta \left(\frac{M}{nFp} \right) It = \eta V_s Q \quad \text{where:}$$

η : Current efficiency

M: Atomic weight of the bond material (M=56gr/mol for Fe)

n: Valence

F: Faraday's constant: 96,485.3 Cb/mol

p: Bond material density

I: Current flowing through the circuit

t: Time

Q: Total charge passed

The current efficiency factor was introduced in order to correct the equation due to effects such as the corrosion of parts of the cupwheel other than the surfaces of the segments that would subsequently take part in the grinding process and the occurrence of other electrochemical reactions due to the current that passes through the grinding

solution other than that of iron going into solution (e.g. oxygen evolution from the electrolysis of water).

The atomic weight used in this equation was that of Fe (M= 56 g/mol) and the valence was assumed to be n=2, which is the valence of bivalent iron going into solution. The bond material density was also assumed to be that of iron (7.9 g/cm^3).

The following figure (figure 4.1) shows a typical graph of the evolution of current and voltage during pre-dressing. The observed increase in voltage and decrease of current signify the growth of the non-conductive layer on the cupwheel.
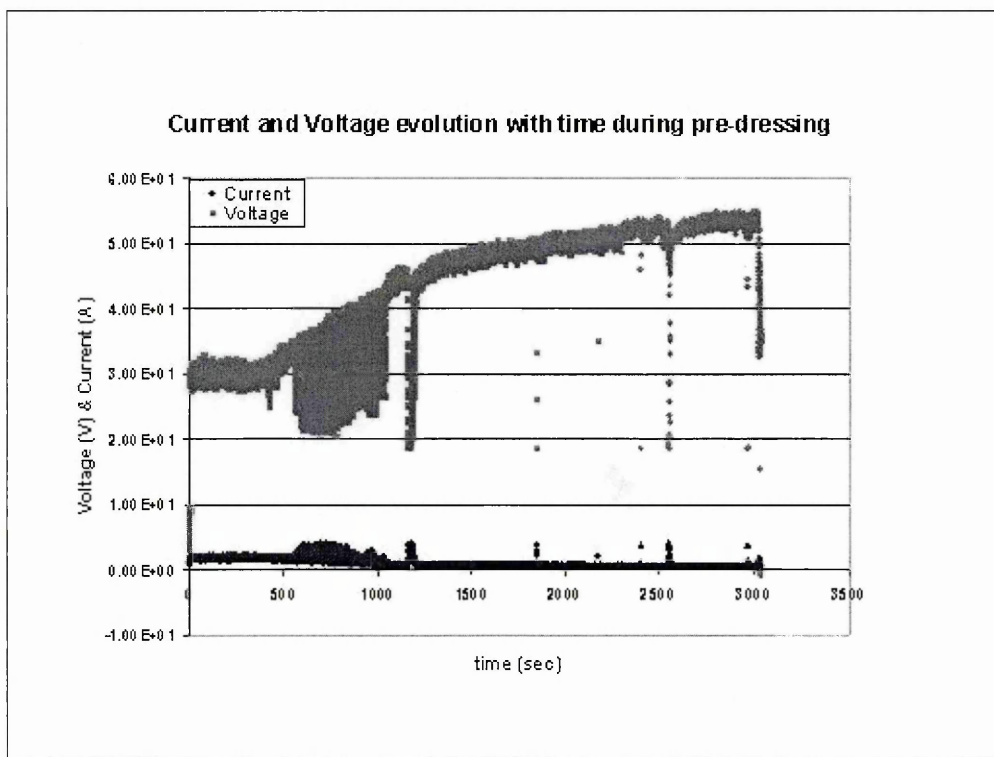
Figure 4.1: Current and Voltage Pre-dressing curves

The pre-dressing parameters that were used are also listed below.

Applied Voltage waveform: Square Pulse

On/Off time: 50%

Peak Voltage: 60V

Wheel Rotation: 1000rpm

Pre-dressing time: 30 min

In order to calculate the value of total charge passed that is contained in the above equation, the values of current were integrated over the time period that the pre-dressing stage lasted (t_p).

$$Q = \int_0^{t_p} I.dt$$

That integral represents the total charge passed through the grinding wheel. In the specific case presented here, which is representative of the conditions during pre-dressing, the value of charge obtained was

$$Q=3,024 \text{ C}$$

Substituting that value in the equation the volume of oxide layer produced is

$$V_o = \eta \ 0.1111 \text{ cm}^3$$

As can be seen, that value is dependent on the value of the current efficiency factor η. As a first approximation, η was assumed to be equal to 1. This means that 100% current that flowed through the circuit was used for the reaction of bivalent iron going into solution. In reality, η is equal to a smaller value, as the flowing current is also used for other electrochemical reactions that are simultaneously taking place. Still, the value of current efficiency in this case was assumed to be high enough so as to safely attribute to η a value close to 1.

Using the geometrical characteristics of the grinding wheel, the surface of each one of the 8 segments on the wheel is measured to be S= 2.54 cm^2. Due to the rotation of the wheel at a constant speed during pre-dressing (1000rpm) equal distribution of the current to the segments was assumed so, 1/8 of the calculated charge passes through each segment. Hence the final oxide layer thickness was calculated to be:

$$H_o = \frac{V_o}{8S} = 55\,\mu m$$

This value agrees with those experimentally observed through the use of the FIB facilities. The difference in structure that was observed (which is highlighted in figure 4.2) when moving deeper into the matrix material of the grinding wheel was attributed to the presence of the fully grown oxide layer that extends to a depth of 50-60 μm, in agreement with the theoretically calculated figure.
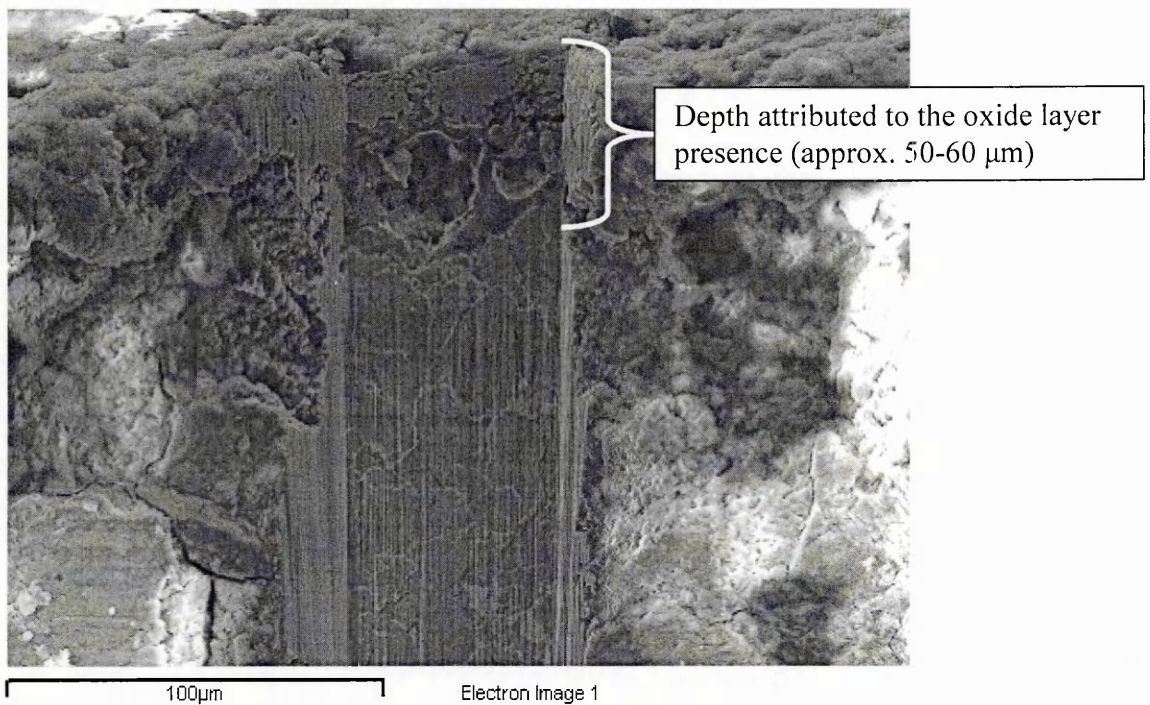
Depth attributed to the oxide layer presence (approx. 50-60 μm)

100μm   Electron Image 1

Figure 4.2: FIB picture for the estimation of the depth into which the fully grown oxide layer extends.

The experimentally observed value and the theoretical calculation are also in good agreement with the values reported in the literature [36], [37]. Depending on the chosen settings for pre-dressing, thicknesses of up to 60 microns are observed. Table 20 gives an overall presentation of the values obtained through the experimental work of this project for various states of the oxide layer grown on the wheel

Table 20- Charge transfer resistance values and corresponding oxide thicknesses

Oxide Description	Corresponding thickness (μm)
No oxide layer	0 (experimental)
Thin post-grinding oxide	~2 (experimental)
Thick post-grinding oxide	~6 (experimental)
Fully grown oxide	50-60 (experimental)

4.A.2 EIS RESULTS-CORRELATION TO OXIDE LAYER THICKNESS

Table 21 summarizes the values of resistance calculated through the EIS plots for different states of the grinding wheel.

Table 21- Overall charge transfer resistance values

	No oxide layer grown	Segment after 10-pass grinding Thin post-grinding oxide	Segment after 20-pass grinding Thick post-grinding oxide	Fully grown oxide layer
Resistance (Ohms)	434.4	776 1027	2,860	11,586

A graphic presentation of these results is given in figure 4.2. In figure 4.3 the linear relationship between charge transfer resistance and oxide layer thickness is presented. The values used for these plots are based on the experimental values obtained through SEM spot analysis and FIB observations that were presented in table 20.
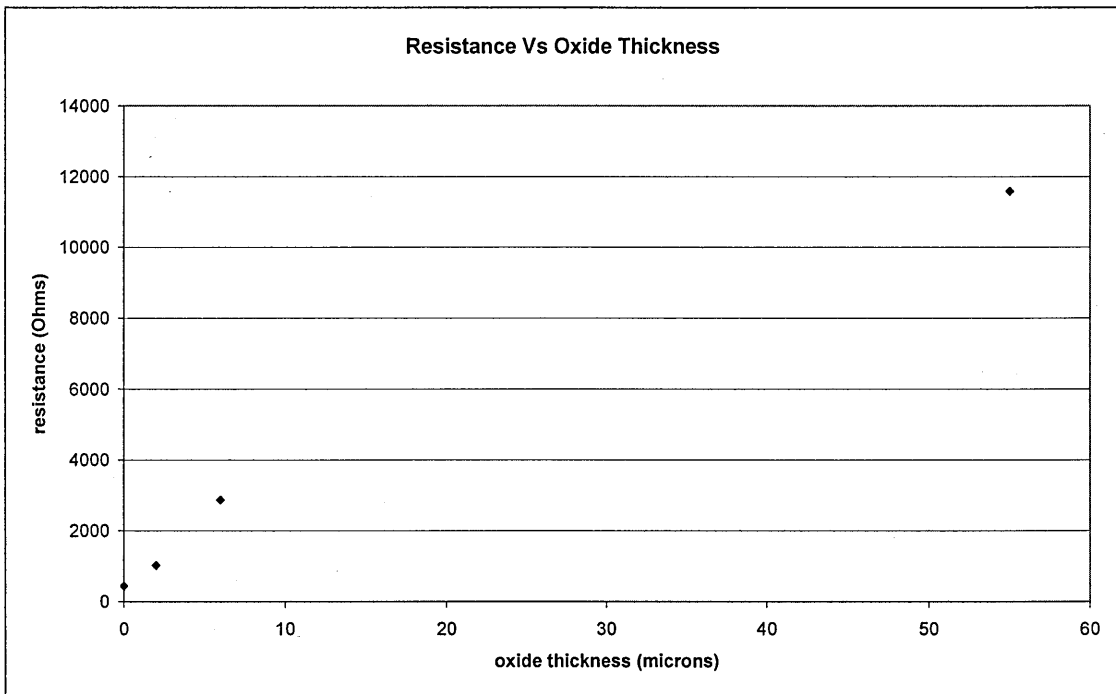
Figure 4.2: Resistance values distribution with oxide layer thickness
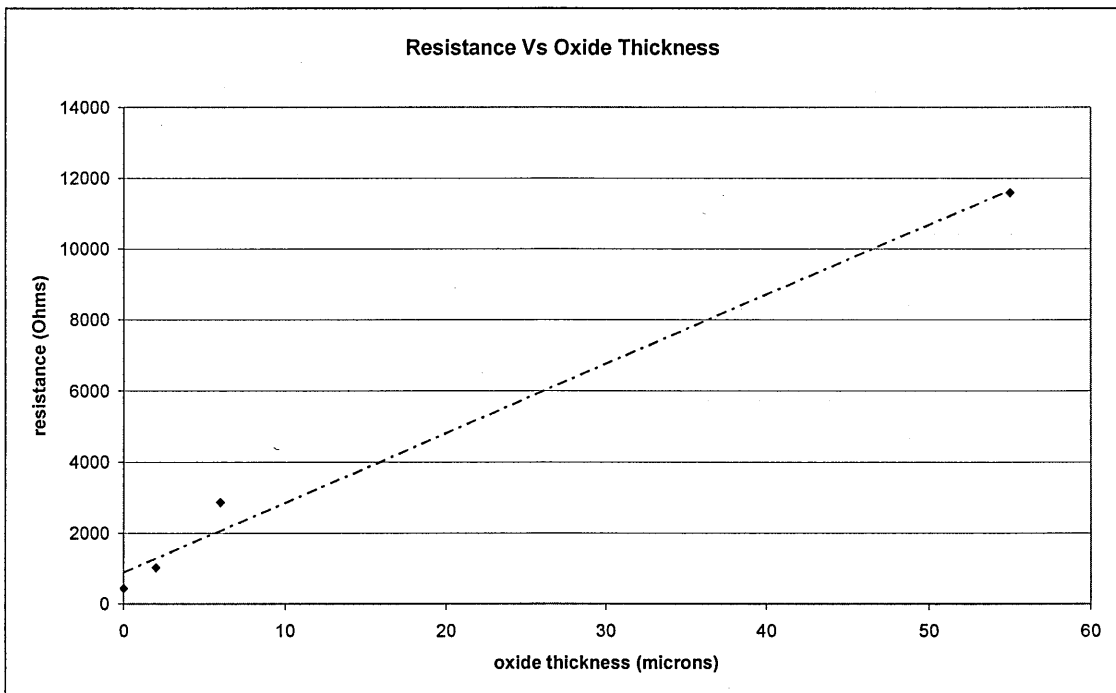
Figure 4.3: Linear distribution of experimental points in the values of charge transfer
resistance and oxide layer thickness

As can be seen in figures 4.2 and 4.3, there is a lack of experimental points for oxide layer thicknesses between 6μm (thickness of oxide layer after grinding) and above 50μm (thickness of oxide layer after pre-dressing). The evolution of the curve would be better understood if a few points of intermediate oxide thicknesses were acquired. Oxide thickness and the corresponding resistance achieved through EIS measurements could be easily acquired by stopping the pre-dressing of the grinding wheel before a fully grown oxide layer is produced, removing the grinding wheel segments and measuring their impedance response. Unfortunately due to time restrictions these experiments were not performed.

The theoretical calculation presented in paragraph 4.a.1 is added into table 22 that was produced from the correlation of charge transfer resistance and the corresponding oxide layer thickness, described in the EIS chapter.

Table 22- Charge transfer resistance values and corresponding oxide thicknesses

Oxide Description	Resistance(Ω)	Corresponding thickness (μm)
No oxide layer	434.4	0(experimental)
Thin post-grinding oxide	1027	~2 (experimental)
Thick post-grinding oxide	2860	~6 (experimental)
Fully grown oxide	11586	50-61 (experimental) (55 theoretical)

A limitation of this method of evaluation of the quality and characteristics of the oxide layer that was built on the grinding wheel segment stems from the solution used during electrochemical impedance spectroscopy data acquisition. EIS experiments were performed in a NaCl solution with the addition of CEM grinding fluid. The solution that is commonly used during ELID grinding does not contain NaCl but, as described previously, such a solution did not give a strong enough signal during the measurements; a more conductive environment was necessary in order to be able to observe the

evolution of the impedance response of the wheel segments with decreasing frequency (i.e. formation of semicircles in the Nyquist plots). The more aggressive environment led to a clearer response acquired from the grinding wheel segments. Charge transfer resistance is a property that is strongly affected by the environment in which it is measured. It is not a characteristic property of the material that is measured alone but is indicative of the combination of the material and the environment in which it is placed during the experimental procedure. Iron ions from the matrix material go into solution easier as the protection of the oxide layer is diminished due to the aggressive nature of the environment in which the segments are placed. Hence, they displayed a much lower charge transfer resistance than the one that would be expected if their response was measured in a less aggressive solution. Because of this effect, the analysis of the evolution of charge transfer resistance could not be applied in the case of an environment that's equivalent to the solution that is used during grinding. In that case, much higher charge transfer resistance would be expected due to the weaker nature of the solution (i.e. Fe ions will not go into solution as readily).

4.A.3 CORRELATION OF OXIDE LAYER THICKNESS AND ACHIEVED SURFACE FINISH

Good correlation between fluctuations of current (attributed to changes in oxide thickness) and the patterns of damage visible on testpiece A was observed (tests on testpieces A and B described in section 3.a.5). On the other hand, Franse described in his thesis [78] the generation of damage patterns on rotating testpieces due to process variables. In order to be able to establish a degree of certainty on whether the observed damage patterns correlate directly to the build up and breakdown of oxide, testpiece B was ground without the use of the rotary table. Figure 4.4 gives an immediate representation of the resulting surface quality achieved after grinding testpiece B. Excellent correlation is observed between the build up of oxide layer (which corresponds to a decrease in current) and its imprint on to the testpiece surface which manifests as surface finish improvement whereas oxide depletion corresponds to surface finish deterioration.
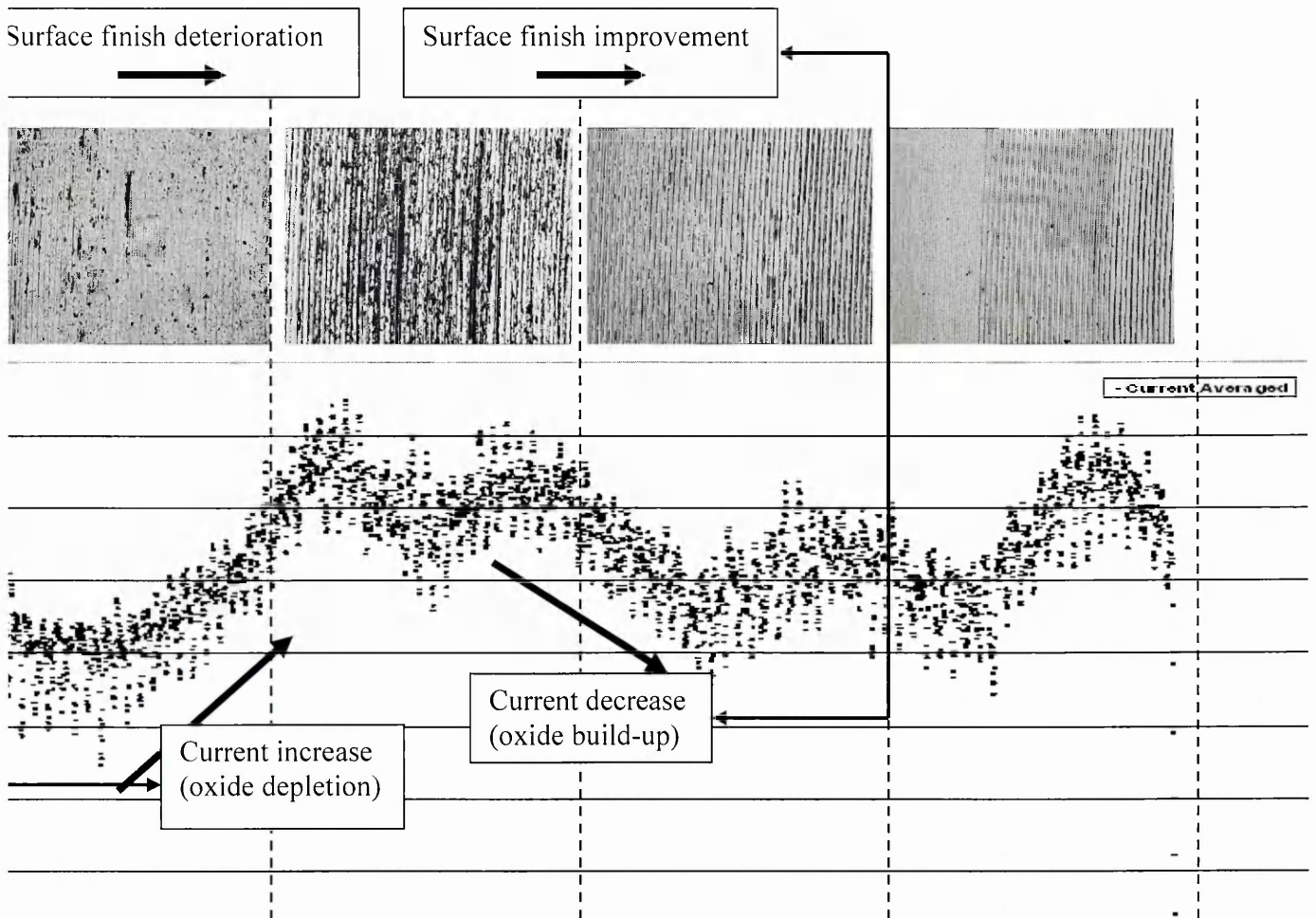
Figure 4.4: Evolution of the ELID current and its imprint on the glass testpiece B

When performing ELID grinding, excellent surface finish requires the presence of adequate oxide on the wheel surface. If the oxide layer is not adequate, it leads to metal to glass contact which manifests with poor surface finish and the presence of defects and scratches on the work piece. This proves the importance of the presence of the soft abrasive (the friable oxide layer) as a lubricating medium in the contact area between the wheel and the glass sample. The soft abrasive that is removed during grinding should be followed by oxide formation, so as to enable the oxide to be present in the interface between the work piece and the wheel. Reaching a state of equilibrium between these two processes (oxide depletion/oxide regeneration) is of the utmost importance if high quality surfaces are to be produced.

4.A.4 SUBSURFACE DAMAGE: EVALUATION OF RESULTS

The experiments performed in order to evaluate the amount of sub-surface damage introduced into BK7 glass when processing it gave an indication of the two major issues one is faced with when manufacturing components from hard and brittle materials:

a. The efficient material removal rate (that corresponds to increased feed rates and depths of cut) while still being able to achieve good surface finishes, in order to minimise the amount of time required to produce each component and

b. The amount of damage that was introduced into the sample and the time required to remove it through time-consuming processes such as polishing.

The correct balance of these two competing factors is of great importance if high quality components are to be produced through the use of a time-efficient (hence cost-effective) process. This means that when deciding on the grinding parameters that will be used on the components to be produced (such as wheel type, grit size, feed rate, depth of cut etc.), there are limitations on the speed with which the process can advance, as lower production times would correspond to the introduction of more damage into the components which would lead to requirements of subsequent refining processes. The low production time is not realistic in these cases as the overall time taken until all damage is removed increases dramatically with the introduction of polishing steps.

The removal of sub-surface damage is critical for sensitive, light-transmitting components and so, polishing continues until all defects are removed leading to compromises in terms of production time but also shape accuracy as well.

The initial experiments which were performed on testpieces as received from the manufacturer, focused attention on the pre-existing damage inside them. 20 μm of material had to be polished away in order to achieve a surface that was free of any damage. Achieving good surface finish after having removed only a few microns of material would leave the testpiece with the remnants of that damage and so its quality would be compromised.

Initial rough grinding with wheels that contain large sized grits (151 μm, 46 μm) also led to the introduction of large amounts of damage up to depths of about 30 μm from the surface of the testpieces. Polishing of such amounts of damage would either impede the wide application of such production methods (as they are rendered inefficient in terms of production times) or increase dramatically the manufacturing cost of such components.

The following figure (figure 4.5) gives an overview of the amount of damage found in each testpiece that was processed and studied. These testpieces had undergone only preparatory processing (rough grinding) and further grinding was required in order to achieve high quality finishes. That is why it is important to assure that further processing would be leading to removal of the pre-existing damage and would not be introducing new defects so as to be able to minimise or altogether avoid polishing steps.

Depth of damage on BK7 glass for different processing methods
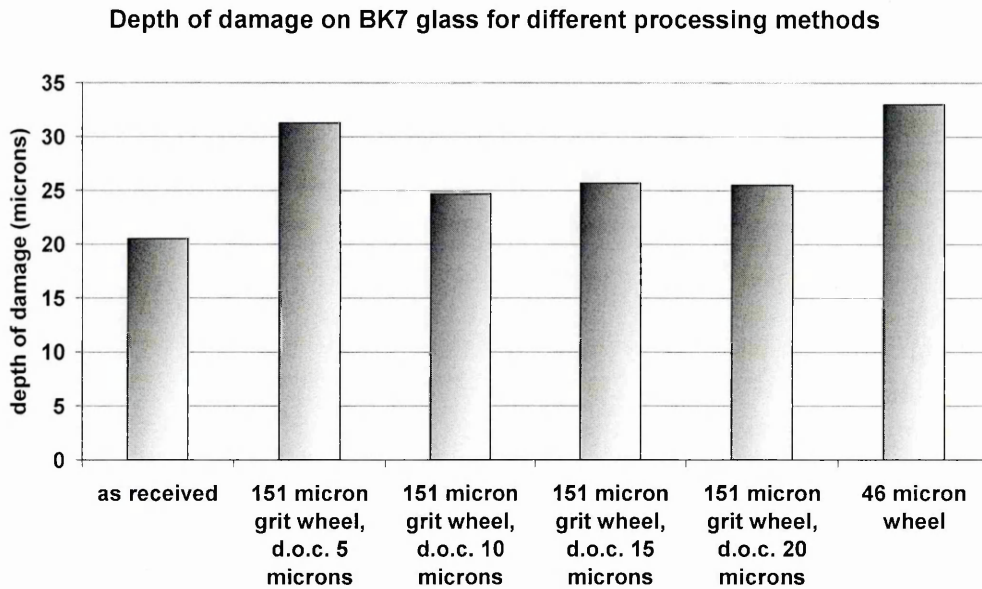
Figure 4.5: Depth of damage for BK7 testpieces under varying processing conditions

The compromise of component quality when pre-existing damage is not taken into account is obvious in the results presented in table 13 (p.120). The clean-up passes performed on the testpiece with the 2 μm grit wheel only removed a few microns of material and a small amount of the damage that was already present before grinding it.

CHAPTER 4: DISCUSSION: ANALYSIS OF EXPERIMENTAL RESULTS

This resulted in the need for long polishing steps in order to achieve a damage-free surface.

The same test was repeated on a testpiece that was previously polished, making sure that no defects existed in the sample's surface or sub-surface. After grinding the testpiece with the 2 µm grit wheel, the amount of damage was much lower and a clean, defect-free surface was achieved after polishing away as little as 5 microns in the case of the slower feed rate of 50mm/min. Figure 4.6 shows the comparison between the depths of damage in the two testpieces and the lower amount of damage present in the polished one.
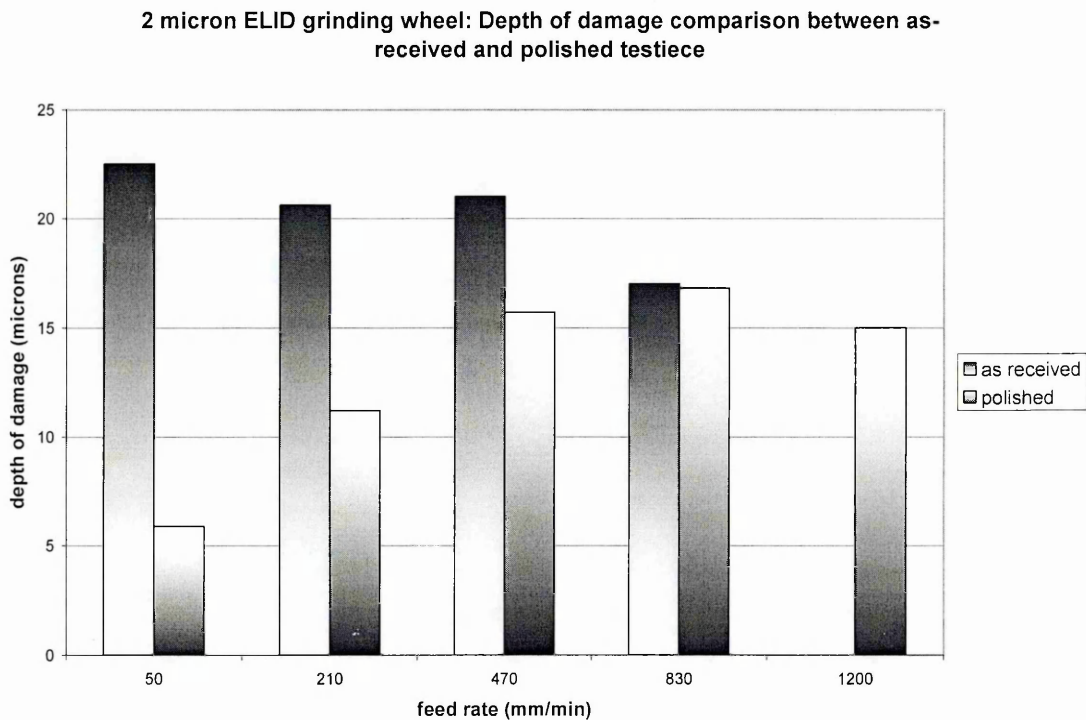
Figure 4.6: Depth of damage for BK7 testpieces when grinding with 2 µm ELID grinding wheel. Comparison between an as-received testpiece and a polished testpiece

Increasing feed rates up to speeds of 1200 mm/min still yielded a clean surface but the amount of damage that was introduced in the sub-surface of the sample increased. Even though adequate surface finish was obtained at very quick grinding times, the need to

remove the sub-surface damage on the testpiece increased the overall processing time by a few hours hence rendering the process inefficient.

4.A.5 SUBSURFACE DAMAGE: MODELLING DEPTH OF DAMAGE

Previously published work indicated the possibility of machining hard and brittle materials by means of plastic flow rather than micro-fracture mechanisms, leading to a fine, crack-free surface. Ductile grinding can generally lead to the production of surfaces with little or no sub-surface damage. Keeping the normal force per grit below some critical level can lead to minimisation or overall avoidance of fracture damage [SunOhnishi].

The transition from brittle fracture to ductile material removal occurs at a critical depth of cut according to Bifano [3]: Larger depths of cut will lead to the propagation of cracks into the material whereas lower depths of cut ensure plastic deformation with no fracture damage introduced. In the above statement, material removal under the critical depth of cut corresponds to grinding conditions where plastic deformation is energetically more favourable than fracture and, encompassing chip thickness theory, maximum chip thickness is lower than the value of critical chip thickness.

Critical depth of cut and chip thickness can be calculated for BK7 glass using equations [SunOhnishi]:

$$d_c = 0.15 \left(\frac{E}{H} \right) \left(\frac{K_c}{H} \right)^2$$

and

$$h_{max} = \left(\frac{4V_w}{V_c Cr} \sqrt{\frac{a_e}{d_c}} \right)^{1/2}$$

The value of critical depth of cut is calculated at 42 nm using the material properties of BK7 (elastic modulus E=81 GPa, fracture toughness K_c=0.82 Gpa.m$^{1/2}$, hardness H=5.8 Gpa) when obtained from a surface without any residual stress or microcracks. Active grit concentration is estimated as 1.0×10^8 /m^2 for the wheels used in the experiments undertaken in this study. The value of r is reported to be in the range of 10-20 [7]; r was assumed to be equal to 10 in this study. The way different processing conditions affect these values is apparent when measuring the hardness and fracture toughness of ground and polished testpieces. The results are a range of values for the critical depth of cut between 40nm and 70nm. Calculations for critical chip thickness, depending on tool geometry, and selected grinding parameters (depth of cut, cutting velocity and wheel speed) result in a value of 50nm at the brittle/ductile transition position. Grinding conditions that lead to chip thicknesses under the critical value lead to the production of defect free surfaces and minimal or no sub-surface damage as crack propagation is not energetically favourable.

The results presented for the resin bond wheel of 7micron diamond grit (figure 3.29, p. 122) indicated the transition from a brittle to a ductile regime very clearly, as, there was no sub-surface damage introduced into the testpiece when moving closer to the centre of rotation and consequently to lower feed rates.

The same was observed for the ELID ground testpieces (section 3.c.2 V.); the area ground with a lower feed rate (50mm/min) yields surfaces that contain less subsurface damage than the areas where the feed rates are increased (210mm/min up to 1200mm/min). The decrease of damage indicated the movement towards the transition from a brittle to a ductile material removal regime as the feed rate and consequently the material removal rate decreased.

Although the transition was observed on the rotating resin-bond ground sample, it was not observed in the case of the non-rotating sample. The necessity for even lower feed rates was thus indicated, in order to observe the brittle to ductile transition. On a test piece with no rotational symmetry, the time required to complete the grinding process increases dramatically and such experiments were not performed during this work.

The experimental results for subsurface damage were compared to the damage depth predicted by the model proposed by Zhang and Howes [9].

According to error theory, since the depth of damage is given by equation:

$$h = \frac{l_1 - l_2}{2\tan\frac{\theta}{2}}$$ as presented in section 2.E.2 (p.72)

Errors can be calculated for the experimental points of subsurface damage depth using the following equation:

$$\delta h = \sqrt{\left(\frac{\partial\left(\frac{l_1 - l_2}{2\tan\frac{\theta}{2}}\right)}{\partial l_1}\delta l_1\right)^2 + \left(\frac{\partial\left(\frac{l_1 - l_2}{2\tan\frac{\theta}{2}}\right)}{\partial l_2}\delta l_2\right)^2} = \sqrt{\left(\frac{\delta l_1}{2\tan\frac{\theta}{2}}\right)^2 + \left(\frac{\delta l_2}{2\tan\frac{\theta}{2}}\right)^2}$$

Where δl_1, δl_2 = 1.5μm (observation error) and θ= 136°. When substituting these values we find that the error for each experimental point is:

$$\delta h = 0.43\mu m$$

Figure 4.7 shows the comparison between the experimental results and the theoretically calculated values, using the Zhang-Howes model. The depth of damage is first plotted against increasing feed rate values and then plotted against the equivalent chip thickness that corresponds to those feed rates.

154

Predicted and Experimental Subsurface Damage vs Feed Rate

a.

Predicted and Experimental Subsurface Damage vs Maximum Chip Thickness
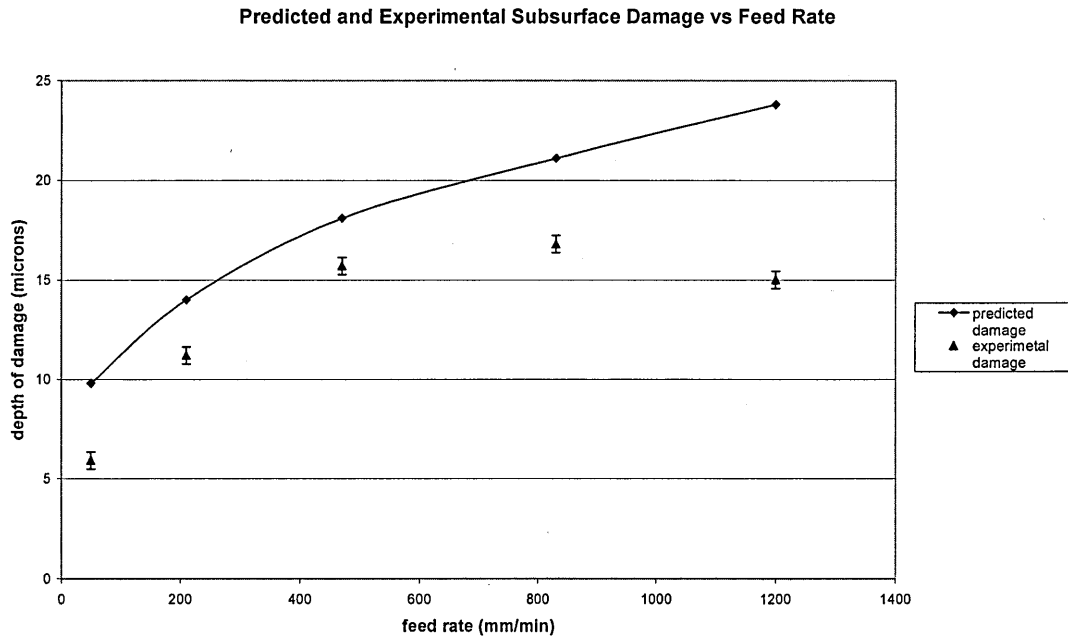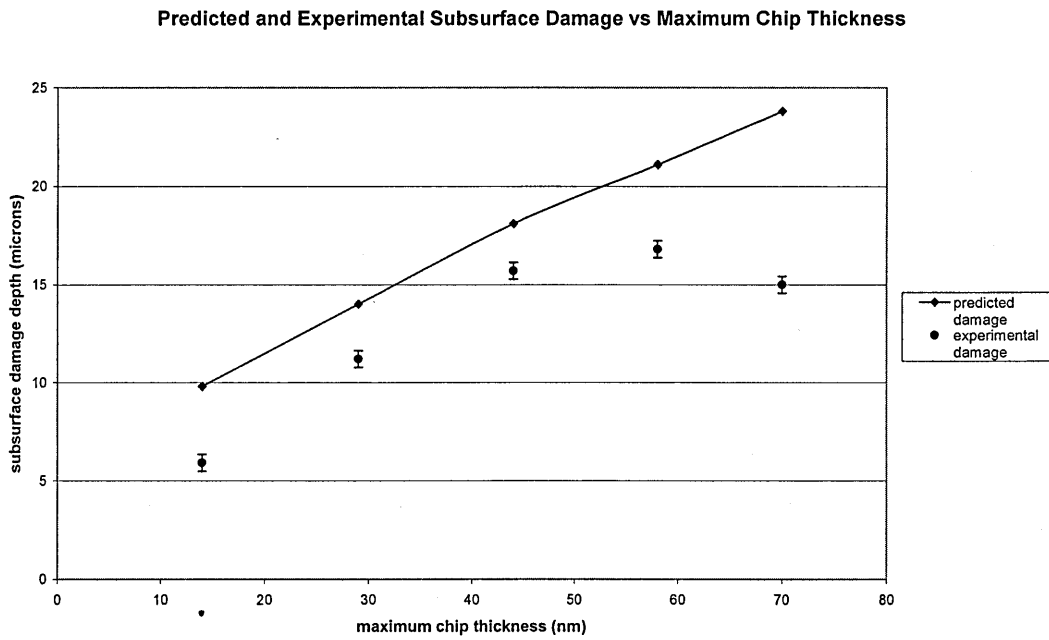
b.

Figure 4.7: Subsurface damage depth vs feed rate (a.)

and maximum chip thickness(b.)

Comparison between experimental results and theoretical prediction

155

Figure 4.7 displays the good correlation that was observed between the theoretical prediction and experimental results. For a given maximum chip thickness, a safe prediction of the damage that was expected to be introduced into the ground work piece was calculated. Differences between the theoretical curve and the experimental points may be due to safety margins taken into account when attributting values to the constants in the model.

The transition from brittle to ductile material removal at the value of the critical chip thickness was not observed as there is a disagreement between its theoretically calculated value and experimental results. That transition would have manifested itself as a damage-free area on the components. According to experiment, this would be expected for maximum chip thicknesses of less than 10μm although theory predicts that transition between 40 and 70μm (figure 4.8). The observed difference could be related to:

a. The characteristics of a spherical wheel are slightly different to those of a cylindrical peripheral wheel. The equation and constant values used in the prediction of critical chip thickness did not incorporate that difference.

b. Residual stresses on the BK7 work piece that might have affected its hardness and fracture toughness characterisitng

c. Existing critical chip thickness equations relate it to material properties alone. A hybrid equation that would incorporate machine and process parameters as well (e.g. bond strength, active grit concentration) might be more representative of the case studied and through its use, a more realistic value for critical chip thickness could be predicted. Development of such a model could lead to more accurate predictions for critical chip thickness that would be closer to the experimental results observed.
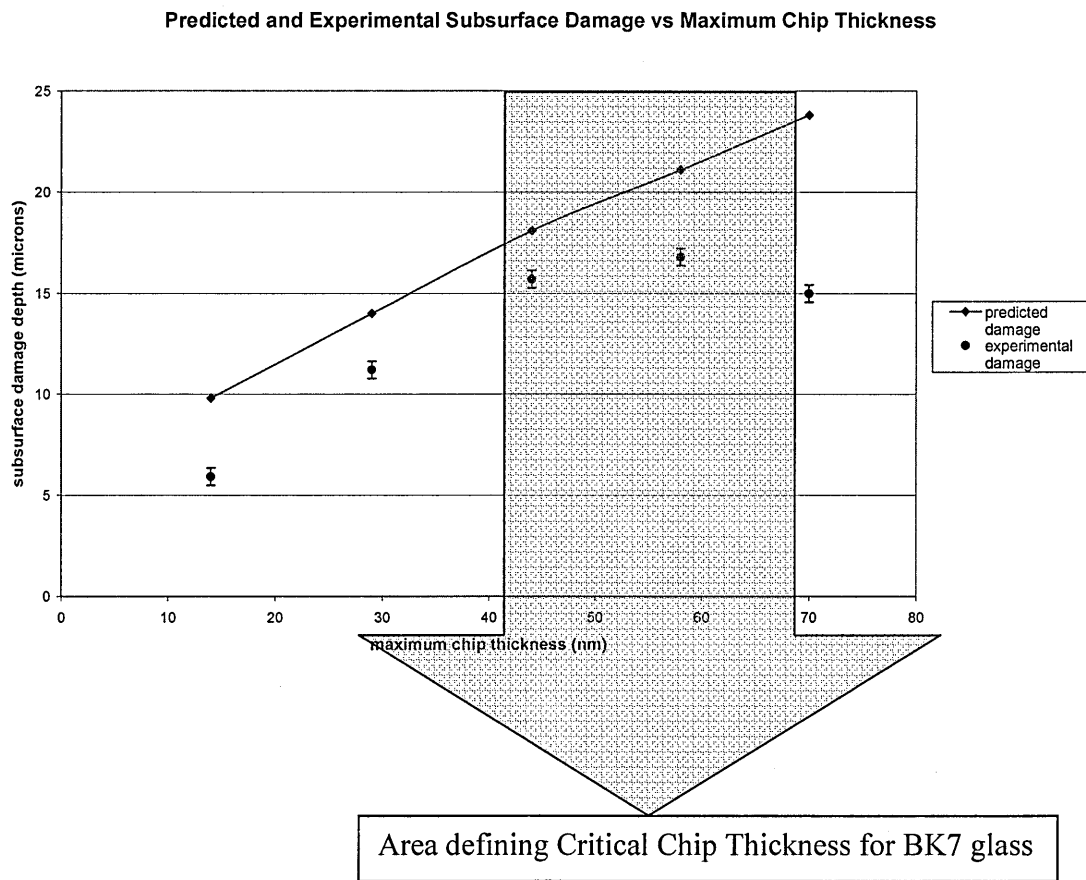
Predicted and Experimental Subsurface Damage vs Maximum Chip Thickness

Figure 4.8: Subsurface damage depth maximum chip thickness. Position of Critical Chip thickness

In order to process the testpieces in a way that would lead to a damage-free surface with no sub-surface damage, there are two options:

a. Slow feed rate and low material removal rate that corresponds to grinding under a ductile regime and low grind forces. Material is removed with no or minimal micro-cracking. Microcracks do not propagate under the new surface and as a result, no damage is introduced. The requirement of increased processing time in

order to achieve the necessary grinding conditions for achieving ductile regime grinding lowers the efficiency of the process.

b. Higher feed rates, lead to a combination of ductile (plastic flow) and brittle (introduction and propagation of microcracks) material removal (corresponding to higher grinding forces). Grinding time is reduced which leads to a more efficient process but leads to an increase in the overall processing time as the introduction of a further polishing step is necessary in order to remove sub surface damage introduced during grinding.

c. With the use of the spherical wheel, the presence of scallops on flat surfaces is unavoidable. In order to be able to reduce processing time, the distance between successive tracks can be increased, but that would lead to a bigger scallop height and subsequently, a longer polishing step.

The limits described above, along with the necessity for a time-efficient, cost-effective process lead to the need for well-defined grinding conditions under which components must be ground. A trade-off between processing time during grinding and the amount of damage introduced is necessary in order to end up with the most efficient overall processing conditions. A lower processing time can be achieved by choosing grinding parameters that lead to a controlled introduction of damage into the testpiece (limited to a 1-2 microns), which will subsequently be removed with a short polishing step. A small polishing step also leads to maintaining better form accuracy on the final testpiece. This is especially true when grinding non –flat surfaces (e.g. freeform optics). The ability to eventually be able to produce damage-free freeform surfaces was one of the major challenges during the Nanogrind project and the Nanogrind machine which will be built as a result of the project aims at achieving an efficient and controlled production of such surfaces.

4.A.6 COMPARISON BETWEEN ELID AND RESIN BOND WHEEL GRINDING - ACOUSTIC EMISSION SIGNALS

The optical micrograph near the leading edge in Figure 4.9a shows that the number of the cutting diamond grits after grinding were significantly decreased compared to the unloaded wheel surface shown in Figure 4.9b. The effect of wheel loading during extended grinding operations reduced the efficiency of the abrasive cutting action resulting in large ploughing and sliding (rubbing) components of grit-workpiece interaction. With increasing wheel wear and loading the energy consumption due to ploughing and sliding components increased, thus accounting for the increasing acoustic emission signals.
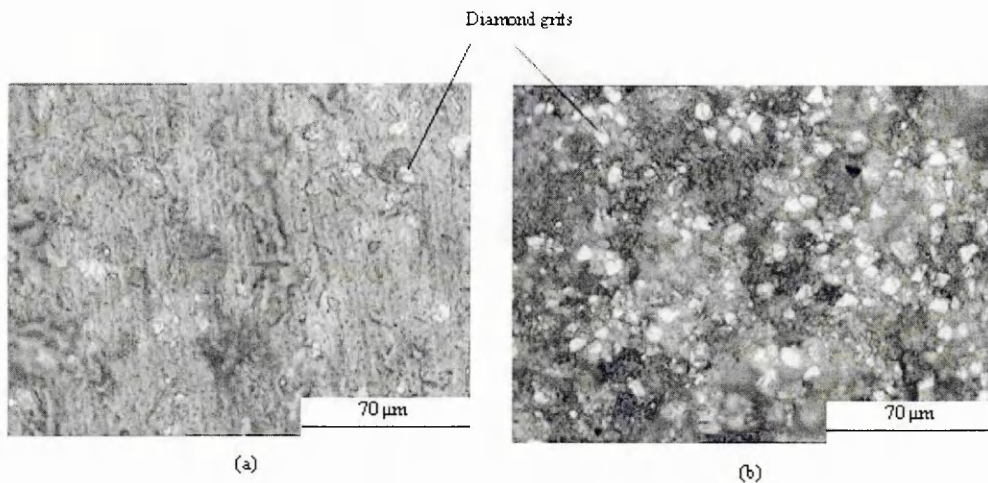
Figure 4.9: Micrographs of (a) loaded resin bond wheel and (b) unloaded resin bond wheel

The results imply that the area of wheel/workpiece contact is a critical factor affecting wheel loading for a resin-bond wheel. Severe wheel loading was developed for a fine grit size resin-bond wheel as the wheel/workpiece contacting area increased. It can be

concluded that a fine grit size CIB cup wheel with ELID grinding performs better in overcoming wheel loading than a resin-bond wheel when the contacting area between the wheel and workpiece is large. The ELID method is therefore more suitable for efficient material removal in precision grinding.

This statement was also verified through the evaluation of the AE results. In figure 4.10, the level of AE for the resin bond wheel was generally lower than the metal bond wheel when the wheel/workpiece contacting area was less than 150 mm^2. However, the AE level increased at a considerable rate with the enlargement of the wheel/workpiece contacting area for the resin bond wheel. Apparently, the wheel/workpiece contacting area largely influenced the AE amplitude during the grinding with the resin bond wheel.
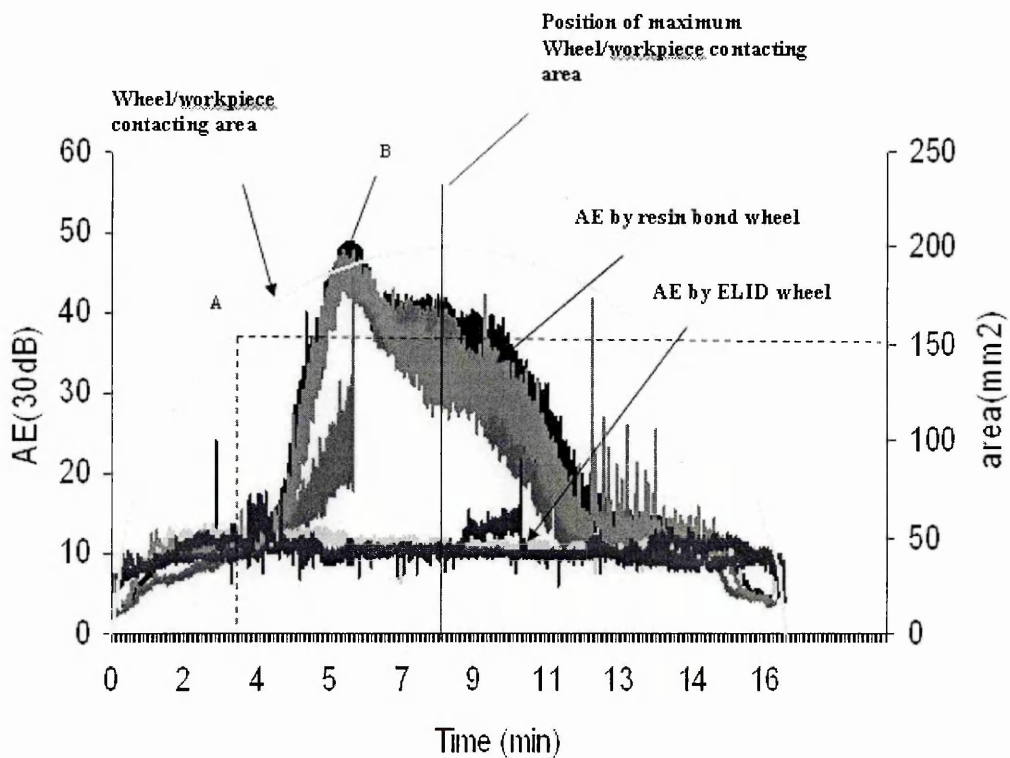
Figure 4.10: AE signals generated by resin bonded wheel (no-ELID) and CIB wheel (ELID) with variable wheel/workpiece contacting area

The positions of the peak value of AE signal correlate with poor surface quality. The AE signals generated by the ELID wheel in figure 4.10 exhibited lower AE levels under the same cutting condition as the resin-bonded wheel. The wheel/workpiece contacting area did not show a significant influence on the AE level for ELID grinding.

The saw-tooth shape AE signals generated by the resin bond wheel (figure 3.38 p. 133) may be attributed to the rubbing/sliding action between the blunt, loaded wheel and workpiece. The amplitudes of the frequency components for grinding with the resin bond wheel increased as a whole compared with ELID grinding (figure 3.38 a and b).

An ELID wheel can quickly enter a stable cutting process after pre dressing. Although loading of the wheel is not as big an issue as it is when grinding with resin bond wheels over large contact areas, with an increase in the amount of material removal or processing time, an ELID wheel can eventually become unable to perform proper cutting due to poor wheel topography. As the grinding wheel has a rough surface and many non-conductive abrasive particles embedded inside, a non-uniform current distribution between the bulk of the electrolyte and the metal surface is expected. The abrasive grains and cavities disturb current flow and cause a local increase in the flux concentration in their periphery area (figure 1.12, p. 20, [41]). The zones exposing metal bond material generated by the friction of chips are also zones of intensive dressing current.

These observations indicated that an uneven electrochemical reaction across the metal matrix surface of the grinding wheel would be generated by the non-uniform current distribution leading to different electrolytic speed on the bond surface. It was noticed that, with the increase in the amount of material removal, AE amplitudes increased and became unstable as presented previously (section 3.e.2, figure 3.39).

The optical micrograph of the surface of the CIB wheel shown in Figure 4.11a indicated the presence of cracks, pits and heavy corrosive areas on the wheel surface after the removal of a large amount of material. The long cracks may have come from short cracks or flaws, which were enlarged under the periodic forces from the workpiece at the wheel –work interface. Electrolytic corrosion could have also promoted the cracking process by concentrating its electrochemical action in these areas.

Figure 4.11b shows a trough generated by ion beam milling, where both vertical and horizontal cracks were observed under the wheel surface. The horizontal cracks could

expand to connect the vertical cracks. With the increase of the number and severity of the cracks, breakage and removal of bond materials could happen, leading to poor wheel topography and, finally, the failure of the wheel. The stochastic distributed AE signals of large amplitude in figure 3.39 b, c and d may correspond to the fractures of bond material. The gradually increased AE level between grinding cycles is consistent with the deterioration in the grinding wheel.
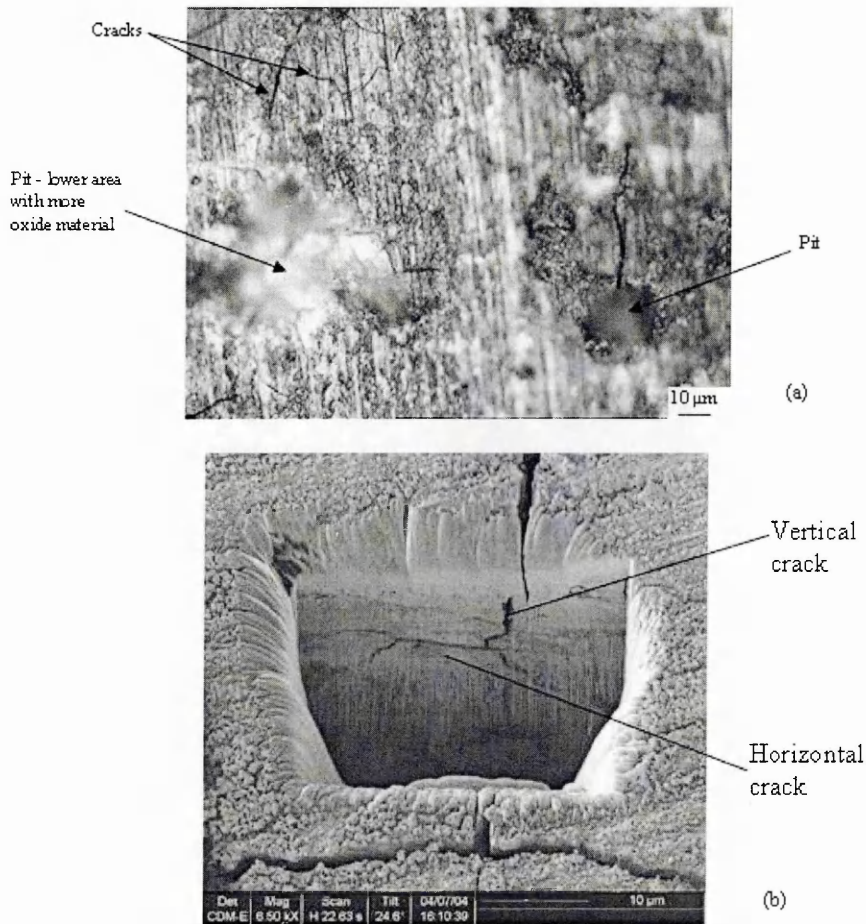
Figure 4.11: (a) Optical micrograph of the surface of CIB wheel, and (b) dent on the wheel surface generated by focus ion beam monitored with SEM micrograph

4.B GENERAL COMMENTS

4.B.1 INNOVATIVE NO-GRIT METAL BOND CUPWHEEL

A few points are highlighted here so as to explain the observed results on the ground samples. The use of a non-typical cupwheel introduced changes in the chosen parameters for grinding, especially when compared to the ones applied when conventional grinding wheels are used.

The chosen wheel speed for these experiments was 1000 rpm. The Tetraform-C capabilities allow for speeds of up to 6000 rpm but in the case of the "no-grit" wheel such speeds lead to poor surface finish achieved. The lack of grits lead to this process resembling a polishing process, since the friable oxide layer was the only surface optimising agent present. Cutting agents were not available and so the primary grinding zone has poor material removal capabilities hence, material removal was mainly achieved in the secondary grinding zone. In this "hybrid" situation, speeds that match better a polishing rather than a grinding process were used.

4.B.2 SUB-SURFACE DAMAGE- CORRELATION TO SURFACE FINISH

When preparing ELID ground testpieces for sub-surface observation, there were no major differences in the surface finish along the different areas of the testpiece surface and so it was not possible to get an indication of the potential presence and depth of sub-surface damage by its direct observation. Polishing back revealed the differences in the amount of damage introduced under different grinding conditions, varying from 5-6μm all the way to almost 20μm. Hence it was concluded that the damage introduced could not be estimated just by examining the surface of the testpiece. Ohmori and Nakagawa [13] observed a n increase in sub-surface damage introduced into the sample correlating with the deterioration of surface quality. In the case of the rotating testpiece that was tested for

subsurface damage, the same deterioration was observed. Moving from minimal or no damage and a surface finish of 2.9nm to areas where damage extended to approximately 7μm and a surface finish of 30nm indicated a correlation of surface finish and extend of sub-surface damage. That correlation is not always observed though and it can be concluded that surface finish cannot be used as an indication of the amount of sub-surface damage present in a component.

4.B.3 GRINDING FLUID CONDUCTIVITY

The intense changes in conductivity of the grinding fluid observed during the experimental part of the process indicated the possibility of effects on ELID current and voltage as well as the corrosion rate of the bond material of the grinding wheel. Grinding fluid conductivity increased three times as the fluid was used over prolonged grinding operations and colour changes where also observed (p. 136). These changes could have an effect on the corrosion rate of the grinding wheel and are mostly important when shape integrity of the wheel and shape accuracy of the samples produced (e.g. freeform surfaces) is crucial. The investigation performed in this project was too limited to extract solid conclusions on the kind of effect fluid conductivity changes have on the overall process hence more detailed work on this topic is required.

4.B.4 KINEMATIC SCALLOPS

Two kinds of scallops could be generated on the workpiece surface, which are "kinematic scallops" and "process scallops". The kinematic scallops are determined by the geometry of the workpiece and tool, and the distance between successive grinding tracks, which are shown in Figure 4.12.

164
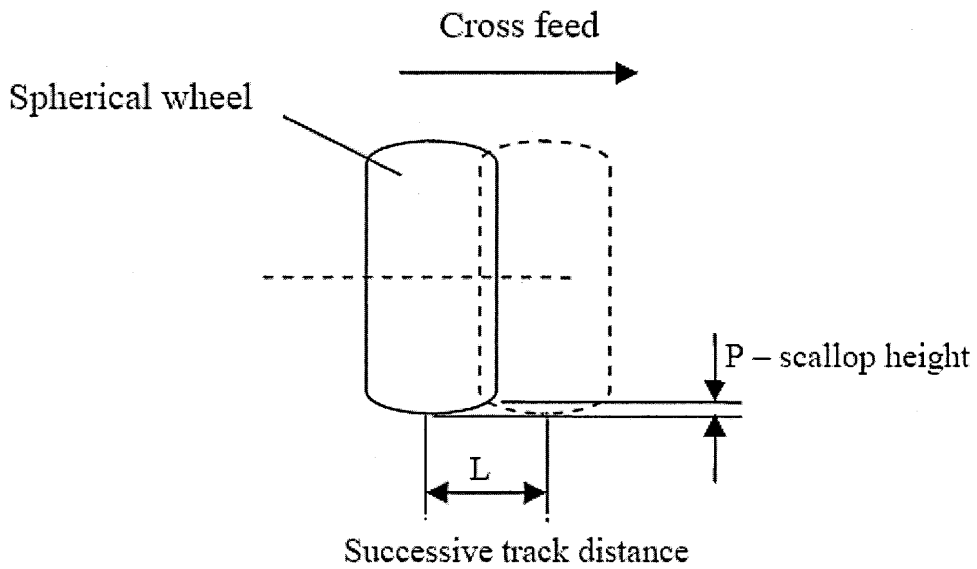
Figure 4.12: Kinematic scallop generated by a spherical wheel

The process scallops are created by the successive active grits on the wheel surface as shown in Figure 4.13.
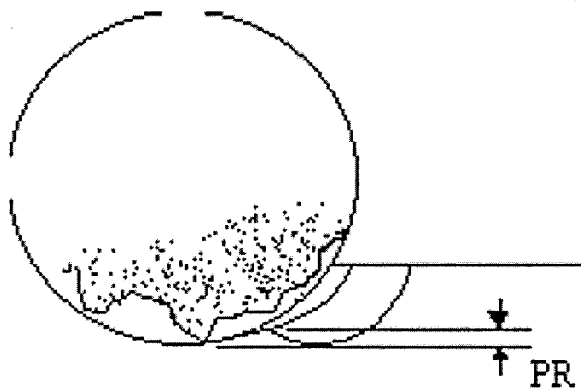
Figure 4.13: Process scallops generated by successive active grits

Through the use of the spherical wheel, kinematic scallops geometrically contribute to the shape accuracy and roughness of a ground surface hence, it is necessary to analyse them.
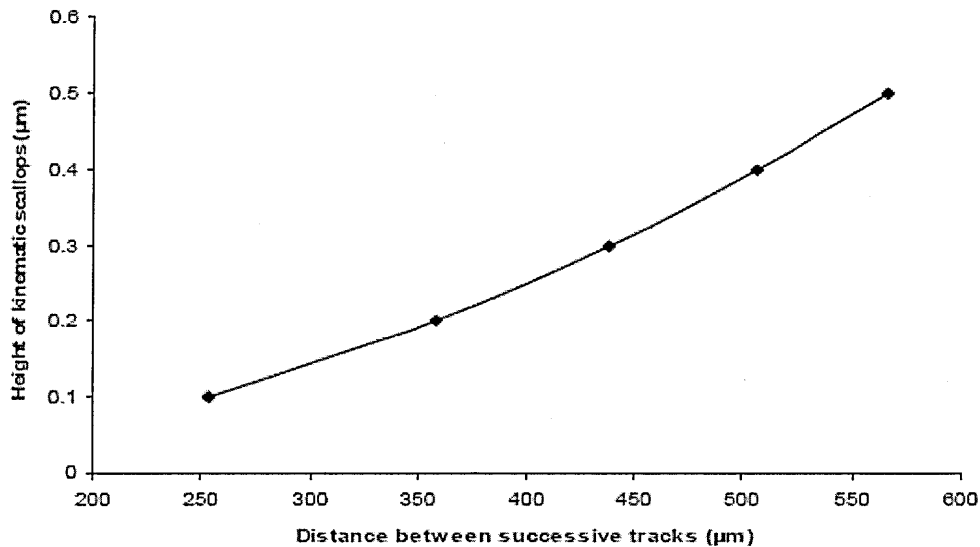
Figure 4.14: Kinematic scallop heights on a flat surface with varying distance between successive tracks

Provided the depth of cut is higher than the scallop height, the smaller the distance between the successive tracks, the greater the overlap between two tracks and the lower the scallops. Based on flat surface grinding using a spherical wheel of diameter 0.08m, the relationship between the scallop height and successive track distance is indicated in Figure 5. From the figure, if a scallop of 0.1 μm height is generated on a flat surface, the distance between successive tracks of the grinding wheel is 253 μm. The successive track distance value could be different for different shapes of ground surfaces. For a 0.1m radius concave part, the successive track distance for a maximum scallop height of 0.1 μm is 566 μm; for a 0.03m radius convex part, the distance is 132 μm. This indicates that different shape of the ground surface will display a different density of grinding tracks on the ground surfaces for a given scallop height.

In terms of industrial application, the difference in distance between successive tracks translates into an increase or a decrease in processing time and thus defines the efficiency of the grinding process. The target kinematic scallop for the Nanogrind project was 0.1 μm and that defined the distance of successive tracks on the flat workpieces that were ground with the spherical wheel. A larger kinematic scallop would mean that a larger polishing step would be necessary in order to remove the surface roughness induced by the presence of scallops. The necessity rises once more for an efficient trade off between grinding time and the follow-up polishing time (step necessary in order to remove scallops and sub-surface damage potentially induced in the sample while processing) in order to acquire the final component with minimal or even no damage at all, at a reasonable production rate.

CHAPTER 5: CONCLUSIONS

5.A CONCLUSIONS

I. Surface integrity and acoustic emission experiments indicated that ELID grinding with a fine grit size cup wheel was less likely to encounter wheel loading compared to a resin bonded wheel when the wheel/workpiece contacting area increased. This effect is attributed to the removal of friable oxide layer and grinding debris during the in-process dressing stage of the ELID process. Therefore, ELID grinding is recommended for use in efficient precision grinding, when components are relatively large. The significant increase in AE amplitude for the resin-bond wheel corresponded to severe rubbing on the ground surface. This indicated that a resin bond wheel could not perform effective self dressing when the wheel/workpiece contacting area was large. The resin bond wheel became loaded, with blunt grits that could not perform efficient cutting and thus was rendered inefficient during grinding. This effect lead to the presence of big defects on the components produced.

II. The beneficial effect of the oxide layer growth when grinding with ELID was demonstrated through the use of the innovative no-grit wheel. At lower wheel speeds than grinding, in a hybrid situation between a constant displacement/constant force material removal process, the oxide was used in the secondary grinding zone in a dual role- as a polishing and lubrication medium- in the contact area between the wheel and the workpiece. Thinning and thickening of the oxide layer (varying between 2 and 6μm) affected the final surface finish which was another indication that the oxide layer does more than just expose sharper grits by its removal. Excellent correlation between varying oxide layer thickness and surface finish achieved proves the benefits of the presence of oxide. The presence of thicker oxide lead to surface finish values of 5nm R_a whereas thinning of the oxide layer lead to Ra values of 20nm R_a. Measuring current intensity during ELID

grinding proved to be a promising in-process monitoring technique as, excellent correlation was observed between achieved surface finish and changes in the current that flowed through the circuit. Increased current values led to lower quality surface finish whereas lower current values, translated into higher quality surface finish.

III. Through electrochemical impedance spectroscopy measurements, charge transfer resistance was successfully estimated. Very good correlation was achieved between charge transfer resistance values and oxide layer thickness on the grinding wheel segments. Experiments performed in an aggressive NaCl environment proved the change in charge transfer resistance R_t with the change of the oxide layer thickness. R_t was around 440Ω when no oxide is present and increased to approximately 12,000Ω with a fully grown oxide layer of approximately 60μm. The necessity of observing voltage oscillation of just a few hundred mV which are difficult to detect when ELID voltage applied is around 60V limit the possibility of application of EIS for in-process monitoring purposes.

IV. Critical chip thickness theory applied to the experiments undertaken with resin bond wheels identify a transition region from brittle to ductile material removal where less damage is introduced in the workpiece. Excellent correlation of ELID experimental sub-surface damage results with the depths predicted with the Zhang/Howes model was achieved. Correlation to critical chip thickness theory was not as successful, as the predicted critical chip thickness values (around 40-70nm) are much higher than the ones experimentally observed.

V. A balance in the production speed of components through ELID grinding and the amount of damage introduced was very important. The choice of optimum processing parameters that reduce polishing steps, rendering the process more time efficient and providing better shape accuracy was highlighted, along with the

importance of removing pre-existing sub-surface damage (e.g. from preparative rough grinding) from the processed samples.

VI. The work that was undertaken during this project was primarily aimed towards the optimization of process parameters for ELID grinding, as it is the processing method chosen for the Nanogrind project and the machine tool that will be constructed at the end of it. The Nanogrind machine will be equipped with an ELID power supply and the spherical wheel previously described that will allow processing of more intricate component geometries, such as freeform optics, to a high quality specification.

CHAPTER 6: FUTURE WORK

6.A FUTURE WORK

I. The observed difference between theoretical predictions on critical chip thickness and experimental results observed suggest that a model that would incorporate ELID parameters (e.g. active grit concentration, ELID current) as well as material properties of the components could potentially be more accurate. Further theoretical work in that direction is thus necessary in order to obtain a modeling tool that can accurately predict ELID critical chip thickness.

II. The initial results on grinding fluid conductivity and its increase with grinding time is of interest; as are the potential effects of these conductivity changes on the grinding process. Further investigation is necessary in order to estimate the effects on the surface and shape integrity of the grinding wheels and the final components.

REFERENCES

REFERENCES

[1] www.roymech.co.uk,
www.roymech.co.uk/Useful_Tables/Manufacturing/Grinding.html

[2] F. H. Zhang, Z. J. Qiu, G. W. Kang, Z. J. Yuan, Y. S. Yang and X. K. Shi, *"High efficiency ELID grinding of garnet ferrite"*, Journal of Materials Processing Technology, Volume 129, Issues 1-3, October 2002, pp 41-44

[3] T. Bifano, T. Dow and R. O. Scattergood, *"Ductile-regime grinding of brittle materials: Experimental results and the development of a model"*, SPIE 966 (1988) pp 108-115.

[4] P. N. Blake and R. O. Scattergood, *"Ductile Regime Machining of Germanium and Silicon"*, Journal Am. Ceram. Soc., 73 (1990) pp 949-957.

[5] D. J. Stephenson, *"Surface Integrity Control During The Precision Machining Of Brittle Materials"*, AZojomo, Journal of materials online (ISSN 1833-122X) Volume 2, March 2006

(This paper was also published in print form in "Advances in Technology of Materials and Materials Processing", 8[4] (2006), pp13-22)

[6] S. M. Booij, H. van Brug, J. J. M. Braat, O.W. Fa¨hnle, *"Nanometer deep shaping with fluid jet polishing"*, Optical Engineering, Vol. 41 No. 8, August 2002 pp 1926-1931

[7] M. C. Shaw, *"Principles of abrasive processing"*, Oxford University Press, UK, (1996)

[8] D. J. Stephenson, D. Veselovac, S. Manley and J. Corbett, *"Ultra-precision grinding of hard steels"*, Precision Engineering, Volume 25, Issue 4, October 2001, pp 336-345

{**Weinert in [8]**}, Weinert K, Willsch C., Beitrag zum Vergleich der Oberflachenqualitat beim Seitenschleifen und Umfangsschleifen von Hartmetall. In: Jahrbuch 'Schleifen, Honen, Lappen, und Polieren', Vulkan-Verlag, 1993;57, pp162–170.

[9] B. Zhang, T.D. Howes, *Subsurface evaluation of ground ceramics*, Annals of the CIRP, Vol.44, No1, (1995) pp.263-266

[10] I. Inasaki, *Grinding of hard and brittle materials*, Annals of the CIRP, Vol.36, (1987) pp.1-9

[11] M.C. Shaw, *Precision finishing*, Annals of the CIRP, Vol.44, No1, (1995) pp.343-348

[12] B. R. Lawn and D B Marshall, *"Hardness, Toughness and Brittleness: An Indentation Analysis"*, Journal Am. Ceram. Soc, 62 (1979) pp 347-349.

[13] H. Ohmori, T. Nakagawa, *"Analysis of mirror surface generation of hard and brittle materials by ELID (Electrolytic In-Process Dressing) - Grinding with superfine grain metallic bond wheels"*, Annals of the CIRP, Vol.44, No1, (1995) pp.287-290

[14] A. Büttner, D.A. Lindenbeck "Electrolytic dressing of diamond wheels for use in grinding steels", *Industrial Diamond Review,* November 1969

[15] H. Ohmori, T. Nakagawa, *"Mirror surface grinding of silicon wafers with Electrolytic In-Process Dressing"*, CIRP, Vol. 39, issue 1, (1990) pp. 329-332

[16] B.P. Bandyopadhyay, H. Ohmori, W. Li, A. Makinouchi, *"Efficient and Precision Grinding of Small hard and Brittle Cylindrical Parts by the Centerless Grinding Process with Electro-Discharge Truing and Electrolytic In- Process Dressing"* J. of Mat. Proc. Tech. Vol.98, Issue 3 (2000) pp. 322-327

[17] N. Itoh, H. Ohmori, *"Grinding Characteristics of Hard and Brittle Materials by Fine Grain Lapping Wheels with ELID"*, J. of Mat. Proc. Tech. Vol.62 (1996) pp. 315-320

[18] B.P. Bandyopadhyay, H. Ohmori, *"The effect of ELID grinding on the flexural strength of silicon nitride"* Int. J. of Machine Tools and Manuf. Vol. 39, Issue 5 (1999) pp. 839-853

[19] B.P. Bandyopadhyay, H. Ohmori, I. Takahashi, *"Efficient and Stable Grinding of Ceramics by ELID1"* J. of Mat. Proc. Tech. Vol.66 (1997) pp. 18-24

[20] J. Qian, W. Li, H. Ohmori. *"Cylindrical grinding of bearing steel with electro lytic in-press dressin"* Precision Eng. Vol.24, Issue 2, (2000) pp.153-159

[21] I.D. Marinescu, C. Miyakawa, H. Ohmori, J. Shibata, *"ELID grinding characteristincs of Silicon Wafers"* Proc. 1st International Conference and general Meeting of the European Society for Precision Engineering and Nanotechnology (ISBN 3-8265-6085-X), pp380-383 (1999)

[22] M. Asami, Y. Fukaya, H. Ohmori, M. Anzai, I. Takahashi, A. Makinouchi, *"High efficiency, Stable and recision grinding for cutting tools fabrication applying ELID technique"*, Proc. 1st International Conference and general Meeting of the European Society for Precision Engineering and Nanotechnology (ISBN 3-8265-6085-X), pp372-375 (1999)

[23] P.A. Beltrao, A.E. Gee, J. Corbett and R.W. Whatmore, *"The use of the ELID method to assist in the "Ductile Machining of Ferroelectric Ceramics"* Proc. 1st International Conference and general Meeting of the European Society for Precision Engineering and Nanotechnology (ISBN 3-8265-6085- X), pp470-473 (1999)

[24] Y. Watanabe, K. Katahira, H. Ohmori, T. Kato, A. Kawana, *"ELID grinding and tribological characteristics of TiAlN film"*, Proc. Of the 3rd euspen International conference, Eindhoven, The Netherlands, Vol. 2, (2002) pp 703-706 (2002)

[25] P. Morantz, C. Maeda, H. Ueda, *"Ultra-precision machining hard metals: turning versus grinding"*, Proc. Of the 3rd euspen International conference, Eindhoven, The Netherlands, Vol. 1, (2002) pp 353-356 (2002)

[26] K. Sawada, A. Yamamoto, H. Ohmori, Y. Yutaka, S. Moriyasu, Y. Muramatsu *"Study on ELID grinding for quartz blank"* RIKEN Review, Vol. 34, pp. 29-34, (2001)

[27] N. Itoh, H. Ohmori, S. Morita, H. Ishibashi, C Uetake, T. Kasai *"Characteristics of ELID grinding of by cast –iron bonded diamond wheel"* RIKEN Review, Vol. 34, pp. 9-12, (2001)

[28] Y. Uehara, H. Ohmori, Y. Yamagata, S. Moriyasu, A. Makinouchi, S. Morita *"Microfabrication grinding by ultraprecision microform generating machine employed with lasma discharge truing and ELID technique"* RIKEN Review, Vol. 34, pp. 25-28, (2001)

[29] H. Ohmori, "Electrolytic in-process dressing (ELID) grinding technique for ultraprecision mirror surface machining" *Int. J. Japan. Soc. Prec. Eng.* Vol.26, Issue 4 (1992), pp. 273-278.

[30] F. Zhang, G. Kang, Z. Qiu, Y. Yang, X. Shi, *"High Efficiency ELID Grinding of Alumina Ceramics"* Key Engineering Materials, Vols.238-239, (2003), pp. 71-76.

[31] T. Suzuki, H. Ohmori, Y. Dai, W. Lin, K. Katahira, A. Manicouchi, H. Tashiro, H. Yokota, M. Suzuki, T. Abe, T. Shimasaki *"Ultraprecision fabrication of glass ceramic aspherical mirrors by ELID grinding with a nano-level positioning Hydrostatic drive system"* Key Engineering Materials, Vols.238-239, (2003), pp. 49-52.

[32] S.W. Lee, H.Z. Choi, H. Lee, J. Choi, H.D. Jeong *"A study of micro tool machining using electrolytic in-process dressing and an evaluation of the characteristics "* Key Engineering Materials, Vols.238-239, (2003), pp. 35-40.

[33] www.ajexdiamond.com/wheels.htm

[34] K. Fathima, A. Senthil Kumar, M. Rahman, H.S. Lim, *"A study on wear mechanism and wear reduction strategies in grinding wheels used for ELID grinding"*, Wear, Vol. 254, (2003), pp.1247-1255

[35] F. H. Zhang, Z. J. Qiu, G. W. Kang, Z. J. Yuan, Y. S. Yang and X. K. Shi, *"High efficiency ELID grinding of garnet ferrite"*, Journal of Materials Processing Technology, Vol. 129, Issues 1-3 , pp. 41-44, (2002)

[36] Y. Pan, T. Sasaki, N. Ito, H. Ohmori, Y. Yamagat, Y. Uenara, W. Lin, "An ELID grinding system with a minimum quantity of Liquid", *Key Engineering Materials,* Vols.238-239, (2003), pp. 23-28.

[37] H. Ohmori, T. Nakagawa, "Utilization of non-linear conditions in precision grinding with ELID (Electrolytic In-Process Dressing) for fabrication of hard material components" *Annals of the CIRP.*, Vol. 46, Issue 1, pp. 261-264, (1997)

[38] H.W. Kim, J.H. Ahn, Y.H. Seo, *"Study on the estimation of wheel state in Electrolytic In-process Dressing (ELID) grnding"*, ISIE 2001, Pusan, Korea, pp 1615-1618 (2001)

[39] H.W. Kim, J.H. Ahn, Y.H. Seo, I.H. Paik, *"In-process measurement of ELID grinding status - thickness of insulating layer "*,KSME international journal, vol. 15, n°9, pp. 1268-1273, (2001)

[40] E.S. Lee, J.D. Kim, *"A study on the analysis of grinding mechanism and development of dressing system by using optimum in-process electrolytic dressing"* Int. J. Mach. Tools Manufact., Vol. 37(12), pp 1673-1689 (1997)

[41] Nanogrind deliverable D_22

[42] J. Qian, H. Ohmori, W. Lin, *"Internal mirror grinding with a metal/metal-resin bonded abrasive wheel"* Int. J. of Machine Tools and Manuf. Vol. 41, Issue 2 (2001) pp. 193-208

[43] R.S. William, *Static and dynamic electricity*, 3rd edition, Hemisphere Publishing Corporation, 1989.

[44] M. Rahman, A. Senthil Kumar, H. S. Lim and K. Fatima, *Nano finish grinding of brittle materials using electrolytic in-process dressing (ELID) technique*, SADHANA - Academy Proceedings in Engineering Sciences, Vol. 28, Part 5, October 2003, pp. 957–974.

[45] T. Matsuzawa, H. Ohmori, N. Itoh, *"Development and grinding effect of ELID3 grinding method"*, Proc. 1st International Conference and general Meeting of the European Society for Precision Engineering and Nanotechnology (ISBN 3-8265-6085-X), pp. 282-285 (1999)

[46] N.Itoh, H. Ohmori, T. Kasai, Y. Yaamoto, S. Moriyasu, S. Morita, *"Mirror Surface finishing on double sided lapping machine with ELID"* Proc. 1st International Conference and general Meeting of the European Society for Precision Engineering and Nanotechnology (ISBN 3-8265-6085-X), pp. 266-269 (1999)

[47] K. Katahira, H. Ohmori, J. Nagata, M. Mizutani, J. Komotori, Y. Watanabe, "Fabirication of high-quality surfaces on biomaterials usinga new electrical grinding technique", Proc. Of the 3rd euspen International conference, Eindhoven, The Netherlands, Vol. 1, (2002) pp 217-220 (2002)

[48] H. Ohmori,W. Lin, S. Moriyasu, Y. Yamagata "Microspherical lens fabrication by cup grinding wheels applying ELID grinding" RIKEN Review, Vol. 34, pp. 3-5, (2001)

[49] L C Zhang and N Yasunaga , *Advances in abrasive technology*, Abrasives Mall, (1999)

[50] N. Itoh, H. Ohmori, "Development of Metal free Conductive Bonded Diamond Wheel for Environmentally-Friendly Electrolytic In-Process Dressing (ELID) Grinding", *New Diamond and frintier Carbon technology*, Vol. 14, No. 4, pp. 227-238 (2004)

[51] T. Kato, N. Itoh, H. Ohmori, K. Katahira, W. Lin and K. Hokirigawa, *"Estimation of Tribological Characteristics of Electrolyzed Oxide Layers on ELID-Grinding Wheel Surfaces"*, Key Engineering Materials, pp. 257-262 (2004)

[52] FUJI Die Co., Ltd.: *www.fujidie.co.jp*

[53] J.D. Kim, E.S. Lee, *"A study of the mirror-like grinding of sintered carbide with optimum in-process electrolytic dressing"* Int. J. Adv. Manufact. Technol, Vol. 15., pp. 215-623 (1999)

[54] D. Kramer, F. Rehsteiner, *"ECD (Electrochemical In –Process Controlled dressing), a new method for grinding of modern high performance cutting materials to highest quality"*, Annals of the CIRP, Vol. 48, No. 1, pp. 265-268, (1999)

[55] H.S. Lim, K. Fathima, A. Senthil Kumar, M. Rahman, *"A fundamental study on the mechanism of electrolytic in-process dressing (ELID) grinding"*, Int. J. of Machine Tools & Manuf., Vol. 42, pp.935-943, (2002)

[56] G. W. Walter, *"A review of impedance plot methods used for corrosion performance analysis of painted metals"*, Corrosion Science, Vol.26, No.9, pp.681-703, (1986)

[57] F. Mansfeld, M.W. Kendig, S. Tsai. *"Evaluation and Corrosion Behaviour of Coated Metals with AC Impedance Measurements"*, Corrosion-NACE, Vol. 38, No. 9, pp.478-485, (1982)

[58] F. Mansfeld. *"Recording and Analysis of AC impedance Data for Corrosion Studies I. Background and methods of Analysis"*, Corrosion-NACE, Vol. 36, No. 5, pp.301-307, (1981)

[59] W.J. Lorenz, F. Mansfeld. *"Determination of Corrosion Rates by Electrochemical DC and AC Methods"*, Corr. Science, Vol. 21, No.9, pp.647-672, (1981)

[60] A.A. Aksut, W.J. Lorenz, F. Mansfeld, *"The Determination of Corrosion Rates by Electrochemical D.C. and A.C. Methds. –II. Systems with Discontinuous Steady State Polarisation Behaviour"*, Corr. Science, Vol. 22, No. 7, pp.611-619, (1982)

[61] F. Mansfeld, M.W. Kendig. *"Impedance Spectroscopy as Quality Control and Corrosion Test for Anodized Aluminium Alloys"*, Corrosion-NACE, Vol. 41, No. 8, pp.490-492, (1985)

[62] F. Mansfeld, M.W. Kendig, S. Tsai. *"Recording and Analysis of AC impedance Data for Corrosion Studies II. Experimental Approach and Results"*, Corrosion-NACE, Vol. 38, No. 11, pp.570-580, (1982)

[63] F. Mansfeld, M.W. Kendig, S. Tsai. *"Evaluation and Corrosion Behaviour of Coated Metals with AC Impedance Measurements"*, Corr. Science, Vol. 22, No. 5, pp.455-471, (1982)

[64] F. Mansfeld, S.L. Jeanjaquet, M.W. Kendig, *"An Electrochemical Impedance Spectroscopy Study of Reactions at the Metal/Coating Interface"*, Corr. Science, Vol. 26, No.9, pp.735-742, (1986)

[65] GAMRY Instruments
www.gamry.com/App_Notes/EIS_Primer/ EIS_Primer.htm

[66] T.W. Hwang, *"Acoustic emission monitoring of high speed grinding of silicon nitride"*, Ultrasonics , Vol. 38, pp. 614-619 (2000)

[67] W. Hundt, *"An approach to monitoring of the grinding process using acoustic emission (AE) technique"*, Annals of the CIRP Vol. 43, issue 1, pp. 295–298 (1994)

[68] T.G. Bifano, Y. Yi, *"Acoustic emission as an indicator of material-removal regime in glass micro-machining"*, Precision Engineering Vol. 14, issue 4, pp. 219-228 (1992)

[69] D. Dornfeld , H.G. Cai. *"An investigation of grinding and wheel loading using acoustic emission"*, Transactions of ASME , Vol. 106, pp.28-33 (1984)

[70] H.V. Ravindra, Y.G. Srinivasa, R. Krishnamurthy, *"Acoustic emission for tool condition monitoring in metal cutting"*, Wear, Vol. 212, pp. 78-84 (1997)

[71] A.A. Mokbel, T.M.A. Maksoud, *"Monitoring of the condition of diamond grinding wheels using acoustic emission technique"*, Journal of Materials processing Technology , Vol. 101, (2000)

[72] R.E. Williams, *"Acoustic emission characteristics of abrasive flow machining"*, Transactions of the ASME: Journal of Manufacturing Science and Engineering, Vol. 120, pp. 264-271 (1998)

[73] R. Teti, U. La Commare, *"Cutting conditions and work material state identification through acoustic emission methods"*, Annals of the CIRP, Vol. 41, Issue 1, pp. 89-92 (1992)

[74] C.M. Valente, D. Dornfeld, *"Analysis of Tool and Workpiece Interaction in Diamond Turning using Graphical Analysis of Acoustic Emission"*, posted at the eScholarship Repository, University of California,
(http://repositories.cdlib.org/lma/pmg/2002 valente), (2003)

[75] N. Taniguchi, *"Current status in, and future trends of, ultraprecision machining and ultrafine materials processing"*, Annals of the CIRP, Vol. 32, Issue 2 (1983)

[76] *Nano Grind*, Project number:GRD1-2001-40538, Start/End date: 01.06.2002-30.06.2006
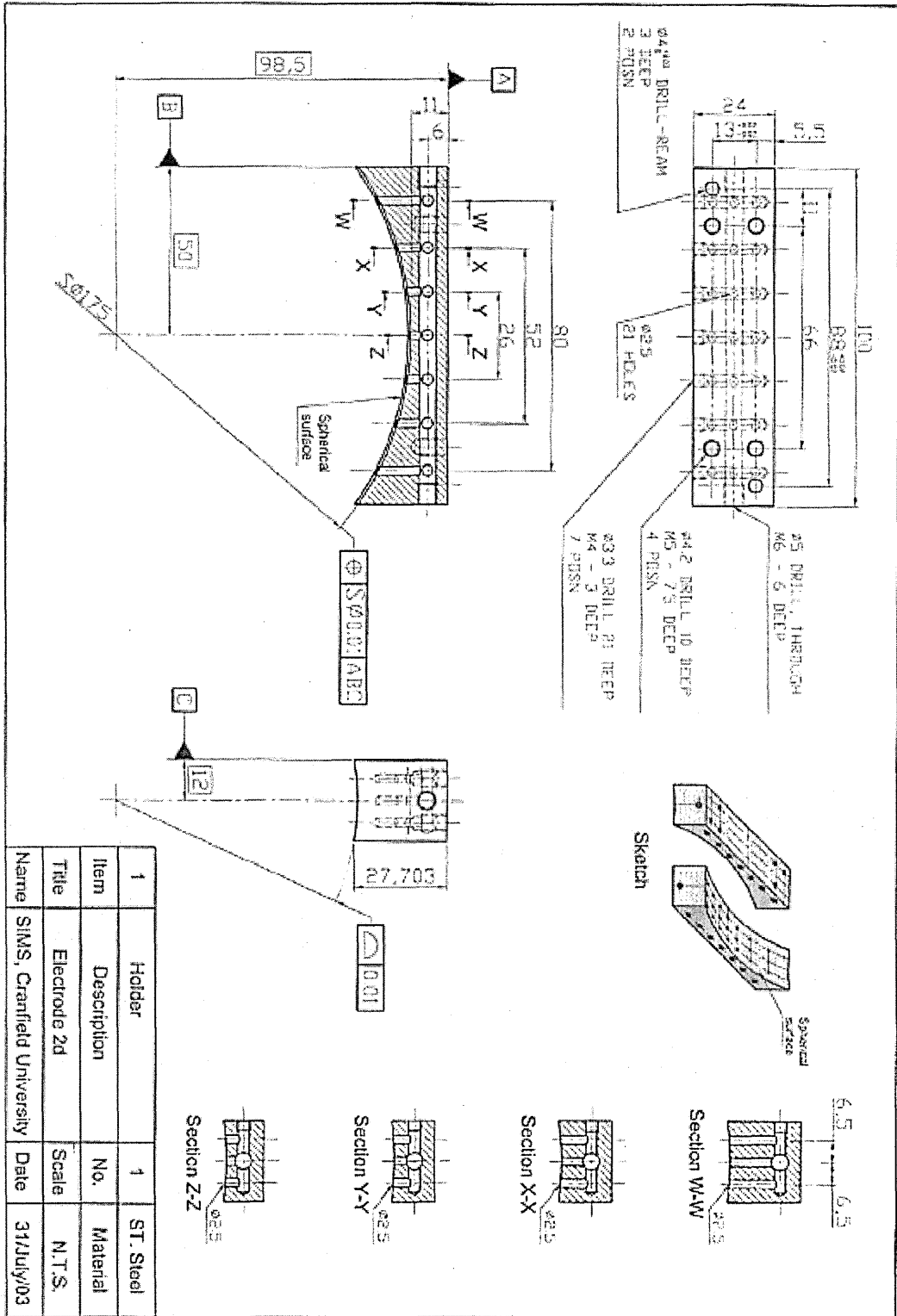http://nanogrind.euspen.com

[77] T. Matsuzawa, H. Ohmori, etc., *"Micro-Spherical Lens Mold Fabrication by Cup-Type Metal-Bond Grinding Wheels Applying ELID (Electrolytic In-Process Dressing)"*, Key Engineering Materials, Vol. 196, pp. 167-176 (2001)
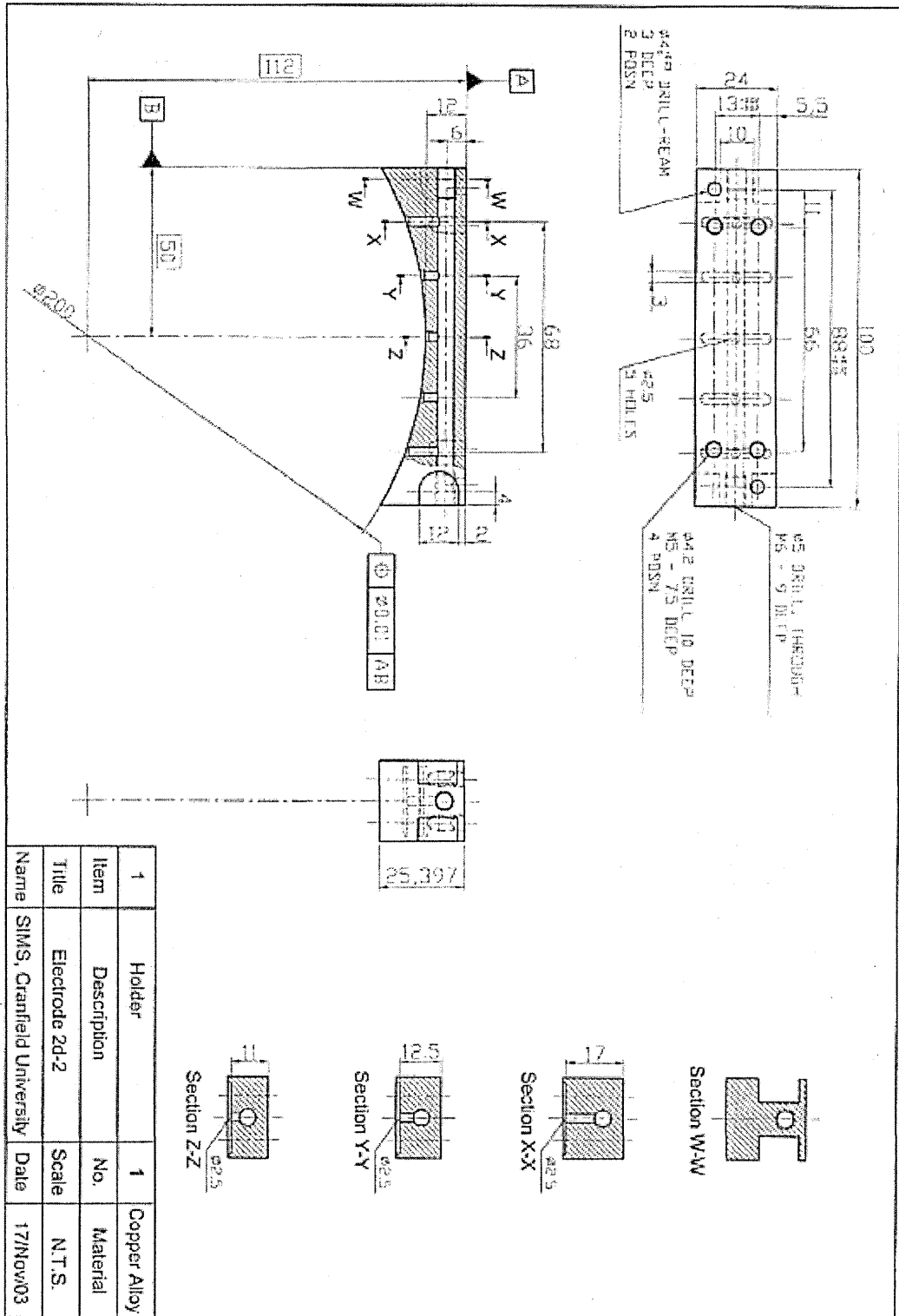
[78] J. Franse, *"Aspects of Precision (Part roughness, form accuracy and a basic study of the brittle to ductile removal transition)"*, PhD Thesis, (1991)
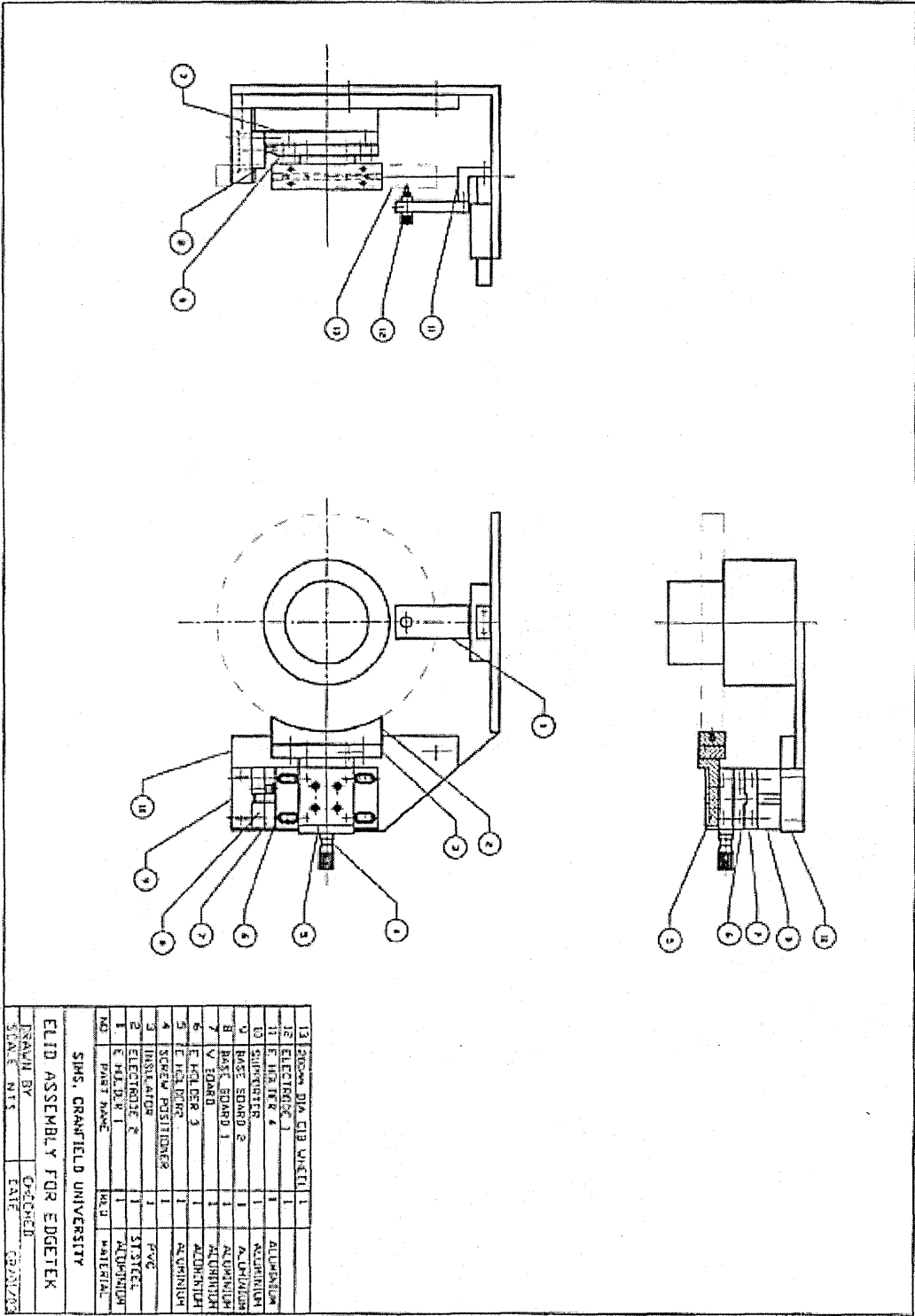
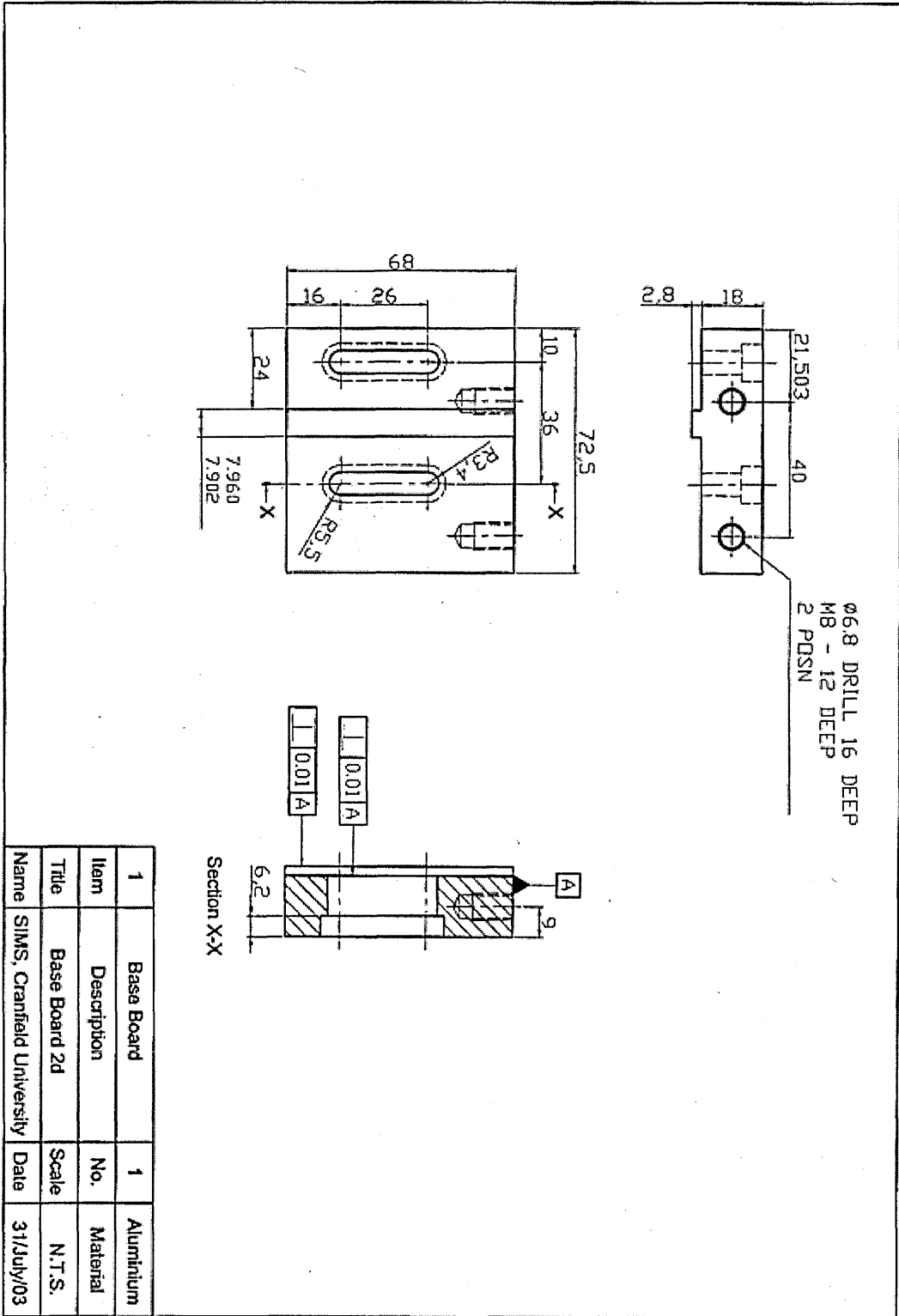[79] J. Kruger, *"Electrochemistry of corrosion"*, The Johns Hopkins University Baltimore, MD 21218, USA, *http://electrochem.cwru.edu/ed/encycl/index-tc.html*
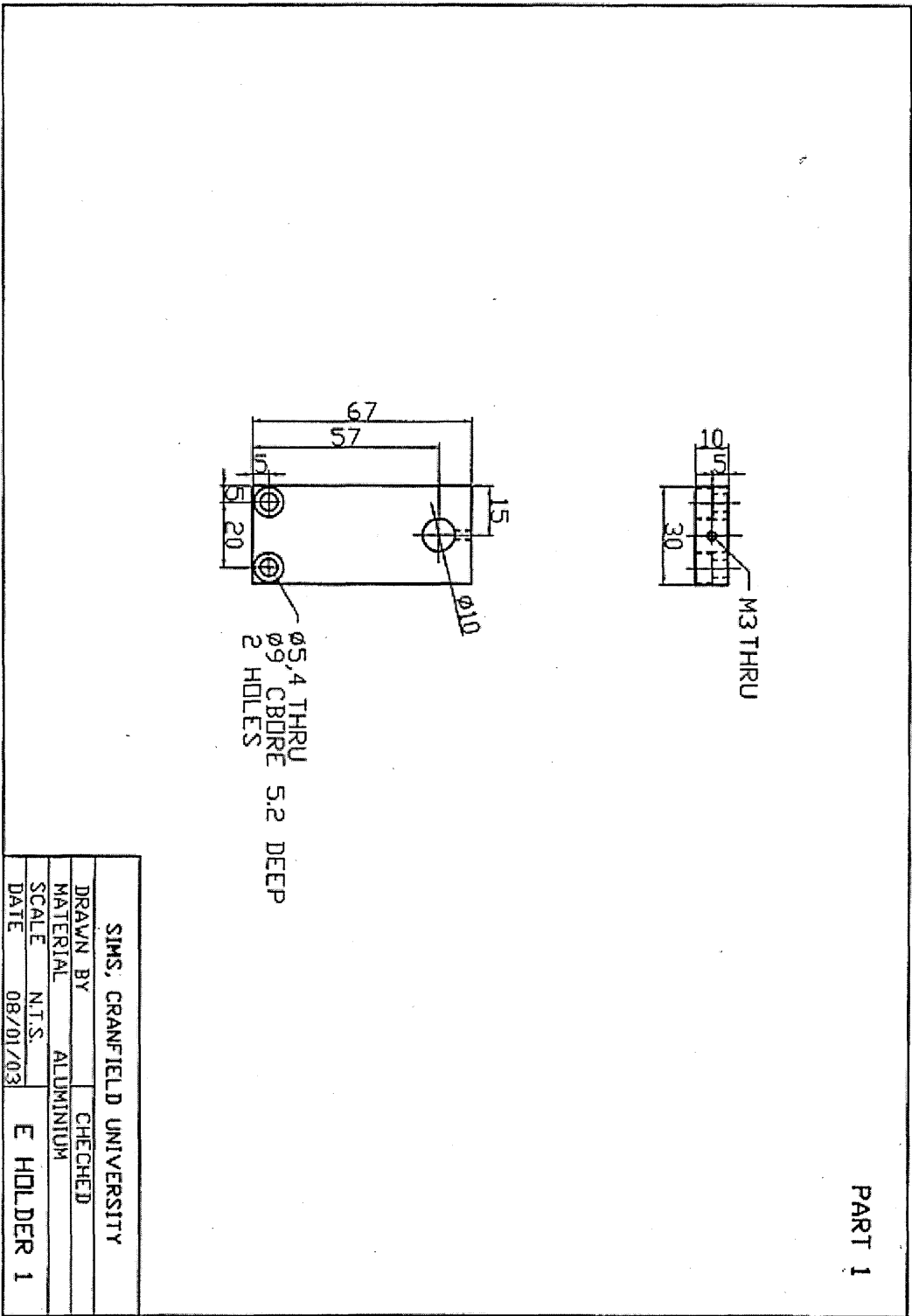
APPENDIX

Appendix 1
ELID electrode for spherical grinding wheel and peripheral wheel, and parts of electrode holder

Item	Description	No.	Material
1	Holder	1	Copper Alloy

Title	Electrode 2d-2	Scale	N.T.S.
Name	SIMS, Cranfield University	Date	17/Nov/03

Section W-W

Section X-X — 17

Section Y-Y — 12.5

Section Z-Z — 11

Section X-X

1		Base Board	
Item	Description	No.	Aluminium
Title	Base Board 2d	Scale	Material
Name	SIMS, Cranfield University	Date	31/July/03
			N.T.S.

Ø6.8 DRILL 16 DEEP
M8 - 12 DEEP
2 POSN

67
57
15
ø10

ø5,4 THRU
ø9 CBORE 5.2 DEEP
2 HOLES

5
20

10
5
30

M3 THRU

PART 1

SIMS, CRANFIELD UNIVERSITY	
DRAWN BY	CHECHED
MATERIAL	ALUMINIUM
SCALE	N.T.S.
DATE	08/01/03
E HOLDER 1	

SIMS, CRANFIELD UNIVERSITY

DRAWN BY	CHECHED	
MATERIAL	PVC	
SCALE	N.T.S.	INSULATOR
DATE	08/01/03	
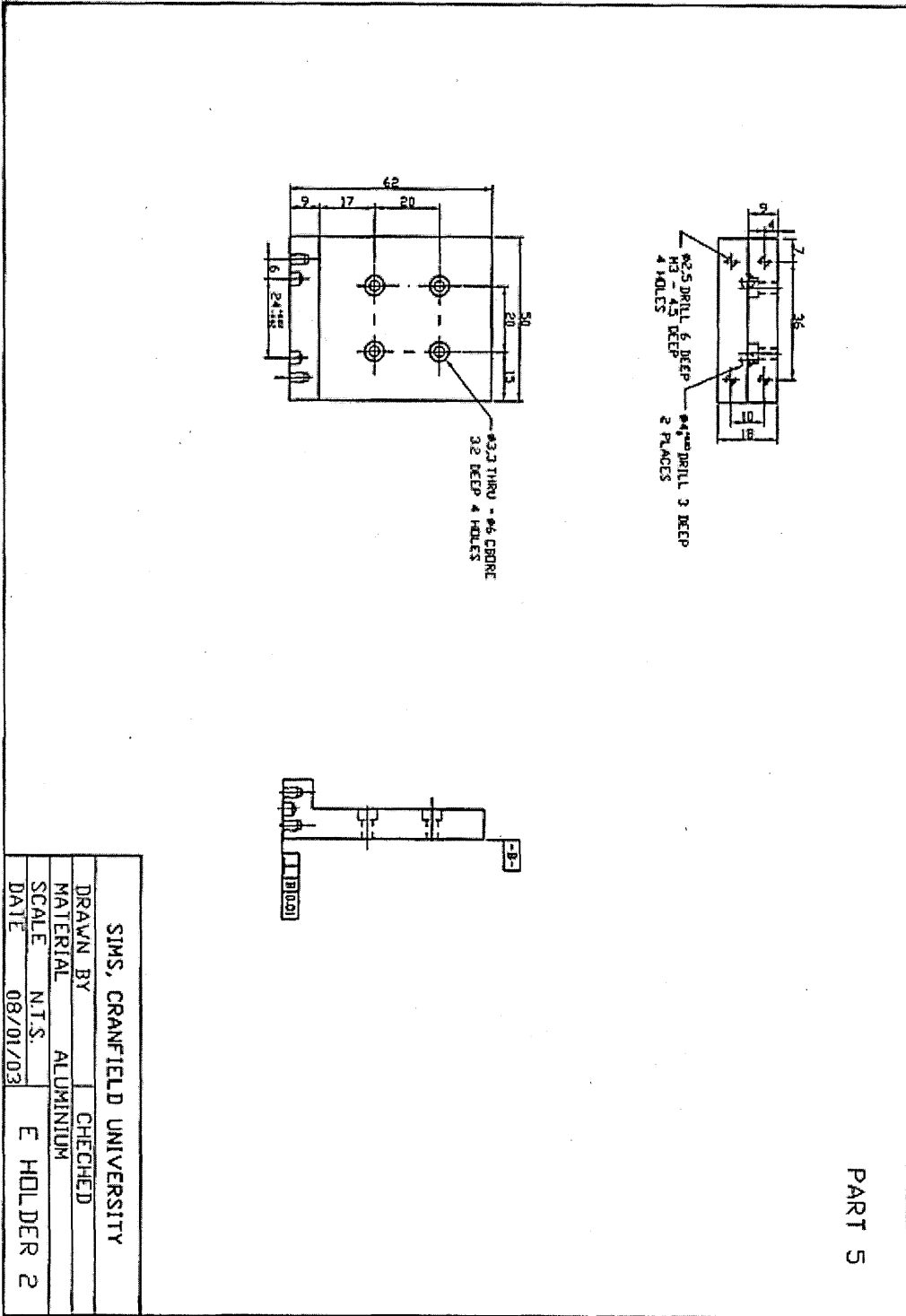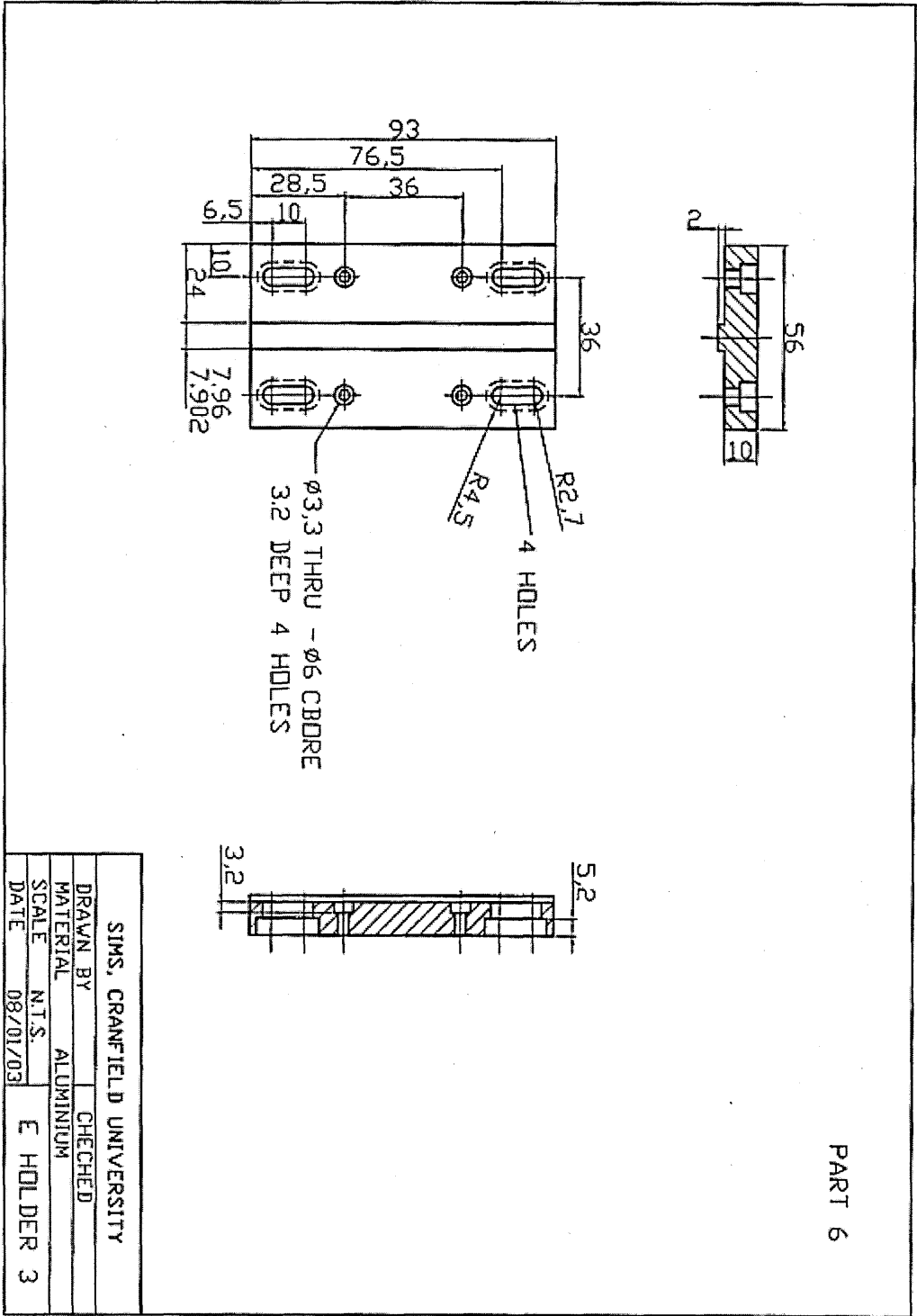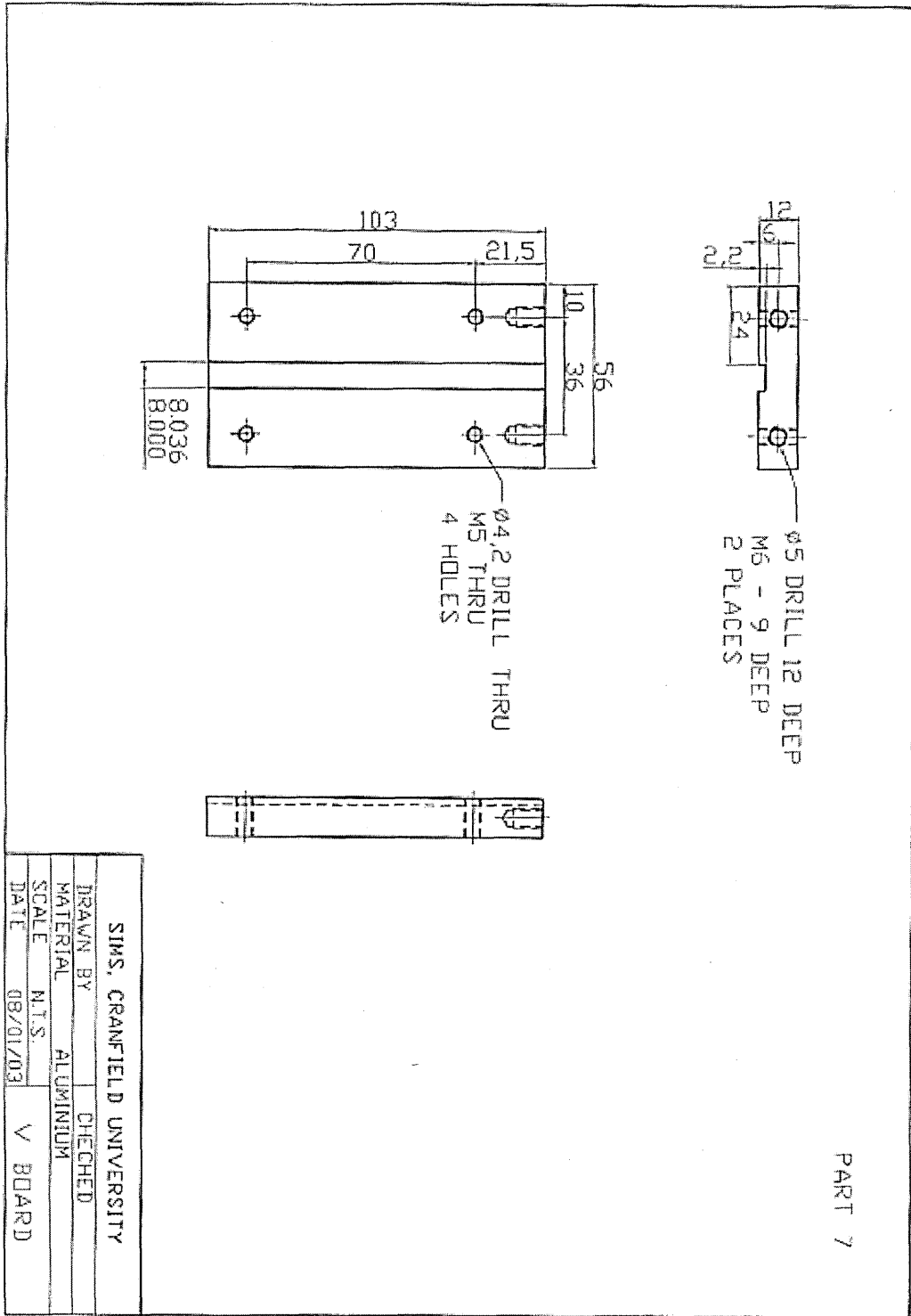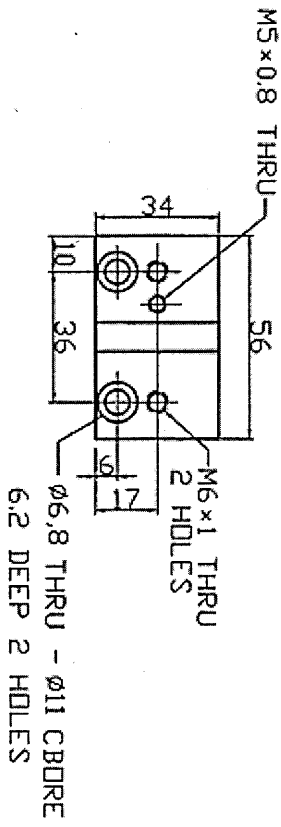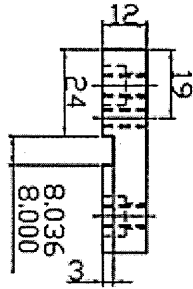
PART 3

$\emptyset$3.3 THRU
P6 CBORE 32 DEEP
4 HOLES

$\emptyset$5.4 THRU
P9 CBORE 5.2 DEEP
4 HOLES

$\emptyset$3.9DRILL 6 DEEP
4 HOLES TWO SIDES

PART 5

SIMS, CRANFIELD UNIVERSITY

DRAWN BY	CHECHED	
MATERIAL	ALUMINIUM	
SCALE	N.T.S.	
DATE	08/01/03	E HOLDER 2

⌀2.5 DRILL 6 DEEP
M3 - 4.5 DEEP
4 HOLES

⌀4 DRILL 3 DEEP
2 PLACES

⌀3.3 THRU - ⌀6 CBORE
3.2 DEEP 4 HOLES

PART 8

M5×0.8 THRU

34

10

36

56

M6×1 THRU
2 HOLES

6

17

Ø6,8 THRU - Ø11 CBORE
6.2 DEEP 2 HOLES

12

24

19

8.036
8.000

3

SIMS, CRANFIELD UNIVERSITY		
DRAWN BY	CHECHED	
MATERIAL	ALUMINIUM	
SCALE	N.T.S.	
DATE	08/01/03	
BASE BOARD 1		

X

PART 9

68
16 26
7.96
7.902
24
10
R5.5
R5.5
R3.4
8
56
40

2.8 18
36
Ø6.8 DRILL 16 DEEP
M8 - 12 DEEP
2 PLACES

6.2
9

SIMS, CRANFIELD UNIVERSITY		
DRAWN BY	CHECHED	
MATERIAL	ALUMINIUM	
SCALE	N.T.S	BASE BOARD 2
DATE	08/01/03	

Ø10.8 THRU
2 HOLES

80

206.5

139

106.5

9
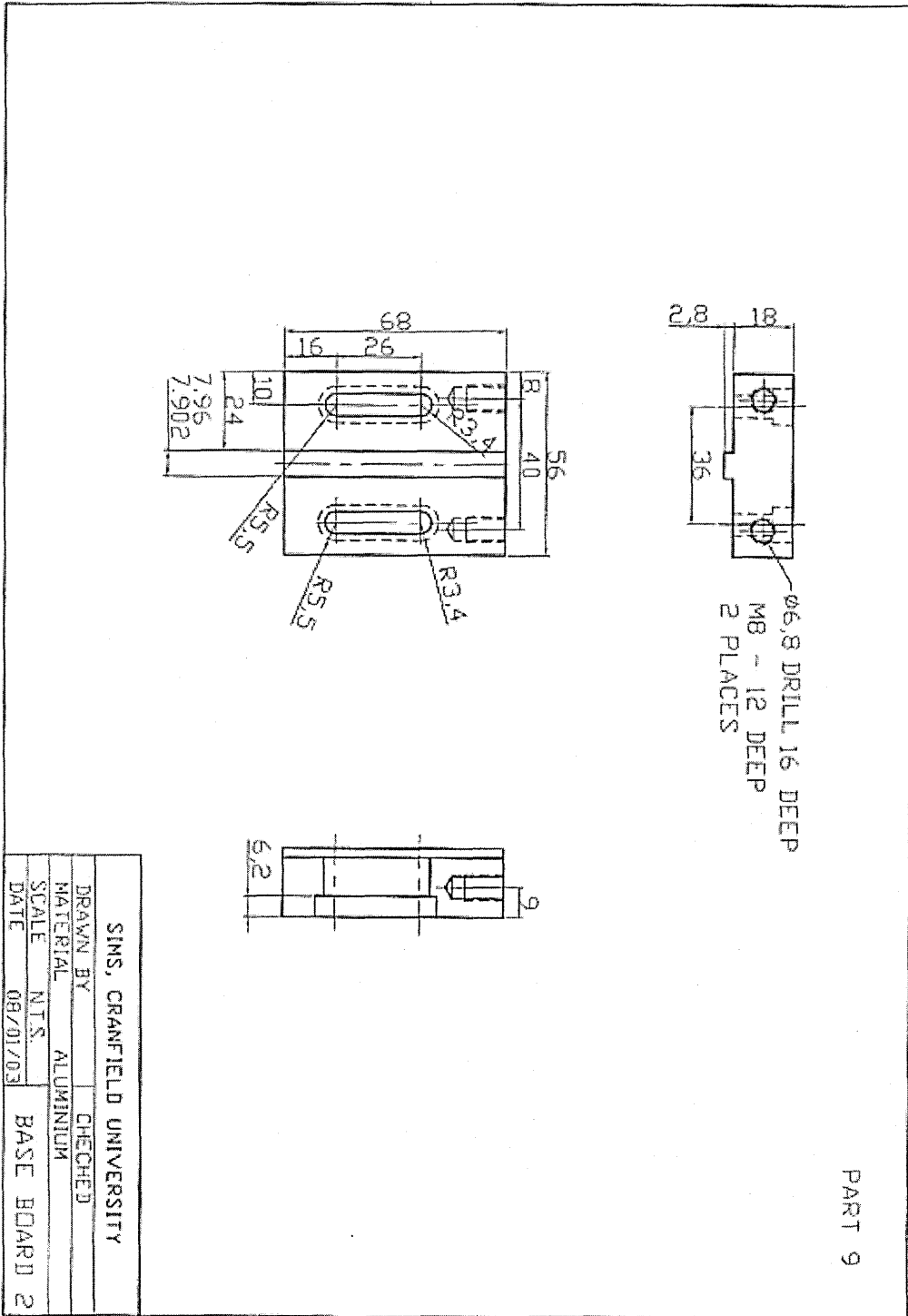
40

37

87

Ø8.8 THRU
2 HOLES

29

14

21

13

SIMS, CRANFIELD UNIVERSITY

DRAWN BY   X SUN   CHECKED

MATERIAL   ALUMINIUM

SCALE   1:1

DATE   08/01/03

SUPPORTER

PART 10

24,5

5

30

5

20

ø5,4 THRU
2 HOLES

ø4,2 DRILL-10 DEEP
M5-7.5 DEEP
2 PLACES

10

31

30

8

SIMS, CRANFIELD UNIVERSITY

DRAWN BY	CHECHED
MATERIAL	ALUMINIUM
SCALE	N.T.S.
DATE	08/01/03

E HOLDER 4

PART 11

SIMS, CRANFIELD UNIVERSITY		
DRAWN BY	CHECHED	
MATERIAL ST. STEEL	REQ	4
SCALE N.T.S.	POSITION PIN	
DATE 08/01/03		

Appendix 2
Insulating rings

Ø120

Ø90

Ø76.2

4.8

9.8

SIMS, CRANFIELD UNIVERSITY

DRAWN BY | CHECHED
MATERIAL PVC | REQ 2
SCALE N.T.S.
DATE | INSULATOR 2